

IAHS Publication 343
ISSN 0144-7815



GRACE, Remote Sensing and Ground-based Methods in Multi-Scale Hydrology

Edited by
Mohsin Hafeez

Co-Editors
*Nick van de Giesen, Earl Bardsley,
Frederique Seyler, Roland Pail &
Makoto Taniguchi*

GRACE, Remote Sensing and Ground-based Methods in Multi-Scale Hydrology



GRACE, Remote Sensing and Ground-based Methods in Multi-Scale Hydrology

Edited by

MOHSIN HAFEEZ

*International Centre of Water for Food Security (IC Water)
Charles Sturt University, Australia*

Co-Edited by

NICK VAN DE GIESEN

*Civil Engineering & Geosciences
TU Delft, Netherlands*

EARL BARDSLEY

*Department of Earth and Ocean Sciences
University of Waikato, New Zealand*

FREDERIQUE SEYLER

Directrice de Recherche IRD, France

ROLAND PAIL

*Institute of Astronomical and Physical Geodesy
Technische Universität München, Germany*

MAKOTO TANIGUCHI

*Research Institute of Humanity and Nature,
Kyoto, Japan*

Proceedings of Symposium J-H01 held during IUGG2011 in Melbourne,
Australia, July 2011

IAHS Publication 343
in the IAHS Series of Proceedings and Reports

Published by the International Association of Hydrological Sciences 2011

IAHS Publication 343

ISBN 978-1-907161-18-6

British Library Cataloguing-in-Publication Data.

A catalogue record for this book is available from the British Library.

© IAHS Press 2011

This publication may be reproduced as hard copy, in whole or in part, for educational or nonprofit use, without special permission from the copyright holder, provided acknowledgement of the source is made. No part of this publication may be electronically reproduced, transmitted or stored in a retrieval system, and no use of this publication may be made for electronic publishing, resale or other commercial purposes without specific written permission from IAHS Press.

The papers included in this volume have been reviewed and some were extensively revised by the Editors, in collaboration with the authors, prior to publication.

IAHS is indebted to the employers of the Editors for the invaluable support and services provided that enabled them to carry out their task effectively and efficiently.

The information, data and formulae provided in this volume are reproduced by IAHS Press in good faith and as finally checked by the author(s); IAHS Press does not guarantee their accuracy, completeness, or fitness for a given purpose. The reader is responsible for taking appropriate professional advice on any hydrological project and IAHS Press does not accept responsibility for the reader's use of the content of this volume. To the fullest extent permitted by the applicable law, IAHS Press shall not be liable for any damages arising out of the use of, or inability to use, the content.

The designations employed and the presentation of material throughout the publication do not imply the expression of any opinion whatsoever on the part of IAHS concerning the legal status of any country, territory, city or area or of its authorities, or concerning the delimitation of its frontiers or boundaries.

The use of trade, firm, or corporate names in the publication is for the information and convenience of the reader. Such use does not constitute an official endorsement or approval by IAHS of any product or service to the exclusion of others that may be suitable.

Publications in the series of Proceedings and Reports are available from:
IAHS Press, Centre for Ecology and Hydrology, Wallingford, Oxfordshire OX10 8BB, UK
tel.: +44 1491 692442; fax: +44 1491 692448; e-mail: jilly@iahs.demon.co.uk

Printed by Information Press

Preface

Climate change and rapid population growth pose a serious threat to global water availability, which result in changing the water cycle, sea level, and rainfall variability, and thus crop production and the frequency and scale of floods and droughts. The water cycle operates across all scales, from the global to the smallest stream catchment, and involves the movement of water in terms of precipitation, evaporation, transpiration, vapour transport, surface runoff, subsurface return flow and groundwater flow. Accurate knowledge and accounting of various hydrological processes (evapotranspiration, rainfall, runoff, and seepage, etc.) and different factors (land-use changes) affecting these hydrological processes, both spatially and temporally, is of paramount importance. The spatial scales considered can vary from pixel to continent. Ground-based measuring and monitoring techniques have very limited ability to capture the spatial and temporal variation of different hydrological variables at regional and continental scales.

Recent, state-of-the-art advances in measuring hydrological variability by means of satellite gravimetric techniques such as the Gravity Recovery and Climate Experiment (GRACE) mission, other remote sensing platforms (TRMM, Landsat and MODIS), and ground-based methods have provided a great potential to estimate spatio-temporal surface water balance, spatially-averaged water budgets, hydrodynamics, hydrological processes, and characterization of groundwater systems in gauged and ungauged basins at regional and global scales. New satellites, such as GRACE, SMOS, and METOP, are starting to generate hydrological parameters that have large potential for water managers in data sparse environments. Sensors such as radar altimeters, primarily designed for ocean or ice studies, are now used for monitoring continental waters. Optical-thermal satellites (Landsat and MODIS) have been extensively used for estimation of vegetation health parameters and actual evapotranspiration from various land-use classes over the past two decades. Finally, the “Predictions in Ungauged Basins” initiative (PUB) is focusing on remote sensing models and estimates of spatially-averaged water budget components across scales and beyond catchment boundaries. In parallel, advances in ground-based measurement techniques, such as distributed temperature sensing, geological weighing lysimeters (gwl), and geophysical surveys are finding their way into research and practice for characterizing the hydrological parameters by more efficient means.

To bring together the broad interest of specialists on the subjects of satellite gravimetry, remote sensing and ground-based methods in multi-scale hydrology and water resources management over the full range of terrestrial spatial scales from pixel to continent, a joint symposium (J-H01) entitled: *GRACE, other remote sensing platforms and ground-based methods for estimating multi-scale surface water budgets, groundwater system characterization and hydrological processes* was held during the 25th General Assembly of the International Union of Geodesy and Geophysics (IUGG), *Earth on the Edge: Science for a Sustainable Planet*, in Melbourne, Australia, from 28 June to 7 July 2011. The joint symposium was led by the International Association of Hydrological Sciences (IAHS) with other IUGG Associations including the International Association of Geodesy (IAG) and International Association of Meteorology and Atmospheric Sciences (IAMAS). This IAHS publication contains 30 peer-reviewed papers from different disciplines to provide a review on the state-of-the-art on one or more aspects of GRACE, Remote Sensing and Hydrological Models for understanding of multi-scale hydrological processes. The papers have been

organized into three general categories: GRACE Application, Satellite Application, and Hydrological Application.

The editors are grateful to the symposium participants for their scientific contributions, which together form an impressive volume on the topic of state of the art application of remote sensing and ground-based methods for multi-scale hydrology. We also thank symposium participants for their prompt submission of manuscripts and adherence to a tight publication schedule. Penny Perrins and Cate Gardner at IAHS Press are graciously thanked for their tireless effort in preparing the papers for publication. Lastly, the editors thank Dr Tamara Jackson for an English review and editing of the accepted papers, Mr Josh Sixsmith for preparing the front page picture, Mr Kaleem Ullah for help in session planning and Pierre Hubert (Secretary General of IAHS) for coordinating the joint symposia details.

EDITOR-IN-CHIEF

Mohsin Hafeez

*International Centre of Water for Food Security (IC Water)
Charles Sturt University (CSU)
Wagga Wagga, NSW 2678, Australia*

CO-EDITORS

Nick van de Giesen

*Civil Engineering & Geosciences
TU Delft
2628 CN Delft, Netherlands*

Earl Bardsley

*Department of Earth and Ocean Sciences
University of Waikato
Hamilton 3240, New Zealand*

Frederique Seyler

*Directrice de Recherche IRD
France*

Roland Pail

*Institute of Astronomical and Physical Geodesy
Technische Universität München
München 80333, Germany*

Makoto Taniguchi

*Research Institute of Humanity and Nature (RIHN)
Kyoto 602-0878, Japan*

Contents

Preface by *Mohsin Hafeez, Nick van de Giesen, Earl Bardsley, Frederique Seyler, Roland Pail & Makoto Taniguchi* v

1 GRACE Application

Groundwater resources assessment based on satellite GRACE and hydrogeology in Western Australia *Makoto Taniguchi, Keiko Yamamoto & Priyantha Ranjan Sarukkalige* 3

Analysis of regional variations in soil moisture by means of remote sensing, satellite gravimetry and hydrological modelling *S. Abelen, F. Seitz, M. Schmidt & A. Güntner* 9

Use of twin GRACE satellite gravity data and geoid signals in the characterization of major underlying aquifer regimes and tectonic structure of the Middle Indus Basin, Pakistan *Z. Ahmad & M. Sadiq* 16

Monitoring surface and groundwater variations using multisatellite observations and hydrological modelling *Frédéric Frappart, Frédérique Seyler, Fabrice Papa, Jean-Michel Martinez, Thuy Le Toan, Joecila Santos Da Silva, Catherine Prigent & William B. Rossow* 22

Analysis of widespread fissures associated with groundwater depletion and extreme rainfall using multi sensor data *Ramesh P. Singh, Waseem Mehdi, Majid Naeimi, Alok Sahoo & Rajesh Kumar* 28

A global network of area-integrated water budget monitoring for climate change detection? *Earl Bardsley* 34

2 Satellite Application

A spatial hydrological model for estimation of unaccounted water diversions in the northern Murray-Darling Basin of Australia *Mohsin Hafeez, Masoud Edraki, Umair Rabbani, Yann Chemin, Kaleem Ullah & Josh Sixsmith* 41

Estimation of evaporative fraction from top-of-atmosphere radiance *Jian Peng & Yuanbo Liu* 47

Use of field observations and SEBS to retrieve heat fluxes for irrigation areas of Australia *Weiqliang Ma, Mohsin Hafeez, Rabbani Umair, Yaoming Ma & Bob Su* 53

On utilizing river widths measured from synthetic aperture radar images for calibrating rainfall–runoff models in ungauged basins <i>Wenchao Sun, Hiroshi Ishidaira, Satish Bastola & Sushu Wu</i>	59
TRMM-forced rainfall–runoff modelling for water management purposes in small ungauged basins <i>Bruno Collischonn & André R. Pante</i>	66
Using TRMM rainfall estimates in hydrological and hydrodynamic modelling of the Amazon Basin <i>Rodrigo Cauduro Dias De Paiva, Diogo Costa Buarque, Walter Collischonn, Mino S. Sorribas, Daniel Gustavo P. Allasia, Carlos André B. Mendes, Carlos E. M. Tucci & Marie-Paule Bonnet</i>	72
Flood monitoring of the Inner Niger Delta using high resolution radar and optical imagery <i>Alain Dezetter, Denis Ruelland & Camille Netter</i>	78
Evaluation of high-resolution satellite precipitation products for streamflow simulation in Mishui Basin, south China <i>Liliang Ren, Shanhu Jiang, Bin Yong, Xiaoli Yang & Bang Yang</i>	85
Altimeter-derived soil moisture determination – global scope and validation <i>Philippa A. M. Berry & John Carter</i>	92
Satellite-based estimates of vegetation density over Australia during 1988–2008 <i>Yi Liu, Richard De Jeu, Matthew McCabe, Jason Evans & Albert Van Dijk</i>	98
Global inland water monitoring from satellite radar altimetry – a glimpse into the future <i>Philippa A. M. Berry, Mark K. Salloway, Richard G. Smith & Jérôme Benveniste</i>	104
Third Pole Environment (TPE) program: a new base for the study of atmosphere–land interaction over the heterogeneous landscape of the Tibetan Plateau and surrounding areas <i>Yaoming Ma, Maoshan Li, Xuelong Chen, Shuzhou Wang, Rongsheng Wu, Weiqiang Ma, Lei Zhong, Binbin Wang, Chunling Zhu & Tandong Yao</i>	110
Estimating root-layer soil moisture for north China from multiple data sources <i>Xingguo Mo, Jianxiu Qiu, Suxia Liu & Vahid Naeimi</i>	118
Modelling water re-uses of a tank cascade irrigation system based on satellite and field observations <i>Xueliang Cai, Yuanlai Cui & Nicolas Roost</i>	125

3 Hydrological Application

A remote sensing based ET algorithm for Australian agro-ecosystems: SAM-ET <i>Mohsin Hafeez, Yann Chemin & Umair Rabbani</i>	133
Estimating soil heat flux using Distributed Temperature Sensing <i>J. H. A. M. Jansen, P. M. Stive, N. C. van de Giesen, Scott W. Tyler, S. C. Steele-Dunne & L. Williamson</i>	140

A study on actual evapotranspiration estimation based on the Todorovic method <i>Guoshui Liu, Mohsin Hafeez, Yu Liu & Di Xu</i>	145
Surface-layer sensible heat flux using large-aperture scintillometer over irrigated horticulture in Murrumbidgee irrigation area <i>U. Rabbani, M. Hafeez, R. Faux & J. Louis</i>	151
Irrigation demand forecasting using remote sensing and meteorological data in semi-arid regions <i>Kaleem Ullah & Mohsin Hafeez</i>	157
Ground-based laserscanning – a new method for measuring fluvial erosion on steep slopes? <i>F. Haas, T. Heckmann, M. Becht & B. Cyffka</i>	163
A preliminary analysis of the total column water vapour retrieved from COSMIC data <i>Weijia Wang & Xinjia Zhou</i>	169
The impact of temporal and spatial resolution on developing risk maps: case study of the Tubma basin, Thailand <i>S. Visessri, N. McIntyre & C. Maksimovic</i>	175
A new automatic calibration approach based on rating curves: first results with ENVISAT altimetric data <i>Augusto C. V. Getirana</i>	181
Informing hydrological models with ground-based time-lapse relative gravimetry: potential and limitations <i>Peter Bauer-Gottwein, Lars Christiansen & Dan Rosbjerg</i>	187
Key word index	195

1 GRACE Application

Groundwater resources assessment based on satellite GRACE and hydrogeology in Western Australia

MAKOTO TANIGUCHI¹, KEIKO YAMAMOTO¹
& PRIYANTHA RANJAN SARUKKALIGE²

¹ Research Institute for Humanity and Nature, 457-4 Motoyama, Kamigamo, Kyoto 603-8047, Japan
makoto@chikyu.ac.jp

² Curtin University, Western Australia, Australia

Abstract Groundwater resources assessment in Western Australia has been made by using satellite GRACE (Gravity Recovery and Climate Experiment) and *in situ* hydrological, meteorological and hydrogeological data. Changes in land water storage analysed by satellite GRACE showed the decreasing trends at both northern Western Australia and southern Western Australia during 2002–2008, even though the values of precipitation minus evaporation remain the same. This is attributed to the depletion of groundwater storage which is confirmed by *in situ* data with the decrease in groundwater level. The degree of depletion of groundwater storage depends on the hydrogeology, which has higher permeability with higher depletion in northern Western Australia and lower permeability with lower depletion in southern Western Australia.

Key words satellite GRACE; hydrogeology; Western Australia; groundwater assessment

INTRODUCTION

Groundwater is the world's largest accessible store of freshwater. Groundwater is also the primary source of drinking water for nearly half of the world's population and, as the dominant source of water for irrigated land, is critical to global food security. Despite this dependence, our understanding of the impacts of climate change on groundwater resources remains limited. Strategies to adapt to more variable freshwater resources will increase dependence upon groundwater. Many parts of the world will suffer a decrease in water resources due to global climate changes, and rapid global population growth will enhance the stress on water resources (Kundzewicz *et al.*, 2007).

In order to maintain sustainable water management, basin-scale or continental-scale Land Water Storage (LWS) monitoring is necessary. However, traditional methods cannot evaluate large-scale LWS variations accurately. Previous ground and satellite techniques can evaluate individual components such as soil moisture (Njoku *et al.*, 2003) and surface water (Alsdorf & Lettenmaier, 2003). However, they cannot evaluate groundwater or total LWS changes. Numerical models can be used to evaluate LWS changes; however, they have limitations such as insufficient knowledge of surface structure, process description or parameterization, as well as errors in model input data (e.g. precipitation data), which can all cause large uncertainty (Hasegawa *et al.*, 2008).

The GRACE (Gravity Recovery and Climate Experiment) satellite was launched in March 2002 to solve this problem. GRACE has been providing monthly global gravity field data with an unprecedented accuracy as a series of the Stokes coefficients (a set of coefficients of the spherical harmonic expansion of the Earth's gravity field) (Tapley *et al.*, 2004). GRACE can recover temporal variations of the Earth's gravity fields due to mass redistribution in and on the Earth (Wahr *et al.*, 1998). Many previous studies concluded that GRACE-inferred annual changes of LWS agree reasonably well with hydrological model estimates in certain large river basins, for instance, the Amazon (Tapley *et al.*, 2004), Mississippi (Chen *et al.*, 2005), Illinois (Yeh *et al.*, 2006), Indochina (four major combined basins) (Yamamoto *et al.*, 2007), and India (Rodel *et al.*, 2009).

Studies on the dependency of hydrogeology on LWS change are limited. WHYMAP (2009) recently developed a worldwide hydrogeological map with five categories of recharge rates; (1) very high recharge (>300 mm/year), (2) high recharge (100–300 mm/year), (3) medium recharge (20–100 mm/year), (4) low recharge (2–20 mm/year), and (5) very low recharge (<2 mm/year), and three categories of aquifer types: (1) major groundwater basin, (2) complex hydrogeological structure, and (3) local and shallow aquifers. Although this information is limited qualitatively, it provides a broad knowledge of global-scale hydrogeological characteristics.

Australia suffered severe drought during 2006, in particular in the Murray-Darling basin. Many hydrological studies have been made, including the use of GRACE (Hasegawa *et al.*, 2008). Water shortage was also reported during that period in Western Australia (WA); however, the detailed studies at a large scale have not been made yet, e.g. by using GRACE.

In this paper, we evaluated the changes in LWS from GRACE gravity data, and compared it with *in situ* meteorological, hydrological, and hydrogeological data. The purpose of this study is to assess the regional water resources in WA, where groundwater is a dominant water resource.

The GRACE monthly gravity field solution

For the estimation of GRACE mass variation over Australia, version 02 of the GRGS every 10 day gravity field solutions are used in this study (Lemoine *et al.*, 2007). The solution was calculated in Stokes coefficients up to a degree/order of 50 from GRACE GPS and K-band range-rate data and LAGEOS-1 and 2 Satellite Laser Ranging data. Smoothing or filtering was not applied when we used them, because they have already been stabilized during their generation process. We used the data from July 2002 to October 2008. After removing the average of the whole data period, mass variations of each time period was estimated using equation (1) of Wahr *et al.* (1998):

$$\Delta\sigma(\theta, \lambda) = \frac{a\rho_E(2l+1)}{3(1+k_l')} \sum_{l=0}^{50} \sum_{m=0}^l (\Delta\bar{C}_{lm} \cos m\lambda + \Delta\bar{S}_{lm} \sin m\lambda) \bar{P}_m(\sin\theta) \quad (1)$$

where $\Delta\sigma(\theta, \lambda)$ is mass change rate at the latitude θ and the longitude λ , a is the equatorial radius of the Earth, ρ_E is the average density of the Earth, k_l' is the load Love number of degree l , $\Delta\bar{C}_{lm}$ and $\Delta\bar{S}_{lm}$ is variable components of fully normalized GRACE spherical harmonic coefficients of degree l and order m .

Spatial and temporal variations of LWS in Australia during 2002 to 2008

We obtained the spatial distribution of inter-annual mass change trend over Australia by fitting the annual linear trend components to the mass variations calculated by equation (1). Figure 1(a) shows the result of the changes in LWS from 2002 to 2008 over the Australian continent. The depletions of LWS are found in Western Australia as well as in the Murray Darling basin (MDB). As shown in Fig. 1(a), the depletion of LWS in northern WA is the largest, followed by southern WA. The increases in LWS in the western coastal zone were also noticed. To evaluate the regional differences of LWS trend, we grouped the common areas having similar patterns of LWS

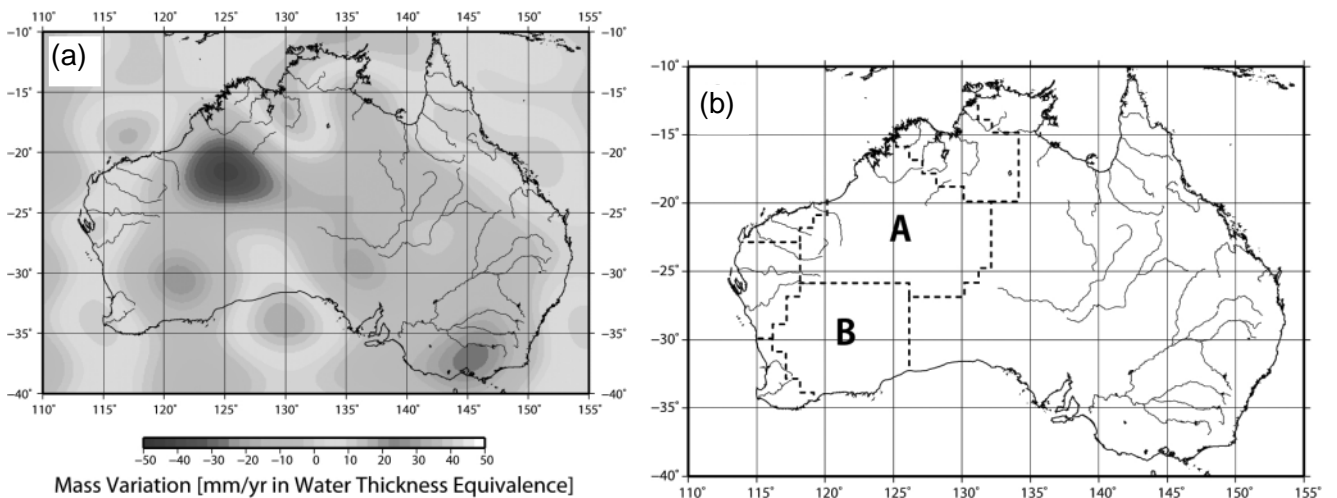


Fig. 1 Trends of land water changes during 2002 and 2008 by GRACE in (a) Australia, and (b) spatial classifications depending on the trend.

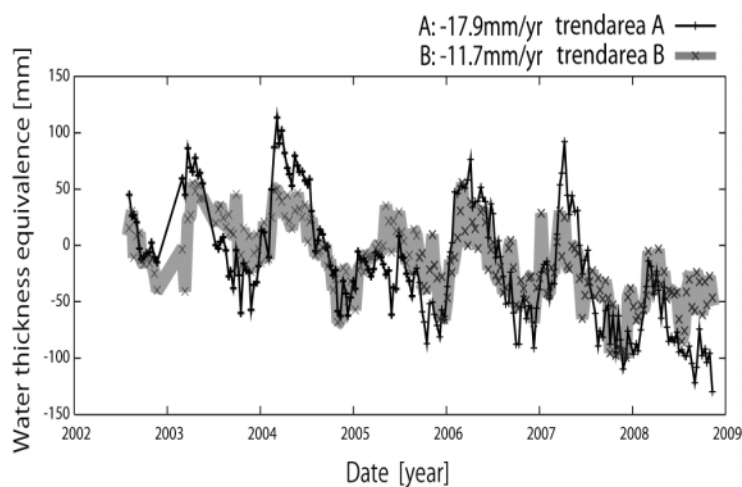


Fig. 2 Temporal changes of LWS in A and B.

variation. This spatial classification is shown in Fig. 1(b). Two critical areas with higher decreases in LWS can be clearly identified in Western Australia; northern WA and southern WA (Areas A and B, as shown in Fig. 1(b)).

To characterize the time variation of LWS in Western Australia, we evaluated the regionally averaged time variations of LWS over northern WA (A in Fig. 1(b)) and southern WA (B in Fig. 1(b)) where the significant negative LWS anomalies were detected in Fig. 1(a). As shown in Fig. 2, there are seasonal variations of LWS and long-term trends of depletion of LWS are found in both A and B. The long-term average of the depletion of the LWS in A and B areas are 17.9 mm/year and 11.7 mm/year, respectively.

Empirical Orthogonal Function (EOF) analyses for each WATER component of the changes in LWS

In order to evaluate the factors affecting the changes in LWS, EOF analysis, which is routinely used for the study of oceanography and meteorology, has been carried out. EOF analysis is the method to analyse the whole spatial-temporal data set at once, by seeking the eigen values of the data. First we made a matrix for the analysis using mass variation data sets over Australia by packing mass variations of each grid point to each row, so that each time period map becomes a new column. Applying eigen value decomposition, we obtained the eigen values, each of which is associated with an eigenvector (a spatial map) and the corresponding time variation, the principal value (a 1-D time series). These eigen values and the corresponding eigenvectors represent the principal components or most significant modes in the data when they are ordered from largest to smallest. Figure 3(a)–(e) depict the obtained spatial patterns of the 1st, 2nd, 3rd, 4th and 5th EOF modes. The 1st, 2nd, 3rd, 4th, and 5th modes explain 46.5, 18.2, 8.4, 5.6 and 3.9% of the data, respectively, and these first five modes together account for 82.6% of the variance.

As can be seen from Fig. 3, the most dominant factor is the seasonal variation of the LWS (Fig. 3(a)), with the highest in February and March and the lowest in October and November due to precipitation change. The second dominant factor is the long-term trend of the LWS change (Fig. 3(b)). The third dominant factor shows the bimodal variation of LWS (Fig. 3(c)) with highest in June/July and March/April. The fourth dominant factor (Fig. 3(d)) shows a decreasing trend during late 2005 and 2006, when severe drought occurred over the whole of Australia. The fifth dominant factor (Fig. 3(e)) also shows the bi-modal variation; highest in January and April.

According to the spatial distributions of the five factors of the variation of LWS, the area with the larger 1st factor (seasonal variation) is located in the Northern Territory of Australia. The areas with the larger 2nd factor (long-term depletion trend) are located in northern WA, southern WA, central Australia, and southeast Australia (southern MDB). The area with larger third and fifth

factors (both bimodal variation) are not very clear. The area with the larger fourth factor (depletion after 2005 drought) is located in the MDB.

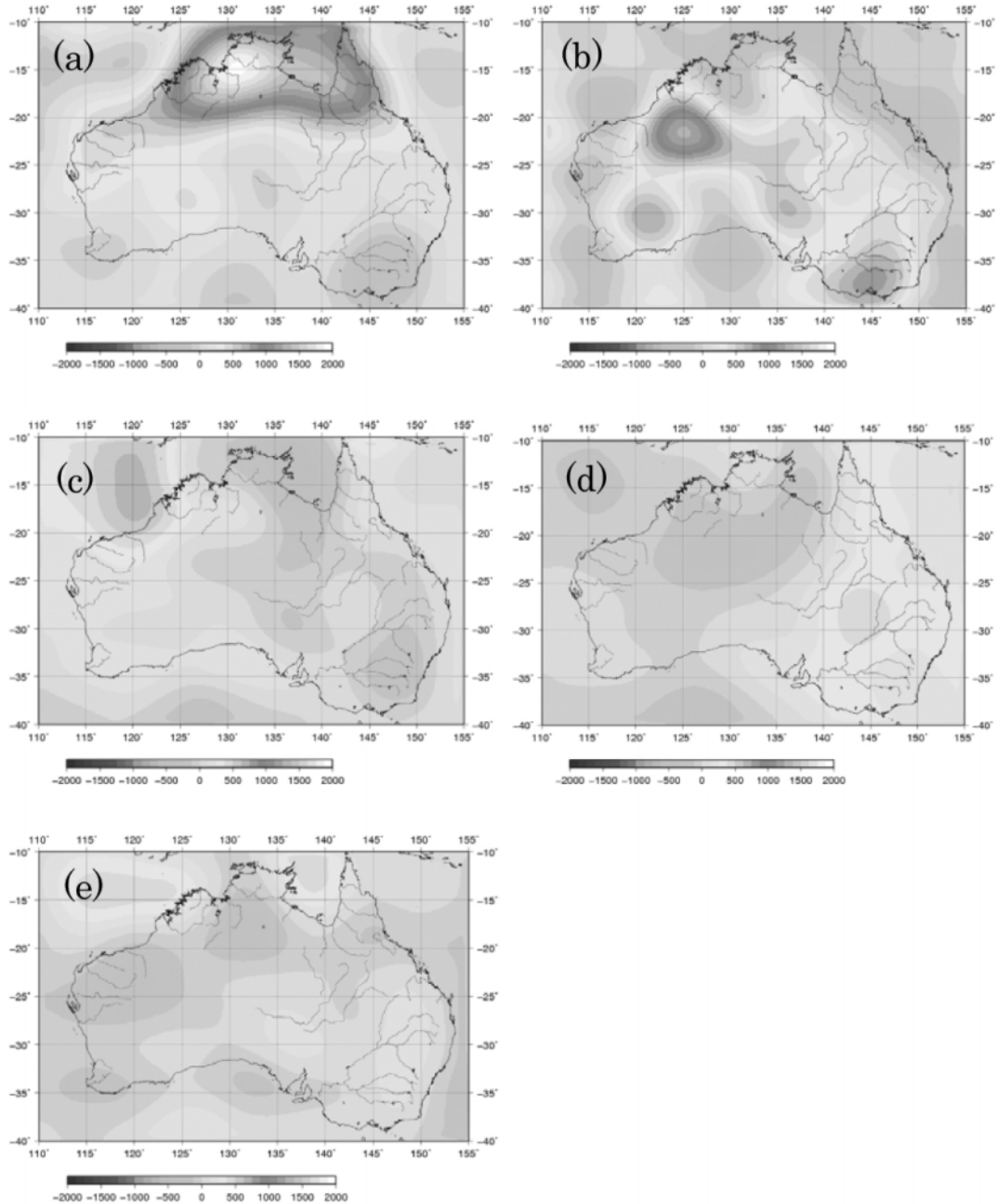


Fig. 3 Temporal changes of land water by EOF analyses with (a) 1st, (b) 2nd, (c) 3rd, (d) 4th, and (e) 5th dominant.

Analyses with meteorological, hydrological and hydrogeological data

In order to evaluate the water balance in Western Australia, three types of major hydrological data are used; precipitation, evaporation, and groundwater level. The precipitation and groundwater level data were obtained from the Department of Water, Australia, and the evaporation data was collected from the Australian Government Bureau of Meteorology (BoM). After analysing a series of these meteorological data records, data for 186 meteorological stations for precipitation, 37 stations for evaporation and 14 borehole locations for groundwater levels were used for this

analysis. These selected observation stations show a continued data series from 2002 to 2008, which is compatible with the GRACE data set time scale.

In order to evaluate the effect of hydrogeology on the change in LWS, the hydrological information was obtained from the hydrogeological map made by the World-wide Hydrogeological Mapping and Assessment Program (WHYMAP, 2009). WHYMAP (2009) illustrates that the hydrogeology in northern WA is a major groundwater basin with high recharge (100–300 mm/year) to medium recharge rates (20–100 mm/year). However, the hydrogeology of southern WA is categorized as a local and shallow aquifer system with medium–very low recharge (<100 mm/year). Therefore the hydrogeology in A (northern WA) and B (southern WA) is very different in terms of recharge rate and other characteristics (such as storage).

Temporal variations of LWS from GRACE data show the long-term trend of LWS depletion in both A and B (Fig. 2). The depletion ratio is larger in A (northern WA) than that in B (southern WA). This may be attributed to the difference of hydrogeology, if the meteorological condition is the same in both areas. Figure 2 also shows that the seasonal variation of LWS is larger in A (northern WA) than that in B (southern WA). This also may be attributed to the difference of hydrogeology, if the meteorological condition is the same in both areas.

To evaluate the water balance during 2002 to 2008 in both A (northern WA) and B (southern WA), a simplified water balance concept, precipitation minus evaporation (P–E) is considered. The collected precipitation and evaporation data are used for the analysis. First, we developed the spatial distribution grid data map for each evaporation data (each time period), using observed data which are uniformly distributed over a large area. We used the minimum curvature surface interpolation method to develop the spatial distribution and then estimated the evaporation value at the precipitation observation locations by bilinear interpolation. The precipitation minus evaporation (P–E) at six stations in area A (northern WA) and four stations in area B (southern WA) are examined. There are double peaks of P–E in area A in January/February and June/July. However, there is a single peak of P–E in area B in June. Although the single or double peaks of P–E exist, the long-term trend of P–E is almost constant, therefore the decrease of LWS detected by GRACE cannot be explained by the change in P–E. Therefore, the only reason why the LWS depleted during 2002 to 2008 in both A (northern WA) and B (southern WA) is the depletion of water in the vadose zone including groundwater.

In order to confirm the reason for the decrease in LWS, the variation of groundwater level in area A and B are examined, although there are only six boreholes in A (northern WA) and eight boreholes in B (southern WA). Some borehole data in area A show seasonal changes in groundwater level, but others do not. Almost all groundwater levels in area B (southern WA) show a seasonal change. The average of the groundwater depletion in area A is 0.147 m/year. Although some boreholes show an increasing trend and others show a decreasing trend, the average of groundwater depletion in area B is 0.095 m/year. Therefore, the decreasing ratio of groundwater level in area A (northern WA) is larger than that in area B (southern WA). If the variable porosities of the soil are assumed to be 0.1, the depletions of groundwater are 0.015 m/year in area A, and 0.0095 m/year in area B.

According to the long term trends of LWS variation obtained from GRACE data, the depletion ratio was 0.0179 m/year in area A, and 0.0117 m/year in area B (Fig. 2). These numbers agreed relatively well with the values observed in groundwater level change in area A and B. Therefore, the depletions of LWS in area A (northern WA) and area B (southern WA) are caused by depletion of groundwater. The satellite GRACE can detect large scale LWS variation, including groundwater depletion; therefore GRACE is useful for global assessment of groundwater which is important for water resources management.

CONCLUSION

Changes in land water storage obtained from the satellite GRACE showed the decreasing trends in both the northern part of Western Australia (–17.9 mm/year) and the southern part of Western

Australia (−11.7 mm/year) from 2002 to 2008. The depletion of LWS in both areas was found, even though the values of precipitation minus evaporation remain the same, which suggested the depletion of soil water and groundwater in the vadose zone. Depletion values obtained from GRACE agreed relatively well with the *in situ* groundwater measurements of depletion of 0.015 m/year in area A, and 0.0095 m/year in area B. Therefore the depletion of LWS is caused by the depletion of groundwater in both northern WA and southern WA.

Hydrogeology in the northern part of WA is categorized as a major groundwater basin with high recharge (100–300 mm/year) to medium recharge rate (20–100 mm/year). However, the hydrogeology of southern WA is categorized as a local and shallow aquifer system, with medium to very low recharge (<100 mm/year). Therefore the hydrogeology in northern WA and southern WA is very different in terms of recharge rate and other characteristics (such as storage). The degree of depletion of groundwater storage depends on the hydrogeology, which has a higher recharge rate with higher depletion in northern WA and a lower recharge rate with lower depletion in southern WA.

The satellite GRACE (Gravity Recovery and Climate Experiment) is a useful tool for basin and continental scale groundwater assessment.

REFERENCES

- Alsdorf, D. E. & Lettenmaier, D. P. (2003) Tracking fresh water from space. *Science* **301**, 1491–1494.
- Chen, J. L., Rodell, M., Wilson, C. R. & Famiglietti, J. S. (2005) Low degree spherical harmonic influences on Gravity Recovery and Climate Experiment (GRACE) water storage estimates. *Geophys. Res. Lett.* **32**, L14405, doi:10.1029/2005GL022964.
- Chen, J. L., Wilson, C. R., Famiglietti, J. S. & Rodell, M., (2007) Attenuation effect on seasonal basin-scale water storage changes from GRACE time-variable gravity. *J. Geod.* **81**, 237–245, doi:10.1007/s00190-006-0104-2.
- Bettadpur, S. (2007) UTCSR Level-2 Processing Standards Document For Level-2 Product Release 0004. ftp://podaac.jpl.nasa.gov/pub/grace/doc/L2-CSR0004_ProcStd_v3.1.pdf.
- Bureau of Meteorology (2006), Drought Statement Issued 4 December. http://www.bom.gov.au/announcements/media_releases/climate/drought/20061204.shtml.
- Hasegawa, T., Fukuda, Y., Yamamoto, K. & Nakaegawa, T. (2008) The 2006 Australian drought detected by GRACE. In: *From Headwaters to the Ocean* (ed. by M. Taniguchi, W. C. Burnett, Y. Fukushima, M. Haigh & Y. Umezawa), 363–367. Taylor & Francis, London, UK.
- Kundzewicz, Z. W., Mata, L. J., Arnell, N. W., Döll, P., Kabat, P., Jiménez, B., Miller, K. A., Oki, T., Sen, Z. & Shiklomanov, I. A. (2007) Freshwater resources and their management. In: *Climate Change 2007: Impacts, Adaptation and Vulnerability. Contribution of Working Group II to the Fourth Assessment Report of the Intergovernmental Panel on Climate Change* (ed. by M. L. Parry, O. F. Canziani, J. P. Palutikof, P. J. van der Linden & C. E. Hanson), 173–210. Cambridge University Press, Cambridge, UK.
- Lavery, B., Joung, G. & Nicholls, N. (1997) An extended high-quality historical rainfall dataset for Australia. *Aust. Met. Mag.* **46**, 27–38.
- Lemoine, J. M., Bruinsma, S., Loyer, S., Biancare, R., Marthy, J. C., Perosanz, F. & Balmino, G. (2007) Temporal gravity field models inferred from GRACE data. *Adv. Space Res.* **39**, 1620–1629, doi:10.1016/j.asr.2007.03.062.
- Njoku, E. G., Jackson, T. J., Lakshmi, V., Chan, T. K. & Nghiem, S. V. (2003) Soil moisture retrieval from AMSRE. *IEEE Trans. Geosci. Remote Sens.* **41**, 215–229.
- Nohara, D., Kitoh, A., Hosaka, M. & Oki, T. (2006) Impact of climate change on river discharge projected by multimodel ensemble. *J. Hydromet.* **7**, 1076–1089, doi:10.1175/JHM531.1.
- Rodell, M., Houser, P. R., Jambor, U., Gottschalck, J., Mitchell, K., Meng, C. J., Arsenault, K., Cosgrove, B., Radakovich, J., Bosilovich, M., Entin, J. K., Walker, J. P., Lohmann, D. & Toll, D. (2004) The global land data assimilation system. *Bull. Am. Met. Soc.* **85**(3), 381–394.
- Sellers, P. J., Mintz, Y., Sud, Y. C. & Dalcher, A. (1988) Simple Biosphere model (SiB) for use within general circulation model. *J. Atmos. Sci.* **43**, 505–531.
- Swenson, S., Wahr, J. & Milly, P. C. D. (2003) Estimated accuracies of regional water storage variations inferred from the Gravity Recovery and Climate Experiment (GRACE). *Water Resour. Res.* **39**(8), 1223–1235, doi:10.1029/2002WR001808.
- Swenson, S. & Wahr, J. (2006), Post-processing removal of correlated errors in GRACE data. *Geophys. Res. Lett.* **33**, L08402, doi:10.1029/2005GL025285.
- Tapley, B. D., Bettadpur, S., Watkins, M. M. & Reigber, C. (2004) The gravity recovery and climate experiment: mission overview and early results. *Geophys. Res. Lett.* **31**, L09607, doi:10.1029/2004GL019920.
- Wahr, J., Molenaar, M. & Bryan, F., (1998) Time-variability of the Earth's gravity field: Hydrological and oceanic effects and their possible detection using GRACE. *J. Geophys. Res.* **103**(B12), 30 205–30,230.
- Yamamoto, K., Fukuda, Y., Nakaegawa, T. & Nishijima, J. (2007) Landwater variation in four major river basins of the Indochina peninsula as revealed by GRACE. *Earth Planets Space* **59**, 193–200.
- WHYMAP (2009) <http://www.whymap.org/>.

Analysis of regional variations in soil moisture by means of remote sensing, satellite gravimetry and hydrological modelling

S. ABELN¹, F. SEITZ¹, M. SCHMIDT² & A. GÜNTNER³

¹ Earth Oriented Space Science and Technology (ESPACE), TU München, Arcisstr. 21, 80333 Munich, Germany
sarah.abelen@bv.tum.de

² Deutsches Geodätisches Forschungsinstitut, Alfons-Goppel-Str. 11, 80539 Munich, Germany

³ Helmholtz-Centre Potsdam – GFZ German Research Centre for Geosciences, Telegrafenberg, 14473 Potsdam, Germany

Abstract Regional and global variations in soil moisture are commonly assessed by remote sensing and/or hydrological models. Less attention has been paid to the associated large-scale mass changes detectable with satellite gravimetry. Here we analyse variations in soil moisture from remote sensing (satellite sensor AMSR-E) and hydrological modelling (WaterGAP Global Hydrology Model) with respect to mass changes in continental water storage from space gravimetry (satellite mission GRACE). The study is performed for a test area in Central Asia, where mass change in soil moisture is the dominant contributor to the total water storage (TWS). The different data sets are compared with respect to their spatio-temporal characteristics via principal component analyses. Results show high correlation in the annual cycles of all data sets. The high level agreement between the spatial patterns of TWS changes from GRACE and soil moisture variations from AMSR-E suggests an important potential of satellite gravimetry in studies related to regional variations in soil moisture.

Key words soil moisture; remote sensing; satellite gravimetry; principal component analysis; AMSR-E; GRACE; WGHM

INTRODUCTION

The latest IPCC assessment report once more identified land hydrology as the most uncertain component of the global water cycle (Solomon *et al.*, 2007). Total continental water storage (TWS) and its temporal variation play a key role in the Earth's water, energy and biogeochemical cycles. TWS is composed of a variety of storage compartments, including the unsaturated soil or rock zone, groundwater, snow, ice and surface water bodies. Depending on the respective storage characteristics, hydrological variations cover sub-daily to decadal time scales, and the contributions of individual storage compartments to the overall dynamics of land hydrology vary spatially as a function of, for instance, topography, soil characteristics and climate conditions (Güntner *et al.*, 2007; Syed *et al.*, 2008). The particular contributions of individual compartments to TWS and their interactions are not well known. Such knowledge, however, would be a prerequisite for a better understanding of processes of the hydrological cycle and of continental mass variations in general.

Since 2002 the satellite gravity field mission GRACE allows for a global assessment of TWS variations at spatial scales of a few 100 km at a temporal resolution of one month and better (Tapley *et al.*, 2004; R. Schmidt *et al.*, 2006; M. Schmidt *et al.*, 2008; Seitz *et al.*, 2008). But by its integrative nature, GRACE is unable to resolve the contributions of individual compartments to TWS variations. In order to separate the integral signal from GRACE, additional data from other sources must be incorporated into the analysis. Besides ground-based observation systems and simulations from various hydrological models, today a multitude of simultaneously operating satellite systems offers a broad spectrum of information (e.g. Wagner *et al.*, 1999; Singh & Gan, 2000; Alsdorf *et al.*, 2007).

This paper addresses the compartment of soil moisture. Applying multi-sensor data from remote sensing, GRACE and hydrological modelling we study the detectability of soil moisture signatures in observed TWS variations from GRACE and elaborate on the question in which way satellite gravimetry can contribute to a better understanding of variations in soil moisture. Results of this study are therefore valuable for scientists from both hydrology and geodesy disciplines.

Our work is organized as follows: variations in soil moisture are deduced from products of the satellite sensor AMSR-E and from the WaterGAP Global Hydrology Model (WGHM). *In situ*

observations are not integrated into the study since soil moisture products from satellite missions have already gone through a calibration process incorporating ground truth data. TWS changes are computed from GRACE gravity field observations. We perform a regional study for a test area in Central Asia, where the change of water storage in soil moisture is dominant with respect to other hydrological contributions and thus expected to be identifiable in the GRACE signal. The observed and modelled data sets for soil moisture and TWS are compared with respect to their spatio-temporal characteristics. For this purpose, a principal component analysis (PCA) is applied to the time-variable fields of soil moisture and TWS from the different data sources. The final section provides conclusions and directions for future research.

DATA SETS

Remote sensing

Existing permanent measurement stations and field campaigns have not mapped soil moisture over larger areas and extended time periods. In order to cover continental or global scales, satellite missions have been put in operation, giving global records of soil moisture with temporal resolutions of up to one day. Therefore active as well as passive microwave sensors have been employed (Wood, 1993; Wigneron, 2000; Barrett *et al.*, 2009).

This study focuses on the passive sensor AMSR-E (Advanced Microwave Scanning Radiometer on the Earth Observing System Aqua), launched in 2002. The sensor operates at 6.8 GHz (C-band) with a nominal spatial resolution of 60 m and a temporal resolution of 2–3 days (Jackson, 2005). The National Snow and Ice Data Center of the University of Colorado at Boulder provides Level-3 products (25 km grid) of global surface soil moisture, including additional information on vegetation-water content and quality control variables (Njoku, 2008). We apply this data for the time span 2003–2009. The processing is described by Njoku *et al.* (2003). AMSR-E operates at a low microwave frequency (implying higher penetration), but an accuracy of 0.06 g/cm^3 can only be achieved in areas with less than 1.5 kg/m^2 vegetation-water-content (Njoku *et al.*, 2003). Furthermore soil moisture can only be recorded for the first centimetre of the top layer of the soil.

Satellite gravimetry

The GRACE gravity field mission has been monitoring temporal variations of the Earth's gravity field continuously since 2002. The largest part of the signal (tides, atmosphere and oceans) is removed during pre-processing (Flechtner *et al.*, 2010), so that remaining variations over non-polar regions mainly reflect changes of terrestrial water storage. Here we analyse monthly GRACE gravity fields in terms of equivalent water mass (Wahr *et al.*, 1998), computed from the latest global spherical harmonic solution RL04 of the German Research Centre for Geosciences (GFZ). Due to GRACE orbit characteristics and measurement limitations, which result in an inability to separate spherical coefficients at all degrees and orders, errors in the form of longitudinal stripes are present in the current solutions. In order to reduce correlations in the coefficients, we apply a 2nd degree Savitzky-Golay least-squares smoothing filter. In addition, noisy short wavelength components of the solutions due to high-frequency aliasing are reduced using an isotropic Gaussian filter of 300 km half-width (Wahr *et al.*, 1998).

Hydrological modelling

Model-based analyses of total and compartmental storage variations are derived from the WaterGAP Global Hydrology Model (WGHM) (Döll *et al.*, 2003). WGHM is a state-of-the-art model of the terrestrial hydrological cycle at a spatial resolution of 0.5 degree and a daily simulation time step. In the version used here, the model is forced by monthly fields of terrestrial surface climate and accounts for the hydrological storage compartments groundwater, soil moisture, snow and surface water in rivers, lakes, reservoirs and wetlands. Extensive global and regional analysis of spatio-temporal variations of simulated water storages were carried out by Güntner *et al.* (2007), revealing

the different contributions and characteristics of individual storage compartments for different river basins and climate zones. Large-scale TWS variations from WGHM have also been compared with GRACE-based TWS variations in various studies. While the comparison of WGHM and GRACE revealed a general agreement of seasonal and other periodic characteristics at the global scale, significant differences with respect to phases and amplitudes were detected for some river basins where WGHM tends to underestimate seasonal variations of TWS (R. Schmidt *et al.*, 2006, 2008).

STUDY AREA

The study area was selected on the basis of three criteria: (a) the area is characterized by a relatively high macro-scale variation in soil moisture to induce a detectable change in the Earth's gravity field; (b) it has a sparse vegetation cover with $>1.5 \text{ kg/m}^2$ vegetation water content to give an optimal soil moisture accuracy of 0.06 g/cm^3 ; (c) soil moisture is the most dominant contributor to TWS in order to relate it to the integral mass change measured by GRACE. Figure 1 displays the standard deviation of soil moisture records of AMSR-E over 2003–2009, indicating regions with high and low variations in soil moisture. Flagged areas denote either regions with no or invalid data (e.g. due to snow fall or dense vegetation) and are not suitable test areas. Neither are desert areas (0 to 0.025 g/cm^3) with little precipitation and thus little variation in soil moisture. From three suitable regions (northeast Canada, the catchment area of the Euphrates and Tigris rivers, and an area in Central Asia east of the Caspian and south of the Aral Sea) we chose the latter in order to avoid major influences of snow fall and river flow on the gravity signal. Simulations with WGHM (Fig. 2) reveal that variations of TWS in the region between 33°N 55°E (southwest corner) and 41°N 64°E (northeast corner) are clearly dominated by changes in soil moisture. Hence the region fulfils the selection criteria mentioned above.

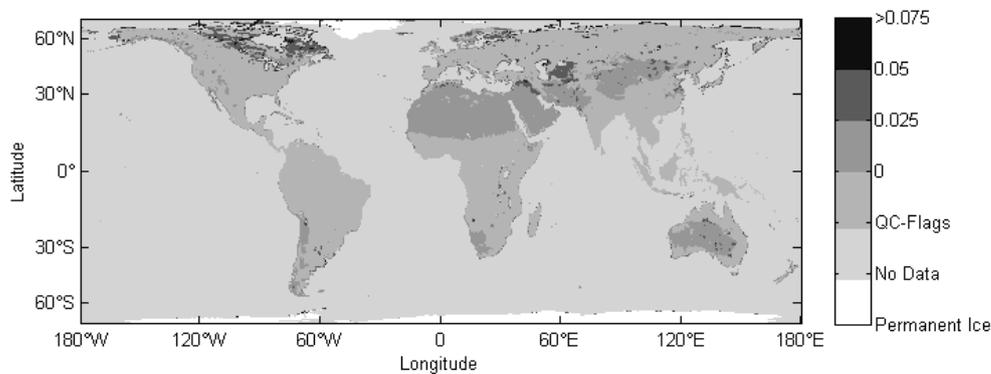


Fig. 1 Standard deviation of daily records of soil moisture in g/cm^3 acquired by AMSR-E for the years 2003–2009. Areas with vegetation-water-content $>1.5 \text{ kg/m}^2$ are flagged by quality-control (QC).

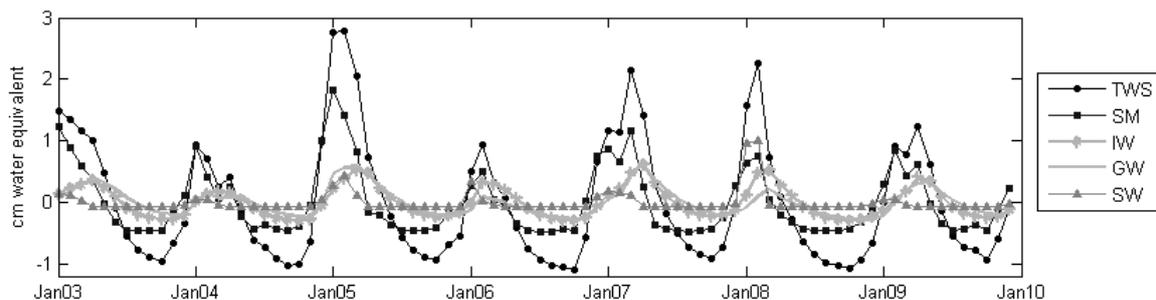


Fig. 2 Modelled contributions of the subsystems soil moisture (SM), inland surface waters (IW), groundwater (GW) and snow water (SW) to the change of TWS for the test area in Central Asia from WGHM.

CROSS-VALIDATION

Methodology

For cross-validation we first contrast soil moisture measurements from AMSR-E with modelled soil moisture values from WGHM. The comparison cannot be done in a straightforward way as the signal of AMSR-E only represents the first centimetre of the top layer of the soil. Given the simulation result of WGHM we apply a scaling transformation to the AMSR-E data in order to adapt the relative measures of soil water content to realistic amplitudes. A scaling factor of 20 was found to be optimal to scale the AMSR-E surface data to the simulated overall soil moisture by WGHM. Furthermore we investigate how TWS changes from GRACE and WGHM compare with soil moisture variations from AMSR-E by applying principle component analyses (PCA) to the data sets. Through PCA a spatio-temporal input signal is split into a series of orthonormal spatial base functions (empirical orthogonal functions, EOFs) and corresponding series coefficients which represent the temporal behaviour of the signal (principal components, PCs) (Preisendorfer & Mobley, 1988). Spatial patterns (EOFs), derived from an eigenvalue and eigenvector decomposition of the input's covariance matrix, and time series (PCs) occur in matched pairs, which are referred to as modes. The first mode describes the most dominant part of the signal, whereas higher modes account for minor contributions. Below, only those modes are presented which in sum account for more than 80% of the signal.

RESULTS

Figure 3 displays the variation of soil water from WGHM and rescaled AMSR-E data. Both signals are highly correlated with respect to their seasonal characteristics. WGHM features higher amplitudes during some winter seasons (e.g. 2004/05) and lower values during some summer seasons (e.g. 2008), indicating that soil moisture variations are larger in deeper soil layers during anomalously dry or wet periods than what can be observed by AMSR-E surface data. Nevertheless, a high level agreement between WGHM and the rescaled AMSR-E data is obvious.

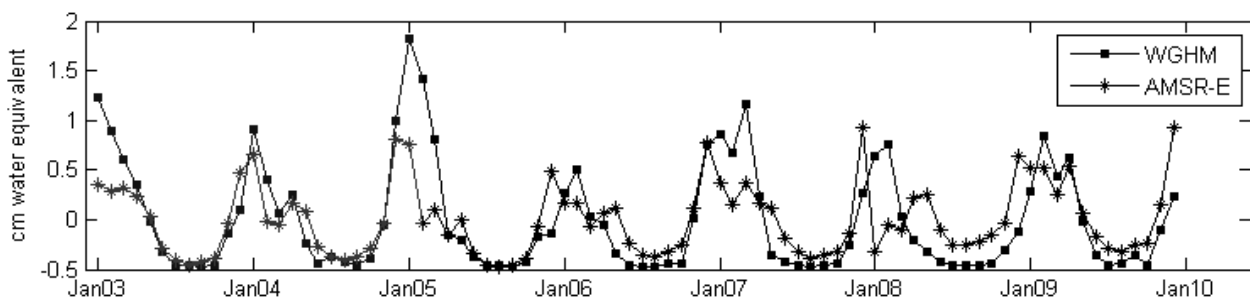


Fig. 3 Variations of soil water in units of cm equivalent water height with respect to monthly mean values from WGHM and rescaled soil moisture data from the satellite sensor AMSR-E.

The results of the PCA of WGHM, AMSR-E and GRACE are displayed in Figs 4 and 5. All data sets have been scaled to units of cm of equivalent water height. The storage variations of total water (GRACE) and soil water (AMSR-E) are not directly comparable with respect to their absolute amplitudes due to the presence of other (minor) hydrological variations in other compartments (cf. Fig. 2). Therefore, the goal of the PCA is the identification of similarities in the spatio-temporal behaviour of the data sets. The analysis revealed that the first two modes are capable of explaining more than 80% of the input signal for all data sets. Figure 4 displays the PCs of the first two modes of the three data sets. In the first mode (upper panel) all signals show a clear annual cycle, being especially uniform over the analysed time span in the case of WGHM. The phases of the annual signals of the data sets match very well: An increasing TWS signature is apparent in GRACE and

WGHM by the beginning of the year, when soil moisture reaches its maximum. By the end of 2008 GRACE shows, unlike WGHM and AMSR-E, an extreme minimum. The origin of this feature is so far unresolved. Mode 2 is significantly weaker and does not follow a periodic behaviour. It features comparable characteristics for WGHM and AMSR-E, while the curve for GRACE is very irregular.

In Fig. 5 the corresponding EOFs for modes 1 and 2 are shown. The spatial pattern of GRACE is very smooth as a consequence of the destriping process. Nevertheless, mode 1 of GRACE and AMSR-E are similar, showing low values in the south and higher values in the north. In mode 2, the values in the east of the test area show comparable signatures for both satellite systems (north: negative; south: positive). However, the spatial pattern of WGHM differs significantly from those of GRACE and AMSR-E. Especially in the north, WGHM shows low values where the signals of GRACE and AMSR-E are strong. It is assumed that the higher variation in the soil moisture signal (AMSR-E) and the TWS signal (GRACE) are caused by an unmodelled (WGHM) hydrological influence of the Aral Sea, its southern part having, to a large extent, dried up.

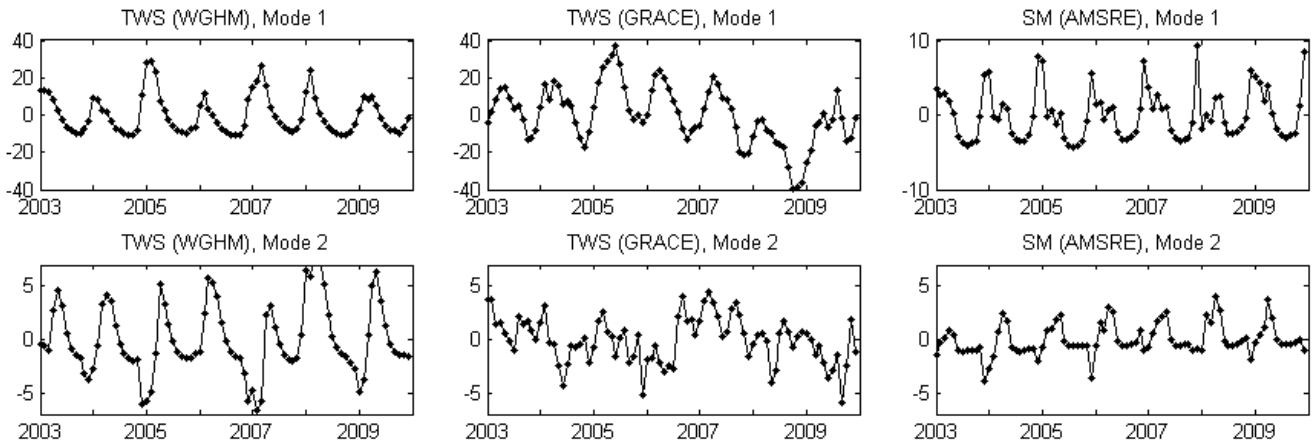


Fig. 4 PCs of the first two modes for TWS (WGHM, GRACE) and SM (AMSR-E), 2003–2009.

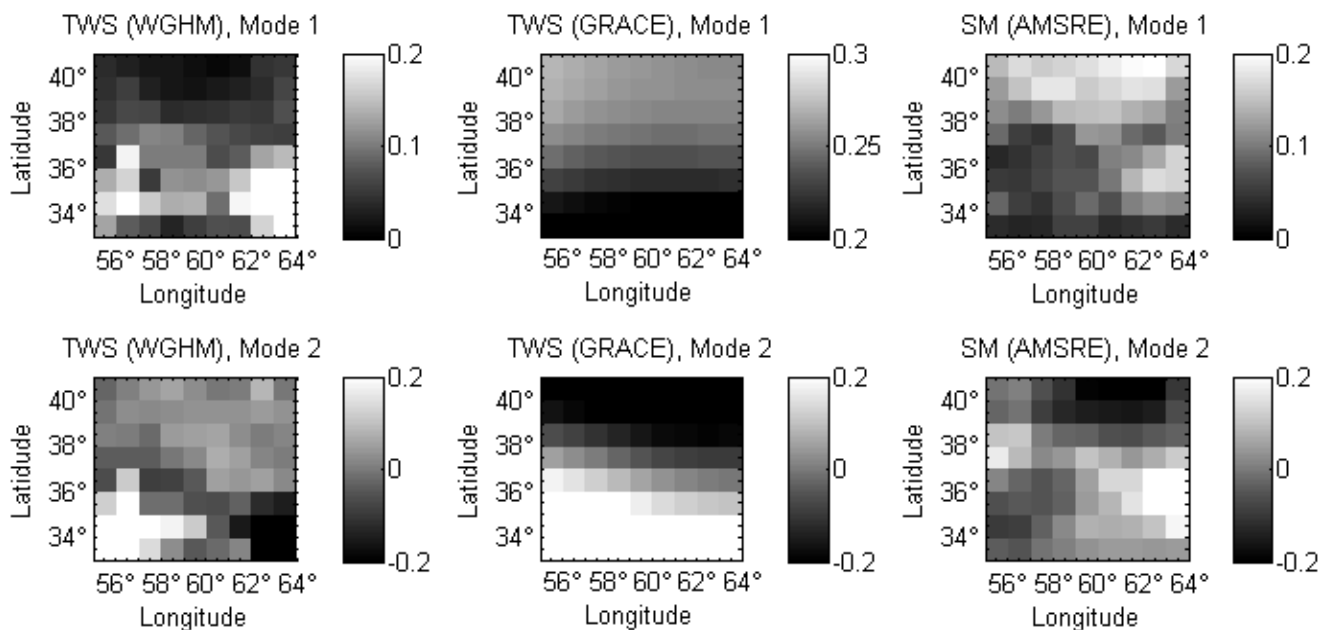


Fig. 5 Corresponding EOFs of the first two modes for TWS (WGHM, GRACE) and SM (AMSR-E).

CONCLUSION AND OUTLOOK

Observed and modelled area integrated soil moisture variations from AMSR-E and WGHM are highly correlated with respect to their overall signal characteristics (Fig. 3). We applied an empirical scaling transformation of the observed values in order to relate the observations near the surface to an actual mass change in soil water. Over the entire time span, such a transformation may be seen as reasonable approximation. But larger discrepancies are obvious for especially wet and dry periods. Therefore further studies are required, putting an emphasis on the incorporation of information about the infiltration behaviour.

Mode 1 of the PCA provides information about the seasonal variation of TWS and SM, showing high values in winter and low values in summer. The curve for GRACE is more irregular since the observed gravity signal contains an integral effect of other mass variations that may not be strictly seasonal. The comparison of EOFs revealed a stronger correlation between the spatial patterns of GRACE (TWS) and AMSR-E (SM) observations than between the patterns of GRACE and WGHM (TWS). As indicated, deviations in the case of WGHM may be based on the underestimation of influences from the Aral Sea area in the northern part of the test area. Hence, satellite observations of SM provide a valuable source of information for the analysis of the spatial pattern of the GRACE signal in this region. The selection of regions in which remotely sensed soil moisture data can contribute to an improved GRACE data analysis is mainly limited by the disturbance of the SM signal by vegetation. It can, however, be expected that satellite sensors operating in L-Band, as implemented within the SMOS mission, will increase possibilities of multi-level cross validation, as introduced in this paper. The application of smoothing and destriping algorithms on the global spherical harmonics strongly influences the GRACE signal. Here improvements can be expected from regional GRACE models based on localizing functions such as spherical wavelets (Schmidt *et al.*, 2008).

Acknowledgment This study was performed in the frame of the project CLIVAR-Hydro (Signals of Climate Variability in Continental Hydrology from Multi-Sensor Space and *In situ* Observations and Hydrological Modelling) funded by the International Graduate School of Science and Engineering (IGSSE) of the Technische Universität München.

REFERENCES

- Alsdorf, D., Rodriguez, E. & Lettenmaier, D. (2007) Measuring surface water from space. *Rev Geophys.* **45**, RG2002, doi:10.1029/2006RG000197.
- Barrett, B., Dwyer, E. & Whelan, P. (2009) Soil moisture retrieval from active spaceborne microwave observations: an evaluation of current techniques. *Remote Sensing* **1**(3), 210–242. doi:10.3390/rs1030210.
- Döll, P., Kaspar, F. & Lehner, B. (2003) A global hydrological model for deriving water availability indicators: model tuning and validation. *J. Hydrol.* **270**, 105–134.
- Flechtner, F., Thomas, M. & Döbslaw, H. (2010) Improved non-tidal atmospheric and oceanic de-aliasing for GRACE and SLR satellites. In: *System Earth via Geodetic-Geophysical Space Techniques* (ed. by F. Flechtner *et al.*), 131–142, doi:10.1007/978-3-642-10228-8_11, Springer, Berlin, Germany.
- Güntner, A., Stuck, J., Werth, S., Döll, P., Verzano, K. & Merz, B. (2007) A global analysis of temporal and spatial variations in continental water storage. *Water Resour. Res.* **43**(5), W05416, doi:10.1029/2006WR 005247.
- Jackson, T. (2005) Remote sensing soil moisture. In: *Encyclopedia of Soils in the Environment* (ed. by D. Hillel) **3**, 392–398, Elsevier, Oxford, UK.
- Njoku, E. (2008) AMSR-E/Aqua Daily L3 Surface Soil Moisture, Interpretive Parameters, & QC EASE-Grids V002. National Snow and Ice Data Center. Boulder, Colorado USA.
- Njoku, E., Jackson, T., Lakshmi, V., Chan, T. & Nghiem, S. (2003) Soil moisture retrieval from AMSR-E. *IEEE Trans. Geosci. Rem. Sens.* **41**(2), 215–229, doi:10.1109/TGRS.2002.808243.
- Preisendorfer, R. & Mobley, C. (1988) *Principle Component Analysis in Meteorology and Oceanography*. Elsevier, Amsterdam, The Netherlands.
- Schmidt, M., Seitz, F. & Shum, C. K. (2008) Regional four-dimensional hydrological mass variations from GRACE, atmospheric flux convergence, and river gauge data. *J. Geophys. Res.* **113**(B10), 1–10. doi:10.1029/2008JB005575.
- Schmidt, R., Schwintzer, P., Flechtner, F., Reigber, Ch., Güntner, A., Döll, P., Ramillien, G., Cazenave, A., Petrovic, S., Jochmann, H. & Wunsch J. (2006) GRACE observations of changes in continental water storage. *Glob. Planet. Change*, **50**(1–2), 112–126. doi:10.1016/j.gloplacha.2004.11.018.
- Schmidt, R., Petrovic, S., Güntner, A., Barthelmes, F., Wunsch, J. & Kusche, J. (2008) Periodic components of water storage changes from GRACE and global hydrology models. *J. Geophys. Res.* **29**, 319–334.
- Seitz, F., Schmidt, M. & Shum, C. K. (2008) Signals of extreme weather conditions in Central Europe in GRACE 4-D hydrological mass variations. *Earth Planet. Sci. Lett.* **268**(1–2), 165–170. doi:10.1016/j.epsl.2008.01.001.

- Singh, P. & Gan, T. (2000) Retrieval of snow water equivalent using passive microwave brightness temperature data. *Remote Sensing Environ.* **74**, 275–286.
- Solomon, S., Qin, D., Manning, M., Chen, Z., Marquis, M., Averyt, K., Tignor, M. & Miller, H. (2007) *Climate Change 2007: The Physical Science Basis*. Cambridge University Press, Cambridge, United Kingdom and New York, NY, USA.
- Syed, T., Famiglietti, J., Rodell, M., Chen, J. & Wilson, C. (2008) Analysis of terrestrial water storage changes from GRACE and GLDAS. *Water Resour. Res.* **44**, W02433, doi:10.1029/2006WR005779.
- Tapley, B., Bettadpur, S., Ries, J., Thompson, P. & Watkins, M. (2004) GRACE measurements of mass variability in the Earth system. *Science* **305**(5683), 503–505. doi:10.1126/science.1099192.
- Wagner, W., Lemoine, G. & Rott, H. (1999) A method for estimating soil moisture from ERS Scatterometer and soil data. *Remote Sensing Environ.* **70**, 191–207.
- Wahr, J., Molenaar, M. & Bryan, F. (1998) Time-variability of the Earth's gravity field: hydrological and oceanic effects and their possible detection using GRACE. *J. Geophys. Res.* **103**, 30205–30229.
- Wigneron, J. (2003) Retrieving near-surface soil moisture from microwave radiometric observations: current status and future plans. *Remote Sensing Environ.* **85**(4), 489–506. doi:10.1016/S0034-4257(03)00051-8.
- Wood, E. (1993) Intercomparisons between passive and active microwave remote sensing, and hydrological modeling for soil moisture. *Adv. Space Res.* **13**(5), 167–176. doi:10.1016/0273-1177(93)90541-I.

Use of twin GRACE satellite gravity data and geoid signals in the characterization of major underlying aquifer regimes and tectonic structure of the Middle Indus Basin, Pakistan

Z. AHMAD & M. SADIQ

Department of Earth Sciences, Quaid-i-Azam University, Islamabad, Pakistan
fz97@hotmail.com; sdq@geo.qau.edu.pk

Abstract Geoid signals provide important information about the subsurface density structure of the Earth and can be effectively utilized for the identification of mass anomalies at depth with respect to the characterization of buried features, i.e. aquifers, minerals, oil and gas reservoirs, and tectonic boundaries. Due to long wavelength characteristics, geoid signals can be more useful in studying regional and global anomalous structures. Longer wavelength geoids correspond to the lower mantle signals and shorter wavelengths depict the heterogeneities in the lithosphere. Moreover, underlying aquifers of various characteristics tend to exist due to the tectonic hierarchy, active fault plains, and the nature of terrains consisting of alluvial flood plains and potwar strata. This study encompasses the impact of geoid models, gravity, topographic and satellite data that was used in the detection of specific plate tectonic boundaries responsible for generating the earthquakes and vast plains along fault lines containing unconfined and confined groundwater aquifers of variable yielding capabilities. To circumvent the hypothesis, a precise gravimetric geoid model was determined for Pakistan and surrounding areas using the EGM2008 gravity model. In addition to this, twin GRACE satellite gravity data have been utilized in the detection of major tectonic boundaries and aquifer characterization. The monthly gravity solutions of GRACE satellite data have been compared for the year 2005 to establish the relationship of time variable gravity fields with tectonic, geological and water bearing structures. With the conclusive findings from the study, it has been observed that the horizontal gradient of the geoid, density variation in buried masses, aquifer geometry and characterization, and tectonic structure can be related to each other. A significant correlation can be seen between the lateral geoid gradient and the distribution of vast flood plains in the Middle Indus Basin. The density of the buried masses is attributed to the location of suitable aquifers in the areas of maximum geoidal slope.

Key words geoid; gravity; geoidal slope; EGM 2008; GRACE satellites; Indus Plain

INTRODUCTION

The geoid is the vertical reference surface that corresponds to undisturbed mean sea level and is an important parameter that has many applications in different geoscience fields. One major application of the geoid pertains to the conversion of ellipsoidal heights to orthometric heights in this era of GPS technology. Geoid signals can be used to find important information about the density structure of the Earth. Geoid undulations have been used to understand the viscosity structure of the mantle by different researchers (Hager, 1984; Cadek & Fleitout, 1999; Kido & Yuen, 2000). Chase (1979) and Stunff & Ricard (1995) have pointed out that longer wavelength geoids have their source in the lower mantle and shorter wavelength anomalies are related to the heterogeneities in the crustal part of Earth. Using spherical harmonic decomposition, one could use geoid data to study a particular area with short wavelength variations (Hwang *et al.*, 1998).

The launches of gravity mission satellites such as CHAMP and GRACE have contributed significantly towards understanding the static and temporal gravity field of the Earth and geoid signals (Tapley *et al.*, 2005). These measure gravity changes due to mass redistribution related to hydrology, sea level, glaciology, hydrocarbon, solid earth and atmosphere. This work mainly deals with the use of global geoid models, especially EGM2008 and GRACE satellite-derived height anomalies, for the assessment of regional crustal structures in Pakistan and adjoining areas, and the Indus Plain's underlying aquifer regimes. The data from a recent gravimetric geoid model have also been used to observe the variation of low negative anomalies over the Indus Plain.

Tectonic settings of the subcontinent

The Himalayan mountains in the north, mid-oceanic ridges in the south and earthquake belts surrounding the Indian plate all show that the subcontinent has undergone extensive tectonic

deformation in the geological past. Pakistan, which is part of the subcontinent, includes the active fault zone, and is an important area from the point of view of seismic activity and geodynamical processes (Fig. 1). The Pakistani Himalayas can broadly be subdivided into five tectono-stratigraphic terrains, delineated by regional fault boundaries. From north to south these are the Karakorum block (Main Karakorum Thrust (MKT)), Kohistan Island arc (Main Mantle Thrust (MMT)), northwestern deformed fold and thrust belt (Main Boundary Thrust (MBT)), southern deformed fold and thrust belt (Salt Range Thrust (SRT) and Trans Indus Ranges Thrust (TIRT)) and the Indo-Gangetic foredeep in the southern most part. Studies by Coward *et al.* (1986) and Searle *et al.* (1987) provide further details.

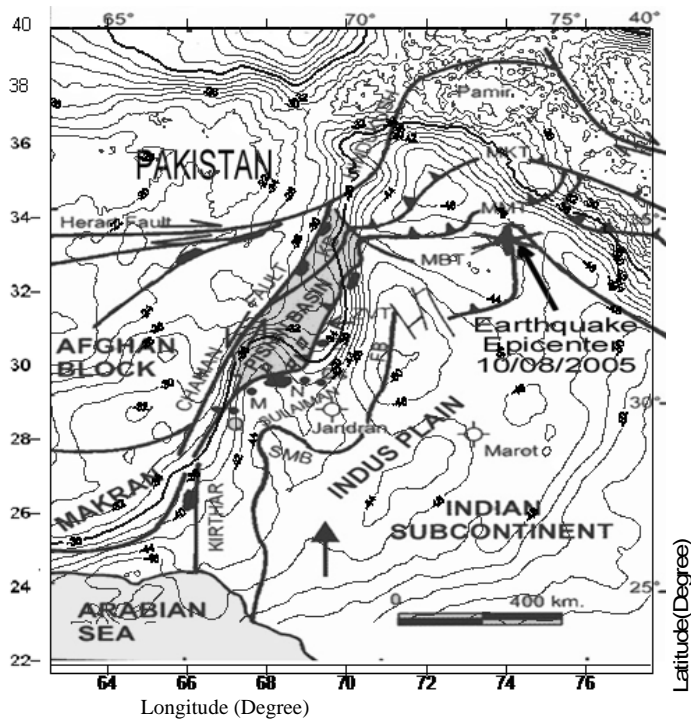


Fig 1 EGM2008 geoid and the tectonic setting of subcontinent.

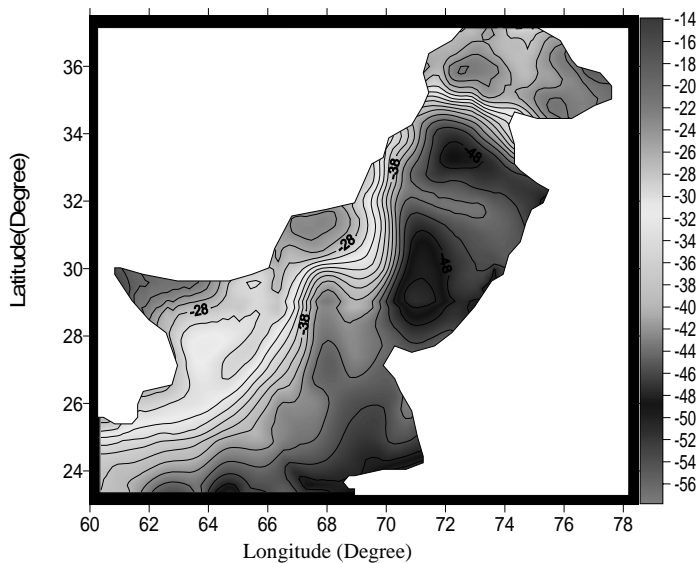


Fig. 2 Total gravimetric geoid of Pakistan.

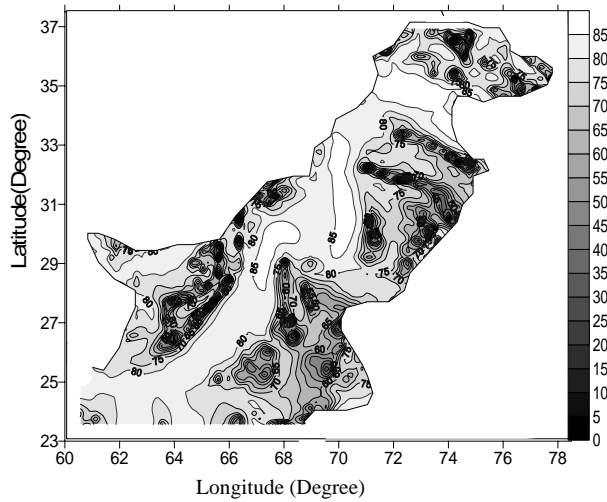


Fig. 3 Terrain slope of geoid from obs. gravity data.

The MMT dips northwards, at between 25' and 45' (Malinconico, 1986) and is the southernmost thrust involving lower crust crystalline rocks of the Indo-Pakistani shield (Lefort, 1975; Bard, 1983a).

Data processing for gravity and geoid signals

Processed data establishes the development of a relationship between gravity and geoid signals with structural style and negative gravity anomalies, over aquifers of the Indus Plain in Pakistan. Data was sourced from a recently developed gravimetric geoid of Pakistan and model-based geoids, i.e. from EGM2008 and GRACE satellite based global models.

The residual geoid determined using gravimetric observations are shown in Figs 2 and 3.

The corresponding model based gravity and height anomaly/geoid values were determined from the spherical harmonic expansions. For mathematical aspects, the reader is referred to studies by Wahr *et al.* (1998), Chambers (2006), and Pavlis *et al.* (2008). The free air anomaly maps of the two models (i.e. from EGM2008 and monthly solution of Twin GRACE data for September 2005) are shown in Figs 4 and 5. The pattern of the anomaly structure is almost the same, however EGM2008

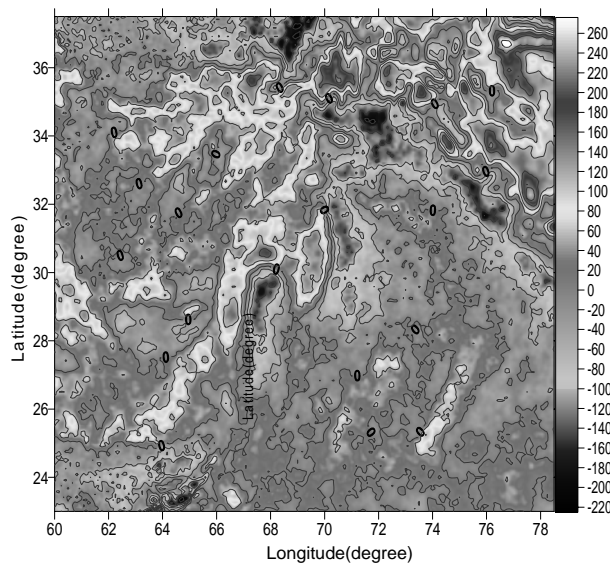


Fig. 4 Free air anomaly from EGM2008.

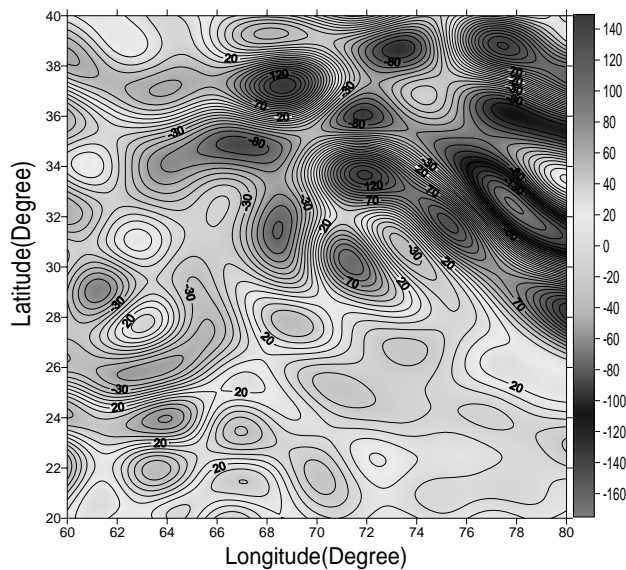


Fig. 5 Free air anomaly of Twin GRACE (Sept. 2005).

has a much better resolution of the gravity field. Sjöberg (1995), Rapp (1997) and Sadiq *et al.* (2009) have explained these studies in detail based on modelled and observed gravity data.

Terrain slope of geoid signal

Terrain slope provides the slope at any grid node on the surface. For a particular point on the surface, the terrain slope is based on the direction of the steepest descent or ascent at that point (i.e. straight downhill or straight uphill at that point). This means that across the surface, the gradient direction can change.

Tectonics identification with the geoid signal

By visual comparison of the structural and topographic maps (Figs 1, 4 and 5), it is clearly visible that there is a general correlation between free air anomaly, topography and earthquake activities. Likewise, a strong correlation between topography, gravity anomaly, geoid and its slope data and depth/occurrences of earthquakes can be seen from Figs 1 and 4–7. The structure of free air anomaly clearly indicates the stress accumulations in the northeast (NE) direction. The fault boundaries and topographic features are identifiable from the free air anomaly data. The structural features are more distinguishable with geoid and its slope taken along east–west and north–south. The major fault structures are visible from geoid and corresponding geoidal slope. This can be seen through a comparison of fault structure (Fig. 1) and geoid and geoid slopes as shown in Figs 6 and 7.

The geoidal terrain slope and free air anomaly have the highest correlation among different parameters for the location of major tectonic structures.

The large positive and negative free air anomalies in (Figs 4 and 5) are lying along the major fault boundaries and may be interpreted to be the result of a higher-density mantle lithosphere. Similar to gravity, the geoid reflects mass variations in the Earth's interior of various wavelengths, but, in contrast to gravity, the geoid primarily reflects the long and medium wavelengths. Figure 2 also shows the new precise geoid model of Pakistan and corresponding map of geoidal slope (Fig. 3). From the first view and in comparing with the simple structural map of the subcontinent (Fig. 1), we can see that there is a clear correlation between the position of the main faults and the geoid undulations. This is particularly clear in the MCT/MMT/MBT and Chaman strike-slip fault and Makran belt in the south.

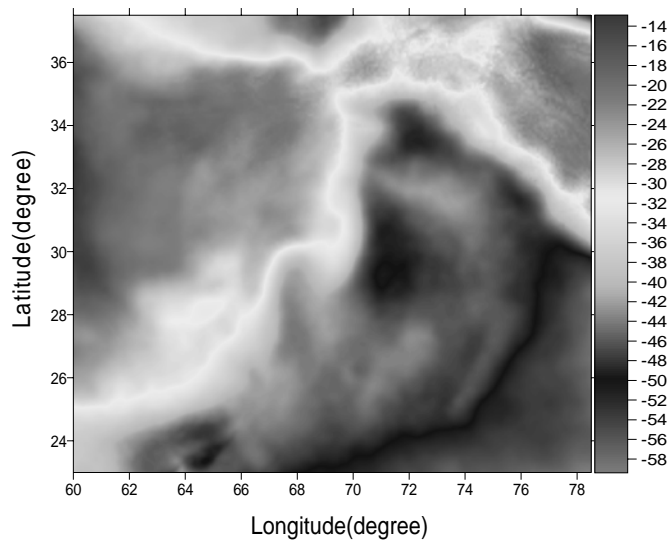


Fig. 6 Geoid signal from EGM2008 model.

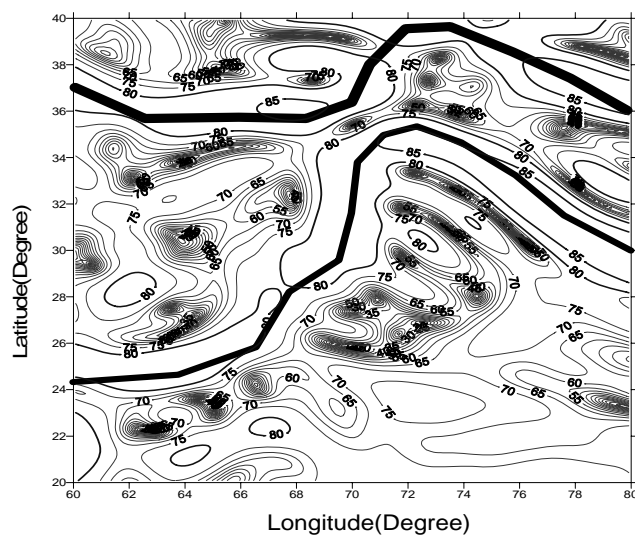


Fig. 7 Terrain slope of the geoid signal from twin GRACE satellite data (monthly solution).

Aquifers of the Indus Plain and gravimetric geoid variations

The Indus River plain is a vast expanse of fertile land, covering about 200 000 square miles (518 000 km²), with a gentle slope from the Himalayan piedmont in the north to the Arabian Sea in the south. It is divisible into two sections, the upper and lower Indus plains, on account of their differing physiographic features. The middle Indus plains stretch between these two and are also famous due to the existence of water reservoirs over the Indus River and the heterogeneous nature of the subsurface lithological features comprising of sand formations of different sizes, gravels, and lenses of impervious clays. The exact thicknesses of the underlying aquifers are unknown, but these are estimated to be more than 600 m. Water wells penetrated in the alluvial aquifers yield greater than 1.0 feet³/sec (0.0283 m³/sec). The total gravimetric geoid of Pakistan (Fig. 2) over the Indus Plains underlying aquifer regimes indicates low negative gravity anomalies ranging from -50 to -46 mgal, while geoid terrain slope of observed gravity data (Fig. 3) refers to low gradient and flatland topography. This can be seen between the north latitudes of 26° to 29° and east longitudes of 70° to 72°.

DISCUSSION OF RESULTS

A new combined gravimetric geoid model for Pakistan (PGM09) has been used for the study of geotectonics. The RMS fit of the combined geoid model *versus* GPS/levelling data is estimated to 21 cm. The RMS from gravimetric geoid is fairly good; however, sources of error might include measured gravity data, the GPS-levelling errors and modelling errors. An integrated approach, including geophysical and geodetic data, such as topography, free air anomaly, geoid, and seismological data, was used to study possible correlations between the location of earthquake occurrence and other parameters. It can be seen from the plots of geoidal slope that there is a significant correlation between the lateral geoid variation/slope and major tectonic activities.

CONCLUSION

The monthly geoidal solutions and its terrain slope of the GRACE data give a clear picture of the major tectonic setting of the subcontinent. The results of geoidal slope plots mark clearly the major tectonic boundaries, e.g. MBT/MMT/MKT, Chaman strike slip fault and Mikran fault. The continuation of the Pamir with Herat fault can be depicted from the geoidal slope data.

The modelling of temporal geoid signal from GRACE and new GOCE data sets can help in better geodynamic studies of major tectonic structures and correlation of gravity anomalies with the Indus Basin aquifers.

REFERENCES

- Bard, J. P. (1983a) Metamorphic evolution of an obducted island arc: example of the Kohistan sequence (Pakistan) in the Himalayan collided range. *Geological Bull., University of Peshawar* **16**, 105–184.
- Cadek, O. P. & Fleitout, L. (1999) A global geoid model with imposed plate velocities and partial layering. *J. Geophys. Res.* **104**(B12), 29055–29075.
- Chambers, D. P. (2006) Evaluation of new GRACE time-variable gravity data over the ocean. *Geophys. Res. Lett.* **33**(17), L17603.
- Chase, C. G. (1979) Subduction, the geoid and lower mantle convection. *Nature* **282**, 464–468.
- Coward, M. P., Windley, B. F., Broughton, R., Luft, I. W., Petterson, M., Pudsey, C., Rex, D. & Asif Khan, M. (1986) Collision tectonics in the NW Himalayas. In: *Collision Tectonics* (ed. by M. P. Coward & A. C. Ries). *Spec. Publ. Geol. Soc. Lond.* **19**, 203–219.
- Hager, B. H. (1984) Subducted slabs and the geoid: constraints on mantle rheology and flow. *J. Geophys. Res.* **89**, 6003–6016.
- Hwang, E., Kao, C. & Parsons B. (1998) Global derivation of marine gravity anomalies from Seasat, Geosat, ERS-1 and TOPEX/POSEIDON altimeter data. *Geophys. J. Int.* **134**, 449–459.
- Kido, M. & Yuen, D. A. (2000) The role played by a low viscosity zone under a 660 km discontinuity in regional mantle layering. *Earth Planet. Sci. Lett.* **181**, 573–583.
- Lefort, P. (1975) Himalaya: the collided range. Present knowledge of the continental arc. *Am. J. Sci.* **275**(A), 1–44.
- Malinconico, L. L. (1986) The structure of Kohistan Island-Arc terrain in northern Pakistan inferred from gravity data. *Tectonophysics* **124**, 297–307.
- Nahavandchi, H. (2002) Two different methods of geoidal height determinations using a spherical harmonics representation of the geopotential, topographic corrections and height anomaly-geoidal height difference. *J. Geodesy* **76**, 345–352.
- Rapp, R. H. (1997) Use of potential coefficient models for geoid undulation determinations using a spherical harmonic representation of the height anomaly/geoid undulation difference. *J. Geodesy* **71**, 282–289.
- Sadiq, M., Ahmad, Z. & Akhter, G. (2009) A study on the evaluation of the geoid-quasigeoid separation term over Pakistan with solution of 1st and 2nd order height terms. *Earth Planet and Space* **61**, 1–9.
- Searle, M. P., Windley, B. F., Coward, M. P., Cooper, D. J. W., Rex, A. J., Rex, D., Li, T. D., Xiao, X. C., Jan, M. Q., Thakur, V. C. & Kumar, S. (1987) The closing of Tethys and the tectonics of the Himalaya. *Geol. Soc. Am. Bull.* **98**, 678–701.
- Sjöberg, L. E. (1995) On the quasigeoid to geoid separation. *Manuscripta Geodaetica* **20**, 182–192.
- Stunff, Y. & Ricard, Y. (1995) Topography and geoid due to lithospheric mass anomalies. *Geophys. J. Int.* **122**, 982–990.
- Tapley, B. D., Ries, J., Bettadpur, S., Chambers, D., Cheng, M., Condi, F., Gunter, B., Kang, Z., Nagel, P., Pastor, R., Pekker, T., Poole, S. & Wang, Y. M. (2005) GGM02: an improved gravity field model from Grace. *J. Geodesy* **79**, 467–478, doi: 10.1007/s00190-005-0480-z.
- Wahr, J., Molenaar, M. & Bryan, F. (1998) Time-variability of the Earth's gravity field: hydrological and oceanic effects and their possible detection using GRACE. *J. Geophys. Res.* **103**, 32 205–32 229.

Monitoring surface and groundwater variations using multisatellite observations and hydrological modelling

FRÉDÉRIC FRAPPART¹, FRÉDÉRIQUE SEYLER², FABRICE PAPA¹,
JEAN-MICHEL MARTINEZ¹, THUY LE TOAN¹, JOECILA SANTOS DA SILVA³,
CATHERINE PRIGENT⁴ & WILLIAM B. ROSSOW⁵

1 *Université de Toulouse, Observatoire Midi-Pyrénées, 14 Avenue Edouard Belin, 31400 Toulouse, France*
frederic.frappart@get.obs-mip.fr

2 *IRD, US ESPACE, Montpellier, France*

3 *Universidade do Estado da Amazonas, Manaus, Brazil*

4 *CNRS, Observatoire de Paris, LERMA, Paris, France*

5 *NOAA, New York, USA*

Abstract We present a methodology combining information from complementary remote sensing datasets and hydrological modelling for the monitoring of surface and groundwater variations in two large drainage basins, the Negro and the Mekong rivers. Spatiotemporal variations of surface waters can be determined combining observations from satellite imagery (i.e. JERS-1, SPOT VGT, multisatellite products) and radar altimetry (i.e. Topex/Poseidon, ERS-1&2 RA, ENVISAT RA-2). The orbital characteristics and the type of sensors present advantages and drawbacks depending on the nature of the study region, and account for the spatial and temporal resolutions, and the accuracy of the surface water storage estimates. Water stored in aquifers is isolated from the total water storage measured by GRACE by removing the contributions of both the surface reservoir derived from satellite imagery and radar altimetry, and the root zone reservoir simulated by hydrological models.

Key words remote sensing; hydrological modelling; surface waters; groundwater

INTRODUCTION

Among the various reservoirs in which fresh water on land is stored (e.g. ice caps, glaciers, snowpack, soil moisture surface and groundwater), surface waters (rivers, lakes, reservoirs, wetlands and inundated areas) play a crucial role in the global biogeochemical and hydrological cycles (de Marsily *et al.*, 2005). Although wetlands and flood plains cover only 6% of the Earth's surface, they have a substantial impact on flood flow alteration, sediment stabilization, water quality, groundwater recharge and discharge (Maltby, 1991; Bullock & Acreman, 2003). Moreover, flood plain inundation is an important regulator of river hydrology owing to storage effects along channel reaches. Reliable and timely information about the extent, spatial distribution, and temporal variation of wetlands and floods, as well as the amount of water stored, is crucial to better understand their relationship with river discharges, and also their influence on regional hydrology and climate.

Remote sensing techniques have been very useful for studying the climate and hydrology of large river basins. Good capabilities for monitoring inundation extent using passive microwave measurements (Hamilton *et al.*, 2002), multispectral images (Osezmi & Bauer, 2002), SAR images (Hess *et al.*, 2003; Martinez & le Toan, 2007) or combining multisatellite information (Prigent *et al.*, 2007; Papa *et al.*, 2010), water levels and discharges using radar altimetry (Birkett, 1998; Frappart *et al.*, 2006a; Santos da Silva *et al.*, 2010), have already been demonstrated. The Gravity Recovery And Climate Experiment (GRACE) mission, launched in 2002, detects tiny changes in the Earth's gravity field, which can be related to the spatio-temporal variations of the terrestrial water storage (TWS) at 10-day or monthly time-scales (Tapley *et al.*, 2004). Variations in the groundwater storage can be separated from the TWS measured by GRACE using external information on the other hydrological reservoirs such as *in situ* observations (Yeh *et al.*, 2006), model outputs (Rodell *et al.*, 2009), or both (Leblanc *et al.*, 2009). No similar studies have been yet undertaken for large river basins characterized by extensive wetlands or flood plains.

In this paper, we propose a methodology to estimate water storage changes in large river basins by combining imagery-derived inundation extents, altimetry-derived water levels and

gravimetry from space products, and also soil water outputs from hydrological models. We present the analysis of surface water and groundwater storage variations in the Negro River and Mekong basins.

METHODOLOGY

Monthly water level maps

Monthly maps of water level over the flood plains of a large river basin can be determined by combining the observations from a satellite inundation data set, radar altimetry derived water levels, and *in situ* hydrographic stations for the water levels over rivers and flood plains (see Fig. 1 for the location of altimetry-based and *in situ* stations in the Negro and Mekong basins). The water levels are linearly interpolated over the flooded zones determined using satellite imagery. The elevation of each pixel of the water level maps is given with reference to its minimum computed over the observation period. This minimum elevation represents either the bathymetry or very low water stage of the flood plain. More details about the methodology used here can be found in Frappart *et al.* (2005, 2006b, 2008).

Groundwater storage estimates

The time variations of the *TWS* expressed as anomalies are the sum of the contributions of the different reservoirs present in a drainage basin:

$$\Delta TWS = \Delta SW + \Delta RZ + \Delta GW \quad (1)$$

where *SW* represents the total surface water storage including lakes, reservoirs, in-channel and flood plains water; *RZ* is the water contained in the root zone of the soil (representing a depth of 1 or 2 m), and *GW* is the total groundwater storage in the aquifers. These terms are generally expressed in volume (km³) or mm of equivalent water height.

The *GW* anomaly is obtained in equation (1) by calculating the difference between the *TWS* anomaly from GRACE and the *SW* level anomaly maps previously derived from remote sensing and the *RZ* anomaly derived from hydrological models outputs. The *TWS* and *RZ* monthly anomalies are the average of the Level-2 GRACE products, and the outputs from LaD and WGHM, respectively. All the datasets were spatially resampled to 1 degree, and the monthly anomalies of each dataset were computed, removing its average over the 2003–2004 time period.

Water volume variations

For a given month *t*, the regional water volume of *TWS*, *SW*, *RZ* or *GW* storage $\delta V(t)$ in a basin with surface area *S*, is simply computed from the water heights δh_j , with $j = 1, 2, \dots$ (expressed in mm of equivalent water height) inside *S*, and the elementary surface $R_e^2 \sin \theta_j \delta \lambda \delta \theta$ (and the percentage of inundation P_j for *SW* from the multisatellite inundation dataset):

$$\delta V(t) = R_e^2 \sum_{j \in S} P_j \delta h_j(\theta_j, \lambda_j, t) \sin \theta_j \delta \lambda \delta \theta \quad (2)$$

where λ_j and θ_j are co-latitude and longitude, $\delta \lambda$ and $\delta \theta$ are the grid steps in longitude and latitude (generally $\delta \lambda = \delta \theta$), and R_e the mean radius of the Earth (6378 km). The surface and total water volume variations are expressed in km³.

RESULTS AND DISCUSSION

Water levels time series

The altimetry stations where water level time series can be constructed (see Frappart *et al.*, 2005, 2006a; Santos da Silva *et al.*, 2010 for the methodology) are unevenly distributed across the Negro

and Mekong basins (Fig. 1). Due to their orbital characteristics, Topex/Poseidon (T/P) has a better temporal resolution but a larger intertrack spacing than ENVISAT RA-2 (10 against 35 days and 315 against 80 km near the equator).

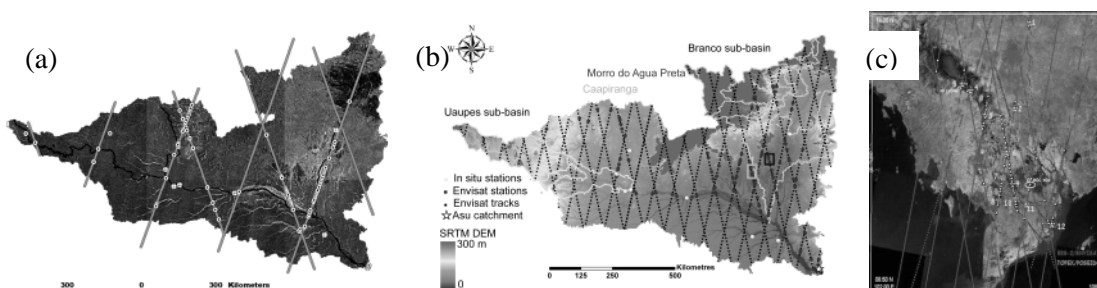


Fig. 1 Map of altimetry tracks and altimetric stations in the Negro and Mekong basins, (a) for T/P in the Negro basin, (b) for ENVISAT RA-2 in the Negro basin, (c) for T/P and ENVISAT RA-2 in the Mekong basin.

In the Negro basin, 86 T/P and 140 Envisat RA-2 altimetric stations corresponding to the intersection between the satellite tracks and rivers or flood plains were defined (Fig. 1(a) and (b)). In the Mekong basin, 80 Envisat RA-2 altimetric stations were defined (Fig. 1(c)). Envisat RA-2 orbit offers a better spatial sampling of the drainage basins than T/P at the expense of a lower temporal sampling. In the tropics, even for large drainage basins such as the Mekong (Fig. 1(c)), T/P is unable to provide a sufficient coverage of the river and its major tributaries.

Altimetric stations permit monitoring of the time variations of water levels both on rivers and flood plains to be monitored with accuracy greater than 50 cm for T/P and 30 cm for RA-2. The better accuracy of RA-2 derived water levels compared with T/P comes from two major reasons. First, T/P was dedicated to the measurement of ocean surface topography whereas RA-2 is devoted to the monitoring of all types of the Earth's surfaces. As a consequence, T/P often lost radar echoes over land, especially for low water stages. Second, T/P echoes were only tracked onboard to estimate the altimeter range (i.e. the distance between the satellite and the surface) whereas ENVISAT Geophysical Data Records (GDR) contains four different estimates of the altimeter range, each of them corresponding to a specific retracking process. Frappart *et al.* (2006a) showed that the Ice-1 retracking scheme was the more suitable for land hydrology.

Inundation extent and surface water volume

Different types of satellite images can be used to delineate floods. In the different cases presented in this paper, SAR, multispectral images and a multisatellite product were employed to characterize the spatio-temporal variations of the flood (Fig. 2). The SAR images, such as the JERS-1 double mosaic used in the Negro basin (Frappart *et al.*, 2005), presents the major advantages of (i) a high spatial resolution (~100 m for JERS-1 double mosaic), (ii) to be used whatever the weather conditions, and (iii) to be able to detect, in C or L band for instance, the presence of water under the forest canopy. Nevertheless, they do not offer a sufficient temporal repetitivity to be used to monitor flood extent at subseasonal time-scales. In the Negro basin, they allowed the flood type (permanent, non-permanent, non-flooded) of each pixel to be characterized and, combined with T/P altimetry-derived water levels, to map the water levels over the rivers and tributaries (Fig. 2(a)), and to estimate the maximum surface water volume stored at the sub-basin scale during the 1995–1996 hydrological cycle. This last result, compared with the measured volume of water that flowed during the same period, provides important information on the residence time of the surface in each sub-basin. The ALOS PALSAR L-band sensor, launched in 2006 by JAXA, now provides images at 100 m of resolution, with a 46-day repeat cycle, at a regional scale, which are very helpful to monitor inundation during the annual hydrological cycle.

The multisatellite inundation dataset (Prigent *et al.*, 2007; Papa *et al.*, 2010), which provides the monthly average inundated areas fraction in a pixel of approximately $25 \times 25 \text{ km}^2$, was also used to characterize the flood in the Negro basin over the period 1993–2004 of common availability of T/P and ENVISAT RA-2 radar altimetry datasets, and of the multisatellite inundation product (Frappart *et al.*, 2008, 2011). It allowed the interannual variations of inundated surfaces and surface water level maps (Fig. 2(b)) exhibit realistic patterns: seasonal and interannual variabilities are consistent with precipitation and river discharges, especially during ENSO years.

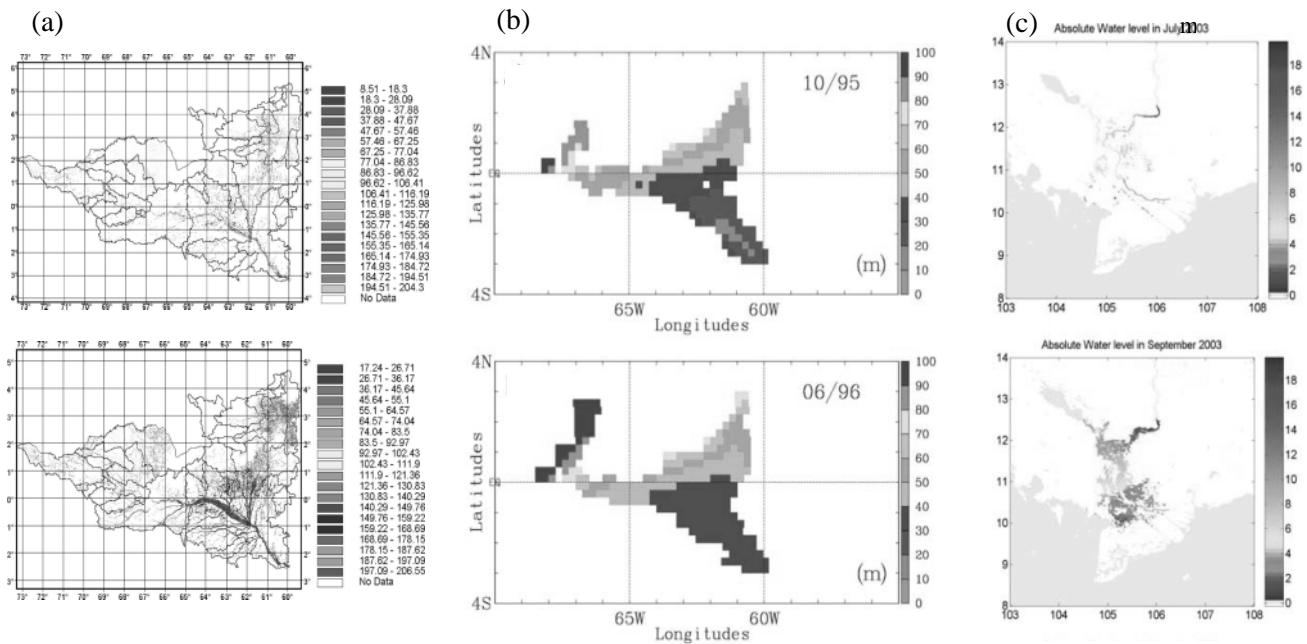


Fig. 2 Map of surface water levels: (a) using JERS-1 and T/P in the Negro basin – low water 1995 (top) and high water 1996 (bottom), (b) using the multisatellite inundation and T/P in the Negro basin – October 1995 (top) and June 1996 (bottom), (c) using SPOT-VGT and ENVISAT RA-2 in the Mekong basin – July 2003 (top) and September 2003 (bottom).

Comparisons have been made with the results obtained by Frappart *et al.* (2005) for the 1995–1996 hydrological cycle. Due to the coarse resolution of the multisatellite product, the flood in the upstream parts of the Negro River and its major tributaries was not detected (Fig. 2(a) and (b)). Considering the same study area, annual surface volume variation from the multisatellite product and T/P is 30% lower than the maximum storage variations estimated using JERS-1 and T/P. The difference in the maximum surface water storage variations between the two methods derives primarily from biases in the flooded area estimates of both multisatellite and SAR products (Frappart *et al.*, 2008).

Medium resolution (1 km) *NDVI* 10-day synthetic images (S10) from SPOT-VGT were used to delineate flood extent in the Mekong basin. To reduce residual cloud contamination, the maximum extent of the flood during the month maps were computed from the union of the three 10-day flood maps (see examples in Fig. 2(c)). An extensive analysis of the basin surface properties show that a pixel can be considered inundated if its *NDVI* value is lower than 0.2. Combined with ENVISAT RA-2 altimetry derived water levels, they allowed us to monitor at monthly time-scales the floods between July and December over the period 1996–2004 (Frappart *et al.*, 2006b). The major drawbacks of multispectral images are the impossibility to detect water under dense vegetation cover and the sensitivity to clouds.

Time variations of the GW anomaly

Time variations (and deviation at each time step) of the water storage anomalies in the *TWS*, *SW*, *RZ* and *GW* reservoirs for 2003 and 2004 were estimated in the Negro basin (Fig. 3(a)). The deviations correspond to the extreme values of GRACE-derived *TWS* from Level-2 CSR, GFZ and JPL solutions and associated errors, of *RZ* from WGHM and model outputs, and of *SW*, taking into account errors in inundated surfaces and heights. The *TWS* signal is dominated during the high waters (May to July) by the *SW* variations (Frappart *et al.*, 2011). The *RZ* varies in phase with both *TWS* and *SW*, and the amplitude of its variations represents a third of the amplitude of *TWS* variations, which is similar to what was obtained by Kim *et al.* (2009) for the whole Amazon basin. The resulting *GW* variations exhibit a more complex profile with two peaks. Its time variations follow the bimodal distribution of the precipitation resulting from the geographical location of the basin in both hemispheres (Fig. 1(b)). A large variability, reaching several months, is observed in the timing of the extremes across the basin: *GW* storage is maximum (minimum) in July–August (December–March) in the western part (Uaupes and west of the Negro), in June–July (February to April) in the centre of the basin and the downstream of the Branco, in August–September in the upper part of the Branco, and in May–June (October–December) for the downstream part of the Negro basin. These results are consistent with *in situ* measurements from sites located in the downstream part of the Negro basin (Do Nascimento *et al.*, 2008; Tomasella *et al.*, 2008) and are closely related to the timing of *GW* recharge and the soil thickness. In Manaus, the time-lag between the maxima of rainfall and *GW* is 3 months, which is similar to what is observed with *in situ* measurements.

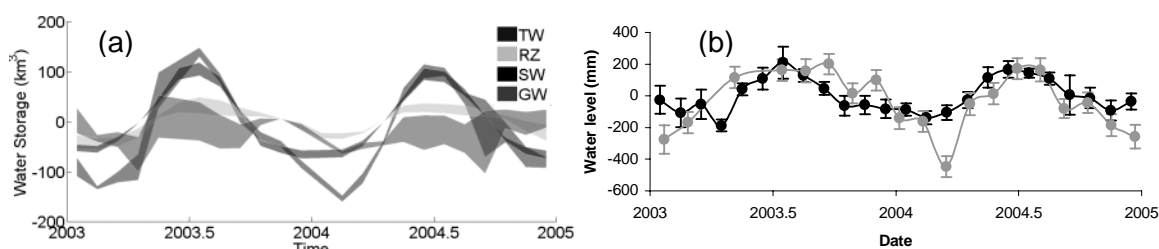


Fig. 3 (a) Time variations of the water storage contained in the different hydrological reservoirs: *TWS*, *RZ*, *SW*, *GW*. (b) Time variations of the surface water levels (grey) and the groundwater (black) in the swamps of Caapiranga.

The groundwater table permanently reached the surface in several parts of the Negro basin. Two of these regions, the Caapiranga and Morro da água preta swamps (Fig. 1(b)), are flooded and can be monitored using radar altimetry. In these cases, we expect *GW* to have similar time variations as water levels. A time series of *SW* and corresponding *GW* anomalies over 2003–2004 are presented in Fig. 3(b) for Caapiranga. Except for February 2004, where the *SW* derived from radar altimetry present an abnormally low level (larger errors on altimetry-derived stages during the low water season, due to the presence of dry land or vegetation in the satellite field of view, have been also observed in different studies (see for instance Frappart *et al.*, (2006a) or Santos da Silva *et al.*, (2010)), both time series agree well ($R = 0.76$ for Caapiranga and 0.73 for Água do Morro Preta) and exhibit similar temporal patterns and amplitudes.

CONCLUSION

The combination of dense altimetry-based water levels with satellite imagery provides an interesting new methodology for remotely measuring surface water volumes over extensive flood plains in large river basins. This combination provides valuable information on the dynamics of

the inundation of river flood plains in large river basins. These results are also of great interest for the preparation of the future wide swath altimetry mission SWOT (Surface Water and Ocean Topography) that will measure 2-D water levels at a spatial resolution of 1 km over a 120 km swath. The complementarity between remote sensing derived hydrological products (altimetry, imagery and gravimetry from space) allowed us to estimate the time variations of the total soil storage. Adding information from hydrological modelling, we were able to estimate realistic time variations of the anomaly of water contained in the aquifers of a large river basin characterized with extensive flood plains.

REFERENCES

- Birkett, C. M. (1998) Contribution of the TOPEX NASA radar altimeter to the global monitoring of large rivers and wetlands *Water Resour. Res.* **34**(5), 1223–1239.
- Bullock, A. & Acreman, M. (2003) The role of wetlands in the hydrological cycle. *Hydrol. Earth Syst. Sci.* **7**, 358–389.
- Do Nascimento, N. R., Fritsch, E., Bueno, G. T., Bardy, M., Grimaldi, C. & Melfi, A. J. (2008) Podzolization as a deferralization process: dynamics and chemistry of ground and surface waters in an Acrisol – Podzol sequence of the upper Amazon basin. *European J. Soil Sci.* **59**, 911–924.
- Frappart, F., Martinez, J. M., Seyler, F., León, J. G. & Cazenave, A. (2005) Flood plain water storage in the Negro River basin estimated from microwave remote sensing of inundation area and water levels. *Remote Sens. Environ.* **99**(4), 387–399.
- Frappart, F., Calmant, S., Cauhopé, M., Seyler, F. & Cazenave, A. (2006a) Preliminary results of ENVISAT RA-2 derived water levels validation over the Amazon basin. *Remote Sens. Environ.* **100**(2), 252–264.
- Frappart, F., Do Minh, K., L’Hermitte, J., Cazenave, A., Ramillien, G., Le Toan, T. & Mognard-Campbell, N. (2006b) Water volume change in the lower Mekong basin from satellite altimetry and imagery data. *Geophys. J. Int.* **167**(2), 570–584.
- Frappart, F., Papa, F., Famiglietti, J. S., Prigent, C., Rossow, W. B. & Seyler, F. (2008) Interannual variations of river water storage from a multiple satellite approach: a case study for the Rio Negro River basin. *J. Geophys. Res.* **113**(D21), D21104.
- Frappart, F., Papa, F., Güntner, A., Werth, S., Santos da Silva, J., Tomasella, J., Seyler, F., Prigent, C., Rossow, W. B., Calmant, S. & Bonnet, M. P. (2011) Total water storage decomposition and estimates of groundwater variations in the Negro River Basin *Remote Sens. Env.* **115**(6), 1588–1594.
- Hamilton, S. K., Sippel, S. J. & Melack, J. M. (2002) Comparison of inundation patterns among major South American flood plains. *J. Geophys. Res.* **107**(D20), 10.129–10.143.
- Hess, L. L., Melack, J. M., Novo, E. M. L. M., Barbosa, C. C. F. & Gastil, M. (2003) Dual-season mapping of wetland inundation and vegetation for the central Amazon basin *Remote Sens. Env.* **87**(4), 404–428.
- Kim, H., Yeh, P. J.-F., Oki, T. & Kanae, S. (2009) Role of rivers in the seasonal variations of terrestrial water storage over global basins. *Geophys. Res. Lett.* **36**, L17402.
- Leblanc, M. J., Tregoning, P., Ramillien, G., Tweed, S. O. & Fakes, A. (2009) Basin-scale, integrated observations of the early 21st century multiyear drought in southeast Australia. *Water Resour. Res.* **45**, W04408.
- Maltby, E. (1991) Wetland management goals: wise use and conservation. *Landscape Urban Plann.* **20**, 9–18.
- de Marsily, G. (2005) Eaux continentales. *C. R. Geosci.* **337**, 1–2.
- Martinez, J.-M. & Le Toan, T. (2007) Mapping of flood dynamics and spatial distribution of vegetation in the Amazon flood plain using multitemporal SAR data. *Remote Sens. Environ.* **108**(3), 209–223.
- Ozesmi, S. L. & Bauer, M. E. (2002) Satellite remote sensing of wetlands. *Wetlands Ecol. Manage.* **10**, 381–402.
- Papa, F., Prigent, C., Aires, F., Jimenez, C., Rossow, W. B. & Matthews, E. (2010) Interannual variability of surface water extent at global scale. *J. Geophys. Res.* **115**, D12111.
- Prigent, C., Papa, F., Aires, F., Rossow, W. B. & Matthews, E. (2007) Global inundation dynamics inferred from multiple satellite observations. 1993–2000. *J. Geophys. Res.* **112**, D12107.
- Roddel, M., Velicogna, I. & Famiglietti, J. (2009) Satellite-based estimates of groundwater depletion in India. *Nature* **460**, 999–1003.
- Santos da Silva, J., Calmant, S., Seyler, F., Rottuno Filho, O. C., Cochonneau, G. & Mansur, W. J. (2010) Water levels in the Amazon basin derived from the ERS 2 and ENVISAT radar altimetry missions. *Remote Sens. Environ.* **114**(10), 2160–2181.
- Tapley, B. D., Bettadpur, S., Watkins, M. M. & Reigber, C. (2004) The Gravity Recovery and Climate Experiment; mission overview and early results. *Geophys. Res. Lett.* **31**(9), L09607.
- Tomasella, J., Hodnett, M. G., Cuartas, L. A., Nobre, A. D., Waterloo, M. J. & Oliveira, S. M. (2008) The water balance of an Amazonian micro-catchment: the effect of interannual variability of rainfall on hydrological behaviour. *Hydrol. Processes* **22**, 2133–2147.
- Yeh, P. J.-F., Swenson, S. C., Famiglietti, J. S. & Rodell, M. (2006) Remote sensing of groundwater storage changes in Illinois using the Gravity Recovery and Climate Experiment (GRACE). *Water Resour. Res.* **42**, W12203.

Analysis of widespread fissures associated with groundwater depletion and extreme rainfall using multi sensor data

RAMESH P. SINGH^{1,2}, WASEEM MEHDI², MAJID NAEIMI³, ALOK SAHOO⁴ & RAJESH KUMAR⁵

1 School of Earth and Environmental Sciences, Chapman University, Orange, California 92866, USA
rsingh@chapman.edu

2 Research and Technology Development Centre, Sharda University, Greater Noida, India

3 Institute of Geodesy, University of Hanover, Schneiderberg 50, 30167 Hanover, Germany

4 Department of Civil and Environmental Engineering, Princeton University, Princeton, New Jersey 08544, USA

5 People's Science Institute, 252 Vasant Vihar Phase I, Dehradun 248006, India

Abstract During June 2008, widespread fissures were observed in the northern flank of the Indian Peninsular shield of the Indo-Gangetic plains. These fissures were found to be up to 2 km-long and emerged after excessive rainfall. At some places, these cracks/fissures were found to be up to 10 m deep. The emergence of such cracks in widespread regions attracted the attention of people living in the surrounding regions and was believed to be a sign of an impending earthquake. A detailed analysis of multiple satellite sensors (GRACE, TRMM, AMSR-E) and ground data was carried out to study the long term behaviour of the water storage equivalent and soil moisture. The rainfall and soil moisture data were analysed for the period 2000–2008 and a decline in the rainfall and soil moisture were observed during summer (March–May), showing poor recharge of groundwater in the region. The monthly water storage equivalent retrieved from GRACE satellite data also showed low water storage in the entire region representing a low groundwater table and low soil moisture, which is quite obvious due to the poor monsoon and steep population growth during 2000–2008. Such a declining trend in the soil moisture, especially in the peninsular shield covered by a thin soil layer, make it liable to the formation of cracks and fissures after excessive rainfall due to a sharp vertical gradient in the stress.

Key words cracks; GRACE; fissures; Peninsular shield; Indo-Gangetic plains; remote sensing; soil moisture; rainfall

INTRODUCTION

The Indo-Gangetic plain is one of the largest basins in the world, and home to 600 million people. The basin has a very dense drainage network with huge groundwater resources and thick alluvial deposits. The thickness of the alluvial deposits is shallow in the western part and deep in the eastern part of the basin (Singh *et al.*, 1992). The basin adjacent to the peninsular shield in the southern part has a thin cover of alluvial deposits (Singh *et al.*, 1992, 1995, 1997) which are above some hard rock formation. The shield is exposed to the surface in some regions. The area is considered as a hard rock area, where deep tubewells do not exist and groundwater is tapped through dug wells. During summer, an acute groundwater problem exists. With the increasing population in the last five decades, the number of dug wells increased from 3.86 million to 9.6 million, shallow tubewells from 3000 to 8.36 million and deep tubewells from negligible to 0.53 million. Electric pump sets have increased from negligible to 14.81 million and diesel pumps from 66 000 to about 6.34 million. There has been a steady increase in the area irrigated by groundwater from 6.5 million hectares (M-ha) in 1951 to ~45 M-ha in 2001. The area is considered to be one of the most heavily irrigated regions of the world (Rodell *et al.*, 2009; Tiwari *et al.*, 2009). In some of the areas, the unscientific development of this resource without any regulation/incentives for management has led to a decline in groundwater levels that have affected the groundwater quality. The soil moisture levels show high spatial and temporal variability over India due to variability in geological terrain and tectonic settings (Singh *et al.*, 2005).

With the continuously increasing groundwater demand in the industry and irrigation sectors, due to population growth, the water tables have decreased very quickly. Due to increasing groundwater withdrawals, the region is prone to ground subsidence at local and regional scales (Mishra *et al.*, 1993). Such decline in groundwater levels is further affected by poor monsoon

rainfall and delays in the onset of the monsoon. This leads to a decline in the soil moisture level, affecting the vertical stress regime between the upper soils and underlying rock strata. Such a stress regime is likely to be responsible for the formation of the recent ground cracks and fissures. During 2008, widespread ground fissures and cracks were observed in the central parts of the Indo-Gangetic basin and also in the southern flanks, i.e. in the northern side of the peninsular shield. In the present paper, detailed analysis of monthly water storage, soil moisture and rainfall from multiple satellite sensors and ground data, show that sudden rainfall caused an immediate increase in the soil moisture in the upper part which affected the vertical stress, and as a result widespread ground fissures/cracks were formed.

HYDROGEOLOGY OF THE REGION

Groundwater resources in India generally show spatial and temporal variability due to diversified geological terrain with contrasting variation in lithological, geophysical and complex tectonic settings and climatic variations. The region is mainly an undulating plain with irregular granitic hillocks which are intruded in the alluvial soil of the Indo-Gangetic plains. The alluvial thickness shows variations; the alluvial plain is very thin in the southern flank of the basin, about 300 m in the central part and around 1200 m in the northern flanks of the Indo-Gangetic plains (Singh *et al.*, 1995). The elevation of the area in general ranges between 180 and 200 m above MSL, whereas the elevation of isolated granite hillocks rises up to 302 m. The area is drained by a river and its tributaries (Prakash & Mohan, 1996). The quartz reefs act as a natural barrier across local streams forming shallow lakes.

Groundwater exploration in the Indo-Gangetic plains has shown the existence of potential aquifers down to 1000 m or more. Annual replenishable groundwater resources of this region are ~200 billion cubic meters (BCM) which is more than 45% of the country’s total. It also has vast in-storage groundwater resources down to a depth of 450 m. Deeper confined aquifers get their recharge from distant recharge zones and have groundwater of varying ages. In some of the areas, the deeper aquifers are under auto-flow conditions. The quality of groundwater in these aquifers is also good. These aquifers can support large scale development through both shallow and deep tubewells. The depth to the water table varies from 5 to 15 m, and the monsoon rainfall and rivers and their tributaries are the sources of groundwater recharge in the area. These resources support most of the groundwater development for irrigation, drinking and industrial purposes. The upper surface of the soil is comprised of clay, sand, kankar and weathered zone, which supplies groundwater to shallow depth dug-wells. The depth to water levels in dug-wells varies from 1 to 10 m below the surface.

The population in Uttar Pradesh and Madhya Pradesh has increased drastically in recent years (1951–2008; Fig. 1). Poor monsoon rainfall and a shift in the onset of the monsoon have affected the rate of decline of the groundwater level in this region, especially in the summer season.

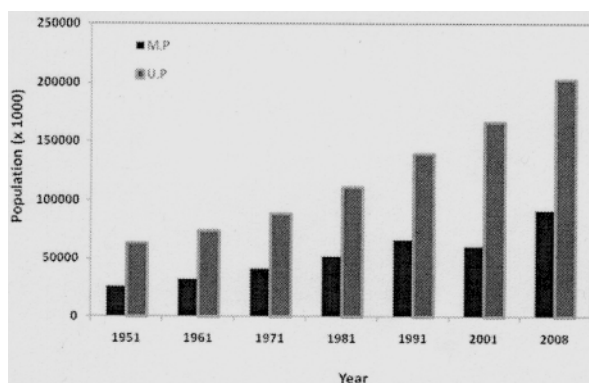


Fig. 1 The population growth in Uttar Pradesh and Madhya Pradesh during 1951–2008. In Uttar Pradesh and adjacent Madhya Pradesh state, the population steadily increased during this period.

OBSERVED WIDESPREAD FISSURES AND CRACKS

Ground fissures of varying sizes have been observed in several villages located in 12 adjacent districts in southern and eastern Uttar Pradesh and northern parts of Madhya Pradesh. These cracks were observed soon after the first rains of the monsoon on 9 June 2008. As the rains progressed, the news of the ground fissures spread to several other villages. Fissures were found of different shapes and sizes, in generally curvilinear and reticulate patterns at places with varying width and length up to 2 km. These fissures were found in several villages; Kalpi (lat. N 26°07.203', long. E 79°45.800') close to the River Yamuna, Nyamatpur (lat. N 26°13.145', long. E 79°32.971') about 5 km from the River Yamuna, Abdullahpur (lat. N 26°25.312', long. E 79°27.729') 1 km from Yamuna bank, Hanumanthpura (lat. N 26°30.409', long. E 79°05.094') 1.5 km from to the Chambal River, Sindaus (lat. N 26°28.253', long. E 79°06.134') close to a tributary of the Chambal River, and very long cracks were found in Kupra village running from lat. 25°52.018', long. E 79°52.451' to lat. N 26°07.203', long. E 79°52.471'. Fissures were found up to 10 m deep at several places. The cracks were slowly widened because of subsequent collapse of the edges of the walls leading to an increase in their aperture. These cracks developed in the top soil, comprising of silty clay and clay. Most of the cracks/fissures were observed either in the vicinity of the river or near a water body like ponds. In the last several years, the groundwater withdrawal has increased and proper recharge has been affected due to poor monsoon rainfall. Figure 2 shows examples of fissures with multiple directions. The ground fissures were mostly observed in the villages having few deep tubewells.

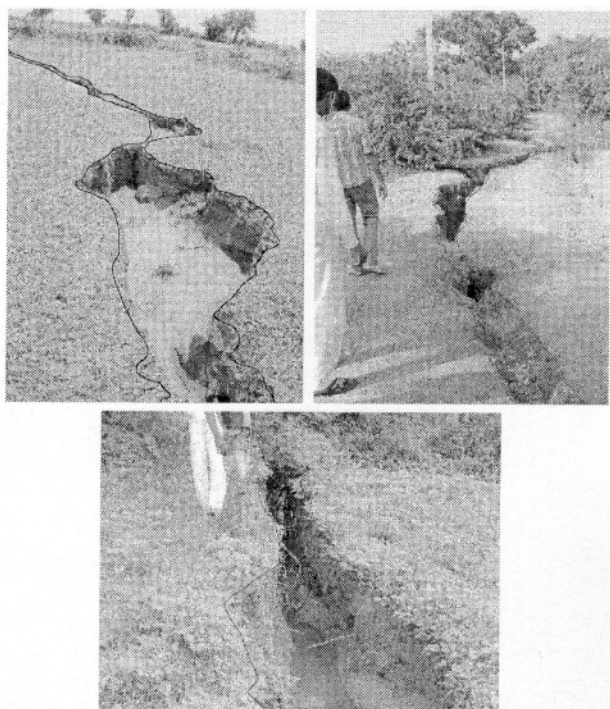


Fig. 2 Observed ground fissures/cracks after excessive rainfall.

AMSR-E SOIL MOISTURE RETRIEVAL DATA

AMSR-E is a passive microwave radiometer launched aboard NASA's Aqua Satellite (Parkinson, 2003). The local crossing time of AMSR-E is 0130 LST (Descending pass) and 1330 LST (Ascending pass). This instrument measures brightness temperatures at six frequencies ranging from 6.9 to 89.0 GHz in horizontal and vertical polarizations at each frequency for a total of 12

channels. The AMSR-E C- (6.9 GHz) and X-band (10.7 GHz) channels are strongly related to land surface soil moisture variability (Njoku *et al.*, 2003). Daily Level-2B and Level-3 land products are available from the National Snow and Ice Data Center (NSIDC) from 19 June 2002. Soil moisture is not retrievable where significant fractions of snow cover, frozen ground, dense vegetation, precipitation, open water, or mountainous terrain occur within the sensor footprint. The products are generated on an Earth-fixed grid with ~ 25 km nominal grid spacing. The AMSR-E satellite overpass frequency over any geographic region in the mid-latitudes area is in every 2–3 days (Njoku *et al.*, 2003). Soil moisture represents average soil moisture from 1 to 2 cm of soil. In Fig. 3(a), daily soil moisture in Jhansi region is shown for May and June in descending mode for the years 2003–2008. The soil moisture was found to be low before rainfall on 2 June and also likely due to a decrease in water table. After the rainfall, the soil moisture was found to increase in June. Figure 3(b) shows soil moisture retrieved from AMSR-E for the period June 2002–December 2008 for ascending and descending modes. The minimum soil moisture is observed in May showing low soil moisture level during summer months. This decrease in soil moisture is due to a decrease in water table and excessive demand of groundwater for drinking and irrigation purposes. After the monsoon rainfall, the soil moisture increases and the higher peak of soil moisture is observed in June 2008 (Fig. 3(a),(b)).

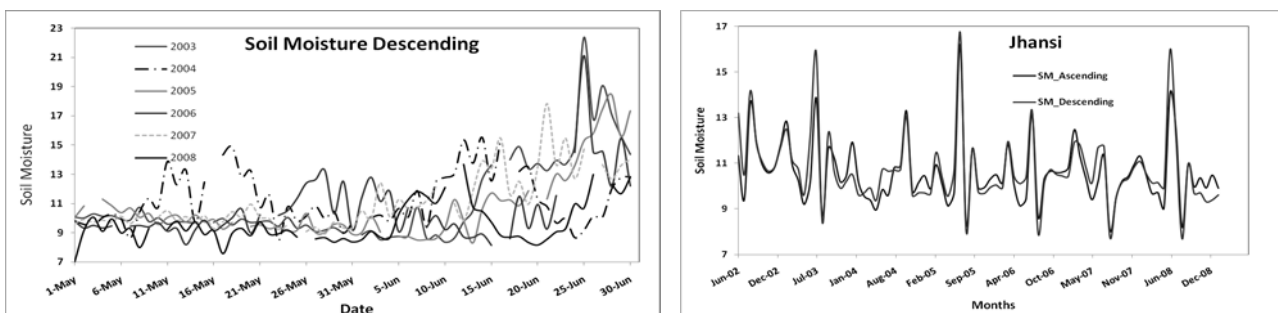


Fig. 3 (a) Daily variations of soil moisture (% vol/vol) during May–June for 2003–2008 in Jhansi region retrieved from AMSR-E using descending pass data. (b) Variation of soil moisture (% vol/vol) at Jhansi (latitude 25.43, longitude 78.58).

GRACE DATA

GRACE (Gravity Recovery and Climate Experiment) is a joint US-German satellite mission dedicated to studying the Earth's gravity field and its temporal variations. Since the launch of the twin satellites, the Earth's gravitational potential is measured every month with a spatial resolution of about several hundred kilometres. GRACE satellites orbit the Earth at an initial altitude of about 500 km above the Earth's surface on a near-polar orbit. The distance between the two satellites is approximately 220 km and is measured precisely using a precise microwave inter-satellite ranging system (Velicogna *et al.*, 2001). GRACE monthly gravity fields are being released in terms of Stokes' coefficients up to a certain degree and order. The differences between monthly solutions reveal time variable components of the Earth's gravity field, which are caused because mass redistribution in the Earth system (i.e. atmosphere, oceans and solid Earth). Well-known components of this mass transport (i.e. Earth tides, ocean tides, atmospheric variability and so on) are already removed during GRACE data processing. Thus, temporal changes revealed by GRACE monthly solutions are due to other natural phenomena whose mechanisms are not well understood yet. However, the main parts of the short-term variability are assumed to happen in the Earth's fluid envelope since fluids (water and gases) are much more mobile than rock (Velicogna *et al.*, 2001).

Several studies have been carried out showing the capability of GRACE data to trace hydrological cycles at global and regional scales (Velicogna *et al.*, 2001; Wahr *et al.*, 2006). Based

on GRACE data, a declining trend in groundwater has recently been observed over the different regions of India (Rodell *et al.*, 2009; Tiwari *et al.*, 2009). We have analysed GRACE data and estimated monthly variations of equivalent water thickness on a regional grid of one degree over India. We have also performed an isotropic smoothing filter with a radius of 400 km to reduce the noise level in high-degree coefficients. We estimated monthly deviation in an equivalent water column for the period February 2003–December 2008 for different locations in India, covering the Indo-Gangetic plains, central India and southern parts of India. In Fig. 4, we show the deviation in equivalent water column (m) observed in Kanpur (St #1 – latitude 24.46, longitude 80.35) and Jhansi (St #2 – latitude 25.43, longitude 78.58). A declining trend is observed in these two locations, which lie in the Indo-Gangetic plains and also the southern flank of the Indo-Gangetic basin; such trends are not observed in the southern parts of India (results are not shown).

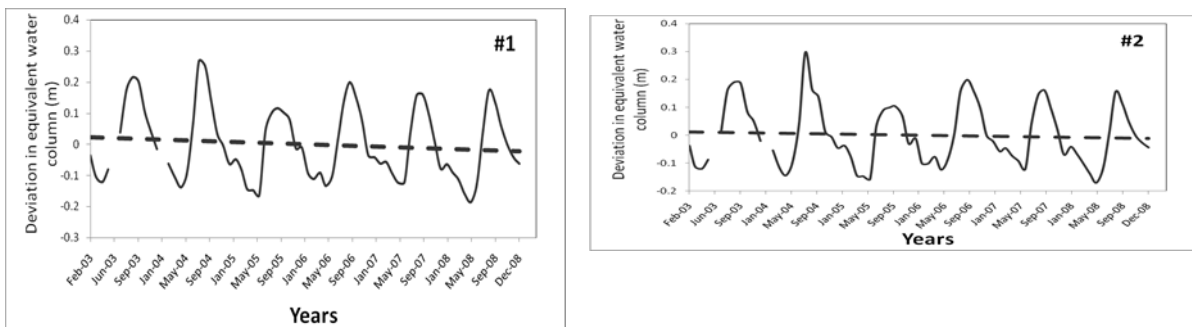


Fig. 4 Deviation in equivalent water column (m) observed at Kanpur (St #1, latitude 24.46 and longitude 80.35) and Jhansi (St #2, latitude 25.43 and longitude 78.58).

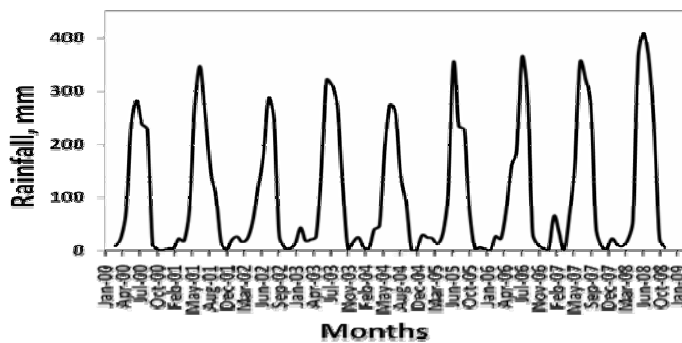


Fig. 5 Monthly rainfall time series for the period 2000–2008.

RAINFALL

Rainfall data observed from raingauges operated by the Indian Meteorological Department are used in this study. Monthly average rainfall data over the Indo-Gangetic plains covering Kanpur and Jhansi are considered for the period 2000–December 2008. Low rainfall is observed during March–May 2008 compared to other years (Fig. 5). This shows that the groundwater recharge was poor in 2008. Such conditions will provide a high stress regime between the upper earth surface and near the surface, and may provide a pronounced stress contrast.

DISCUSSION

The probable mechanism for the development of the ground fissures may be attributed to excessive drying of the soil mass due to low soil moisture in the area during summer. Drought

conditions for the last 4–5 years, and extensive withdrawal of groundwater in adjoining regions, has likely caused the excessive drying of soil, as a result of which the shrinkage of soil and tensile failure occurred. The tension failure near the surface may have given rise to more or less vertical cracking. The ingress of water during heavy precipitation increased the pore pressure in the clay, which in turn resulted in an overall reduction of strength of clay and in the formation of ground fissures and cracks. Besides these, the groundwater withdrawal in the absence of recharge was also observed as favourable conditions for local subsidence, which may have also led to the formation of ground fissures and cracks. The widespread ground fissures and cracks observed during June 2008 is very likely due to the rain water that may have percolated through heterogeneous soil masses, and moved preferentially through the most permeable upper surface zones. Fine sands and silts, which are commonly present in the region, are most susceptible to vertical failure and the conditions may have also occurred due to the high hydraulic gradient, which is where there is a rapid loss of head over a short distance. All the ground fissures in the adjoining Jhansi area are located either near some stream or some water body, where the hydraulic gradient could be maximum. The orientation of many of the fissures may be related to the stress field, as indicated by the regional structures. It is very likely that the fissures are caused by the excessive recharge of the groundwater.

REFERENCES

- Mishra, S. K., Singh, R. P. & Chandra, S. (1993) Prediction of subsidence in Indo-gangetic basin due to groundwater withdrawal. *Engng Geol.* **33**(3), 227–239.
- Njoku, E. G., Jackson, T. J., Lakshmi, V., Chan, T. K. & Nghiem, S. V. (2003) Soil moisture retrieval from AMSR-E. *IEEE Trans. Geosci. Remote Sens.* **41**(2), 215–229.
- Parkinson, C. L. (2003) Aqua: An Earth-Observing Satellite Mission to examine water and other climate variables. *IEEE Trans. Geosci. Remote Sens.* **41**(2), 173–183.
- Prakash S. R. & Mohan, R. (1996) Hydromorphological mapping of Panwari area, Hamirpur district, Uttar Pradesh using satellite data. *J. Indian Soc. Remote Sens.* **24**, 97–105.
- Rodell, M., Velicogna, I. & Famiglietti, J. S. (2009) Satellite-based estimates of groundwater depletion in India. *Nature* **460**, doi:10.1038/nature08238, 999–1003.
- Singh, R. P., Kant, Y. & Rastogi, A. (1992) Prospects of hydrocarbon in Indo-Gangetic plains and Himalayan foothills region using magnetotelluric method. *Indian J. Petroleum Geology* **1**(2), 258–271.
- Singh, R. P., Kant, Y. & Vanyan, L. (1995) Deep electrical conductivity structure beneath the southern part of the Indo-Gangetic plains. *Phys. Earth and Planet. Int.* **88**(3–4), 287–294.
- Singh, R. P. & Singh, U. K. (1997), Tectonic Settings of Indo-Gangetic Basin Revealed from MT data. *Current Sci.* **73**(3), 281–284.
- Singh, R. P., Mishra, D. R., Sahoo, A. K., *et al.* (2005) Spatial and temporal variability of soil moisture over India using IRS P4 MSMR data. *Int. J. Remote Sens.* **26**, 2241–2247.
- Tiwari, V. M., Wahr, J. & Swenson, S. (2009) Dwindling groundwater resources in northern India, from satellite gravity observations. *Geophys. Res. Lett.* **36**, L18401.
- Velicogna, I., Wahr, J. & Van den Dool, H. (2001) Can surface pressure be used to remove atmospheric contributions from GRACE data with sufficient accuracy to recover hydrological signals?. *Geophys. Res. Lett.* **106**(B8), 16415–16434.
- Wahr, J., Swenson, S. & Velicogna, I. (2006) The accuracy of GRACE mass estimates. *Geophys. Res. Lett.* **33**, doi:10.1029/2005GL025305.

A global network of area-integrated water budget monitoring for climate change detection?

EARL BARDSLEY

Department of Earth Sciences, University of Waikato, Private Bag 3105, Hamilton, New Zealand
e.bardsley@waikato.ac.nz

Abstract Time series of ecosystem-scale water storage change should signal climatic change because storage amount reflects the integrated environment. Direct measurement of area-averaged land storage change is now possible through either gravity observations or geological weighing lysimeters (GWL). Gravity satellite systems such as GRACE monitor water storage changes over extensive regions at coarse time scales, while GWL stations monitor over hectares and in real time. The GWL approach comprises accurate measurements of deep static pore water pressures (derived, for example, from seismic monitoring) which respond to surface water load changes. Similarly, direct gravity monitoring to detect the local storage change signal of climate change might be achieved using existing deep underground physics laboratories. By the combined use of new and existing monitoring, it is suggested that a global network of ecosystem storage change be set up in localities likely to be most impacted by climate change effects.

Key words storage change; gravity monitoring; mass change; climate change

INTRODUCTION

It is well known that climate change effects will impact some regions more than others, and there is a need for observational data systems for the purposes of early detection of environmental changes. One approach here is to seek some spatial mixture of recorded variables which most accurately detects early climatic change (Groisman *et al.*, 2004; Ribes *et al.*, 2010). Alternatively, it can be useful to focus on some net effect environmental measures where conditions allow. For example, this can include monitoring of wetlands (Ebrahimi *et al.*, 2009), arid region streams (Dahm & Molles, 1990), river flows generally (Villar *et al.*, 2009) and lake level changes (Jones *et al.*, 2001).

It is increasingly recognised that subsurface water storage can play an important role in both reflecting and influencing climatic trends. This applies to both groundwater (Bierkens & van den Hurk, 2007; Schaller & Fan, 2009) and soil moisture content (Hanesiak *et al.*, 2009; Jung *et al.*, 2010; Krakauer *et al.*, 2010; Lorenz *et al.*, 2010; Seneviratne *et al.*, 2010). Therefore, it would seem that total water storage monitoring could be useful as an indicator of climate change, as it is an integrated quantity reflecting both soil and groundwater storage changes. On the larger spatial scale, gravity satellite systems like GRACE can monitor land water storage change trends as a consequence of climatic change or direct human effects (Rodell *et al.*, 2009). However, sometimes land surface/climate feedback effects may be particularly evident at smaller scales (Koster *et al.*, 2004; Notaro, 2008). While it may be possible to downscale GRACE data to incorporate groundwater flow effects via models (Niu *et al.*, 2007), there still remains a lack of water budget ground truthing at the smaller scale for climatic change detection, particularly for arid and semi-arid regions (Henderson-Sellers *et al.*, 2008). The purpose of this brief note is to make a case for establishing a global monitoring network of total land water storage change at the ecosystem scale as a convenient integrated environmental measure well suited to detecting climatic change.

LOCAL STORAGE CHANGE MONITORING

Area-integrated water storage change can be monitored at the local scale by geological weighing lysimeters (GWL) or from direct gravity measurements. The GWL concept is particularly simple but requires suitable subsurface hydrogeology with confined isolated aquifers having pore pressures influenced only by static effects due to surface loading. That is, there must be no dynamic effects due to recharge/discharge or groundwater extraction. A confined aquifer serves as a GWL when pore water pressure changes are a consequence only of surface and near-surface water mass change and

atmospheric loading. The aquifer pore water pressure thus acts as a weighing fluid and total ecosystem storage change as length units of water is derived by utilisation of the aquifer loading coefficient. This enables storage change to be monitored in real time over a scale of hectares from a confined aquifer in the order of 50 m below the ground surface (Van der Kamp & Schmidt, 1997).

In practice, the assumption of GWL isolation from dynamic groundwater effects can never be directly confirmed, so it is necessary to have vertical replication over at least two aquifers with different loading coefficients to verify independent estimates of the same storage change at the land surface. A two-aquifer system can yield quite accurate measurements of surface and subsurface water storage change. For example, Fig. 1 shows a period of time at a field site where water storage change is almost entirely taken up as rain water accumulating in the soil without evident evaporative loss.

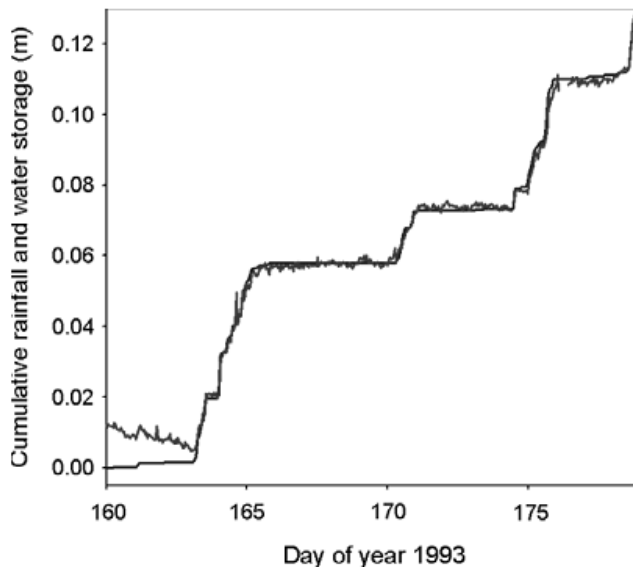


Fig. 1 Correspondence between recorded cumulative rainfall (lower line at left) and storage change as estimated from a 2-aquifer GWL at a New Zealand field site. The two aquifers are 40 and 163 m below ground surface, respectively (Bardsley & Campbell, 2007).

When two aquifers have similar porosities and saturated Poisson ratios, the expression for surface storage change over a specified time interval is particularly simple:

$$\Delta S = C_1 \Delta L_1 - C_2 \Delta L_2 \tag{1}$$

where ΔS is storage change over some specified time interval, ΔL_1 and ΔL_2 are corresponding water level changes in two piezometers in the respective aquifers, and C_1 and C_2 are constant terms determined by the barometric coefficients of the respective aquifers (Bardsley & Campbell, 2007).

A GWL system for ΔS monitoring is simple to set up in an appropriate hydrogeological setting. However, it may also happen that there sometimes exist suitable monitoring stations developed in another context. In particular, seismic observation networks often include pore pressure monitoring and some seismic monitoring data could also serve as a GWL system for storage change. For example, Bardsley & Campbell (2000) note an evident storage change derived from cumulative rainfall, with respect to a seismic monitoring site in Parkfield, California, USA.

The other approach to direct storage change monitoring at the ecosystem scale is by way of direct gravity monitoring, where mass changes due to water storage changes are detected as slight changes in gravity. However, monitoring gravity from the land surface only reflects mass changes in close proximity to the gravity meter rather than integrating over the desired wider area. To obtain the desired areal integral for climatic change detection the meter must be located in a stable

environment some distance below the ground surface. This could be achieved by emplacing gravity metres down deep bore holes or in Deep Underground Laboratories (for fundamental particle studies), provided the land surface above was of interest by way of being sensitive to climate change via water storage change monitoring.

CONCLUSION

Establishing time series of area-integrated water storage changes represents a useful means of monitoring for climate change. In conjunction with storage changes over regional scales as monitored by gravity satellite systems, there is also a need for a global network of ecosystem-scale water storage monitoring at selected sites where climatic change effects are anticipated to be most evident. Depending on the local situations a network of this type is likely to be a hybrid system comprised of new geological weighing lysimeters, existing seismic networks for pore water pressures, and direct gravity monitoring where current underground physics experiments or deep boreholes permit. Coupled with satellite gravity monitoring, representative ecosystem storage change monitoring would provide a powerful Earth observation tool for detecting and monitoring climate change.

REFERENCES

- Bardsley, W. E. & Campbell, D. I. (2007) An expression for land surface water storage monitoring using a two-formation geological weighing lysimeter. *J. Hydrol.* **335**, 240–246.
- Bardsley, W. E. & Campbell, D. I. (2000) Natural geological weighing lysimeters: calibration tools for satellite and ground surface monitoring of subsurface water mass change. *Nat. Resour. Res.* **9**, 147–156.
- Bierkens, F. P. & van den Hurk, B. J. J. M. (2007) Groundwater convergence as a possible mechanism for multi-year persistence in rainfall. *Geophys. Res. Lett.* **34**, L02402, doi:10.1029/2006GL028396.
- Dahm, C. N. & Molles, M. C. (1990) Streams in semiarid regions as sensitive indicators of global climate change. In: *Symposium on Global Climate Change and Freshwater Ecosystems* (ed. by P. Firth & S. G. Fisher), 250–260. Springer-Verlag, New York, USA.
- Ebrahimi, E., Filizadeh, Y. & Asgari, K. (2009) Anzali wetland hydrology monitoring to detect the effects of land use and climate change. In: *Proc. Second International Conference on Environmental and Computer Science (IEEE)*, 122–127.
- Groisman, P. Y., Knight, R. W., Karl, T. R., Easterling, D. R., Sun, B. M. & Lawrimore, J. H. (2004) Contemporary changes of the hydrological cycle over the contiguous United States: Trends derived from *in situ* observations. *J. Hydrometeorol.* **5**, 64–85.
- Hanesiak, J., Tat, A. & Raddatz, R. L. (2009) Initial soil moisture as a predictor of subsequent severe summer weather in the cropped grassland of the Canadian Prairie provinces. *Int. J. Climatol.* **29**, 899–909.
- Henderson-Sellers, A., Irannejad, P. & McGuffie, K. (2008) Future desertification and climate change: evaluation improvement. *Global & Planetary Change* **64**, 129–138.
- Jones, R. N., McMahon, T. A. & Bowler, J. M. (2001) Modelling historical lake levels and recent climate change at three closed lakes, Western Victoria, Australia (c. 1840–1990). *J. Hydrol.* **246**, 159–180.
- Jung, M., Reichstein, M., Ciais, P., Seneviratne, S. I., Sheffield, J., Goulden, M. L., Bonan, G. B., Cescatti, A., Chen, J., de Jeu, R., Dolman, A. J., Eugster, W., Gerten, D., Gianelle, D., Gobron, N., Heinke, J., Kimball, J. S., Law, B. E., Montagnani, L., Mu, Q., Mueller, B., Oleson, K. W., Papale, D., Richardson, A. D., Roupsard, O., Running, S. W., Tomelleri, E., Viovy, N., Weber, U., Williams, C., Wood, E., Zaehle S. & Zhang, K. (2010) Recent decline in the global land evapotranspiration trend due to limited moisture supply. doi:10.1038/nature09396.
- Koster, R. D., Dirmeyer P. A., Guo, Z., Bonan, G., Chan, E., Cox, P., Gordon, C.T., Kanae, S., Kowalczyk, E., Lawrence, D., Liu, P., Lu, C.H., Malyshev, S., McAvaney, B., Mitchell, K., Mocko, D., Oki, T., Oleson, K., Pitman, A., Sud, Y. C., Taylor, C. M., Verseghy, D., Vasic, R., Xue, Y. & Yamada T (2004) Regions of strong coupling between soil moisture and precipitation. *Science* **305**, 1138–1140.
- Krakauer, N. Y., Cook, B. I. & Puma, M. J. (2010) Contribution of soil moisture feedback to hydroclimatic variability. *Hydrol. Earth System Sci.* **14**, 505–520.
- Lorenz, R., Jaeger, E. B. & Seneviratne, S. I. (2010) *Geophys. Res. Letters* **37** L09703, doi:10.1029/2010GL042764.
- Niu, G.-Y., Yang Z.-L., Dickinson, R. E., Gulden, L. E. & Su, H. (2007) Development of a simple groundwater model for use in climate models and evaluation with gravity recovery and climate experiment data. *J. Geophys. Res.* **112**, D07103, doi:10.1029/2006JD007522.
- Notaro, M. (2008) Statistical identification of global hot spots in soil moisture feedbacks among IPCC AR4 models. *J. Geophys. Res.* **113**, D09101, doi:10.1029/2007JD009199.

- Ribes, A., Azais, J. M. & Planton, S. (2010) A method for regional climate change detection using smooth temporal patterns. *Climate Dynamics* **35**, 391–406.
- Rodell, M., Velicogna, I. & Famiglietti, J. S. (2009) Satellite-based estimates of groundwater depletion in India. doi:10.1038/nature08238.
- Schaller, M. F. & Y. Fan, Y. (2009) River basins as groundwater exporters and importers: Implications for water cycle and climate modeling. *J. Geophys. Res.* **114**, D04103, doi:10.1029/2008JD010636.
- Seneviratne, S. I., Corti, T., Davin, E. L., Hirschi, M., Jaeger, E. B., Lehner, I., Orlowsky, B. & Adriaan J. Teuling, A. J. (2010) Investigating soil moisture–climate interactions in a changing climate: A review. *Earth Sci. Rev.* **99**, 125–161.
- Van der Kamp, G. & Schmidt, R. (1997) Monitoring of total soil moisture on a scale of hectares using groundwater piezometers. *Geophys. Res. Letters* **24**, 719–722.
- Villar, J. C. E., Guyot, J. L., Ronchail, J., Cochonneau, G., Filizola, N., Fraizy, P., Labat, D., Oliveira, E. D., Ordoñez, J. J. & Vauchel, P. (2009) Contrasting regional discharge evolutions in the Amazon basin (1974–2004). *J. Hydrol.* **375**, 297–311.

2 Satellite Application

A spatial hydrological model for estimation of unaccounted water diversions in the northern Murray-Darling Basin of Australia

MOHSIN HAFEEZ, MASOUD EDRAKI, UMAIR RABBANI, YANN CHEMIN, KALEEM ULLAH & JOSH SIXSMITH

International Centre of Water for Food Security (IC Water), Charles Sturt University, Wagga Wagga, New South Wales, Australia

mhafeez@csu.edu.au

Abstract Hydrological knowledge of irrigated farms within the inundation plains of the Murray-Darling Basin (MDB) is very limited in both quality and reliability of the observation network. This paper focuses on Land Surface Diversions (LSD) that encompass all forms of surface water diversion, except the direct extraction of water from rivers, watercourses and lakes by farmers for the purposes of irrigation, stock and domestic supply. Its accurate measurement is very challenging, due to the practical difficulties associated with separating the different components of LSD and estimating them accurately for a large catchment. A hydrological water balance model coupled with a remote sensing (RS) technique was developed to estimate unaccounted LSD for selected catchments of the northern areas of the basin. For accurate accounting of diversions and reduction of errors due to the inclusion of non-cropped portions of the catchments, a detailed methodology was implemented, which includes the estimations of actual evapotranspiration (ET_a) and other water balance components of the irrigated areas. Results showed that LSD varied between different catchments and increased with the size of irrigated cropped area. The developed methodology has a great potential to estimate unaccounted diversions in other basins across the globe.

Key words unaccounted water; Land Surface Diversions; RS; SAM-ET; MODIS; Australia

INTRODUCTION

Recent drought in Australia and concerns about climate change have highlighted the need to manage agricultural water resources more sustainably, especially in the MDB, which utilizes more than 60% of extracted water for food production. Rainfall over most of the MDB has greatly reduced in recent years, and as a result the inflow to the Murray River in 2008–2009 dropped to about 40% of its historical long-term average (MDBA, 2009).

The severity of low river flows and adverse consequences for downstream communities and ecosystems prompted the basin authorities to impose a “cap” on diversions in 1995, which limited the amount of water that can be taken for consumptive use to sustainable levels (MDBC, 2006). In 1999, the Murray-Darling Basin Ministerial Council commissioned a comprehensive review of the operation of the Cap and focused on how it can be refined to better meet the needs of the basin. One of the key conclusions and recommendations of the review adopted by the council was that all forms of water use, such as diversions from flood plains and overland flows, should be included in the cap, as they are recognised and can be quantified (MDBC, 2000). LSD encompass all forms of surface water diversion except the direct extraction from rivers, watercourses and lakes by farmers for the purposes of irrigation, stock and domestic supply. In the northern New South Wales (NSW) and southern Queensland (Qld) catchments of the MDB, a significant proportion of total water diversions is captured through the interception of flood water and overland flow during sporadic storm events, which is collected in on-farm storages (OFS) or used for direct irrigation, thus preventing runoff from naturally entering a watercourse or infiltrating into the flood plain (MDBC, 2006). Proper assessment of LSD is challenging due to practical difficulties associated with accurate estimation of different components of LSD. Hydrological data, especially the actual water diversions to irrigated farms located within the flood plains of the northern NSW and southern Qld areas of the MDB, is very limited. The inadequacy of current methods of measuring and monitoring LSD poses severe limitations on existing and proposed policies for managing such diversions.

The study describes the development of a hydrological water balance model at the catchment scale in northern NSW and southern Qld valleys of the MDB, and the computation of the LSD

using a RS technique coupled with on-ground hydrologic parameters. The developed model will help the MDB Authority (MDBA) to maintain the integrity of the cap processes by providing an accurate, reliable system of data collection, estimation, storage, and reporting of LSD contribution to the water diversion for the ungauged catchments.

Study area

The natural catchment boundary of the study area, based on the MDB cap valley maps for the region, was delineated as shown in Fig. 1. The catchment boundary of the study area was selected along the natural topography of the region providing a closed catchment with one outlet at the southwestern corner. The selection of a closed catchment was possible due to the presence of the Great Dividing Range at the eastern border, which serves as a barrier between the catchments and the outside area. The total land area of the catchment is 37.7 million ha. The area incorporates several river valleys across northern NSW and southern Qld, including the Condamine-Balonne, Border Rivers, Moonie, Namoi, Gwydir, Castlereagh, Macquarie-Bogan and the upper reaches of the Barwon-Darling regions. More details about the catchment areas are given in Hafeez *et al.* (2010).

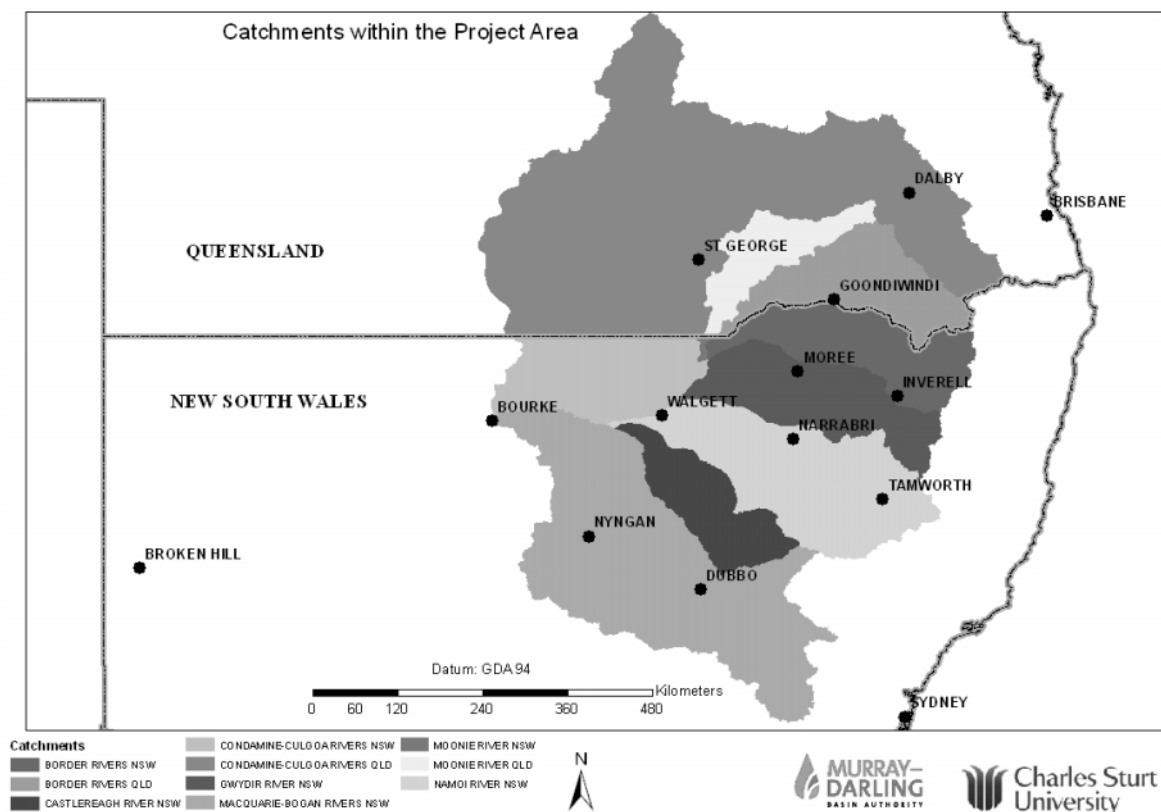


Fig. 1 Boundary of the study area within the Murray Darling Basin.

METHODOLOGY

The volume of LSD can be estimated by accurate quantification of all hydrological variables of a water balance model at catchment scales. Typically, the hydrological water balance components include irrigation inflow, outflow, rainfall, runoff, ET_a , soil moisture change and deep percolation. With the exception of ET_a , all components of a hydrological water balance model can be measured using traditional hydrological monitoring techniques and methods. The accurate measurement of

ET_a can significantly enhance the accuracy of a hydrological water balance model at any scale (from farm to catchment). ET_a estimates using RS techniques provide a practical option for accurate and an efficient computation of actual crop water use. These computations, along with other hydrological variables, were used to calculate the volume of LSD in a hydrological water balance model at both farm and catchment scales. Figure 2 shows the LSD as a component of the overall water balance at the catchment scale.

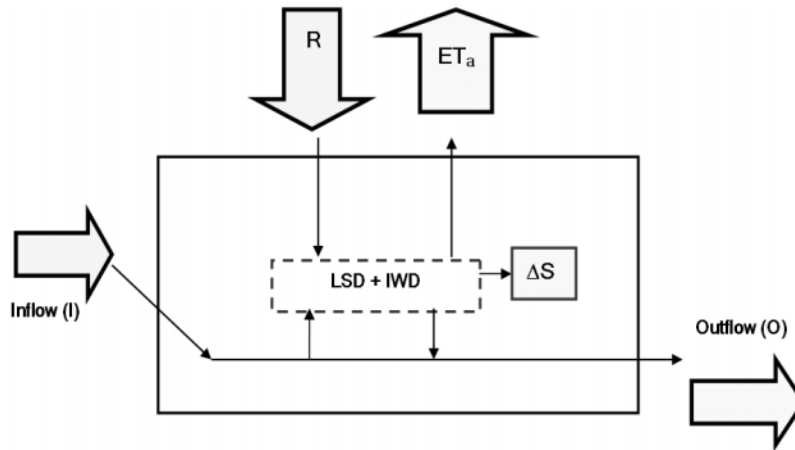


Fig. 2 Sketch of the catchment water balance components involving LSD.

LSD is the water harvested from rainfall (R), and encompasses all forms of surface water diversions other than licensed irrigation water diversions (IWD), which are the direct extraction of water from rivers and groundwater, watercourses, lakes and billabongs by farmers for the purposes of irrigation and stock and domestic supply. ET_a from the cropped area represents the water which has been applied to the cropped area through irrigation water diversions (IWD) and through LSD. It also includes that portion of direct rainfall which has infiltrated into the soil (effective rainfall, R_e). LSD can be estimated using equation (1).

$$LSD = ET_a - IWD - R_e + \Delta S \quad (1)$$

As in equation (1), ΔS is the net change in storages composed of groundwater storage, surface storages and soil moisture. Calculation of LSD at the catchment scale from a hydrologic water balance model requires basic input parameters, of which ET_a as a major component was computed using a RS based on land surface energy balance. The rest of the inputs were estimated or obtained from on-ground sources.

The monthly totals of rainfall were calculated from the climatic time series data of more than 700 weather stations within the boundary of these catchments. The surface of the rainfall for the boundary was determined for each of the study periods using the kriging method. Later, effective rainfall was calculated from monthly rainfall data using USDA-SCS method (USDA-SCS, 1972; Smith, 1992).

For estimation of daily ET_a , 224 Terra/MODIS level 3 (L3) product images were acquired for the period July 2007–June 2008. The MODIS satellite images for overpass days were calibrated using the climatic data from SILO's Patched Point datasets from the Bureau of Meteorology's (BoM's) network of weather stations in the region. The images were pre-processed using the Spatial Algorithm for Mapping ET (SAM-ET) algorithm, a two source energy balance algorithm based on thermodynamic flux and radiation equilibrium within the Earth skin surface (Hafeez *et al.*, 2009; Hafeez & Chemin, 2010). After analysing the quality flags, daily images were selected for SAM-ET modelling and a daily ET_a image of the catchment was produced by multiplying an instantaneous evaporative fraction (Λ) at each pixel of the images with average net radiation over a

24-hour period for the study area. The daily ET_a derived from MODIS satellite imagery along with the reference ET at the reference weather site (Morse *et al.*, 2000) were used to calculate monthly actual ET. Later, seasonal actual ET was calculated by integrating monthly ET_a values over the required period.

The primary aim of this study was to estimate the amount actual water used to grow crops; therefore, it was essential to estimate the irrigated area using satellite imagery. Irrigated area estimation for the MDB study area was done through a dual process. An initial GIS database of irrigation infrastructure acquired from the MDBA was collated into a GIS format to estimate where open channel irrigation infrastructure had been sighted. Once identified as a high potential area for open channel irrigation, an expansion was performed using proximity analysis tools in GIS to provide a larger, plausible area of where open channel irrigation schemes might be. While restricted to open channel irrigation only, this is the most straight forward method to gather high probability information to map irrigated area. Another dimension of probability was added with the addition of a high-resolution spatially aggregated digital elevation model. Using grid mathematics, accurate slope information was derived and thresholding was applied to discard the area where slope prevents the setting up of typical irrigated cropped areas, particularly clumped field size. The advantage of this dual approach of probability expansion and neighbourhood dependency across two very different sources of data is that it provides probabilities of non-irrigated areas with some human and physical restriction certainties. However, this does not indicate that there is a crop at that selected high probability point in time, or whether that crop is indeed irrigated. For the identification of crops, we used a combination of vegetation indices and Land Surface Temperature (LST) to extract the irrigated cropped from the trapezoidal index of vegetation temperature, where the angularity of the vegetation development stage across cold regimes permits discrimination of the non-irrigated crop from the irrigated one.

Licensed water diversions from rivers and groundwater in the two states of NSW and Qld were collected from NSW Department of Water and Energy and Qld Department of Natural Resources and Environment, respectively. The extraction data were available to the project as a yearly lump sum for each catchment at the end of year (July 2007–June 2008).

RESULTS AND DISCUSSION

The rainfall determined for the period July 2007–June 2008 shows a decreasing trend in the overall rainfall (mm) from east to west, i.e. from 296 mm to 1316 mm. The spatial variation in effective rainfall ranges from 264 mm to 912 mm within the study catchments for 2007–2008. Volumes of effective rainfall for irrigated cropped areas of each catchment were also calculated. The map of irrigated crops grown within the study area was created from the satellite images for 2007–2008. Overall, the irrigated area for 2007–2008 was 352 509 ha.

A spatial seasonal ET_a map estimated from the SAM-ET algorithm is valuable for closing the water balance for the entire water year of 2007–2008 (July 2007–June 2008). MODIS derived seasonal ET_a ranged from 87 mm to 1650 mm, with a mean value of 826 mm and a standard deviation value of 257 mm. The monthly trend of ET_a shows that the lowest monthly mean ET_a value (39 mm) occurred in June 2008 and the highest mean ET_a value was 117 mm for the month of December 2007. Seasonal ET_a for the irrigated cropped areas was also calculated, which shows a different range in ET_a to that of the overall area in Fig. 3(a). The seasonal ET_a for the irrigated cropped area ranged from 800 mm to 1548 mm. The comparison of mean monthly reference evapotranspiration, calculated from the average ET_o of all 700 BoM weather stations, and mean ET_a , estimated from MODIS images, shows that both follow a similar trend as illustrated in Fig. 3(b). ET_o represents a theoretical maximum ET rate from a short green healthy grass, completely shading the ground, of uniform height and with adequate water status in the soil profile. This is an ideal situation and does not occur on-ground all the time. Therefore, the magnitude of ET_a has become less than reference ET, so that the ET_a/ET_o ratio varied from 0.3 to 0.8 during this period.

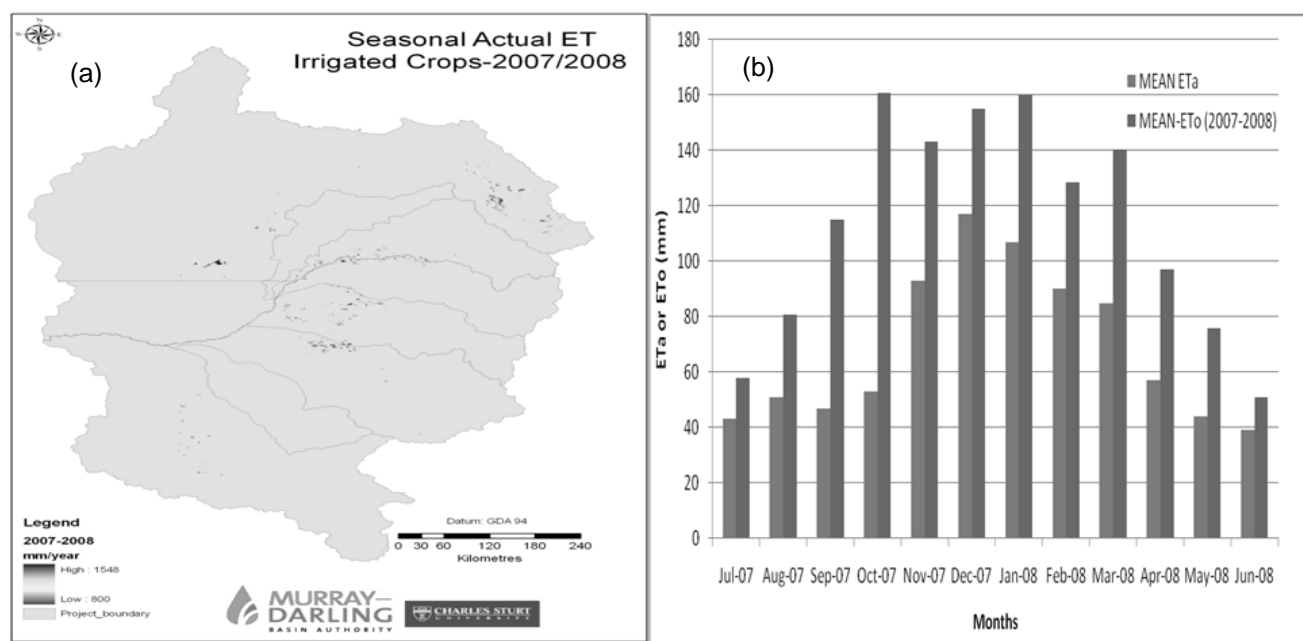


Fig. 3 (a) Spatial variation of actual ET for the irrigated cropped area; and (b) comparison of mean monthly actual and reference ET in the study area.

Table 1 Calculation of LSD at the catchment scale using cropped irrigated areas 2007–2008.

Catchments	Cropped area (ha)	Seasonal Actual ET (GL)	Effective Rainfall	River Extractions	GW Extractions	LSD
Condamine–Culgoa Rivers (Qld)	109 039	1103	571	776	251	
Condamine–Culgoa Rivers (NSW)	250	3	1			2
Border Rivers (Qld)	34 930	392	158	201	13	19
Border Rivers (NSW)	38 744	405	174	131	5	95
Moonie River	5730	71	29	41		1
Gwydir River	76 265	730	355	89	77	209
Namoi River	47 972	535	220	142	162	11
Castlereagh River	210	2	1			1
Macquarie-Bogan Rivers	39 368	397	165	75	74	83
TOTAL	352 509	3638	1674	1455	583	421

The extracted volumes from rivers and groundwater within the regulated catchments of the NSW and Qld catchments were 1455 and 583 GL for 2007–2008. To reduce the errors associated with the calculation of LSD at the catchment scale, LSD were computed only for the irrigated cropped areas of each catchment. Therefore, as the size of the area was limited to the irrigated cropped areas, changes in the volume of the major storages were eliminated. This methodology ignores the change in on-farm storages over a long time and assumes that they are insignificant compared with the rest of the parameters in the water balance equation. Table 1 shows the calculation of LSD from the water balance components of the irrigated cropped area within the study catchments for 2007–2008.

Water balance results gave a total estimated value for LSD of 421 GL for all catchments, excluding the Condamine-Culgoa River (Qld), during the period of 2007–2008. The estimated LSD at the catchment scale are reasonable and indicate the robust and reliable performance of the combined RS technique and hydrological modelling.

The reported river extractions for Condamine-Culgoa (776 GL) seems to be unrealistic and does not represent the historical irrigation diversions from the river in this catchment. Total diversions during three months of summer (December 2007, January–February 2008) have been reported to be 660 GL. If all this water was applied onto the cropped area, it would represent an average application rate of 6 ML/ha, which in addition to an effective rainfall of 267 mm or 2.6 ML/ha during the same period, the average application rate would be more than 8 ML/ha for the entire cropped area, which is not realistic. Two possibilities can be explored. One is error in measurement or reporting of the diversions. The other is the storage of the extra water in on-farm storages by the irrigators. Both possibilities could not be verified in this study and require further research.

CONCLUSIONS

The estimated LSDs at the catchment scale are reasonable and indicate the robust and reliable performance of the combined RS technique and hydrological modeling. This is the first time such a combined methodology has been implemented to estimate unaccounted diversions at the basin scale, where there is a dearth of knowledge in unmetered diversions. The hydrological water balance models at the catchment scale provide reliable quantification of LSD. Improved LSD estimates can guide water management decisions at farm to catchment scales and could be instrumental for enhancing the integrity of the water allocation process, making them fairer and more equitable for all stakeholders.

REFERENCES

- Hafeez, M. M. & Chemin, Y. (2010) *An Australian Algorithm for ET: SAM-ET*. 15th ARSPC Conference, Alice Springs, Australia.
- Hafeez, M. M., Chemin, Y. & Rabbani, U (2009) *Spatial Observation and Models for Crop Water use in Australia*. EOS Trans. American Geophysical Union (AGU), 90(52), Fall Meeting Suppl., 14–18 December 2009, San Francisco, USA,
- MDBC (2000) *Review of the Operation of the Cap: Overview Report of the Murray-Darling Basin Commission*. Murray Darling Basin Commission, Canberra, Australia.
- MDBA (2009) *Drought Update*. Issue 20: August 2009.
- MDBC (2006) *Land Surface Diversions Status Report* Final Report.
- Morse, A., Tasumi, M., Allen, R. & Kramber, W. (2000) *Application of SEBAL Methodology for Estimating Consumptive Use of Water and Stream Flow Depletion in the Bear River Basin of Idaho through Remote Sensing*. Final Report.
- Smith, M. I. (1992) CROPWAT, a computer program for irrigation planning and management. In: *FAO (Food and Agriculture Organization) Irrigation and Drainage Paper 46*, FAO, Rome, Italy.
- USDA-SCS (1972) *SCS National Engineering Handbook*, Section 4, *Hydrology*. Chapter 10. Estimation of direct runoff from storm rainfall. Washington, DC, USA.

Estimation of evaporative fraction from top-of-atmosphere radiance

JIAN PENG^{1,2} & YUANBO LIU¹

1 Nanjing Institute of Geography and Limnology, Chinese Academy of Sciences, Nanjing 210008, China
ybliu@niglas.ac.cn

2 Graduate University of Chinese Academy of Sciences, Beijing 100049, China

Abstract The evaporative fraction (EF) is the ratio of evapotranspiration to available energy on the Earth's surface. Recent studies have successfully estimated the EF using a contextual interpretation of satellite-retrieved land surface temperature (LST) and normalized difference vegetation index (NDVI). However, satellite retrieval is often complicated and the retrieved LST is criticized for its uncertainties and limitations, which may result in a false EF. This study proposed a simple retrieval algorithm for the EF, based on radiative transfer theory and Planck's law. The algorithm can determine the EF value for each pixel using top-of-atmosphere (TOA) radiance instead of satellite-retrieved LST. It was validated using the Moderate Resolution Imaging Spectro radiometer (MODIS) data over a heterogeneous area of the Poyang Lake basin of China. Our results showed that the TOA radiance-based EF values agreed quite well with the LST-based values by a high correlation coefficient ranging from 0.956 to 0.977. The biases between the TOA radiance-based and the LST based EF values varied from -0.024 to 0.016, and the root mean square error (RMSE) from 0.030 to 0.058, all of which indicated that the proposed algorithm using the TOA radiance was accurate enough for determining the EF. Notably, the proposed algorithm has fewer assumptions and thus can avoid the uncertainties associated with the LST retrieval. It should be highly valuable for determining EF and for satellite data processing as well.

Key words evaporative fraction; land surface temperature; TOA radiance

INTRODUCTION

Evapotranspiration (ET), including water evaporation from soil and transpiration from vegetation, is an important variable in water and energy balances on the Earth's surface. Accurate estimation of the temporal and spatial distribution of ET is of great significance for agricultural, hydrological and climatic studies (Moran *et al.*, 1994; Allen *et al.*, 2007). Conventional ground-based methods (Bowen ratio, eddy covariance, lysimeter systems) can provide accurate measurements of ET at the field scale (Farahani *et al.*, 2007). However, these systems are not applicable over large heterogeneous areas. Satellite remote sensing has been recognized as the most useful tool to provide spatially distributed regional ET. Over the last few decades, a large number of remote sensing based methods that vary in complexity have been proposed to estimate ET (Kalma *et al.*, 2008; Verstraeten *et al.*, 2008). These methods usually need ancillary surface and atmospheric data, like wind speed, air temperature and vapour pressure, as remote sensing cannot readily measure these variables. Therefore, it is still challenging to map the global ET distribution using satellite remote sensing with few or no ground observations. A direct calculation of evaporative fraction (EF), expressed as a ratio of ET to the available energy on the Earth's surface, has the advantage of avoiding the complexity related to the determination of sensible heat (Nishida *et al.*, 2003; Tang *et al.*, 2010). One popular and widely used approach for estimation of the EF is the land surface temperature/vegetation index (LST/NDVI) triangle method. This method, based on the spatial contextual information of the LST *versus* NDVI triangle relationship, has been applied successfully with remote sensing data to estimate EF in many studies (Jiang & Islam, 2001; Nishida *et al.*, 2003; Venturini *et al.*, 2004; Batra *et al.*, 2006; Wang *et al.*, 2006; Stisen *et al.*, 2008; Tang *et al.*, 2010).

In practice, accurate estimation of the EF using the triangle method relies on unbiased LST retrieval. In order to estimate LST from thermal infrared remote sensing data, various techniques and algorithms have been proposed. However, these methods all involve atmospheric and radiative transfer corrections, which are often difficult and troublesome. Besides, the accuracy of LST is also questionable, because there are considerable uncertainties and limitations about the estimation

of LST (Kalma *et al.*, 2008). They are caused by the atmospheric effects, variation in sun-target-satellite geometry, and estimation uncertainties related to land surface emissivity (Jiang *et al.*, 2004; Liu *et al.*, 2007). The uncertainties associated with satellite-derived LST are on the order of several K (Prata & Cechet, 1999; Peres & DaCamara, 2004), which may result in false calculation of the EF.

In this study, we developed a novel algorithm using top of the atmosphere (TOA) radiance instead of retrieved LST to estimate the EF, which could avoid the complex correction procedures related to LST retrieval and uncertainties associated with the LST products. In the theory section we give a mathematical derivation of the methodology demonstrating the feasibility of the TOA radiance, based on thermal radiance transfer equation and Planck's radiance equation. Then, we further validated the methodology using Moderate Resolution Imaging Spectroradiometer (MODIS) LST products and the TOA radiance.

METHODOLOGY

Theoretical basis

On the basis of the triangle relationship between LST and NDVI, EF is defined as follows:

$$EF = \frac{LE}{R_n - G} = \Phi \frac{\Delta}{\Delta + \gamma} \quad (1)$$

where LE is the latent heat flux (Wm^{-2}), R_n is the net radiation (Wm^{-2}), G is the soil heat flux (Wm^{-2}), Δ is the slope of saturated vapour pressure at air temperature (T_a) and γ is the psychrometric constant (hPa K^{-1}). Φ is the parameter that accounts for aerodynamic and canopy resistances, and it can be estimated from the following equation (Jiang & Islam, 2001):

$$\Phi = \Phi_{\max} \frac{T_{\max} - T_s}{T_{\max} - T_{\min}} \quad (2)$$

where T_s is the observed surface temperature for a given pixel whose NDVI value is NDVI_i , and T_{\max} and T_{\min} are the corresponding highest and lowest surface temperatures which have the same NDVI_i value. Φ_{\max} is the Priestly-Taylor coefficient of 1.26. Consequently, the Φ value for each pixel can be determined using the triangle method. Because the spatial variation in LST could reduce the need for absolute atmospheric corrections, there exists the opportunity to estimate Φ using the TOA radiance directly rather than using LST.

On the basis of the radiance transfer equation, the TOA radiance measured from sensors in channel i can be expressed as (Prata *et al.*, 1995):

$$L_i = t_i \varepsilon_i B_i(T_s) + t_i (1 - \varepsilon_i) I_{\downarrow} + I_{\uparrow} \quad (3)$$

where L_i is the TOA radiance received by the sensor in channel i , t_i is the total transmittance of the atmosphere in channel i , ε_i is the surface emissivity, T_s is the land surface temperature, $B_i(T_s)$ is the radiance emitted by a blackbody at temperature T_s , I_{\downarrow} is the down-welling radiance, and I_{\uparrow} is the upwelling atmospheric radiance in channel i . It is noted that the above magnitudes also depend on the satellite viewing angle, also known as satellite nadir angle. The expression for $B_i(T_s)$ is defined by Planck's function as (Dozier, 1981):

$$B_i(T_s) = \frac{C_1}{\lambda^5 (e^{C_2/\lambda T_s} - 1)} \quad (4)$$

where C_1 and C_2 are the spectral constants with $C_1 = 1.19104 \times 10^8 \text{ w } \mu\text{m}^4 \text{ m}^{-2} \text{ sr}^{-1}$ and $C_2 = 1.43877 \times 10^4 \text{ } \mu\text{m K}$. $B_i(T_s)$ is given in $\text{w m}^{-2} \text{ sr}^{-1} \mu\text{m}^{-1}$ if wavelength λ is given in μm .

The upwelling atmospheric radiance I_{\uparrow} and the down-welling radiance I_{\downarrow} are usually given by (Sobrino *et al.*, 1991):

$$I_{\uparrow} = (1 - t_i) B_i(T_a) \quad (5)$$

$$I_{\downarrow} = (1 - t_i)(1 - \varepsilon_i)B_i(T_a) \quad (6)$$

where T_a represents the effective mean temperature of the atmosphere. It should be noted that the derivation of I_{\uparrow} and I_{\downarrow} needs some reasonable simplifications and analysis (see Sobrino *et al.*, 1991 for further details).

On the basis of equations (5) and (6), equation (3) can be rewritten as:

$$L_i = t_i \varepsilon_i B_i(T_s) + (1 - t_i)[1 + (1 - \varepsilon_i)t_i]B_i(T_a) \quad (7)$$

Derivation

In order to develop our method, we need to approximate the Planck function using the first-order Taylor expansion around a given temperature value (\bar{T}) (Franca & Cracknell, 1994). Thus, the Taylor expansion of the Planck function can be written as:

$$B_i(T_s) = B_i(\bar{T}) + (T_s - \bar{T}) \left(\frac{\partial B_i}{\partial T_s} \right)_{\bar{T}} = T_s \left(\frac{\partial B_i}{\partial T_s} \right)_{\bar{T}} + B_i(\bar{T}) - \bar{T} \left(\frac{\partial B_i}{\partial T_s} \right)_{\bar{T}} \quad (8)$$

Based on equations (7) and (8), Φ can be obtained using the following equation:

$$\Phi = \Phi_{\max} \frac{\frac{L_i^{\max} - (1 - t_i^{\max})[1 + (1 - \varepsilon_i^{\max})t_i^{\max}]B_i(T_a^{\max})}{t_i^{\max} \varepsilon_i^{\max}} - \frac{L_i^s - (1 - t_i^s)[1 + (1 - \varepsilon_i^s)t_i^s]B_i(T_a^s)}{t_i^s \varepsilon_i^s}}{\frac{L_i^{\max} - (1 - t_i^{\max})[1 + (1 - \varepsilon_i^{\max})t_i^{\max}]B_i(T_a^{\max})}{t_i^{\max} \varepsilon_i^{\max}} - \frac{L_i^{\min} - (1 - t_i^{\min})[1 + (1 - \varepsilon_i^{\min})t_i^{\min}]B_i(T_a^{\min})}{t_i^{\min} \varepsilon_i^{\min}}} \quad (9)$$

In this equation, the surface emissivity ε_i is constant for a given NDVI value (Valor & Caselles, 1996; Sobrino *et al.*, 2001). Besides, the atmospheric transmittance t_i and atmospheric temperature T_a show very little spatial variation over the image for a cloud-free and clear atmosphere. On the basis of the above reasons, equation (9) can be derived as:

$$\Phi = \Phi_{\max} \frac{L_i^{\max} - L_i^o}{L_i^{\max} - L_i^{\min}} \quad (10)$$

Therefore, EF can be calculated using the following equation:

$$EF = \Phi \frac{\Delta}{\Delta + \gamma} = \Phi_{\max} \frac{L_i^{\max} - L_i^o}{L_i^{\max} - L_i^{\min}} \frac{\Delta}{\Delta + \gamma} \quad (11)$$

CASE STUDY

Study area and data processing

The study area is located on the Poyang Lake basin of China, with the latitude ranging from 27.6°N to 28.6°N and longitude from 114.6°E to 116.8°E. It is a heterogeneous land cover area characterized by agricultural fields, grassland, bare soil surface, forestland and inland water surfaces. Figure 1 shows the land cover features over the study area, acquired from MODIS data collected on 2 May 2007.

MODIS data products used in this study are land surface temperature (MOD11_L2), TOA radiance (MOD02_1KM), surface reflectance (MOD09_GA), geolocation (MOD03) and atmospheric temperature (MOD07_L2). These data were acquired from the Earth Observing System Data Gateway (EDG) and re-projected onto Universal Transverse Mercator (UTM) with a datum of World Geodetic System (WGS)-84. NDVI is determined from the following equation:

$$NDVI = (\alpha_{nir} - \alpha_{red}) / (\alpha_{nir} + \alpha_{red}) \quad (12)$$

where α_{nir} and α_{red} are the surface reflectances in near infrared band and red band from the MOD09_GA product.

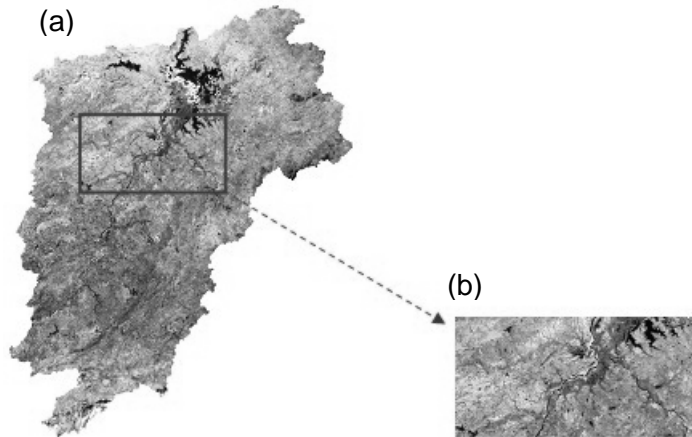


Fig. 1 The false image of MODIS (RGB: band 621) for the study area, dated 2 May 2007. (a) Poyang Lake basin; (b) the study area.

In order to obtain an EF value for each pixel in a remotely sensed image, the most important procedure is the determination of the Φ value. The highest temperature pixel and lowest temperature pixel for each NDVI interval should be determined first. The next step is to interpolate within each NDVI class between the extreme temperatures using equation (2). Based on the interpolation scheme, the Φ value was calculated for each pixel. Thus, the EF value in the study area was calculated from MODIS LST and TOA radiance (band-31), respectively, using equations (1) and (11).

RESULTS AND DISCUSSION

Figure 2 shows scatter plots of LST-EF and TOA_radiance-EF for different NDVI values. Table 1 compares LST-EF and TOA_radiance-EF in terms of mean, and standard deviation (SD) derived from LST and TOA radiance for different NDVI values.

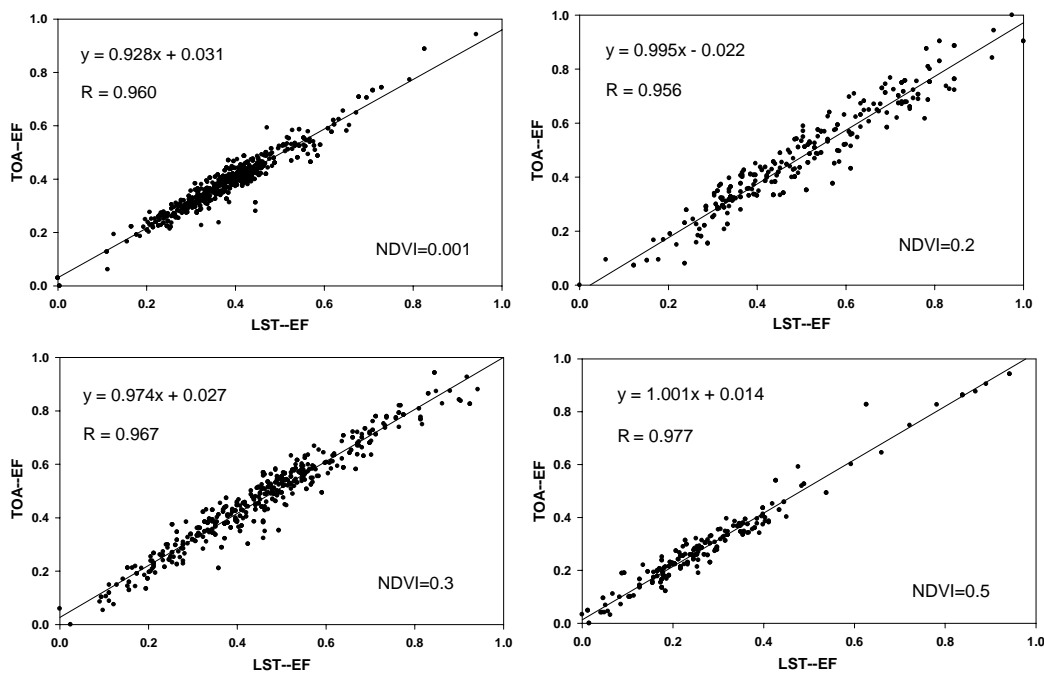


Fig. 2 Comparison of the EF value calculated from LST and TOA radiance (band-31) for different NDVI values in the study area.

Table 1 Statistical comparison of the EF calculated from LST and TOA radiance (band-31).

NDVI	LST–EF		TOA–EF		RMSE	Bias	R
	Mean	SD	Mean	SD			
0.001	0.383	0.108	0.387	0.104	0.030	0.004	0.960
0.2	0.468	0.174	0.443	0.181	0.058	–0.024	0.956
0.3	0.455	0.172	0.471	0.173	0.046	0.015	0.967
0.5	0.274	0.164	0.290	0.169	0.040	0.016	0.977

EF values calculated from LST and TOA radiance have a maximum difference of ± 0.025 in the mean, while SD values are similar for both. The root mean square errors (RMSE), bias and correlation coefficient (R) derived from LST-EF and TOA-EF are also displayed in Table 1. The RMSEs and biases vary from 0.030 to 0.058 and from –0.024 to 0.016, respectively, which indicates that the EF estimates are comparable. Furthermore, the high R values, ranging from 0.956 to 0.977, indicate good agreement between the EF estimated from MODIS LST product and TOA radiance. In general, the results suggest that our theoretically derived equation is promising and practicable.

CONCLUSIONS

Accurate estimation of the EF relies on the satellite-derived LST. However, there are many uncertainties associated with the retrieved LST, which may result in false estimation of EF. This study proposed a practical approach for calculating the EF with TOA radiance. The proposed algorithm was derived theoretically on the basis of the radiance transfer equation and Planck's law. The case study over a heterogeneous area of the Poyang Lake basin showed the effectiveness of the proposed approach. Consequently, we argue that the use of TOA radiance appears to be applicable and feasible for the determination of EF.

Acknowledgements This work was supported by a Key Program of The Knowledge Innovation Program of The Chinese Academy of Sciences (KZCX2–YW–337). MODIS data were obtained from the Warehouse Inventory Search Tool at <https://wist.echo.nasa.gov/~wist/api/imswelcome/>. We thank Mr D. Zhao for his assistance in data preprocessing.

REFERENCES

- Allen, R. G., Tasumi, M. & Trezza, R. (2007) Satellite-based energy balance for Mapping Evapotranspiration with Internalized Calibration (METRIC) – Model. *J. Irrig. Drain. Engng* **133**(4), 380–394.
- Batra, N., Islam, S., Venturini, V., Bisht, G. & Jiang, L. (2006) Estimation and comparison of evapotranspiration from MODIS and AVHRR sensors for clear sky days over the Southern Great Plains. *Remote Sens. Environ.* **103**(1), 1–15.
- Dozier, J. (1981) A method for satellite identification of surface temperature fields of subpixel resolution. *Remote Sens. Environ.* **11**, 221–229.
- Farahani, H. J., Howell, T. A., Shuttleworth, W. J. & Bausch, W. C. (2007) Evapotranspiration: progress in measurement and modeling in agriculture. *Trans. ASABE* **50**(5), 1627–1638.
- Franc, G. B. & Cracknell, A. P. (1994) Retrieval of land and sea surface temperature using NOAA-11 AVHRR data in north-eastern Brazil. *Int. J. Remote Sens.* **15**(8), 1695–1712.
- Jiang, L. & Islam, S. (2001) Estimation of surface evaporation map over southern Great Plains using remote sensing data. *Water Resour. Res.* **37**(2), 329–340.
- Jiang, L., Islam, S. & Carlson, T. N. (2004) Uncertainties in latent heat flux measurement and estimation: implications for using a simplified approach with remote sensing data. *Can. J. Remote Sens.* **30**(5), 769–787.
- Kalma, J., McVicar, T. & McCabe, M. (2008) Estimating land surface evaporation: a review of methods using remotely sensed surface temperature data. *Surv. Geophys.* **29**(4), 421–469.
- Liu, Y. B., Yamaguchi, Y. & Ke, C. Q. (2007) Reducing the discrepancy between ASTER and MODIS land surface temperature products. *Sensors* **7**(12), 3043–3057.
- Moran, M. S., Clarke, T. R., Kustas, W. P., Weltz, M. & Amer, S. A. (1994) Evaluation of hydrologic parameters in a semiarid rangeland using remotely sensed spectral data. *Water Resour. Res.* **30**(5), 1287–1297.

- Nishida, K., Nemani, R. R., Running, S. W. & Glassy, J. M. (2003) An operational remote sensing algorithm of land surface evaporation. *J. Geophys. Res.* **108**(D9), 4270.
- Peres, L. & DaCamara, C. (2004) Land surface temperature and emissivity estimation based on the two-temperature method: sensitivity analysis using simulated MSG/SEVIRI data. *Remote Sens. Environ.* **91**(3–4), 377–389.
- Petropoulos, G., Carlson, T., Wooster, M. & Islam, S. (2009) A review of Ts/VI remote sensing based methods for the retrieval of land surface energy fluxes and soil surface moisture. *Progr. Phys. Geogr.* **33**(2), 224–250.
- Prata, A. & Cechet, R. (1999) An assessment of the accuracy of land surface temperature determination from the GMS-5 VISSR. *Remote Sens. Environ.* **67**(1), 1–14.
- Prata, A. J., Caselles, V., Coll, C., Sobrino, J. A. & Ottlé, C. (1995) Thermal remote sensing of land surface temperature from satellites: Current status and future prospects. *Remote Sens. Rev.* **12**(3), 175–224.
- Sobrino, J., Coll, C. & Caselles, V. (1991) Atmospheric correction for land surface temperature using NOAA-11 AVHRR channels 4 and 5. *Remote Sens. Environ.* **38**(1), 19–34.
- Sobrino, J. A., Raissouni, N. & Li, Z.-L. (2001) A comparative study of land surface emissivity retrieval from NOAA data. *Remote Sens. Environ.* **75**(2), 256–266.
- Stisen, S., Sandholt, I., Nørgaard, A., Fensholt, R. & Jensen, K. H. (2008) Combining the triangle method with thermal inertia to estimate regional evapotranspiration – applied to MSG-SEVIRI data in the Senegal River basin. *Remote Sens. Environ.* **112**(3), 1242–1255.
- Tang, R., Li, Z.-L. & Tang, B. (2010) An application of the Ts-VI triangle method with enhanced edges determination for evapotranspiration estimation from MODIS data in arid and semi-arid regions: Implementation and validation. *Remote Sens. Environ.* **114**(3), 540–551.
- Valor, E. & Caselles, V. (1996) Mapping land surface emissivity from NDVI: Application to European, African, and South American areas. *Remote Sens. Environ.* **57**(3), 167–184.
- Venturini, V., Bisht, G., Islam, S. & Jiang, L. (2004) Comparison of evaporative fractions estimated from AVHRR and MODIS sensors over South Florida. *Remote Sens. Environ.* **93**(1–2), 77–86.
- Verstraeten, W., Veroustraete, F. & Feyen, J. (2008) Assessment of Evapotranspiration and Soil Moisture Content Across Different Scales of Observation. *Sensors*. **8**(1), 70–117.
- Wang, K., Li, Z. & Cribb, M. (2006) Estimation of evaporative fraction from a combination of day and night land surface temperatures and NDVI: a new method to determine the Priestley-Taylor parameter. *Remote Sens. Environ.* **102**(3–4), 293–305.

Use of field observations and SEBS to retrieve heat fluxes for irrigation areas of Australia

WEIQIANG MA^{1,2}, MOHSIN HAFEEZ², RABBANI UMAIR², YAOMING MA³ & BOB SU⁴

¹ Key Laboratory of Land Surface Process and Climate Change in Cold and Arid Regions, Cold and Arid Regions Environmental and Engineering Research Institute, Chinese Academy of Sciences, Lanzhou, 730000, Gansu Province, China

wqmacn@gmail.com or wma@csu.edu.au

² International Centre of Water for Food Security, Charles Sturt University, Wagga Wagga, New South Wales 2678, Australia

³ Laboratory of Tibetan Environment Changes and Land Surface Processes, Institute of Tibetan Plateau Research, Chinese Academy of Sciences, Beijing, 100085, China

⁴ Faculty of Geo-Information Science and Earth Observation, University of Twente, Enschede, The Netherlands

Abstract This study deals with the application of a Surface Energy Balance System (SEBS) algorithm based on Terra/ASTER data and field observations to derive energy balance fluxes (net radiation, soil heat, sensible heat and latent heat) over the Coleambally Irrigation area (CIA), located in the southwest of New South Wales (NSW), Australia. We have selected six ASTER scenes covering the time period of 2002, 2004, 2005, 2006, 2008 and 2009 for estimating the land surface heat fluxes over the study area. To validate the proposed methodology, the ground-measured land surface heat fluxes (net radiation, soil heat, sensible heat flux and latent heat flux) measured from an eddy covariance flux tower were compared with the ASTER derived surface fluxes values for the study area, which are the basis for calculating evapotranspiration using meteorological observations.

Key words ASTER; Australia; irrigation areas; land surface heat fluxes; SEBS

INTRODUCTION

A recent drought in Australia and concerns about climate change has highlighted the need to manage water resources more sustainably, especially in the Murrumbidgee catchment, which utilizes bulk water for food production. One of the main components of the water balance is evapotranspiration (ET), and its quantification is very important for water budgeting, efficient irrigation scheduling, cropping practices and water regulation in any irrigation system, especially in arid and semi-arid catchments where water shortage is a critical problem. ET is derived by solving an energy balance into various fluxes (net radiation, sensible heat, soil heat and latent heat). Conventional techniques to estimate ET employ only point measurements to estimate the components of the energy balance, and can only be representative of local scales. Remote sensing can provide representative measurements of several relevant physical parameters at scales from a point to the whole system.

The potential of satellite image-based remote sensing for examining spatial patterns of regional ET has been investigated by a number of authors (Choudhury, 1989; Menenti, 1993; Granger, 2000; Kustas & Norman, 2000; Su, 2002). These efforts have resulted in the development of remote sensing ET algorithms that are quite different in their spatial and temporal scales, ranging from 30 m to 1000 m, and daily to monthly. Many methods for the estimation of actual ET have been developed by combining remote sensing data with ground-based meteorological data for large areas.

This paper deals with the application of a Surface Energy Balance System (SEBS) algorithm using ASTER data to derive land surface flux budgets over the Coleambally Irrigation Area (CIA). Six ASTER scenes, covering the time periods of 2002, 2004, 2005, 2006, 2008 and 2009 were used for estimating the land surface heat fluxes over the study area, and the results were validated with ground based flux data measured from eddy covariance (EC) flux towers.

STUDY AREA

The CIA is located in the lower part of the Murrumbidgee River catchment, approximately 650 km southwest of Sydney in the Riverina District of New South Wales, Australia (Fig. 1). The CIA contains approximately 79 000 ha area of intensive irrigation supplying water to 478 farms owned by 362 business units (CICL, 2008). Water is diverted to the area from the Murrumbidgee River at Gogeldrie Weir through a 41-km-long main canal, and is then distributed through 477 km of supply channels. The principal summer crops grown (November–April) include rice, soybeans, maize (corn), grapes, prunes, sunflowers and lucerne, while principal winter crops (May–October) include wheat, oats, barley, canola, sunflowers and lucerne. Pasture for grazing is grown in both the seasons.

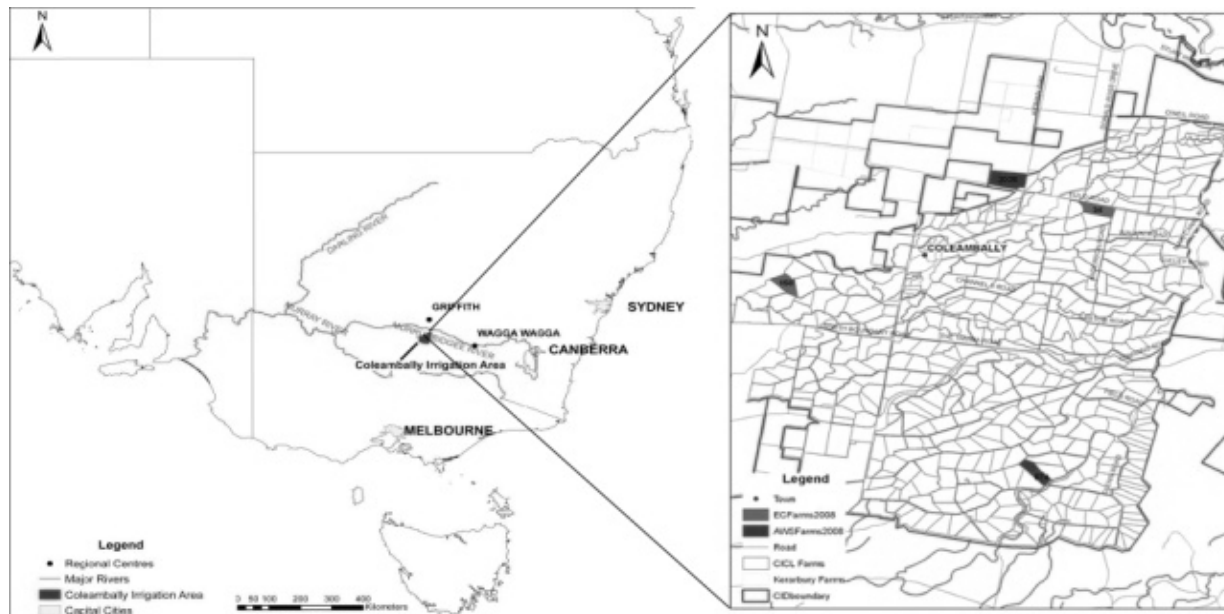


Fig. 1 Location of the Coleambally irrigation area.

The long-term climate averages (1997–2007) from the Bureau of Meteorology (BoM) show that average rainfall is 396 mm per year and the average annual evaporation is 1723 mm. The recent drought, a significant reduction in water allocations and concerns about climate change, have highlighted the need to manage water demand and supply more sustainably (CICL, 2009).

METHODS

The Surface Energy Balance System (SEBS) was proposed to estimate atmospheric turbulent fluxes using satellite Earth observation data, combined with meteorological information (see Su (2002) for more details). In this paper, the SEBS retrieval algorithm was applied to the ASTER data to evaluate its applicability within an Australian environment. Firstly, the ASTER data from the three ASTER instrument subsystems (VNIR, SWIR and TIR) were re-projected into the WGS-84 projection system. The radiative transfer model SMAC (Rahman & Dedieu, 1994) was used for atmospheric correction of the VNIR and SWIR data. NDVI was derived from bands 2 and 3N of ASTER data, while the land surface albedo (r_0) was retrieved from Liang (2001). The land surface temperature (LST) was derived using a method developed by Jimenez-Munoz *et al.* (2006) from multispectral thermal infrared data. Jimenez-Munoz *et al.*, (2006) also evaluated a technique to extract emissivity information from multispectral thermal infrared data by adding vegetation information. The surface net radiation flux (R_n) was determined by combining the retrieved albedo,

surface emissivity and LST from ASTER data, and the downward short and long wave thermal radiation from *in-situ* measurements at the Automatic Weather Stations (AWS). On the basis of the field observations, the soil heat flux (G_0) is estimated from the net radiation flux (R_n) using equation (1) (Su, 2002):

$$G_0 = R_n[\Gamma_c + (1 - f_c) \bullet (\Gamma_s - \Gamma_c)] \quad (1)$$

where the constants $\Gamma_c = 0.05$ for full vegetation canopy and $\Gamma_s = 0.315$ for bare soil (Su, 2002).

The sensible heat flux (H) is estimated from LST (T_{sfc}), air temperature (T_a) and other parameters as described by Su (2002). In order to derive the sensible and latent heat flux, SEBS uses the similarity theory. In the Atmospheric Surface Layer (ASL), the similarity relationships for the profiles of the mean wind speed, u , and the mean potential temperature difference between the surface and the air, $\theta_0 - \theta_a$, are described in integral form as:

$$u = \frac{u_*}{k} \left[\ln \left(\frac{z - d_0}{z_{om}} \right) - \Psi_m \left(\frac{z - d_0}{L} \right) + \Psi_m \left(\frac{z_{om}}{L} \right) \right] \quad (2)$$

$$\theta_0 - \theta_a = \frac{H}{ku_* \rho C_p} \left[\ln \left(\frac{z - d_0}{z_{oh}} \right) - \Psi_h \left(\frac{z - d_0}{L} \right) + \Psi_h \left(\frac{z_{oh}}{L} \right) \right] \quad (3)$$

where z is the height above the surface, u_* is the friction velocity, C_p is specific heat of air at constant pressure, ρ is the density of air, $k = 0.4$ is von Karman's constant, d_0 is the zero plane displacement height, z_{om} is the roughness height for momentum transfer, θ_0 is the potential temperature at the surface, θ_a is the potential air temperature at height z , z_{oh} is the scalar roughness height for heat transfer, Ψ_m and Ψ_h are the stability correction functions for momentum and sensible heat transfer, respectively, and L is the Obukhov length defined as:

$$L = \frac{\rho C_p u_*^3 \theta_v}{kgH} \quad (4)$$

where g is the acceleration due to gravity and θ_v is the virtual potential temperature near the surface. Other parameters can be found in Su (2002). By combining equations (2)–(4) and using an iterative method, we can estimate the sensible heat flux. To estimate the evaporative fraction, SEBS makes use of the energy balance at limiting cases at dry-limit and wet-limit conditions, such that the relative evaporation (ratio of the actual evaporation to the evaporation at wet-limit) can be derived as:

$$\Lambda_r = 1 - \frac{H - H_{wet}}{H_{dry} - H_{wet}} \quad (5)$$

where the H_{wet} is sensible heat flux at the wet limit and H_{dry} sensible heat flux at the dry limit. The estimations of H_{wet} and H_{dry} were detailed in Su (2002). The evaporative fraction (ratio of latent heat flux to available energy) is estimated by:

$$\Lambda = \frac{\lambda E}{R_n - G} = \frac{\Lambda_r \cdot \lambda E_{wet}}{R_n - G} \quad (6)$$

where λE_{wet} is the latent heat flux at the wet-limit (i.e. the evaporation is only limited by the available energy under the given surface and atmospheric conditions). The latent heat flux (λE) can then be calculated by

$$\lambda E = \Lambda(R_n - G_0) \quad (7)$$

RESULTS AND DISCUSSION

ASTER satellite data was selected on clear days to study the spatial distribution of energy budget components into fluxes (net radiation, sensible heat, soil heat and latent heat), as shown in Fig. 2.

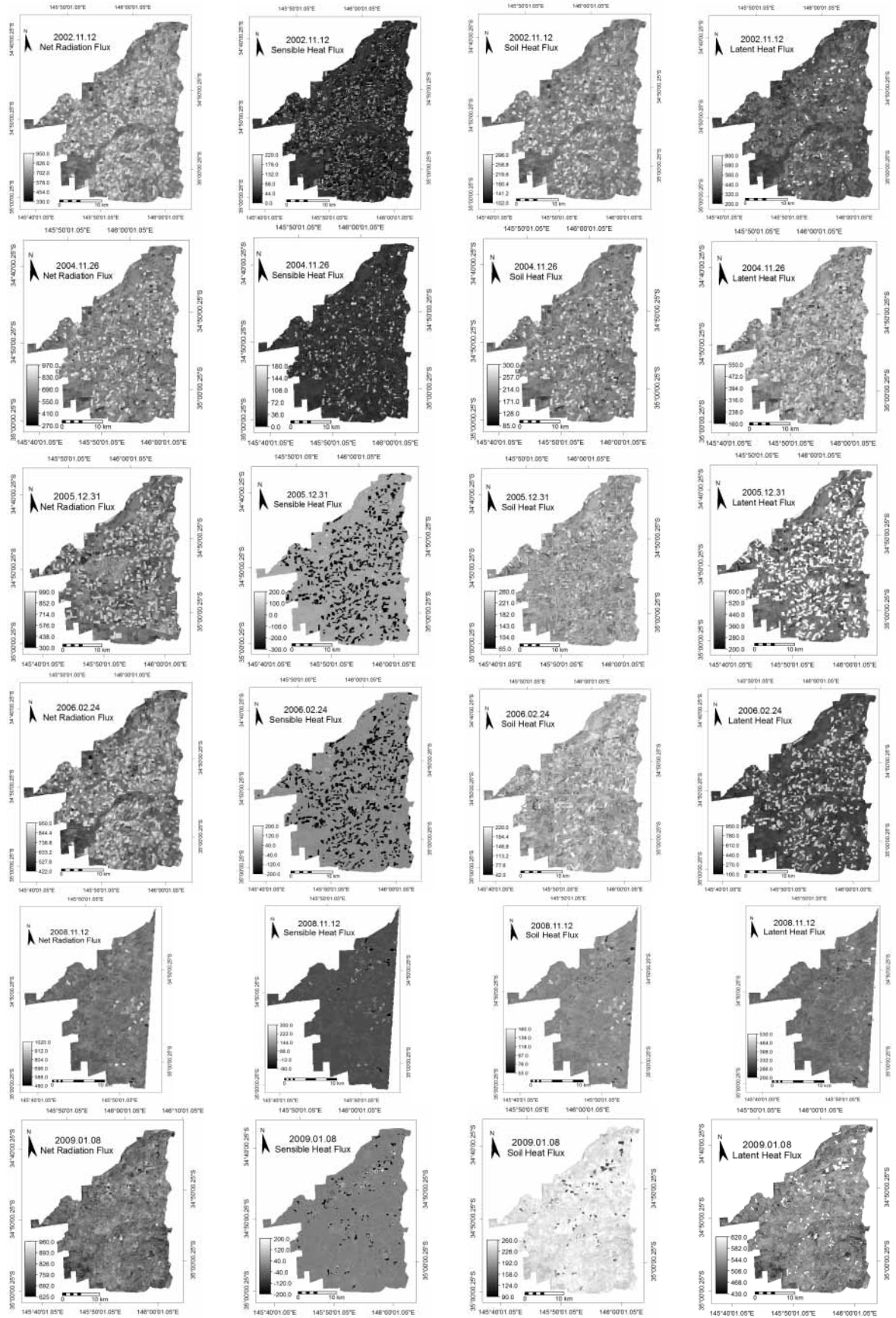


Fig. 2 Distribution maps of land surface heat fluxes (W/m^2) over the CIA, Australia.

The results show that the derived land surface fluxes in different years over the CIA are in good accordance with the land surface status. These parameters show a wide range due to the strong contrast of surface features, such as rice, soybeans, maize (corn), grapes, prunes, sunflowers, lucerne (November–April), wheat, oats, barley, canola, and sunflowers (May–October) in different seasons. The derived remote sensing value of net radiation flux, soil heat flux and latent heat flux in summer are higher than in winter seasons. It is clear that there is much greater evapotranspiration in summer than in winter and other seasons in CIA.

Two EC flux towers were installed in the CIA at separate locations over different crops. This EC data was used for the validation of SEBS estimated fluxes from ASTER data (Fig. 3). The EC data was in consistent agreement with the SEBS output. Minimal difference was observed between the soil heat flux observation and model output. One of the major reasons for the difference between observed and SEBS based net radiation could be the difference in albedo calculated from the EC and the albedo calculation inside SEBS (i.e. no data for short-wave infrared bands). The sensible heat flux output of SEBS is slightly lower than the EC measurements. SEBS calculated R_n lie within 16% of the observed EC data. Similarly, the SEBS based G_0 lie within 10%, H within 20% and λE lie within 17% and 24% of the observations (Fig. 3). In general, the EC data validates the SEBS results for R_n , G_0 , H and λE . As seen in Fig. 3, the latent heat flux observation and model output are in strong agreement with each other, which will validate the ET estimation from farm to irrigation area scales.

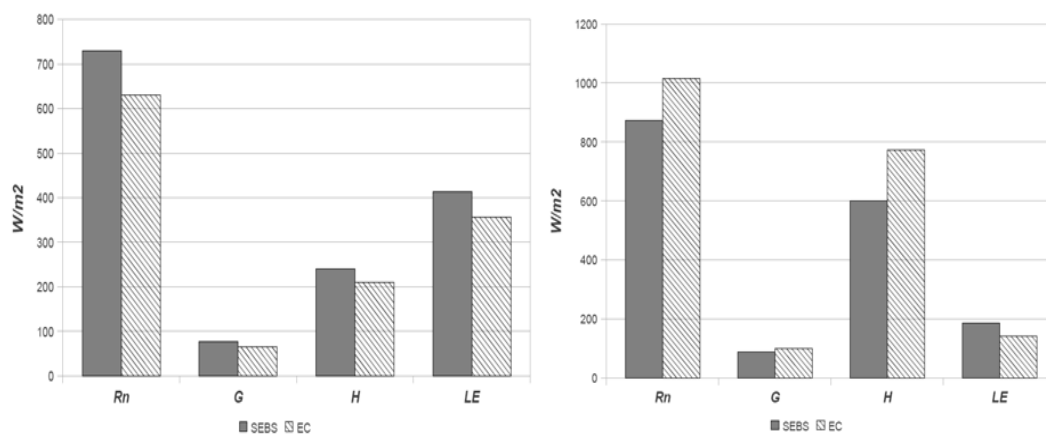


Fig. 3 Comparison of SEBS and EC derived fluxes on 12 November 2008 and 8 January 2009.

Similarly, the observations from the second EC flux tower, which was installed over a rice crop, also show good agreement with the SEBS results. Therefore, it can be observed that despite high net radiation values, the sensible heat flux is quite low and the latent heat flux is high. The derived net radiation fluxes are much closer to the field measurements, i.e. R_n flux from ASTER data at CIA Farm 158 on 12 November 2009 is 823.43 W m^{-2} , and at the same time the observation value is 837.1 W m^{-2} . The absolute percent difference is about 2%. That is to say the parameterization of SEBS for land surface heat flux is reasonable, and can be applied over irrigation systems like the CIA.

CONCLUDING REMARKS

In this paper, the CIA of Australia, SEBS and related parameters are introduced and some general results for estimating land surface energy budget were gained over long-term periods. The regional distributions of land surface heat fluxes (net radiation, soil heat flux, sensible heat flux and latent heat flux) over the CIA are also derived by using ASTER data and field observations. The results

are in good agreement with the EC flux tower field observations. In other words, the regional land surface heat fluxes over a heterogeneous landscape can be determined by using satellite remote sensing and the atmospheric boundary layer observations.

All the results in this paper were obtained from the meso-scale area over the CIA. In order to up-scale the land surface heat fluxes to all of the heterogeneous landscapes of Australia, more field observations and more satellite data should be used in the future. The proposed parameterization method should also be improved to determine the regional land surface heat flux over the whole of Australia.

Acknowledgements This work was carried out as a part of National Water Commission (NWC) funded project SAM-ET, National Project 973 (2010CB951701), Knowledge Innovation Project of CAS (KZCX2-YW-QN309, KZCX2-YW-Q10-2) and NSFC (40905017, 40825015 and 40810059006).

REFERENCES

- Choudhury, B. (1989) Estimating evaporation and carbon assimilation using infrared temperature data: Vistas in modeling. In: *Theory and Applications of Optical Remote Sensing* (ed. by G. Asrar), 628–690. John Wiley, New York, USA.
- Coleambally Irrigation Cooperative Limited (2008) Annual Report for the year ended June 30, 2008, Australia.
- Colyambally Irrigation Cooperative Limited (2009) Annual compliance report. June 2009, Australia.
- Granger, R. (2000) Satellite-derived estimates of evapotranspiration in the Gediz basin. *J. Hydrol.* **229**(1–2), 70–76.
- Jimenez-Munoz, J. C., Sobrino, J., Gillespie, A., et al. (2006) Feasibility of Retrieving Land-Surface Temperature from ASTER TIR bands using two-channel algorithms: a case study of agricultural areas. *IEEE Trans. Geosci. Remote Sens.* **4**(1), 60–64.
- Kustas, W. & Norman, J. (2000) A two-source energy balance approach using directional radiometric temperature observations for sparse canopy covered surfaces. *Agronomy J.* **92**(5), 847.
- Liang, S. (2001) Narrowband to broadband conversions of land surface albedo, I. Algorithms. *Remote Sens. Environ.* **76**, 213–238.
- Menenti, M. (1993) Understanding land surface evapotranspiration with satellite multispectral measurements. *Adv. Space Res.* **13**(5), 89–100.
- Rahman, H., & Dedieu, G. (1994) SMAC: a simplified method for atmospheric correction of satellite measurements in the solar spectrum. *Int. J. Remote Sensing* **15**, 123–143.
- Su, Z. (2002) The Surface Energy Balance System (SEBS) for estimation of turbulent heat fluxes. *Hydrol. Earth Syst. Sci.* **6**, 85–99.

On utilizing river widths measured from synthetic aperture radar images for calibrating rainfall–runoff models in ungauged basins

WENCHAO SUN¹, HIROSHI ISHIDAIRA¹, SATISH BASTOLA² & SUSHU WU¹

¹ Interdisciplinary Graduate School of Medicine and Engineering, University of Yamanashi, 4-3-11, Takeda, Kofu, Yamanashi, 400-8511, Japan
wsun.uy@gmail.com

² National University of Ireland, Maynooth, Co. Kildare, Ireland

Abstract The rainfall–runoff model is a common tool for estimating river discharge in the field of hydrology. The dependence on observed discharge data for calibration restricts its applications. In the last decade, the river cross-sectional water surface width obtained from remote sensing images, especially from the synthetic aperture radar (SAR) which can penetrate the clouds, has proved to be effective in tracing river discharge from space. In this study we present a method using river widths measured from SAR images for calibrating rainfall–runoff models based on at-a-station hydraulic geometry. One distinct advantage is that this calibration is independent of river discharge information. The results of the case study indicate that the satellite observation of river width is a competent surrogate of observed discharge for the calibration of the rainfall–runoff model and the proposed method has the potential for improving reliability of river discharge estimation in basins without any discharge gauging.

Key words river discharge; rainfall–runoff model; river cross-sectional water surface width; synthetic aperture radar; at-a-station hydraulic geometry

INTRODUCTION

River discharge provides essential information for water resource management and flood hazard prevention. Nevertheless, *in situ* networks and access to river discharge information have been reducing in past decades (Vörösmarty *et al.*, 2001). The remote-sensing approach is promising for increasing the spatial coverage of river discharge estimations globally. Average river water surface width over certain reach lengths can be extracted from many kinds of remotely sensed imagery. In particular, river width derived from the synthetic aperture radar (SAR), which can penetrate the clouds, has been proven to be effective in tracing river discharge from space (Smith *et al.*, 1995, 1996). In the field of hydrology, the rainfall–runoff model is a common tool for extending river discharge, both in time and space (e.g. Bastola *et al.*, 2008). The dependence on discharge data at basin outlets for calibration limits its application in ungauged basins. In this study a new calibration scheme for rainfall–runoff models is proposed. The calibration is based on river width time series derived from a series of SAR images for the basin outlet. One distinct advantage of this approach is that the calibration is independent of *in situ* gauged discharge data. Therefore, the proposed method is expected to facilitate the application of rainfall–runoff models in ungauged basins. The details about the methodology will be introduced. Then a case study at Pakse in the Mekong Basin will be demonstrated, which uses river widths derived from Japan Earth Resource Satellite-1 (JERS-1) SAR images as calibration data.

METHODOLOGY

Shifting the calibration objective of rainfall–runoff model to river width at the basin outlet

Essentially, a rainfall–runoff model can be considered as a system as follows:

$$Q = f(I | \eta) \quad (1)$$

where I is the model input, such as rainfall, Q is river discharge at basin outlet as output, η is the vector of model parameters, f is the group of functions representing the system structure. Model calibration is the process making the model closely simulate the river discharge at the basin outlet

by selecting proper values for the parameters. The parameter values being identified are considered as an appropriate representation of the runoff generation process.

River discharge is strongly related to river flow width. This is the basis of the at-a-station hydraulic geometry theory (Leopold & Maddock, 1953) which relates flow width to discharge, at a certain cross-section by the power function:

$$W = aQ^b \quad (2)$$

where Q is discharge, W is river width, a and b are two empirical parameters reflecting the hydraulic condition at the cross-section. The exponent b indicates the sensitivity of variation of river width to the change of discharge, which is mainly determined by the shape of the cross-section (Dingman, 2007). In this study, this function is used to shift the observed basin behaviour, which regulates the simulation made by the rainfall–runoff model, from river discharge data to satellite observed river width time series for the basin outlet. More specifically, the simulated discharge is used as input discharge to calculate cross-sectional water surface width based on equation (2). Consequently, river discharge has become a state variable and the river width at the basin outlet has become the output of the integrated model:

$$W = g(I | \theta) \quad (3)$$

where I is the same input as in equation (1), θ is the vector of model parameters which include all elements of η , a and b , g is the system structure which contains the rainfall–runoff functions and equation (2). The calibration of this integrated model is accomplished by adjusting each element of θ simultaneously to find a good fit between river width estimates and satellite measurements. The identified parameters are considered to reflect the runoff generation process and the “river width generation” process at the basin outlet appropriately.

Calibration using generalized likelihood uncertainty estimation (GLUE)

Using at-a-station hydraulic geometry to describe the relation between discharge and river flow width, errors in satellite observations are the additional sources of error for discharge estimation, besides the limitation of the rainfall–runoff model itself. To quantify the uncertainty in the modelling process, the Generalized Likelihood Uncertainty Estimation (GLUE) (see Beven & Binley, 1992 for details) is used for calibration and uncertainty analysis. The reciprocal of root mean square error (RMSE) is used as likelihood measured:

$$L_y[\theta | Y] = \frac{1}{\sqrt{\frac{1}{n} \sum_{i=1}^n (Y_i - Z_i)^2}} \quad (4)$$

where $L_y[\theta | Y]$ is the value of likelihood measure for parameter set θ conditioned on observations Y , Y_i is the number i satellite observation of river width, Z_i is model simulated value at the time step that the number i observation was made from space, and n is the total number of satellite observations. The threshold for rejecting parameter sets as non-behavioural ones depends on resolution of satellite images, river size and degree of river width variation at the basin outlet. From this cumulative probability distribution of likelihood measure, lower 5% and upper 95% quantiles are obtained at every time step. These two quantiles for all simulation steps constitute the simulation limits, which characterize the uncertainty in the modelling process. We assume that a parameter set, which can make good river width simulation, can also make equally good river discharge estimation. For the same period as calibration, the values of rainfall–runoff parameters in each behavioural parameter set are applied to the rainfall–runoff model alone to make river discharge simulation. The uncertainty limits are drawn as mentioned above.

APPLICATION TO THE MEKONG RIVER AT PAKSE

Description of study area

The Mekong River originates from the Tibetan Plateau and flows through Yunnan Province in China, Myanmar, Laos, Thailand, Cambodia and Vietnam. The climate varies from cold in the

upstream region to tropical climate in the downstream region. The annual average rainfall is around 1570 mm. River discharge estimation was carried out for the Pakse gauging station, which is located in the main stem of the Mekong River, in southwest Laos. The upstream area of Pakse (545 000 km², according to Mekong River Commission, 2003) is treated as our target area for rainfall–runoff modelling.

Extraction of river width from satellite imagery

River widths at Pakse region were extracted from 16 scenes of JERS-1 SAR images (Level 2.1) captured during 1995–1998, with a processed spatial resolution of 12.5 m. Active microwave emitted by the SAR is specularly reflected by smooth open water bodies. Backscatter values from the river water surface are relatively consistent (Smith *et al.*, 1995), which facilitates water area classification. To reduce measurement error and localized variability, average river width (mentioned as “effective width” by Smith *et al.*, 1996) over a selected reach at Pakse was extracted. Spatial extent of the reach is shown in Fig. 1(a). The channel length is roughly 11 times the bankfull width at Pakse gauging station, which conforms to the suggestions of Bjerklie *et al.* (2003) that the reach length should be at least 10 channel widths long. For each image, average width is calculated as:

$$W_e = \frac{a_w}{l} = \frac{a_a - a_i - a_s}{l} \quad (5)$$

W_e is effective width, a_w is water surface area within the reach, l is reach length, a_a is the total area within edge of water surface that contacts with river bank, a_i is the area of permanent islands, and a_s is the area of sandbars. The area components in equation (5) were delineated through visual interpretation, as demonstrated in Fig. 1(a). In Fig. 1(b), the average river widths derived from space are plotted against corresponding daily river discharge data at Pakse station. Based on the regression analysis, the best fitted curve in the form of power function is $W=1221.3Q^{0.0341}$, and the correlation between the two variables is high ($R^2 = 0.92$).

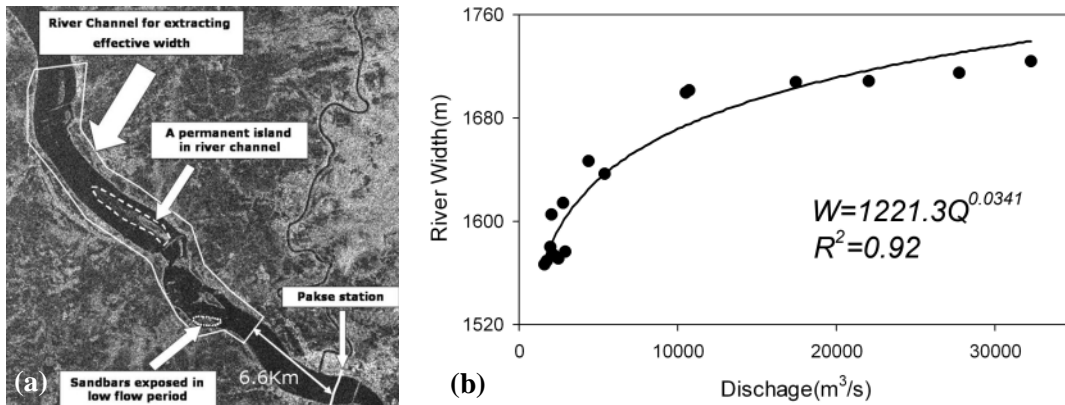


Fig. 1 (a) The selected reach at Pakse for measuring river width from JERS-1 SAR images and examples of the area elements being measured. (b) Plots of effective width derived from JERS-1 SAR images *versus* river discharge measured at Pakse station and the relation obtained from regression.

Rainfall–runoff model and GLUE set-up

The HYdrological MODel (HYMOD) (Boyle, 2001) was used in this demonstrative case study. It is a daily step rainfall excess model based on a nonlinear water storage capacity distribution function. The routing system includes a sequence of three quick-flow tanks which describe surface flow in parallel to a slow-flow tank corresponding to groundwater. The model structure is depicted in Fig. 2 and parameters are listed in Table 1. In this study, HYMOD was revised to account for

spatial variation in rainfall and evapotranspiration. The study area was divided into eight sub-basins. HYMOD was applied to each sub-basin, keeping the values of the three runoff generation parameters (C_{max} , B_{exp} , and α) the same among the sub-basins. The two routing parameters (K_q and K_s) were treated as spatially varied ones, using the distance between each sub-basin and Pakse as a scaling factor. At each time step, the amount of river discharge at Pakse is the sum of the water that comes from each sub-basin, and reaches Pakse at that specific time step. The daily rainfall data from 26 stations for the period of 1995–1998, and Ahn and Tateishi's monthly potential evapotranspiration (Ahn & Tateishi, 1994) were used as inputs. Observed river discharge data at Pakse station was also available for validation. A total of seven parameters, five from HYMOD and the other two from the power relation between discharge and river width at Pakse (see Table 1) are calibrated under the GLUE scheme. For calibration, 50 000 parameter sets were generated using a Latin-Hypercube sampling algorithm.

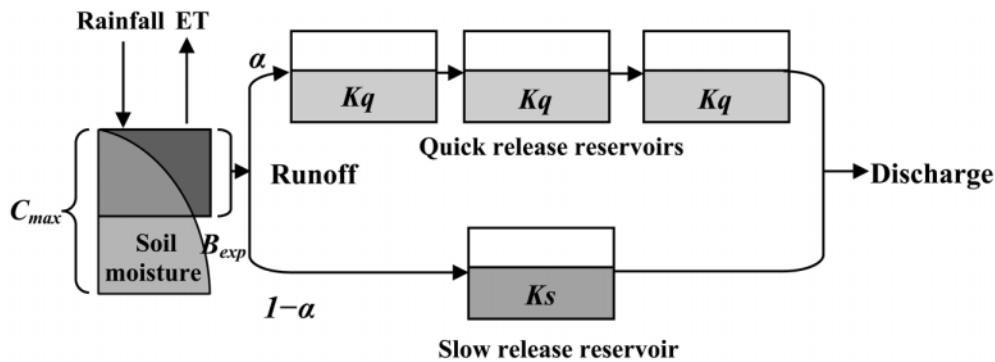


Fig. 2 Conceptual description of the HYdrological MODEL (HYMOD).

Table 1 Parameter descriptions and ranges of random sampling.

Model	Name	Description	Range
HYMOD	C_{max}	Maximum storage capacity	1–500
	B_{exp}	Degree of spatial variability of the soil moisture capacity	0–2
	α	Factor distributing the flow between slow and quick reservoirs	0–1
	K_s	Residence time of the slow release reservoir	0.001–0.5
	K_q	Residence time of the quick release reservoirs	0.5–1.2
At-a-station	a	Coefficient of the power function	1000–2000
Hydraulic geometry	b	Exponent of the power function	0.005–0.1

RESULTS AND DISCUSSION

River width simulation

We chose a low value for the likelihood measure (0.0167, corresponding RMSE: 60 m) as rejection criterion. Out of 50 000 generated samples, 1090 sets were kept as behavioural ones. The resulting uncertainty intervals are demonstrated in Fig. 3. All of the 16 river width observations derived from space are embraced. The match between river width estimates and satellite observations suggests the model input-state-output behaviour is reliable, which is one precondition for making trustworthy river discharge estimation.

River discharge estimation

The rainfall–runoff model parameters values in each behavioural set were applied to HYMOD. Figure 4 depicts the uncertainty intervals of simulated discharge. The 90% uncertainty intervals

are close to observed daily discharge at Pakse, and timing of variation in river discharge is well reproduced. The percentage of observations within simulation intervals is 70.3%, which is comparable with other hydrological modelling studies using GLUE (Montanari, 2005; Jia & Culver, 2008). The inaccuracy of river discharge simulation results from the errors of the rainfall-runoff model itself and the shifting of the calibration objective.

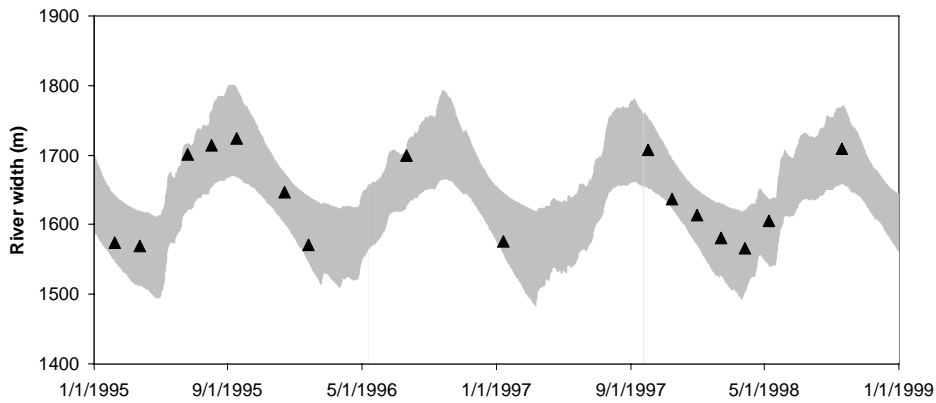


Fig. 3 River widths observed from space (triangles) and the uncertainty band of simulation.

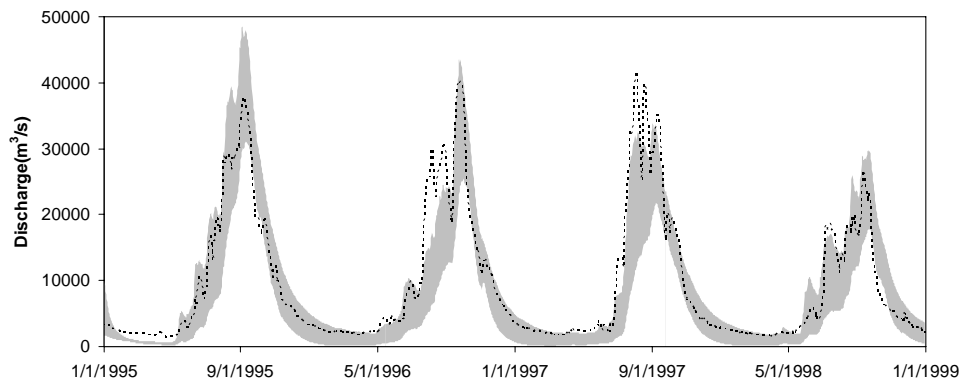


Fig. 4 Observed discharge (dots) at Pakse and the uncertainty band of simulations.

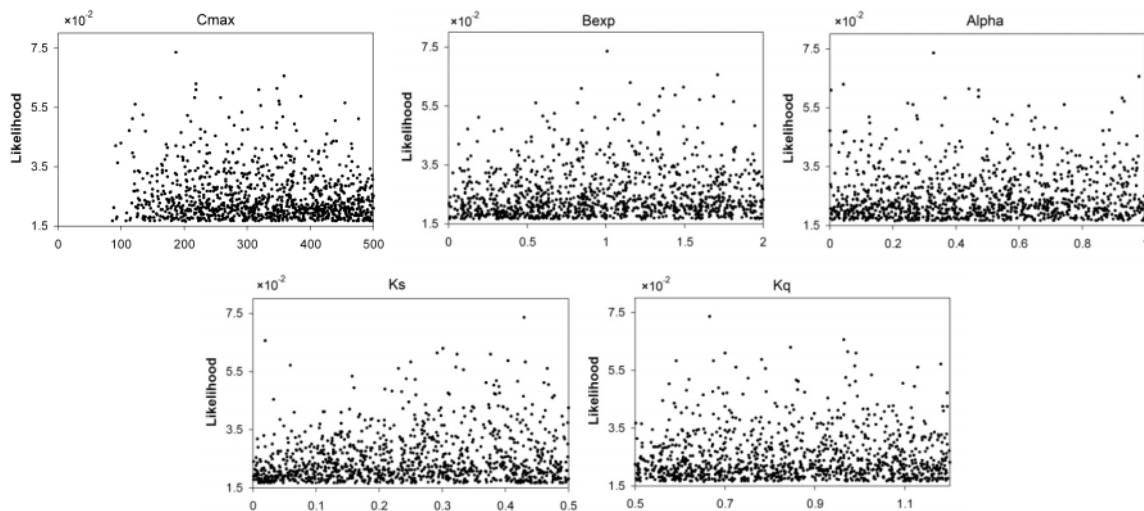


Fig. 5 Plots of likelihood value versus parameter values of HYMOD.

Posterior parameter distributions

Posterior parameter distributions conditioned on calibration data may give us some insights into model reliability (Winsemius *et al.*, 2006). The likelihood values for the 1090 behavioural parameter sets *versus* the values of the parameters of HYMOD and at-a-station hydraulic geometry relation are plotted in Figs 5 and 6, respectively. As an expected representation of equifinality, good values cover the whole original parameter ranges for the five parameters of HYMOD. In contrast, the two parameters of at-a-station hydraulic geometry relation are strongly constrained by calibration. This indicates that these two parameters are sensitive and they do not compensate for the rainfall–runoff model parameters’ effect. The posterior distributions of a and b are in single peak shape, which is consistent with the fact that a strong correlation between river width and discharge exists at Pakse. These facts raise the confidence that the hydraulic relation at Pakse region has been properly reflected by posterior distributions of a and b .

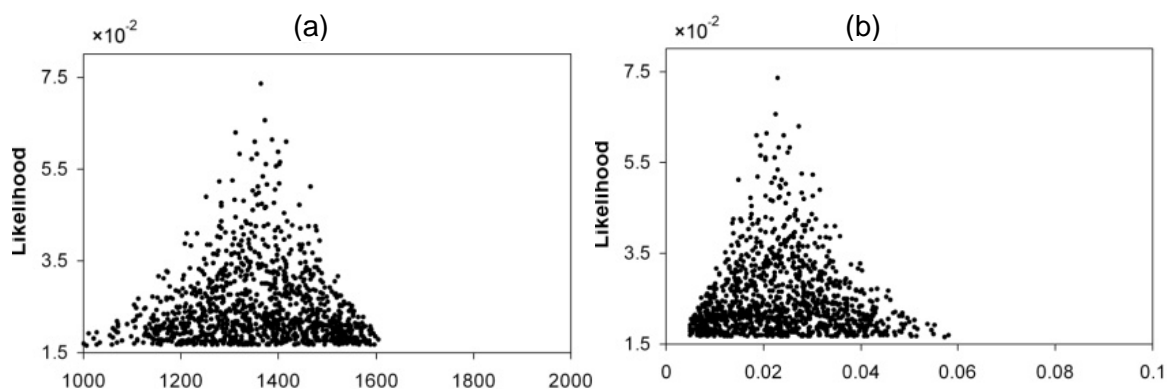


Fig. 6 Plots of likelihood value *versus* parameter values of the at-a-station hydraulic geometry relation.

CONCLUSIONS

In this study, a new calibration scheme for rainfall–runoff models was illustrated, aimed at improving river discharge estimation in ungauged basins. The full scope of this new calibration scheme was explored through a case study at Pakse in the Mekong Basin. The uncertainty intervals can cover all of the river width observations from space. The 90% uncertainty intervals for discharge are close to observed daily discharge at Pakse and satisfactorily reproduce the variation in the timing of discharge. The posterior distributions of two at-a-station hydraulic geometry parameters can reflect the hydraulic condition at Pakse reasonably. It can be concluded that this calibration scheme would have wide applicability for reproducing river discharge time series at daily scale in ungauged basins.

Acknowledgements The authors sincerely acknowledge MEXT Grand-in-aid Scientific Research (no. 21560537) and Global COE Program of University of Yamanashi for supporting this study.

REFERENCES

- Ahn C. H. & Tateishi R. (1994) Development of a global 30-minute grid potential evapotranspiration data set. *J. Jpn Soc. Photogramme. Remote Sens.* **33**(2), 12–21.
- Bastola, S., Ishidaira, H. & Takeuchi, K. (2008) Regionalisation of hydrological model parameters under parameter uncertainty: a case study involving TOPMODEL and basins across the globe. *J. Hydrol.* **357**(3–4), 188–206.
- Beven, K. & Binley, A. (1992) The future of distributed models: Model calibration and uncertainty prediction. *Hydrol. Processes* **6**(3), 279–298.
- Bjerklie, D. M., Moller, D., Smith, L. C. & Dingman, S. L. (2005) Estimating discharge in rivers using remotely sensed hydraulic information. *J. Hydrol.* **309**, 191–209.

- Boyle, D. P. (2000) Multicriteria calibration of hydrological models. PhD Thesis, University of Arizona, USA.
- Dingman, S. L. (2007) Analytical derivation of at-a-station hydraulic-geometry relations. *J. Hydrol.* **334**, 17–27.
- Jia, Y. & Culver, T. B. (2008) Uncertainty analysis for watershed modeling using generalized likelihood uncertainty estimation with multiple calibration measures. *J. Water Resour. Plan. Manage. ASCE* **134**(2), 97–106.
- Montanari, M., Hostache, R., Matgen, P., Schumann, G., Pfister, L. & Hoffmann L. (2009) Calibration and sequential updating of a coupled hydrologic-hydraulic model using remote sensing-derived stages. *Hydrol. Earth Syst. Sci.* **13**, 367–380.
- Mekong River Commission (2003) State of the basin report. ISSN: 1728-3248.
- Smith, L. C., Isacks, B. L., Forster, R. R., Bloom, A. L. & Preuss, I. (1995) Estimation of discharge from braided glacial rivers using ERS 1 synthetic aperture radar: first results. *Water Resour. Res.* **31**(5), 1325–1329.
- Smith, L. C., Isacks, B. L. & Bloom, A. L. (1996) Estimation of discharge from three braided rivers using synthetic aperture radar satellite imagery: Potential application to ungauged basins. *Water Resour. Res.* **32**(7), 2031–2034.
- Vörösmarty, C. J., Askew, A., Barry, R., Birkett, C., Döll, P., Grabs, W., Hall, A., Jenne, R., Kitaev, L., Landwehr, J., Keeler, M., Leavesley, G., Schaake, J., Strzepek, K., Sundarvel, S. S., Takeuchi, K., & Webster, F. (2001) Global water data: a newly endangered species. *Eos (AGU)* **82**(5), 54, 56, 58.
- Winsemius, H. C., Savenjie, H. H. G., Gerrits, A. M. J., Zapreeva, E. A. & Klees, R. (2006) Comparison of two model approaches in the Zambezi river basin with regard to model reliability and identifiability. *Hydrol. Earth Syst. Sci.* **10**, 339–352.

TRMM-forced rainfall–runoff modelling for water management purposes in small ungauged basins

BRUNO COLLISCHONN & ANDRÉ R. PANTE

*National Water Agency, ANA, Setor Policial, Area 5, Quadra 3, Bloco L, 70610-200 Brasilia-DF, Brazil
bruno.collischonn@ana.gov.br*

Abstract River monitoring in Brazil is largely concentrated on medium and large rivers, due to historical reasons related to hydropower generation purposes. In recent years, pressure has increased on small, mostly ungauged rivers for irrigation and urban supply. The National Water Agency (ANA) is responsible for giving out water use rights permits in federal rivers, i.e. rivers that cross interstate borders. In order to estimate water availability in small ungauged basins, and thus enable decision-making, we applied a simplified rainfall–runoff model, based on two parameters (one for infiltration capacity and one for groundwater reservoir depletion). In order to be applied, at least three discharge measurements during one single dry season must be done. Thus, adjustment of the model is focused on hydrograph recessions, which define water availability. We used satellite-estimated rainfall from TRMM as input to the model, with very good results. A graphical interface was also developed to download TRMM data and adjust the model in a user-friendly environment. The advantages of using TRMM estimates instead of raingauge data for this purpose are: the area-based character of TRMM data; the high coverage of TRMM, compared to sparsely distributed raingauges; and the immediate availability of TRMM data, compared with the relatively long time needed to collect and process raingauge data. We believe it to be a much more reliable methodology than the flow regionalization techniques used before.

Key words water; rivers; groundwater

INTRODUCTION – WATER USE RIGHTS AND MONITORING IN BRAZIL

Brazil is a country generally associated with water abundance, largely because of the Amazonian basin, which contains some 15% of all global freshwater (Goulding *et al.*, 2003). However, other regions in Brazil face more pressure for water use. In fact, the metropolitan regions in the southeast and the dry portions of the northeast show a critical water balance.

In recent years, irrigated agriculture is expanding to the central-west of the country, covering the region known as “cerrado”, a savannah-like landscape. Most of the farmers are settlers from the south, where land has become too costly. That shift is a part of a public policy beginning in the 1960s, during which the capital of the country was moved from Rio de Janeiro at the coast, to Brasília, in the high plateaus in the middle of the cerrado, bringing infrastructure and demand for agriculture to the region. This has resulted in an increasing pressure for water use over the small rivers near Brasília, home to more than 2 million people. Lying on the headwaters of three main Brazilian river basins, most rivers in the region have small drainage areas and therefore little water.

Freshwater management in Brazil is a shared task of both the federal and the 27 state governments. Rivers that cross more than one state, as well as transboundary rivers, are regulated by the National Water Agency, or by state water resources departments. Private ownership of water is not foreseen.

Thus, in order to divert water from rivers or lakes for any economic activity (urban water supply, industry, irrigation), one must get a water use right from the corresponding authorities. In Brazilian law these water use rights are known as “outorga”. The outorga is a discretionary decision taken by the State, and its concession depends on water use efficiency and water availability. In other terms, the concession of a new outorga should not jeopardize other users with water use rights in the same basin, i.e. multiple uses must be assured. Moreover, water use should be efficient, otherwise the water rights can be reverted. Irrigation corresponds currently to around 69% of total water rights allocated in Brazil (National Water Agency, 2005).

In practical terms, water availability is defined, for management purposes, as a share of a high-duration flow. At the federal level, ANA generally sets as reference the flow with 95% permanence, which is called the reference flow. Thus, a 5% frequency of failure in the supply is

implicitly accepted. This is considered an acceptable level of risk, since most irrigated crops tolerate short water stress periods. In rivers that supply human consumption, a lower level of risk can be adopted. Generally up to 70% of the reference flow can be granted to consumptive uses or to dilute treated wastewater effluents. In some cases, seasonal reference flows are adopted (typically the flow with 95% permanence each month), thus allowing more water use during wet months and restricting its use during dry periods.

Therefore, reference flows or flow duration curves must be defined for each river section of the basin of interest. In general, this is done by identifying the nearest flow gauge, and transposing the reference flows from one point to another, through a proportion of drainage area.

The problem with this procedure is that flow gauges are very sparsely distributed over the Brazilian territory. Moreover, just less than 1% of them control drainage areas of less than 10 km² and less than 5% control drainage areas smaller than 100 km². Thus, there is a general lack of monitoring in small basins. This lack is largely related to the background of hydrological monitoring in Brazil, which was under the responsibility of the hydropower sector until the end of the 20th century, when the water resources sector was reformed. Therefore, most gauges are located in medium and large basins, which were more promising from a power generation perspective. As a consequence, the hydrological behaviour of headwaters, which in general differs from that of larger rivers, is mostly unknown, making decision-making on whether to give out new water use rights difficult.

Silveira *et al.* (1998) proposed a procedure to overcome this absence of information, based on a simple rainfall–runoff model and a few flow measurements during a single dry period. But in some parts of the country even conventional rainfall data are scarce, and in general are not immediately available. Collischonn *et al.* (2008) used rainfall estimates from the Tropical Rainfall Measuring Mission as input to a rainfall–runoff model for a large basin in the Amazon.

The Tropical Rainfall Measuring Mission (TRMM)

The Tropical Rainfall Measuring Mission (TRMM) is a satellite built and operated jointly by the USA NASA and JAXA, the Japanese Aerospace Agency; it was launched in November 1997 and has provided rain estimates since January 1998. Its purpose was to get a better understanding of the precipitation in the tropics and its influence on global climate (Kummerow *et al.*, 2000).

Several different rainfall estimates are obtained by combining data from the different TRMM sensors. These estimates are termed products, according to the combination of instruments used in the estimation algorithm. Research product 3B42 (Huffman *et al.*, 2007) uses precipitation estimates obtained from TMI, the microwave sensor, adjusted with information about the vertical structure of the cloud, obtained from PR, the onboard precipitation radar.

Estimates are integrated to accumulated monthly values, generating the product known as 3B31. This product has a good spatial resolution of 0.25°, but an inadequate temporal resolution due to the low sampling frequency. Monthly totals are finally used to adjust infrared precipitation estimates from the Geostationary Operational Environmental System (GOES) series, which have a temporal resolution of 3 hours. By this means, a product – called 3B42 realtime, or RT – that combines both high temporal and spatial resolution is obtained. Finally, the 3B42 research product is obtained by scaling the 3-hourly RT values in order to match the monthly sums of a 1 × 1 degree rainfall grid derived from the Global Precipitation Climatology (GPCP) raingauge data (Huffman *et al.*, 2007). Due to this adjustment, 3B42 research product is available within up to 30 days.

In this work, TRMM 3B42 data are used to run the rainfall–runoff model, instead of raingauge data, as a tool to quickly estimate water availability in small watersheds.

DESCRIPTION OF THE MODEL AND STUDY AREA

Silveira *et al.* (1998) proposed a model intended to represent the behaviour of a homogeneous small watershed during dry periods. Provided that some discharge measurements are available, a

rainfall–runoff model can be calibrated in order to generate a low-flow time series, which are of interest for the estimation of reference flows.

The rainfall–runoff model runs usually on a daily time step, and the adjustment of two parameters is required, as follows:

The net precipitation at time step i is given by:

$$P_{net}(i) = P(i) - E(i) \quad (1)$$

where $P(i)$ is measured precipitation and $E(i)$ is an estimate of evaporation (generally a monthly average, since daily time series of evaporation are mostly unavailable), both in millimetres.

The volume that infiltrates into the soil, expressed in millimetres, is then calculated:

$$V(i) = P_{net}(i) \cdot C_{inf} \quad (2)$$

where C_{inf} is a parameter ranging from 0 to 1, corresponding to infiltration coefficient. And runoff is the difference between net precipitation and infiltrated volume:

$$R(i) = P_{net}(i) - V(i) \quad (3)$$

Baseflow (expressed in millimetres) is given by:

$$Q_b(i) = Q_b(i-1) \cdot e^{-1/k_b} + V(i) \cdot (1 - e^{-1/k_b}) \quad (4)$$

where k_b is a recession parameter in days.

Finally, the total flow, in m^3/s , is given by:

$$Q(i) = \frac{(Q_b(i) + R(i)) \cdot A}{86.4} \quad (5)$$

where A is the drainage area, in square kilometres.

To adjust the model, an objective function was chosen, similar to a standard error of the model:

$$SE = \sqrt{\sum_{j=1}^n (Q_{meas}(j) - Q(j))^2} \quad (6)$$

where (j) are the number of flow measurements, from 1 to n , and $Q(j)$ is the total flow calculated for the same time step than the dates of flow measures $Q_{meas}(j)$.

Adjustment is done by a trial-and-error procedure until a minimum of the objective function is reached.

The model has been applied to 12 small watersheds in the surroundings of Brasília, five using raingauge data and seven using both raingauges and TRMM data. The watersheds were chosen based on the existence of water use right requests or potential demand for water. At each river, at least three measurements were made during one single dry period, to anchor model simulations. The measurements were made with a Flowtracker Sontek Acoustic Doppler Velocimeter. Measurements have been made every year since 2006 in different rivers to adjust the model using both raingauge and satellite rainfall estimates from TRMM.

The region has a very well-defined dry season, from May until September. In the rain season, rainfall averages 1400 mm. Moreover, soils are relatively deep and have a good storage capacity, thus maintaining flows over the whole dry period. Therefore, at least a one-month separation between measurements is possible, thus covering longer recession periods. The more the measurements are distant in time, the better the adjustment of the hydrograph recession curve by the rainfall–runoff model. Table 1 shows the characteristics of some of the simulated watersheds, and Fig. 1 shows their location.

For the first two watersheds in Table 1, the rainfall–runoff was initially calibrated using raingauge data (from the nearest raingauge available). The model was then simulated using TRMM 3B42 research data, in order to compare results and validate TRMM simulated hydrographs. For the last watershed, only TRMM data were available, because raingauge data were not already sent to the databases.

Table 1 Characteristics of some monitored streams and measured flows.

Stream	Drain. area (km ²)	Year of measurements	Q _{meas} 1 (L/s)	Q _{meas} 2 (L/s)	Q _{meas} 3 (L/s)
Samambaia Creek	13	2006	141.6	80.6	36.3
Urucuia River	210	2006	1032.5	840.9	807.9
Saia Velha Creek	35	2010	470.1	405.7	344.9

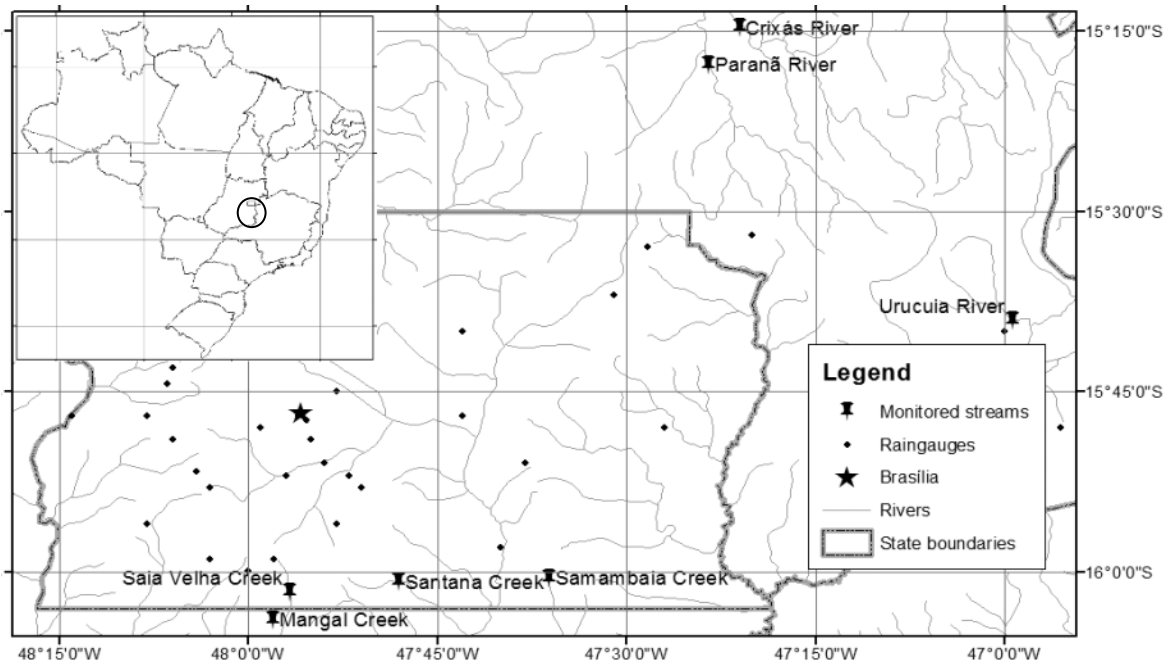


Fig. 1 Location of some of the monitored rivers, raingauges and TRMM pixels, as well as relative location in the Brazilian Territory.

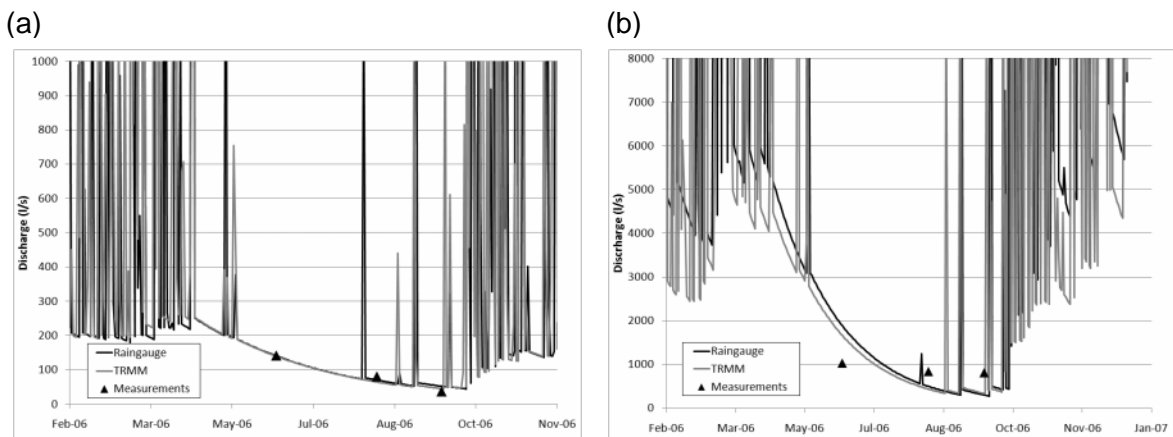


Fig. 2 Rainfall–runoff model adjustment for (a) the Samambaia Creek and for (b) the Urucuia River using raingauge and TRMM data.

RESULTS

Figure 2 shows the results of model calibration using raingauge data and the simulated hydrograph using TRMM data for the Samambaia Creek and for the Urucuia River.

As shown in Fig. 1, a reasonable adjustment of the model could be achieved, especially in the case of the Samambaia creek. The lowest value for the objective function using raingauge data was

obtained for $C_{inf} = 0.3$ and $k_b = 80.1$, and the standard error was 18.7 L/s. Using TRMM data with the same parameters, the standard error was 18.4 L/s.

The model was then simulated using the precipitation time series from 1998 to 2008, in order to estimate reference flows. The 95% flow ($Q_{95\%}$) calculated using raingauges was 35 L/s, while using satellite rainfall was 36 L/s.

In the case of the Urucuia River, the standard error using the nearest raingauge was 1047 L/s. Using TRMM data, the standard error was even smaller (884 L/s). The 95% flow calculated using data from the nearest raingauge was 167 L/s. Using TRMM data, $Q_{95\%}$ was 172 L/s.

In both cases a poor adjustment was achieved, with standard errors higher than the estimated $Q_{95\%}$ flow. Thus, we intentionally opted to stay on the side of safety, forcing model simulations to run below the measured discharges. It must be mentioned that uncertainties in this case are much more related to the model, which is too simple to represent rainfall–runoff transformations in more complex watersheds, than to TRMM rainfall estimates, since raingauge-driven simulations provide very similar results. Table 2 gives an overview of model adjustment for seven small watersheds. One can see that, except for the Urucuia River (mentioned above), most adjustments were good.

Table 2 Adjusted parameters, estimated flows and standard errors of TRMM-driven rainfall–runoff simulations.

Watershed	Drainage area (km ²)	C_{inf}	K_b	$Q_{95\%}$ (L/s)	Standard error (L/s)
Crixás	492	0.12	195	1112	34
Paraná	545	0.18	142	1416	13
Santana	88	0.36	245	634	7
Saia Velha	35	0.54	244	396	3
Samambaia	13	0.30	80	36	18
Urucuia	210	0.30	46	172	884
Mangal	15	0.54	168	136	3

In most cases, there is probably a low correlation between daily rainfall measured at the raingauge and estimated from TRMM. However, since low flows in the region are defined by the amount of rainfall during the rain season, TRMM seem to show good agreement with the total rainfall during the wet season, as well as its duration, because the recession hydrographs in both cases are very similar. Therefore, the rainfall–runoff model run with TRMM data is considered to provide a reliable assessment of reference flows, provided that the watershed of interest is relatively homogeneous.

To enhance user-friendliness of the procedure, a Graphical User Interface (GUI) was developed in Matlab 2010®, allowing the user to quickly adjust the model and estimate reference flows. The GUI allows the user to load both raingauge data and TRMM data as input to the model. In the second case, the user is asked to inform the coordinates of a rectangle containing the watershed. The GUI then downloads the daily 3B42 research time series from 1998 until the most recent data (usually 15–30 days delay) and completes the time series with 3B42 RT data (less than 24 h delay). Thus, it is possible to apply the model right after the measurements are done.

CONCLUSIONS

In this paper, TRMM data are used as input to a simple rainfall–runoff model for the estimation of flow duration curves, focusing on low flows. The results are used to assess water availability for regulation of water uses in Brazil, and allowed a decision-making process based on more reliable information.

Given the large number of small rivers where water needs to be allocated, the application of more complex models is generally not possible, because decision-making, in most cases, needs to

be quick. Irrigation has grown quickly in recent years, and most farmers need the outorga to obtain bank loans; thus there is public pressure for quick decision-making.

The model run with TRMM data gives similar results to those obtained using raingauge data. This is a great advantage, because TRMM data are generally quasi-real-time available, while raingauge data are collected with a frequency of 4–6 months and go through a consistency process before being available in the database.

Another advantage of using TRMM data is that it already provides an area-based average over the studied watershed, compared to the use of raingauge data, which are point data and mostly located outside the basin. TRMM provides data since January 1998, therefore the generated time series of discharge are still relatively short for more sound statistics. However, this period covers a very dry period in most parts of Brazil, from 1998 to 2001, as well as another shorter dry period in 2007–2008. Thus, the generated reference flows are probably underestimated on the side of safety.

The resulting hydrographs, obtained through the TRMM rainfall estimate, are reliable to estimate high-duration flows, like the $Q_{95\%}$ flow. But since no measurements during wet periods are made, this model should not be used to estimate long-term mean flows or peak flows (for example in reservoir design). The Graphical User Interface developed to ease the application of the rainfall–runoff model helps to accelerate the process of obtaining the reference flows.

The authors of this paper intend to continue monitoring the same rivers, in order to adjust the model in different hydrological years. Thus, it will be possible to establish confidence bounds for model parameters and estimate associated uncertainties. Running rainfall–runoff models with satellite-based precipitation estimates is a good alternative for the hydrological assessment of watersheds in countries like Brazil, where most rivers are still ungauged, especially those draining small areas.

More information about the GUI and the model can be obtained by contacting the first author.

REFERENCES

- Collischonn, B., Collischonn, W. & Tucci, C. E. M. (2008) Daily hydrological modelling in the Amazon basin using TRMM rainfall estimates. *J. Hydrol.* **360**(1–4), 207–216.
- Goulding, M., Barthem, R. B. & Ferreira, E. (2003) *The Smithsonian Atlas of the Amazon*. Smithsonian Books, Washington, USA.
- Huffman, G., Adler, R., Bolvin, D., Gu, G., Nelkin, E., Bowman, K., Hong, Y., Stocker, E. & Wolff, D. (2007) The TRMM Multisatellite Precipitation Analysis (TCMA): quasi-global, multiyear, combined-sensor precipitation estimates at fine scales. *J. Hydromet.* **8**, 38–55.
- Kummerow, C., Simpson, J., Thiele, O., Barnes, W., Chang, A. T. C., Stocker, E., Adler, R. F., Hou, A., Kakar, R., Wentz, F., Ashcroft, P., Kozu, T., Hong, Y., Okamoto, K., Iguchi, T., Kuroiwa, H., Im, E., Haddad, Z., Huffman, G., Ferrier, B., Olson, W. S., Zipser, E., Smith, E. A., Wilheit, T. T., North, G., Krishnamurti, T. & Nakamura, K. (2000) The status of the Tropical Rainfall Measuring Mission (TRMM) after two years in orbit. *J. Appl. Met.* **39**, 1965–1982.
- National Water Agency (2005) Water demand and availability in Brazil. *Contributions to the Brazilian National Water Resources Plan*. Brasília.
- Silveira, G. L., Tucci, C. E. M. & Silveira, A. L. L. (1998) Flow estimation in small ungauged basins (in Portuguese). *Revista Brasileira de Recursos Hídricos, Porto Alegre* **3**(3), 111–131.

Using TRMM rainfall estimates in hydrological and hydrodynamic modelling of the Amazon Basin

RODRIGO CAUDURO DIAS DE PAIVA¹, DIOGO COSTA BUARQUE¹,
WALTER COLLISCHONN¹, MINO S. SORRIBAS¹,
DANIEL GUSTAVO P. ALLASIA², CARLOS ANDRÉ B. MENDES¹,
CARLOS E. M. TUCCI¹ & MARIE-PAULE BONNET³

1 Instituto de Pesquisas Hidráulicas – IPH/UFRGS, Av. Bento Gonçalves, 9500 – Agronomia, Campus do Vale, Setor 5, CEP 91501-970 – Porto Alegre/RS, Brazil
rodrigocpaiva@gmail.com

2 Departamento de Hidráulica e Saneamento – UFSM, Av. Roraima, 1000 – Camobi, Cidade Universitária, Prédio 07, salas 518 a 523, Centro de Tecnologia, CEP 97105-900 – Santa Maria/RS, Brazil

3 IRD – Institut de Recherche pour le Développement, UR154 LMTG, 14, Av. Edouard Belin, 31400 Toulouse, France

Abstract Hydrological modelling of the Amazon is an enormous challenge because of its size, limited data, regional climatic diversity and particular hydraulic features, which include low gradients, back-water effects and extensive inundated areas. However, uncertainties in rainfall arising from limited ground-level measurements and low raingauge density impose severe difficulties, particularly in parts of the drainage basin lying outside Brazil. Rainfall estimation by remote sensing using satellite-derived data from the Tropical Rainfall Measuring Mission (TRMM) is a possible means of supplementing raingauge data, having better spatial cover of rainfall fields. This study reports on the use of the MGB-IPH large-scale hydrological model with rain fields obtained from TRMM. The MGB-IPH is a distributed, physically-based model using the Muskingum-Cunge formulation and a full hydrodynamic model for river routing, including backwater effects and seasonal flooding. Applying the model to the whole Amazon basin required development of several pre-processing tools to generate information about river cross-sections, flood plain extent, flood volume, and water slope from the SRTM DEM. Although TRMM under-estimates rainfall in regions with more marked relief, such as the transition region between the Amazon and the Andean regions of Peru, Ecuador and Colombia, results from the model in terms of its ability to reproduce observed hydrographs at several locations throughout the basin are encouraging.

Key words TRMM; hydrological modelling; hydrodynamic modelling; Amazon basin

INTRODUCTION

The climate variability in the Amazon River basin and the anthropogenic pressure of economic development, coupled with population vulnerability, are factors that increase the risk from extreme hydrological events. To minimize these risks it is necessary to act preventively by improving understanding of the natural system and through reduction of vulnerability and uncertainty through the prediction of weather, climate and hydrology. In this sense, hydrological modelling in the Amazon River is an interesting challenge because of its size, limited data, regional climatic diversity and particular hydraulic features which include low gradients, back-water effects and extensive inundated areas. However, uncertainties in rainfall arising from limited ground-level measurements and low raingauge density impose severe difficulties, particularly in parts of the drainage basin lying outside Brazil, and this is a major source of uncertainty in studies of hydrological processes, hydroclimatic variability, biogeochemical analysis and drainage basin response (e.g. Coe *et al.*, 2008; Collischonn *et al.*, 2008; Beighley *et al.*, 2009).

Estimation of rainfall using satellite-mounted instrumentation, on the other hand, avoids the problems of limited spatial coverage of ground-based raingauge networks, although the lengths of record obtainable from such sources are, as yet, fairly short. CMORPH (Joyce *et al.*, 2004), giving 30-min rainfall at a spatial resolution of 8 km at the equator, began in late 2002, whilst the Tropical Rainfall Measurement Mission (TRMM) algorithm 3B42 (Huffman *et al.*, 2007), giving 3-hour rainfall at a spatial resolution of 25 km, dates from 1998. Despite this, compared with raingauge data, the rapidity with which remote-sensed precipitation estimates become available is attractive. In this sense, where the density of ground-level networks of hydrological instruments is sparse, as is true in the Amazon basin, rainfall estimation by remote sensing using satellite-derived

data is a possible means of supplementing the limited data available from surface sites, having better spatial cover of rainfall fields. Several studies have been reported which explored aspects of remote-sensed rainfall in the Amazon, in particular using TRMM data sets (Collischonn *et al.*, 2008; Condom *et al.*, 2010; Getirana *et al.*, 2010; Tian & Peters-Lidard, 2010; Paiva *et al.*, 2011).

As part of a wider project to apply a large-scale, distributed and process based hydrological-hydrodynamic model, named MGB-IPH (Collischonn *et al.*, 2007; Paiva, 2009; Paiva *et al.*, 2011), the present work reports results on the use of this model for the whole Amazon basin (including Amapá State and the Tocantins River basin, as shown in Fig. 1) with rain fields obtained from TRMM 3B42.

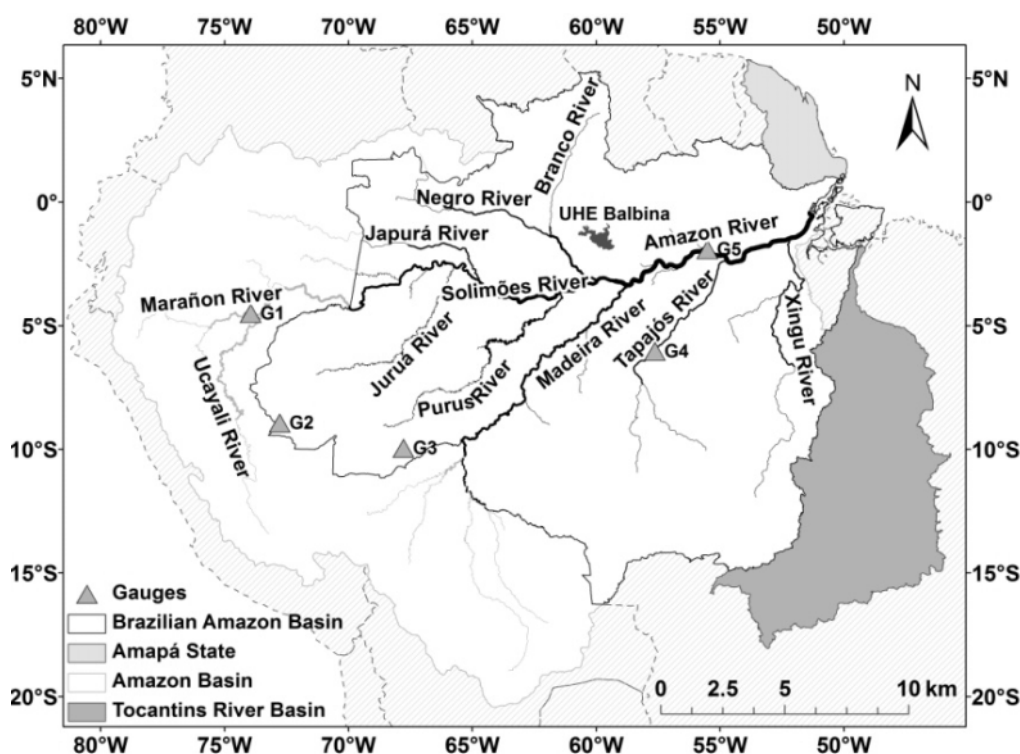


Fig. 1 Amazon River basin with main tributaries and streamgauges (grey triangles) used for analysis of model results.

THE MGB MODEL

The MGB-IPH is a large-scale hydrological model, which has been applied before to several other large-scale basins in South America. The MGB-IPH is a distributed and process-based hydrological model, which uses a catchment based discretization and a Hydrological Response Units (HRU) approach. It uses physical-based equations to simulate the hydrological processes, such as the Penman Monteith model for evapotranspiration, and the Moore and Clarke approach for soil infiltration. River routing is done either using the Muskingum-Cunge method or a full hydrodynamic model, or a combination of both. The hydrodynamic model uses the full Saint Venant equations, a simple flood plain storage model and GIS based parameters extracted from Digital Elevation Models, and is capable of simulating backwater effects and seasonally flooded flood plains. The application of this model to the whole Amazon basin demanded the development of several pre-processing tools, aimed at generating the necessary data for the hydrodynamic model from the SRTM DEM, based on relatively poor information, as river cross sections, flood plain extent and volume, and river slope was developed. Details concerning the model structure can be found in Collischonn *et al.* (2007), Paiva (2009) and Paiva *et al.* (2011).

DATA SET AND MODEL DISCRETIZATION

The study area is the whole Amazon River basin including the Tocantins River Basin as presented in Fig. 1. We used the SRTM DEM (Farr *et al.*, 2007) with 15" resolution (approximately 500 m) for model discretization. The Amazon basin was discretized into 6863 catchments, in which 92% has areas between 100 and 5000 km². An HRU map with 12 classes was developed using soil and vegetation maps from the Brazilian database RADAMBrasil Project (RADAMBRASIL, 1982), SOTERLAC/ISRIC (Dijkshoorn *et al.*, 2005) and the "Vegetation Map of South America" developed by Eva *et al.* (2002). Discharge data from 172 streamgauges was provided by the Brazilian agency for water resources ANA (Agência Nacional das Águas) and model results were analysed in all of those gauges, but analysis for only five streamgauges (Fig. 1 and Table 1) are shown here. Meteorological data were obtained from the CRU CL 2.0 dataset (New *et al.*, 2002). We used the TRMM precipitation data provided by algorithm 3B42 (Huffman *et al.*, 2007), with spatial resolution of 0.25° × 0.25° and daily temporal resolution, for the 8-year period 1998–2005. Data sets from TRMM were then interpolated to each catchment centroids, providing more reliable daily rainfall time series than can be achieved with the sparse ground-based raingauge networks existent due to its spatial cover of rainfall fields.

The MGB-IPH parameters related to soil water budget were calibrated, using discharge data from the 1998–2005 period from 172 streamgauges, with the MOCOM-UA algorithm (Yapo *et al.*, 1998), as described in Collischon *et al.* (2007).

Table 1 Streamgauges used for analysis of model results.

Code	Name	Latitude	Longitude	Point
10070500	San Regis	-4.51000	-73.95000	G1
12370000	Taumaturgo	-8.93985	-72.77709	G2
13600002	Branco River	-9.96061	-67.78580	G3
17500000	Fortaleza	-6.04031	-57.63946	G4
17050001	Óbidos	-1.92322	-55.51858	G5

RESULTS AND DISCUSSION

Figures 2 and 3 present simulated and observed discharges in the gauges shown in Fig. 1 and described in Table 1. Results in the figures are shown only for the 2001–2004 period. The model performance using TRMM 3B42 data is very good near the outlet of the Amazon River basin in the Óbidos streamgauge (Fig. 3(c)). In this site, the Nash and Sutcliffe index is $E_{NS} = 0.89$ and the error in the volume equals $\Delta V = -5.6\%$, showing that the timing of the flood wave in the Amazon mainstream is well represented by the model and the error in the volume is small. Results are also promising in the Amazon main tributaries, exemplified here using results in the Purus and Tapajós rivers. The MGB-IPH model using TRMM 3B42 presented very good results in the Tapajós River, representing very well the peaks of the flood, the flow recessions and total volume ($E_{NS} = 0.95$ and $\Delta V = 0.1\%$). In the Purus River we selected a streamgauge in the upper part of the basin to show model performance in a smaller river basin. Hydrographs in small basins are noisy, with several peaks related to intense rainfall events, different from the lower part where the flood waves are attenuated and delayed due to river and flood plain effects. Results for this selected basin were also good ($E_{NS} = 0.84$ and $\Delta V = 2.7\%$) and the model with TRMM 3B42 was able to simulate mean discharge, low and high flows, although some of the peaks were not well represented.

Although model results were good for most of the streamgauges used for comparisons, poor agreements with observations were found in some regions such as small or headwater catchments, and areas outside Brazil. Figure 3 shows results in parts of the basin where the MGB-IPH with TRMM 3B42 presented some errors. In small river basins such as in upper Jurua River basin (e.g. gauge 12370000, Fig. 3(a)), the MGB-IPH with TRMM data could not resolve intense rainfall events, the peaks in the hydrograph were not represented by the model and the model performance

was low ($E_{NS} = 0.45$ and $\Delta V = -30.6\%$). These errors are perhaps related to the spatial resolution of TRMM 3B42 (~ 25 km), that may be too coarse to represent these intense rainfall events in small catchments.

Model results also presented relevant errors in the Solimões River basin outside Brazil. TRMM data seemed to underestimate rainfall in this region. As a result, in the Marañon River (Fig. 3(b)) the MGB-IPH underestimated streamflow ($\Delta V = -18.2\%$) and model performance was low ($E_{NS} = 0.08$), even though the timing of flood waves have been represented. This may be related to errors in satellite rainfall estimates in the Amazon basin outside Brazil, mainly in the Andean region, that were also shown by Tian & Peters-Lidard (2010), in a global map of uncertainties of satellite precipitation estimates, and by Condom *et al.* (2010).

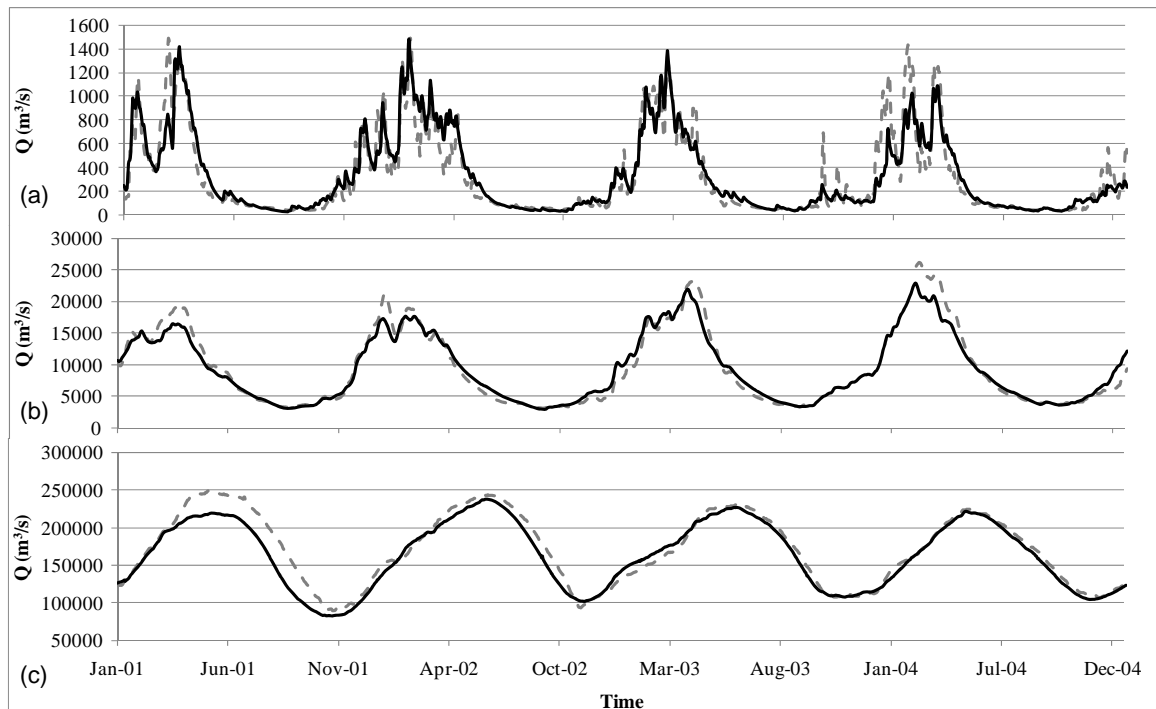


Fig. 2 Observed (dashed grey line) and simulated (black line) daily streamflow in gauges (a) 13600002, (b) 13500000 and (c) 17050001 in the 2001–2004 time period.

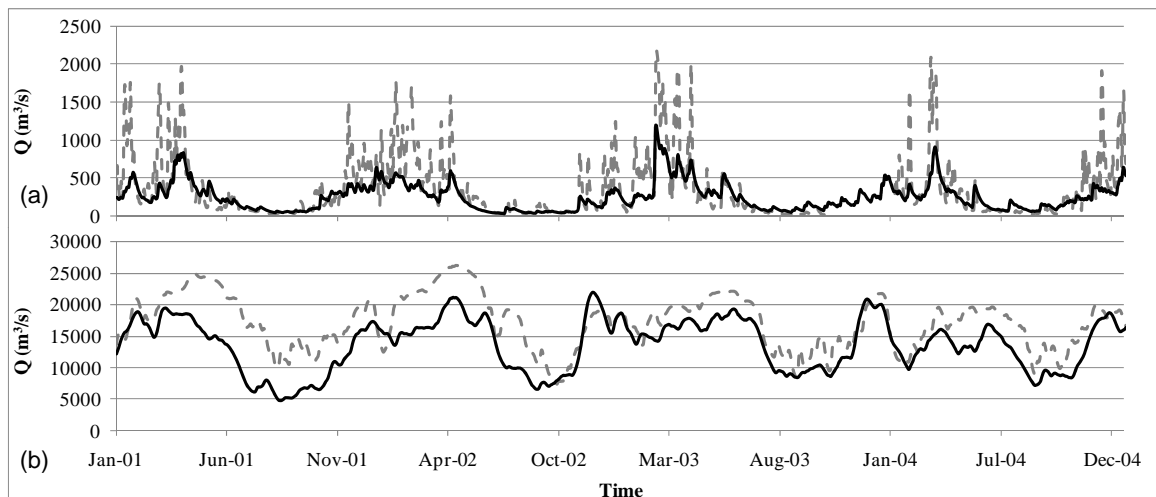


Fig. 3 Observed (dashed grey line) and simulated (black line) daily streamflow in gauges (a) 12370000 and (b) 10070500 in the 2001–2004 time period.

In this paper, we preferred to validate the TRMM data set by comparing the MGB-IPH model outputs with discharge measurements because: (i) the spatial coverage of the ground-based raingauge network is limited in the Amazon, mainly outside Brazil, (ii) the objective of our study is to apply a hydrological model to get discharge estimates in a region with a lack of raingauge data, and (iii) when comparing rainfall fields obtained by satellites with raingauge data several difficulties arise, such as the irregular spatial coverage of the raingauges and differences between point (raingauge) and areal averaged (satellite based) rainfall estimates. Although there are other sources of model errors, such as uncertainty in input data, parameters and model structure, uncertainty in rainfall data is one of the greatest importance, and the above-mentioned difficulties can be reduced by integrating TRMM rainfall fields within a catchment using hydrological modelling and comparing the model results with observed discharges.

CONCLUSION

The MGB-IPH model using TRMM 3B42 data was shown to be able to reproduce observed hydrographs in the Amazon River and main tributaries well. TRMM 3B42 data under-estimates rainfall in the Amazon River basin outside Brazil, in the transition region between the Amazon and the Andean regions of Peru, Ecuador and Colombia, and as a result the model underestimates discharge in parts of such regions. However, comparisons of model results with discharge observations at several locations throughout the basin showed that model performance using TRMM 3B42 data is encouraging.

Acknowledgements The authors are grateful for: the financial and operational support from the Brazilian agencies FINEP and ANA and the TRMM data supplied by NASA and associated agencies.

REFERENCES

- Beighley, R. E., Eggert, K. G., Dunne, T., He, Y., Gummadi, V. & Verdin, K. L. (2009). Simulating hydrologic and hydraulic processes throughout the Amazon River Basin. *Hydrol. Processes* **23**(8), 1221–1235.
- Coe, M. T., Costa, M. H. & Howard, E. A. (2008) Simulating the surface waters of the Amazon River basin: impacts of new river geomorphic and flow parameterizations. *Hydrol. Processes* **22**(14), 2542–2553.
- Collischonn, B., Collischonn, W. & Tucci, C. E. M. (2008) Daily hydrological modeling in the Amazon basin using TRMM rainfall estimates. *J. Hydrol.* **360**(1–4), 207–216.
- Collischonn, W., Allasia, D. G., Silva, B. C. & Tucci, C. E. M. (2007) The MGB-IPH model for large-scale rainfall-runoff modeling. *Hydrol. Sci. J.* **52**, 878–895.
- Condom, T., Rau, P. & Espinoza, J. C. (2010) Correction of TRMM 3B43 monthly precipitation data over the mountainous areas of Peru during the period 1998–2007. *Hydrol. Processes*, doi:10.1002/hyp.7949.
- Dijkshoorn, J. A., Huting, J. R. M. & Tempel, P. (2005) Update of the 1:5 million Soil and Terrain Database for Latin America and the Caribbean (SOTERLAC, version 2.0). *Report 2005/01*, ISRIC – World Soil Information, Wageningen, The Netherlands.
- Eva, H. D., De Miranda, E. E., Di Bella, C. M. & Gond, V. (2002) A vegetation map of South America. *EUR 20159 EN*, European Commission, Luxembourg.
- Farr, T. G., Caro, E., Crippen, R., Duren, R., Hensley, S., Kobrick, M., Paller, M., Rodriguez, E., Rosen, P., Roth, L., Seal, D., Shaffer, S., Shimada, J., Umland, J., Werner, M., Burbank, D., Oskin, M. & Alsdorf, D. (2007) The shuttle radar topography mission. *Rev. Geophysics* **45**(2).
- Getirana, A. C. V., Bonnet, M.-P., Rotunno Filho, O. C., Collischonn, W., Guyot, J. -L., Seyler, F. & Mansur, W. J. (2010) Hydrological modelling and water balance of the Negro River basin: evaluation based on in situ and spatial altimetry data. *Hydrol. Processes*, doi:10.1002/hyp.7747.
- Huffman, G., Adler, R., Bolvin, D., Gu, G., Nelkin, E., Bowman, K., Hong, Y., Stocker, E. & Wolff, D. (2007) The TRMM Multisatellite Precipitation Analysis (TCMA): quasi-global, multiyear, combined-sensor precipitation estimates at fine scales. *J. Hydromet.* **8**, 38–55.
- Joyce, R. J., Janowiak, J. E., Arkin, P. A. & Xie, P. (2004) CMORPH: A method that produces global precipitation estimates from passive microwave and infrared data at high spatial and temporal resolution. *J. Hydromet.* **5**, 487–503.
- New, M., Lister, D., Hulme, M. & Makin, I. (2002) A high-resolution data set of surface climate over global land areas. *Climate Res.* **21**.
- Paiva, R. C. D. (2009) Large scale hydrological and hydrodynamic modeling: the Rio Solimões case study. MSc Thesis, Instituto de Pesquisas Hidráulicas. Universidade Federal do Rio Grande do Sul (in Portuguese).
- Paiva, R. C. D., Collischonn, W. & Tucci, C. (2011) Large scale hydrologic and hydrodynamic modeling using limited data and a GIS based approach. *J. Hydrol.* (in review).

- Paiva, R. C. D., Buarque, D. C., Clarke, R. T., Collischonn, W. & Allasia, D. (2011) Reduced precipitation over large water bodies in the Brazilian Amazon shown from TRMM data. *Geophys. Res. Lett.*, doi:10.1029/2010GL045277.
- RADAMBRASIL (1982) Programa de Integração Nacional, Levantamento de Recursos Naturais. *Ministério das Minas e Energia, Secretaria-Geral*.
- Tian, Y. & Peters-Lidard, C. D. (2010) A global map of uncertainties in satellite-based precipitation measurements. *Geophys. Res. Letters* **37**, L24407, doi:10.1029/2010GL046008.
- Yapo, P. O., Gupta, H. V. & Sorooshian, S. (1998) Multi-objective global optimization for hydrologic models. *J. Hydrol.* **204**, 83–97.

Flood monitoring of the Inner Niger Delta using high resolution radar and optical imagery

ALAIN DEZETTER¹, DENIS RUELLAND² & CAMILLE NETTER¹

¹ IRD, UMR HydroSciences Montpellier, Maison des Sciences de l'Eau, Université Montpellier II, Case Courrier MSE, Place Eugène Bataillon, 34095 Montpellier Cedex 5, France
alain.dezetter@ird.fr

² CNRS, UMR HydroSciences Montpellier, Maison des Sciences de l'Eau, Université Montpellier II, Case Courrier MSE, Place Eugène Bataillon, 34095 Montpellier Cedex 5, France

Abstract This paper describes the monitoring of flooding in the Inner Niger Delta (Mali) from September 2008 to April 2010 using high resolution radar (C-band quad-polarization from Radarsat-2) and optical imagery (SPOT 4 and 5). Treatments, based on statistical parameters calculated using co-occurrence matrices, supervised classifications and three field surveys, were used to classify the images in three categories: open water, flooded vegetation and unflooded land. The overall accuracy evaluated by confusion matrices varies from 81% to 96%. The flooded areas, ranging from 3% to 65% of the surface studied, confirm the significant impact of annual flooding in the region. Radar images can identify soil properties even when remotely-sensed objects are characterized by dense, herbaceous vegetation and are also effective when cloud cover is thick.

Key words Radarsat-2; SPOT; Inner Niger Delta; flood monitoring; Mali

INTRODUCTION

Wetlands are the richest and most diverse ecosystems in the world. They control flooding, prevent drought, improve water quality, maintain water resources, temper erosion and serve as leisure areas (Novitzki *et al.*, 1996). Tropical areas, where a large proportion of food resources are linked to aquatic environments, are very dependent on the sustainability of these ecosystems. In 2007, the Intergovernmental Panel on Climate Change (IPCC) published an alarming report on the consequences of global warming (IPCC, 2007): by 2080, nearly 3.2 billion people will probably suffer from severe water shortages and 600 million from hunger as a result of droughts.

Africa is among the continents most concerned by the impact of climatic fluctuations on water resources. Indeed, the region has been subjected to environmental and particularly climate changes since the 1970s (L'Hôte *et al.*, 2002; Andersen *et al.*, 2005). More than two-thirds of the continent is between the tropics and the major droughts that hit the Sahel in the 1970s had dramatic, lasting consequences for the population. Lake Chad is a spectacular example of the effects of changing climatic conditions in tropical Africa. Its area was more than 22 000 km² in the 1960s, but it now consists of several non-perennial lakes covering less than 2000 km², with serious ecological consequences for the region and for the subsistence of local populations (Lemoalle *et al.*, 2008). The Inner Niger Delta (IND) is the largest flood zone in Mali has faced a similar problem of the sustainability of water resources since the 1970s as the flood zone area has decreased by 60% (Orange *et al.*, 2002; Mariko, 2003). Integrated management of these resources with a view to improving the standard of living of populations and conserving ecosystems, requires knowledge of flood dynamics.

This study proposes a method for monitoring flood dynamics in the IND. Given the scale of the area concerned, the use of satellite images is essential. Studies using optical imagery have already been conducted to trace the evolution of flooded areas in the Inner Niger Delta using the infrared channel of Landsat images for the 1973/1974 hydrological season (Blanck, 1993). Since then, Batti (2001) and Mariko (2003) showed the interest of NOAA-AVHRR images for observing the flooded areas. These images made it possible to work on the scale of the delta and to model the functioning of its hydrosystem. However, all these authors were hindered by cloud cover that prevented regular monitoring at times throughout the year. The vegetation was also a serious hindrance for the plotting of flooded areas (see e.g. Bied-Charreton *et al.*, 1978). In this context, synthetic aperture radar (SAR) constitutes an alternative solution as it can operate "in all weather"

and is sensitive to flooded areas, even when vegetation is present (Henderson & Lewis, 2008). The launching of new very high resolution Radarsat-2 sensors in 2007 generated new ambitions for furthering knowledge about these zones, but studies on the quality of the information are required.

STUDY AREA

The source of the Niger is in the Fouta Djallon mountains in Guinea; the river then flows northeast, crossing the Sahel zone. It subsequently runs southeast to the Gulf of Guinea after flowing for 4200 km. When it crosses Mali, the Niger feeds a huge quantity of water into the IND, one of the most remarkable hydrographic systems in West Africa (Fig. 1). Located in the Sahel zone and covering some 40 000 km², it stretches from Ké-Macina to Timbuktu. The upstream delta (as far as Lake Debo) consists of a set of plains and basins regularly inundated by the floods of the Niger and its tributary the Bani. The downstream delta from Lake Debo to Timbuktu is a very diffuse hydrosystem in a dune/interdune system that limits the flooded areas. The IND slows the annual river flood by about 1–3 months (Batti, 2001) and evaporates about 40% of the flow of the Niger (Mariko, 2003).

A great number of socio-economic issues are related to the size and flood dynamics in the delta, where fishing, farming and grazing alternate according to the annual flooding regime. The IND has a population of over a million people, and crops (rice and sorghum), fisheries (>80% of Malian production) and animal farming are essential to the national economy.

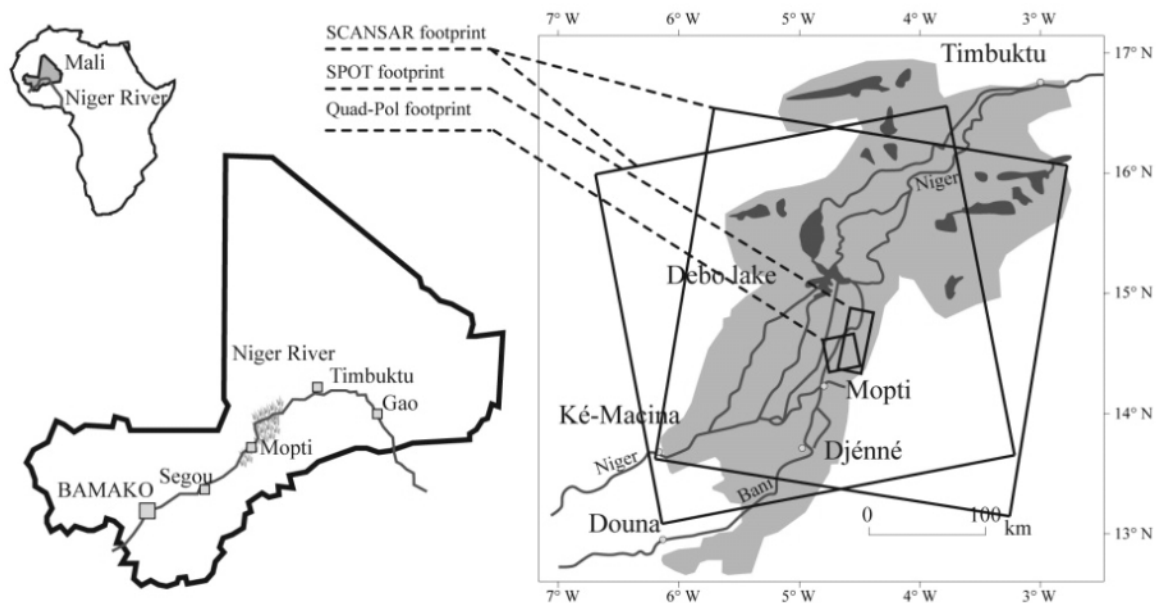


Fig. 1 Location of the Inner Niger Delta in Mali and position of satellite image footprints.

MATERIALS AND METHODS

Satellite images

Ten images from different sensors were acquired for the study (Table 1). Radarsat-2 images were acquired by the SOAR programme (Science and Operational Applications Research for RADARSAT-2) and SPOT images were obtained thanks to the ISIS (*Incitation à l'utilisation Scientifique des Images SPOT*) CNES (*Centre National d'Etudes Spatiales*) programme.

Ground surveys

Ground surveys were used to collect approximately 150 located, described and photographed points during three missions conducted during different hydrological seasons in November 2008, May 2009 and March 2010. Quad-Pol images obtained shortly before each mission were used to locate the reference sites during the survey operations. Each image was first segmented in 16 classes using Whishart's unsupervised polarimetric classification (Lee *et al.*, 1999). All the classes were examined and documented. The field missions were conducted while other Quad-Pol images were being recorded.

Table 1 Satellite images used in the study.

Sensor	Spectral band	Canal	Spatial resolution	Acquisition date	Source	Spatial coverage
Radarsat-2 Quad-Pol	HH	C Band 5.5 cm	11 m	11/11/2008	SOAR	50 × 50 km
	HV			08/04/2009		
	VH			02/05/2009		
	VV			10/11/2009		
				28/12/2009		
				14/02/2010		
				10/03/2010		
		27/04/2010				
SPOT 4	Green –Red –PIR	0.50 – 0.89 µm	20 m	24/04/2009	SPOT image CNES (ISIS)	
SPOT 5	Green –Red– PIR – MIR	0.50 – 1.75 µm	10 m	2/11/2008	SPOT image CNES (ISIS)	60 × 60 km

Classification methods

Radarsat-2 Quad-Pol images The Radarsat-2 Quad-Pol images were processed using the *ESA PolsarPro* program and *ENVI* software using a method synthesised in Fig. 2. The difference in back scattering between the four polarisation methods (HH, HV, VH, VV) of Radarsat-2 is fairly strongly marked (Fig. 2) and varies according to the season. Assessing the flooding dynamics in the IND requires the identification of three types of surface: open water, unflooded land and flooded vegetation. If wind effects are not taken into account, open water is a smooth surface and identified by C-band specular reflection. Its colour is very dark in the image. Unflooded land also has rather dark colours. In contrast, flooded vegetation features strong back scattering and pale colours. The *PolsarPro* program was used to calculate a covariance matrix to provide a complete description of the scatter properties of the target by creating seven derived images (Cloude & Potier, 1996). Processing described by Frost (1982) was then applied to reduce *speckle*, which is an inherent noise in a radar signal that affects radiometric quality (Polidori, 1996). Photo interpretation of the seven images was performed to select those most suitable for the classification of flooded zones according to the season. The images were georeferenced and the training plots surveyed during the field missions were divided into three categories: open water, flooded vegetation and unflooded land. The histograms of these theme plots made it possible to perform the natural setting of thresholds to reduce image dynamics to three classes. Dry season brilliances were very readily differentiated in a single polarisation. Several bands were necessary to reduce high water period images to three classes. The coloured composition was used as a medium for a supervised Mahalanobis classification (1936). Finally, a median filter was applied to smooth the classifications.

HRV SPOT images Prior geometric adjustment was required to work on a 14 km wide strip common to both images. The resampling of the SPOT5 image at the resolution of the SPOT4 image was then performed to homogenise the signal between the images and facilitate comparisons. Identification of open water, flooded vegetation and unflooded land was based on

calculation of the normalised difference vegetation index (NDVI) (Rouse *et al.*, 1973). This index measures chlorophyll activity in the plant cover, even when this is flooded. It is also a good indicator for identifying open water. Each SPOT multispectral image was also reduced to three composite bands representing the first three components of a principal component analysis (PCA,

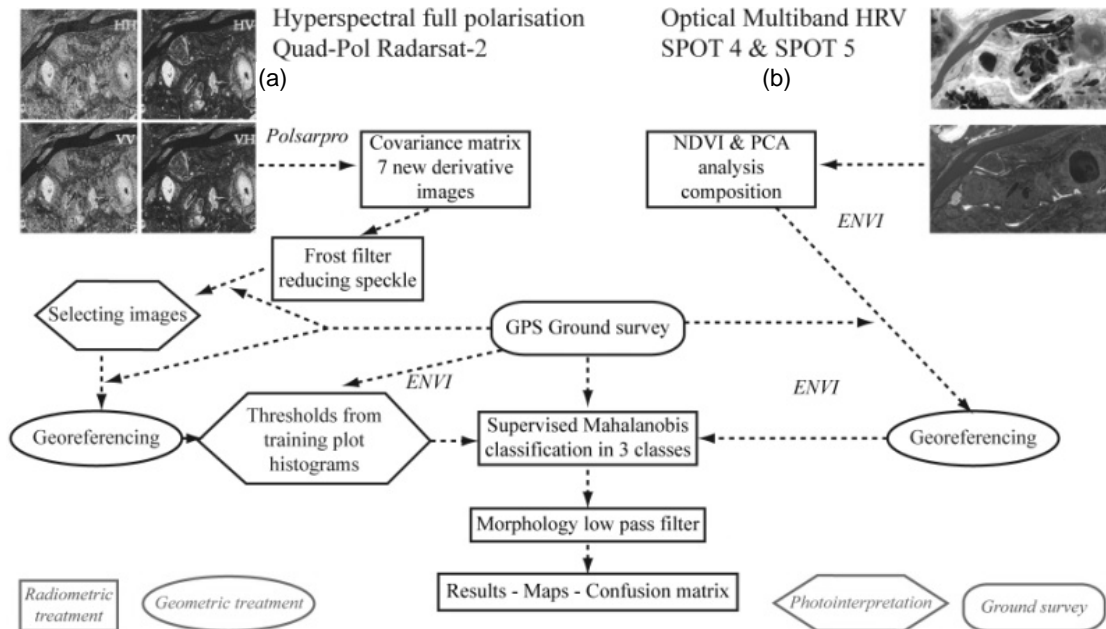


Fig. 2 Treatment methodology: Radarsat-2 Quad-Pol (a) and HRV SPOT (b) images.

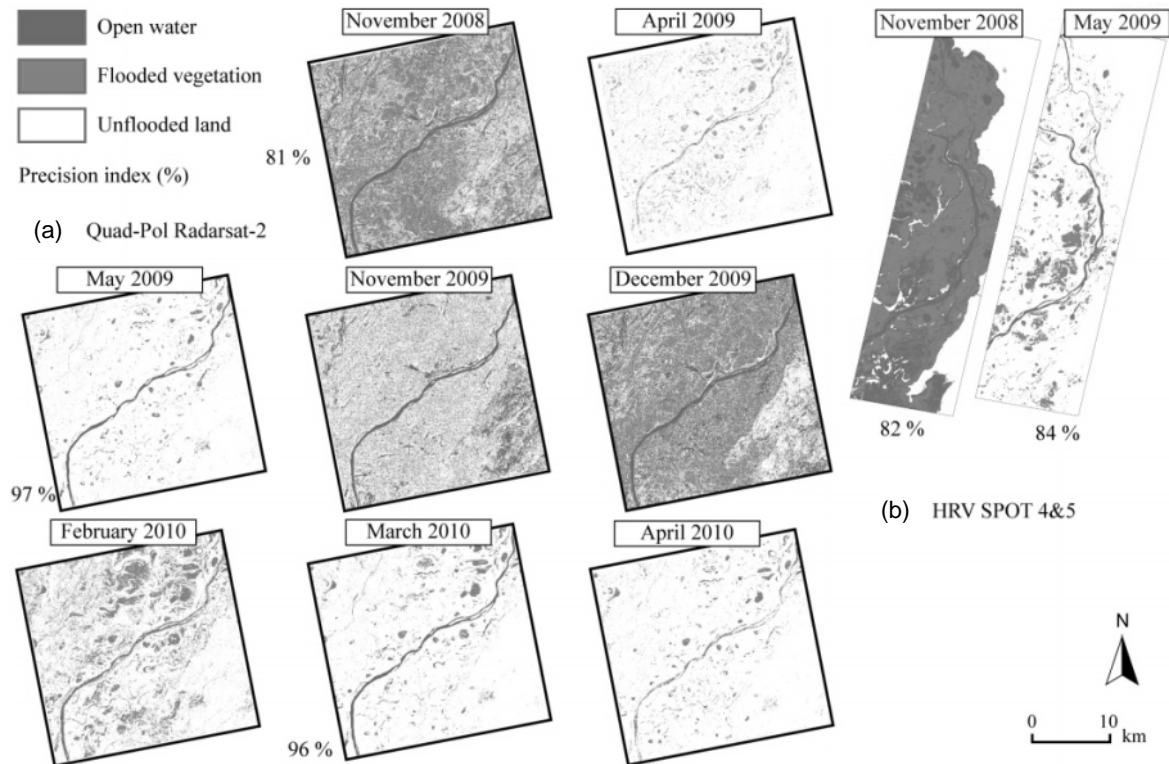


Fig. 3 Monitoring of flooding of the IND from 2008 to 2010 by the classification of (a) Quad-Pol Radarsat-2 images and (b) HRV SPOT 4&5 images.

see e.g. Fung & Ledrew, 1987; Millward *et al.*, 2006). The NDVI for each SPOT image was finally associated with these neochannels using a technique proposed by Ruelland *et al.* (2011).

Plots resulting from the references collected in November 2008 and May 2009 were used for training for a supervised Mahalanobis classification (1936) of the NDVI-PCA combination on the two dates studied. Finally, a median filter treatment was applied to the classifications.

Field data integration and validation The training plots for the date of the images concerned were divided into two samples for processing the Radarsat-2 Quad-Pol images and the SPOT HRV images. One sample was used for classifications and the other for the validation of the results by calculation of confusion matrixes and an index of overall precision.

RESULTS

Overall precision of the classifications of the Quad-Pol images is 81%, 97% and 96%, respectively, for the periods November 2008, May 2009 and March 2010. These results show the quality of the classifications (Fig. 3(a)).

The temporal dynamics of the flood is characterised by a high water period in November 2008, November 2009 and December 2009 and a low water period from February 2010 to April 2010. The classifications are a good reflection of the hydrological regime of the IND. During high water periods, the zone is practically covered by dense flooded vegetation and marshland to which access is difficult. In the dry season, the river flows in its bed and a host of ponds with plants and small channels form a loose mass of water. Open water and flooded vegetation are shown to represent respectively 43% and 22% of the study area in November 2008. The trend is reversed in April and May 2009, with 2.5% open water, 4% flooded vegetation and more than 90% unflooded land. The 2009–2010 hydrological season was monitored in more detail. The flood peaked at the end of December. The proportion of open water was distinctly smaller than it had been in November 2008, but the flooded vegetation was denser. In December, 24% of the area of the image consisted of open water. The fall in the water level took place from January to April with a decrease in the areas of flooded vegetation and open water to low points of 0.3% open water and 3.7% flooded vegetation in April 2010.

The SPOT images were used to monitor flooding of the IND on two dates (Fig. 3(b)): during the flood period (November 2008) and during the dry period (May 2009). The overall precision indexes are 82 and 84%, respectively, for the treatment of these two images. Nearly 50% of the area consisted of flooded vegetation in November 2008 while flooded vegetation plus open water did not exceed 20% in May 2009.

Table 2 Comparison of classifications from Quad-Pol (Radarsat-2) and HRV (SPOT) images.

	November 2008		May 2009	
	Quad-Pol	HRV	Quad-Pol	HRV
Open water (%)	43.6	32.4	2.4	3.2
Flooded vegetation (%)	21.9	49.1	4.4	16.6
Unflooded land (%)	34.5	18.5	93.1	80.2

The flooded areas drawn from the classifications of Quad-Pol and SPOT images were compared (Table 2) in their common coverage on the two common dates. The scales of size are coherent overall, with the differences being greatest for November 2008. The area of flooded vegetation in the SPOT image classification is more than 20% greater than that in the radar image. Conversely, the areas of open water are overestimated in the Quad-Pol classification. As radar is sensitive to ground roughness characteristics and most of the area unflooded in November consists of bare indurated clayey-silty soils, there is confusion between unflooded land and open water. In contrast, confusion between unflooded vegetation and flooded vegetation occurs with the optical

sensor. However, this can be used to distinguish between bare soil and soil with plant cover. A radar signal with a 5.5 cm wavelength is better able to penetrate vegetation than the SPOT-HRV images. This makes it possible to better discriminate flooded vegetation areas from unflooded ones. In May 2009, the areas of open water were equivalent. The area of flooded vegetation indicated by the SPOT image is 12% greater than that of the radar image and, conversely, the area of unflooded land is 13% greater in the radar image.

DISCUSSION AND CONCLUSION

The dynamics of the IND flood characterised here are in agreement with that shown in precedent works (Batti, 2001; Mariko, 2003). The flooded area is 65% greater during the winter period (November–December) while less than 3% of the zone is under water in the dry period (May). These results confirm the considerable impact of the flood on the variation of landscapes in the region and consequently on the remote sensing images studied. The three field missions performed within the framework of the project have been sources of substantial knowledge aimed at ensuring the quality of processing operations. They improved georeferencing, provided training and validation plots and enabled a sensitive approach to the field that is essential for processing.

Radarsat-2 images had never been used to monitor flooding in this zone. It made it possible to overcome meteorological constraints related to dust-bearing mist in the dry season and clouds during the rainy season. The hyperfrequencies reputed to be effective in identifying soil moisture made good results possible for the dry season, especially by means of the precise identification of ponds and islands. With regard to flooded vegetation, radar signals are fully suited to the characterisation of humid zones, as had previously been shown by Henderson & Lewis (2008). Radar imaging has proved its ability to identify flooded vegetation in both the rainy and dry seasons and thus forms a good alternative to optical imaging in this environment.

However, radar also has limits. Surface roughness strongly influences the back scattering of the signal. Waves form on the surface of the Niger when the Harmattan blows in the delta, and modify the specular reflection of the water. Many zones feature indurated bare soil whose roughness is similar to that of a water surface. Optical images also display bias: the angle of incidence, shadows, sun angle, clouds, sandstorms and vegetation on flooded land affect image and classification quality.

The interest of diachronic, multi-source analysis of the flooding of the IND has thus been shown. Two aspects of the complementarity of radar and optical imaging for thematic cartography can be considered. From an operational point of view, the “all weather” feature of radar fills gaps in zones previously plotted using optical images. From a purely thematic point of view, flooded vegetation and bare ground are seen in a very different way by the two types of sensor and this significantly increases the possibility of distinguishing between the two by comparing images. To conclude, radar imaging complements optical imaging within the framework of the monitoring of flooding of the IND.

REFERENCES

- Andersen, I., Dione, O., Jarosewich-Holder, M. & Olivry, J. (2005) *Niger River basin: a Vision for Sustainable Management*. Golitzen, The World Bank, Washington DC, USA.
- Batti, A. (2001) Etude spatio-temporelle par télédétection du cycle crue-décrue dans le delta central du fleuve Niger. Thèse de l'Université Louis Pasteur-Strasbourg I.
- Bied-Charreton, M., Cruette, J., Dandoy, G., Dubee, G., Lamegat, J-P. & Noel, J. (1978) Etude du delta central du fleuve Niger: Projet 'SAPHYR' satellite project hydrology research. In: *Canadian Symposium on Remote Sensing* (Institut aéronautique et spatial du Canada, Ottawa, Canada, Mai 1977), 4, 341–354.
- Blanck, J-P. (1993) Etude diachronique de l'inondation dans le système laguno-dunaire du Bara (Mali) par la crue du Niger en 1973. *Revue de Géomorphologie Dynamique* **XLII**(4), 113–121.
- Cloude, S. R. & Pottier, E. (1996) A review of target decomposition theorems in radar polarimetry. In: *Proc. IEEE Trans. Geoscience and Remote Sensing* (March 1996) **34**(2), 498–518.
- Frost, V. S. (1982) A model for radar images and its application to adaptative digital filtering of multiplying noise. In: *Proc. IEEE Transaction on Pattern Analysis and Machine Intelligence* **4**, 157–165.

- Fung, T. & Ledrew, E. (1987) Application of principal components analysis to change detection. *Photogram. Engng & Remote Sens.* **53**, 1649–1658.
- Henderson, F. M. & Lewis, A. J. (2008) Radar detection of wetland ecosystems: a review. *Int. J. Rem. Sens.* **29**(20), 5809–5835.
- IPCC (2007) *Climate change 2007 – Synthesis Report*. Contribution of Working Groups I, II and III to the Fourth Assessment Report of the Intergovernmental Panel on Climate Change IPCC, Geneva, Switzerland.
- Lee, J. S., Grunes, M. R., Ainsworth, T. L., Du, L. J., Schuler, D. L. & Cloude, S. R. (1999) Unsupervised Classification using Polarimetric Decomposition and the Complex Wishart Distribution. *IEEE Trans Geosci. Remote Sens.* **37**(5), 2249–2259.
- Lemoalle, J., Bader, J.-C. & Leblanc, M. (2008) The variability of Lake Chad: hydrological modeling and ecosystem services. In: *XIIIth World Water Congress* (September 2008, Montpellier, France).
- L'Hôte, Y., Mahé, G., Somé, B. & Triboulet, J. (2002) Analysis of a Sahelian annual rainfall index from 1896 to 2000, the drought continues. *Hydrol. Sci. J.* **47**(4), 563–572.
- Mahalanobis, P. C. (1936) On the generalised distance in statistics. *Proc. Nat. Institute Sci., India* **2**, 49–55.
- Mariko, A. (2003) Caractérisation et suivi de la dynamique de l'inondation et du couvert végétal dans le Delta intérieur du Niger (Mali) par télédétection. Thèse de l'Université Montpellier II.
- Millward, A. A., Piwowar, J. M. & Howarth, P. J. (2006) Time-series analysis of medium-resolution, multisensor satellite data for identifying landscape change. *Photogram. Engng & Remote Sens.* **72**, 653–663.
- Novitzki, R., Smith, R. & Fretwell, J. (1996) Wetland functions, values and assessment. In: *National Water Summary on Wetland Resources*. USGS Water Supply, Washington DC, USA 2425, 79–86.
- Orange, D., Mahé, G., Dembélé, L., Diakité, C., Kuper, M. & Olivry, J.-C. (2002) Hydrologie, agro-écologie et superficies d'inondation dans le delta intérieur du Niger (Mali). Séminaire International: Gestion intégrée des ressources naturelles en zones Inondables Tropicales Bamako, Mali, 20–23 Juin 2000, 209–229.
- Polidori, L. (1996) *Cartographie Radar*. Gordon and Breach Science Publisher, Amsterdam, The Netherlands.
- Rouse, J. W., Haas, R. H., Schell, J. A. & Deering, D. W. (1973) Monitoring vegetation systems in the Great Plains with ERTS. In: *Third ERTS Symposium, NASA SP-351*, 309–317.
- Ruelland, D., Tribotté, A., Puech, C. & Dieulin, C. (2011) Comparison of methods for LUCC monitoring over 50 years from aerial photographs and satellite images in a Sahelian catchment. *Int. J. Remote Sens.* doi:10.1080/01431161003623433.

Evaluation of high-resolution satellite precipitation products for streamflow simulation in Mishui Basin, south China

LILIANG REN¹, SHANHU JIANG¹, BIN YONG¹, XIAOLI YANG¹
& BANG YANG²

¹ State Key Laboratory of Hydrology-Water Resources and Hydraulic Engineering, Hohai University, Nanjing 210098, China
rll@hhu.edu.cn

² Hydrology Bureau of Haihe Water Resources Commission, Tianjin 300170, China

Abstract An attempt was made to evaluate three high-resolution satellite precipitation products (TRMM 3B42V6, 3B42RT and CMORPH) for streamflow simulation in the Mishui basin, south China. Firstly, three satellite precipitation products were compared with the dense raingauged observations at the basin scale from 2003 to 2008. Secondly, satellite precipitation products were used as input into the gridded Xinanjiang model in order to evaluate their hydrological predictive capability. Finally, the authors corrected the systematic bias at monthly and annual time-scales for the two near-real-time 3B42RT and CMORPH products. The direct comparison shows that these three satellite precipitation products perform very well in detecting the occurrence of the precipitation events, while there are some different biases in terms of the quantity of precipitation. 3B42V6 data sets with a bias of -5% fit best with the raingauged observations, while 3B42RT and CMORPH data sets underestimate precipitation by 43% and 41%, respectively, which are much higher than a normal acceptable threshold. The results of the three satellite precipitation products used in streamflow simulation are similar to those of the direct comparison. The behaviour of streamflow simulation from 3B42V6, with a bias of -2% and the daily Nash-Sutcliffe coefficient of 47%, is the optimal amongst the three products. However, it still reveals that the accuracy of daily time-scale distribution of 3B42V6 data sets should provide an increasing possibility to follow the real situation. The 3B42RT and CMORPH data sets produced a larger bias and lower Nash-Sutcliffe coefficient. The correction of monthly-scale bias is better in improving streamflow simulation in the monsoon climatic area than the adjustment of yearly-scale bias with respect to the 3B42RT and CMORPH data.

Key words satellite precipitation product; streamflow simulation; gridded Xinanjiang model; Mishui Basin

INTRODUCTION

Precipitation is a critical element of the global hydrological cycle. Accurate and real-time precipitation data are essential to studying the global hydrological cycle, simulating land surface hydrological processes, and so on (Joyce *et al.*, 2004; Gottschalck *et al.*, 2005; Hong *et al.*, 2007; Yong *et al.*, 2010). During recent years, there have been some global high-resolution satellite precipitation products operationally available, including precipitation estimation from remotely sensed information using artificial neural networks (PERSIANN) (Sorooshian *et al.*, 2000), the Climate Precipitation Center's (CPC) morphing technique (CMORPH) product (Joyce *et al.*, 2004), and the Tropical Rainfall Measuring Mission (TRMM) multi-satellite precipitation analysis (TMPA) products 3B42V6 and 3B42RT (Huffman *et al.*, 2007). These satellite precipitation products have provided quasi-global high-quality precipitation data and attracted vast numbers of hydrologists' interest. However, some of them have large systematic errors. An evaluation of these satellite precipitation products in particular is needed, and further evaluation of the capability of these satellite precipitation products for hydrological prediction is also interesting and important. Specifically, these studies are limited in China. The objective of this study therefore is to evaluate the utility of three commonly-used high-resolution satellite precipitation products, TRMM 3B42V6, TRMM 3B42RT, and CMORPH, for streamflow simulation in the middle-scale Mishui Basin in south China.

STUDY AREA, DATA AND METHODOLOGY

Mishui Basin

The Mishui Basin, a tributary of the Xiangjiang River, is located at the southeast of Hunan Province in south China (Fig. 1). The drainage area upstream of the Ganxi hydrological station, the outlet of

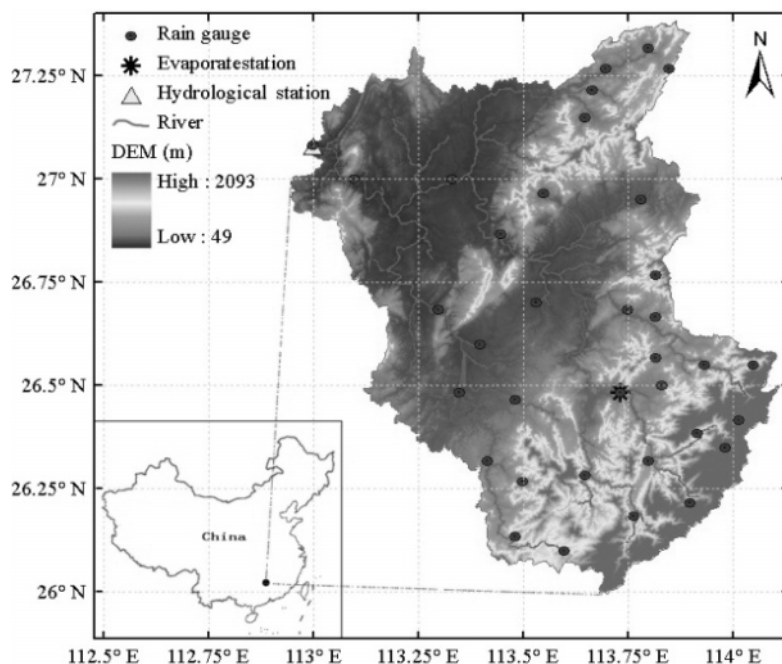


Fig. 1 Location of 35 rain gauge stations, Ganxi hydrological station, Wulipai evaporation station and river network within the Mishui Basin.

the studied basin, is 9972 km². The basin has a humid subtropical monsoon climate. The temporal and spatial distribution of the precipitation within the Mishui Basin is uneven, and most of the annual precipitation occurs from May to September.

Satellite precipitation products

The TRMM 3B42V6 and 3B42RT data are provided by TMPA at 3-h temporal and 0.25° × 0.25° spatial resolution. The 3B42RT data are a near-real-time (about 3–9 h after real time) product while the 3B42V6 data are a post-real-time (about 10–15 d after the end of each month) product, and both of them cover over a global latitude band of 50°NS. The 3B42RT data for the time period since January 2002 are available on the internet, while the 3B42V6 data that we can obtain are from January 1998. The CMORPH technique is a blending technique, and thus it is extremely flexible, such that any precipitation estimates from any microwave satellite source can be incorporated (Joyce *et al.*, 2004). Nowadays, the CMORPH products have two high-resolution versions: one with the same temporal and spatial resolution as TRMM 3B42, and the other with much higher resolutions, 8 km and 30 min, respectively, and both the data covered the area from 60°S to 60°N, globally, beginning in December 2002. In this study, the former CMORPH data was selected.

Hydrological model and observed data

The Xinanjiang model is a famous conceptual hydrological model (Zhao *et al.*, 1980) and it has been successfully and widely used in humid and semi-humid regions in China since its development in the 1970s. In this study, the grid-based Xinanjiang model (Yang, 2010) was applied for runoff computation on each grid cell. Then the discharge series at the hydrological station was obtained by the procedure, taking into consideration hillslope convergence and river network routing, and the model parameters were automatically calibrated by using the Genetic Algorithm method (Holland, 1975).

The gridded Xinanjiang model runs at daily temporal and 1 km × 1 km spatial resolutions from January 2000 to December 2008. The forcing and validation data for the model include precipitation, potential evapotranspiration and streamflow. Observed daily precipitation data from 2000 to 2008 come from 35 rain gauged stations within the Mishui Basin; and for the same-time

period series of daily streamflow and potential evapotranspiration data are collected from Ganxi hydrological station and Wulipai evaporate station, respectively. We used the Inverse Distance Weighting method (IDW; Bartier & Keller, 1996) to obtain the spatial distributed precipitation database within Mishui Basin. The 30 arc-second global digital elevation model (GTOPO30) data were obtained from the US Geological Survey (USGS) and the vegetation type data were obtained from the International Geosphere-Biosphere Programme (IGBP).

Performance statistical indices

To quantitatively evaluate the three satellite precipitation products with the ground-based raingauged observations, three widely-used validation statistical indices, the correlation coefficient (C), relative bias (B), and Nash-Sutcliffe coefficient (C_{NS}) (Nash & Sutcliffe, 1970), and three categories of statistical indices, the probability of detection (P_{OD}), false alarm rate (R_{FA}), and critical success index (I_{CS}), were adopted in our study (for details see Jiang *et al.*, 2010). We also adopted the validation statistical indices of B and C_{NS} to evaluate the hydrological model performance based on the observed and simulated streamflow series.

RESULTS AND DISCUSSION

Comparison of satellite precipitation products

To directly compare the three satellite precipitation products with surface raingauged observations, scatter plots of daily and monthly estimates from the three satellite precipitation products *versus*

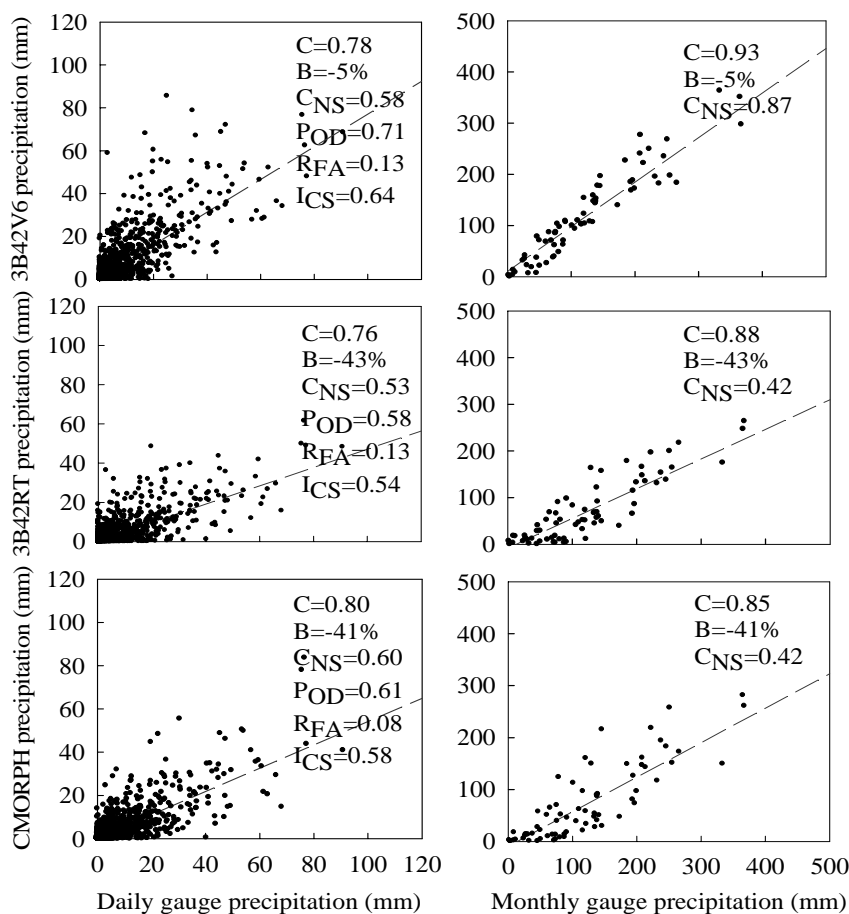


Fig. 2 Scatter plots of raingauged observations vs satellite precipitation products at daily and monthly scales.

raingauged observations for the Mishui Basin are shown in Fig. 2. From the scatter plots, it can be seen that 3B42V6, with a 5% systematic underestimation bias, is much better than 3B42RT and CMORPH, which have 43% and 41% systematic underestimation biases, respectively. The daily P_{OD} and I_{CS} values of 3B42V6 are also much better than those of 3B42RT and CMORPH. CMORPH has the best daily C , C_{NS} and R_{FA} values of 0.80, 0.60 and 0.08, respectively. The values of the three categorical statistics show that all three satellite precipitation products are reasonably good at detecting the precipitation events in the Mishui Basin. Based on the scatter plots analysis, we can infer that 3B42V6, which has incorporated a monthly raingauged data from the Global Precipitation Climatology Project (GPCP) and the World Confederation of Underwater Activities (CMAS), performs a comprehensively better estimation of precipitation than 3B42RT and CMORPH at both daily and monthly scales, and CMORPH shows a little better estimation than 3B42RT at daily scales.

Streamflow simulation of satellite precipitation products

We calibrated the parameters of the gridded Xinanjiang model in the Mishui Basin by using raingauged data from January 2000 to December 2002. Figure 3(a) shows a comparison of the observed discharge with daily values simulated by the gridded Xinanjiang model during the calibration period. Overall, there is a good agreement between the observed and simulated series. The statistical indices which reflect model performance ($C_{NS} = 0.88$ and $B = 3\%$) indicate that the gridded Xinanjiang model can capture key features of the observed hydrograph. Thus we used the calibrated model to verify streamflow simulation from 2003 to 2008. Figure 3(b) demonstrates the comparison of the observed discharge with the daily simulated one. The similar result indicates that there is a good agreement between the observed and simulated results during the verification period as well.

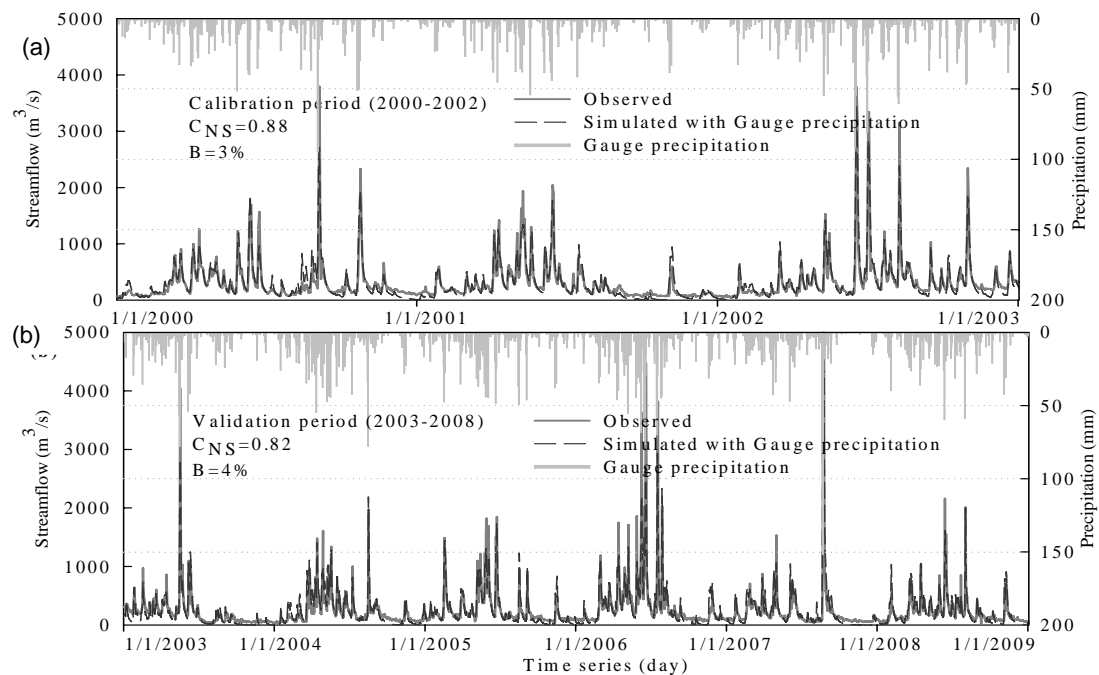


Fig. 3 Observed and simulated streamflow with gauged precipitation for (a) calibration and (b) validation period.

Based on the analysis of the calibration and validation simulations, the model is believed to be suitably robust to evaluate the utility of the satellite precipitation products for streamflow

simulation. The calibrated gridded Xinanjiang model was run by taking those three satellite precipitation products as inputs during the period from 2003 to 2008. From the observed and simulated hydrographs in Fig. 4, it can be seen that the simulation by 3B42V6 data, with a C_{NS} value of 0.47 and B value of -2% , fits best with the observed streamflow series amongst those three products simulations, while the simulation underestimated some high peak flows in rainy seasons and overestimated some low peak flows in dry seasons. The simulation by CMORPH data is slightly better than that by 3B42RT data. Both simulations by 3B42RT and CMORPH data seriously underestimated most of the streamflow series because of their systematic underestimation of the precipitation.

Bias adjustment to 3B42RT and CMORPH data

From the above comparison and streamflow simulation of the two near-real-time satellite precipitation products (3B42RT and CMORPH), we can induce that the large systematic underestimation of precipitation has resulted in the bad performance in streamflow simulation. So, adjustment was made to the monthly and yearly bias of those two near-real-time satellite precipitation products in order to improve their hydrological simulation capability. The detail of the adjustment way is as follows:

$$s_{i-adjusted} = s_i \cdot (\overline{g_i} / \overline{s_i}) \quad (1)$$

where $s_{i-adjusted}$ is the monthly or yearly bias-adjusted satellite precipitation of the i th $0.25^\circ \times 0.25^\circ$ grid cell; s_i represents the satellite precipitation of the i th grid cell; $\overline{g_i}$ and $\overline{s_i}$ are the monthly or yearly gauged and satellite precipitation of the i th grid cell, respectively.

The adjusted satellite precipitation products were used as input to the calibrated gridded Xinanjiang model for streamflow simulation. There is a small improvement in terms of C_{NS} value, 0.40 for 3B42RT and 0.41 for CMORPH, respectively, but a significant amelioration in terms of bias value, increasing from -54% to 6% for 3B42RT, and from -52% to 5% for CMORPH, respectively, if compared to results shown in Fig. 4(b), when a yearly-scale bias was adjusted with respect to the two near-real-time satellite precipitation products. Figure 5 demonstrates that the 3B42RT and CMORPH data sets produce higher values of C_{NS} 0.50 and 0.60, respectively, while the bias values remain the same if compared to the case of the yearly-scale bias adjustment, as the monthly-scale bias was adjusted for use in streamflow simulation.

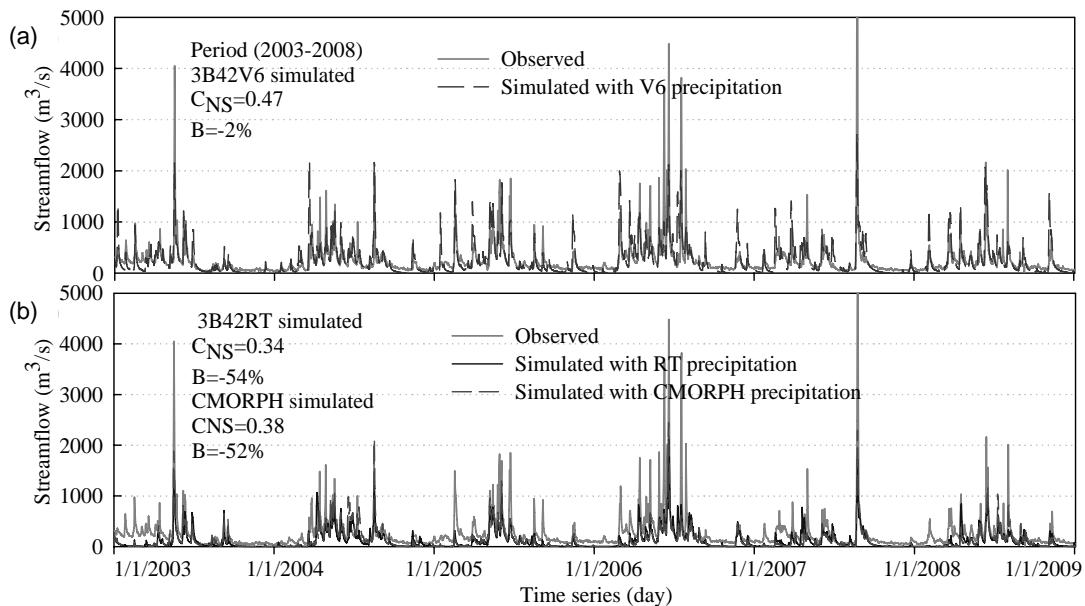


Fig. 4 Observed and simulated streamflow with satellite precipitation products from 2003 to 2008.

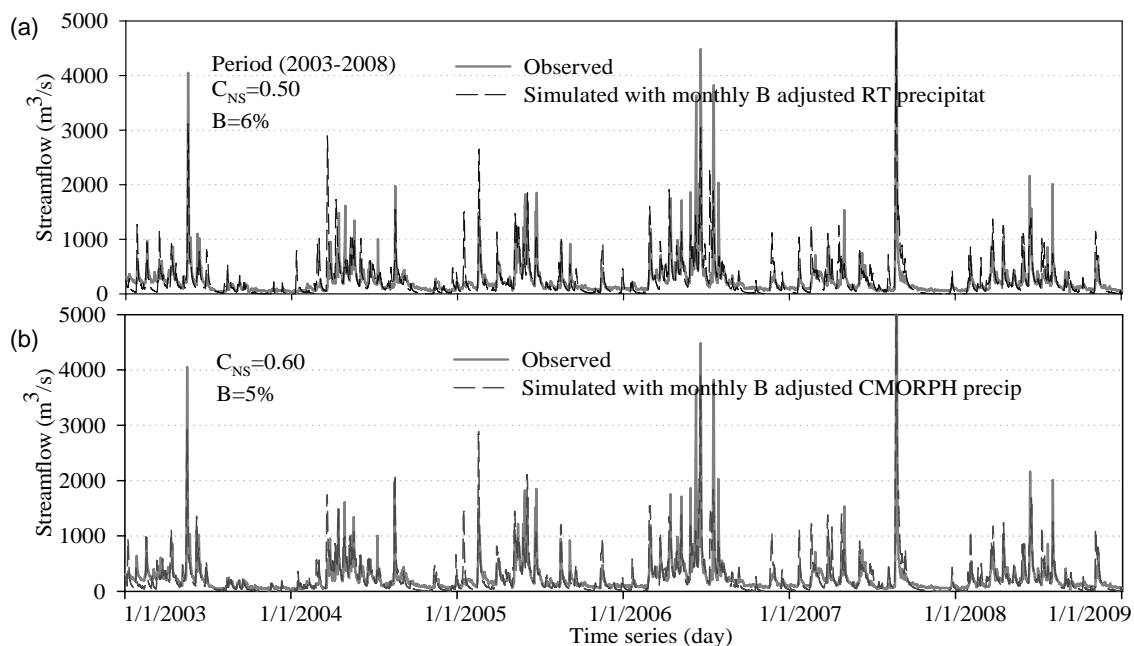


Fig. 5 Observed and simulated streamflow with monthly bias-adjusted (a) 3B42RT and (b) CMORPH precipitation products.

CONCLUSIONS

In this study three high-resolution satellite precipitation products (TRMM 3B42V6, 3B42RT and CMORPH) were evaluated for streamflow simulation within the Mishui Basin, south China. The above analyses support the following conclusions. The direct comparison shows that the 3B42V6 data set fits best with the raingauged observation with a bias of -5% , while the 3B42RT and CMORPH data sets have a large underestimation of precipitation. The evaluation of hydrological predictive capability demonstrates that the streamflow modelling resulting from 3B42V6 data is the best amongst those three products with a bias of -2% and daily C_{NS} of 47% , and 3B42RT and CMORPH data produce larger absolute biases and lower C_{NS} . The correction of monthly-scale bias is better in improving streamflow simulation in the monsoon climatic area than the adjustment of yearly-scale bias with respect to the 3B42RT and CMORPH data.

Three satellite precipitation products have good potential in hydrological simulation in the Mishui Basin, but there are some large errors for the near-real-time products (3B42RT and CMORPH). The bias adjustment for the near-real-time satellite precipitation products is necessary. Although the bias-adjusted method is still imperfect and is some distance away from a near-real-time application for the bias-adjusted program (usually at a monthly scale), the bias adjustment presented in this study has a signal improvement over the near-real-time satellite products for streamflow simulation within the Mishui Basin. Therefore, more studies should be made in the future to develop better near-real-time bias-adjustment or assimilation methods.

Acknowledgements This study is financially supported by the Innovative Research Team Project of the State Key Laboratory of Hydrology-Water Resources and Hydraulic Engineering (grant no. 2009585412), the Special Basic Research Fund by the Ministry of Science and Technology, China (grant no. 2009IM020104), the Special Research Funds for Public Welfare by Ministry of Water Resources, China (grant no. 2008001), the Programme of Introducing Talents of Discipline to Universities by the Ministry of Education and the State Administration of Foreign Experts Affairs, China (the 111 Project, grant no. B08048), and the Fundamental Research Funds for the Central Universities (grant nos. 2010B13614 and 2009B11614).

REFERENCES

- Bartier, P. M. & Keller, C. P. (1996) Multivariate interpolation to incorporate thematic surface data using inverse distance weighting (IDW). *Computer and Geosciences* **22**(7), 795–799. doi:10.1016/0098-3004(96)00021-0.
- Gottschalck, J., Meng, J., Rodell, M. & Houser, P. 2005. Analysis of multiple precipitation products and preliminary assessment of their impact on Global Land Data Assimilation System land surface states. *J. Hydromet.* **6**(5), 573–598.
- Holland, J. H. (1975) *Adaptation in Natural and Artificial Systems*. University of Michigan Press, Ann Arbor, Michigan, USA.
- Hong, Y., Adler, R. F., Hossain, F., Curtis, S. & Huffman, G. J. (2007) A first approach to global runoff simulation using satellite rainfall estimation. *Water Resour. Res.* **43**(8), W08502. doi:10.1029/2006WR005739.
- Huffman, G. J., Adler, R. F., Bolvin, D. T., Gu, G., Nelkin, E. J., Bowman, K. P., Hong, Y., Stocker, E. F. & Wolff, D. B. (2007) The TRMM multi-satellite precipitation analysis (TMPA): Quasi-global, multi-year, combined-sensor precipitation estimates at fine scales. *J. Hydromet.* **8**(1), 38–55. doi: 10.1175/JHM560.1.
- Joyce, R. J., Janowiak, J. E., Arkin, P. A. & Xie, P. (2004) CMORPH: a method that produces global precipitation estimates from passive microwave and infrared data at high spatial and temporal resolution. *J. Hydromet.* **5**(3), 487–503.
- Jiang, S. H., Ren, L. L., Yong, B., Yang, X. L. & Shi, L. (2010) Evaluation of high-resolution satellite precipitation products with surface raingauged observations from Laohahe Basin in northern China. *Water Sci. & Engng* **3**(4), 405–417. doi:10.3882/j.issn.1674-2370.2010.04.004.
- Nash, J. E. & Sutcliffe, J. V. (1970) River flow forecasting through conceptual models, Part 1: a discussion of principles. *J. Hydrol.* **10**(3), 282–290. doi:10.1016/0022-1694(70)90255-6.
- Sorooshian, S., Hsu, K. L., Gao, X., Gupta, H., Imam, B. & Braithwaite, D. (2000) Evaluation of PERSIANN system satellite-based estimates of tropical rainfall. *Bull. Am. Met. Soc.* **81**(9), 2035–2046. doi:10.1175/1520-0477(2000)081<2035:EOPSSE>2.3.CO;2.
- Yong, B., Ren, L. L., Hong, Y., Wang, J. H., Gourley, J. J., Jiang, S. H., Chen, X. & Wang, W. (2010) Hydrologic evaluation of TRMM standard precipitation products in basins beyond its inclined latitude band: a case study in Laohahe Basin, China. *Water Resour. Res.* **46**, W07542. doi:10.1029/2009WR008965.
- Yang, B. (2010) Distributed hydrological modeling approach to flood forecasting and application in small and middle scales of catchments. PhD Dissertation. Hohai University, Nanjing, China (in Chinese).
- Zhao, R. J., Zhang, Y. L., Fang, L. L., Liu, X. R. & Zhang, Q. S. (1980) The Xinanjiang model. In: *Hydrological Forecasting* (Proc. Symp. on the Application of Recent Developments in Hydrological Forecasting to the Operation of Water Resource Systems) (Oxford, 1980), 351–356. IAHS Press, Wallingford, UK

Altimeter-derived soil moisture determination – global scope and validation

PHILIPPA A. M. BERRY¹ & JOHN CARTER²

¹ De Montfort University, EAPRS Lab, Faculty of Technology, Leicester LE1 9BH, UK
pamb@dmu.ac.uk

² Queensland Climate Change Centre of Excellence, Department of Environment and Resource Management, Ecosciences Precinct, 41 Boggo Rd. Dutton Park 4102, Australia

Abstract The SMOS mission offers the exciting potential for global soil surface moisture data; earlier soil moisture estimates are available from several remote sensing techniques, but these encounter difficulties in arid regions. However, there is one technique that can yield soil moisture estimates in arid areas globally: satellite radar altimetry. This novel approach involves the construction of detailed Dry Earth Response (DER) models using multi-mission altimeter backscatter measurements, to encapsulate the high frequency spatial variation in the Earth's response to Ku band nadir illumination. This removes the requirement for detailed surface geophysical data and allows the derivation of soil surface moisture. This technique has now been validated over two regions of Australia, the Western Desert and the Simpson Desert, using ground truth from the AussieGRASS model run by the Queensland Climate Change Centre. This paper presents the quantitative results from this validation and assesses the global scope of this novel technique.

Key words soil moisture; satellite altimetry; arid regions

INTRODUCTION

A number of remote sensing techniques are currently utilized to yield soil moisture estimates of varying spatial and temporal resolutions and accuracies, including scatterometry (Bartalis *et al.*, 2007) and Synthetic Aperture Radar, SAR (Barrett *et al.*, 2009); however, these techniques encounter difficulties in arid and semi-arid regions (*ibid*). This paper presents validation results from a novel technique using satellite radar altimetry to derive accurate profiles of surface soil moisture under the satellite track.

Altimeters illuminate the surface at nadir with a series of chirped pulses (the primary frequencies are at Ku band, 10.9–22 GHz), and record the returned echoes, acquiring the echo shape and measuring the surface brightness, σ_0 . Whilst they provide profiles of information under the satellite track rather than the spatial coverage of, for example, SAR scenes, the complexity of the equations relating σ_0 to surface characteristics is reduced by the nadir angle of illumination. These equations still require such detailed knowledge of the surface that an analytical solution necessitates either ground truth or series of assumptions about the surface roughness and composition. However, there is an alternative approach, made possible because the surface is illuminated at nadir; to use existing altimeter datasets to make detailed empirically-based surface models.

DATASETS

In this paper, data from ERS1 and ERS2 (Capp, 2001) are used for model building; data from EnviSat RA2 Ku band are also utilised (Benveniste, 2002). These altimeter missions orbit the Earth in a 35-day repeat cycle, acquiring data with global sampling but not global coverage, and retrieving echoes at roughly 330 m intervals along-track. The repeat cycles pass over the same ground track, within the orbit tolerance of ± 1 km. Because instrument characteristics vary, data from different missions/modes of operation must be cross-calibrated; the only absolute σ_0 calibration that has been performed is for EnviSat (Roca *et al.*, 2000).

For this study, data from ocean and ice modes of operation of ERS1 and ERS2, and ocean mode from EnviSat were included. σ_0 was recalculated from the waveform shape and engineering parameters, and previously determined σ_0 cross-calibration offsets were used (Berry *et al.*, 2000) to bring all data into a common frame of reference.

INITIAL INVESTIGATION

The altimeter surface backscatter as seen in Ku band varies in a complex and intricate way over the Earth’s land surfaces, responding both to the surface roughness and composition on a range of spatial scales, and to the changing surface moisture. To investigate this variation, a series of repeat passes from both ERS1/2 and EnviSat (Ku band) were examined over desert surfaces where the moisture component is less of a factor. For illustration, Fig. 1 shows a series of repeat passes of EnviSat over part of the Simpson Desert. Here, the most obvious change is due to an increase in surface moisture following a rain event (the high track) acquired on 24 May 2004. Waveform analysis indicates the presence of standing surface water in part of this track, and saturated surface elsewhere.

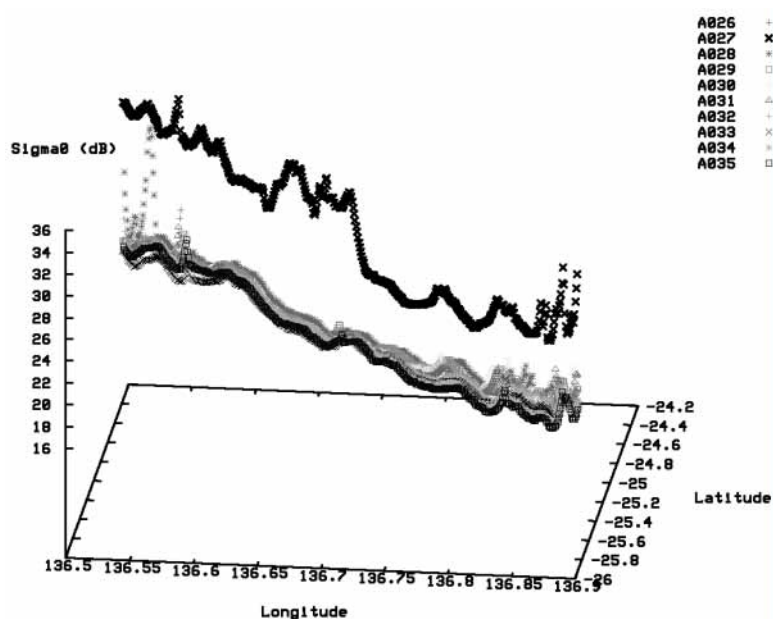


Fig. 1 Repeat passes of EnviSat (Ku band) over the Simpson Desert, showing ephemeral water and soil moisture signal.

The 3-D plot also reveals that the fine-scale sigma0 changes do not precisely align from track to track. The across-track repeat location changes of up to ± 1 km result in small changes to the features in the profiles and migrations in position across adjacent profiles. The primary reason for this is that land (apart from water and salar surfaces) is a relatively poor reflector of Ku band energy, and this limits the spatial extent of the surface footprint contributing to the returned echoes, allowing even small changes in satellite position to affect the returned power.

To develop this approach, the Simpson Desert was chosen as the primary test area. This region is characterized by sand heaped into parallel ridges, 5–35 m high, up to 200 km long and running in a north–northwest/south–southeast direction. Between sand dunes are clay pans that retain surface water after rainfall events. The alignment of the dune systems, the micro-topography of the dunes and soil texture changes between dune and inter-dune complicate the spatial and temporal patterns of the return signal. The consistency of a nadir-only view allows the resolution of several of these problems. However, deriving a theoretical model to calculate soil moisture is unlikely to be effective for practical application, since information on the surface roughness and composition would be required in such detail as to preclude this technique being successfully applied unless dedicated ground surveys had been carried out. In order to utilise altimeter sigma0 for soil moisture estimates, a different approach must be adopted. The key is to develop empirical “dry earth models”.

MODEL DEVELOPMENT

The existing multi-mission altimeter data can be utilised to form a detailed σ_0 model of the surface at (or close to) zero soil moisture. Then the moisture can be estimated from the σ_0 difference (measured – “dry earth” model). In order to create spatial models of σ_0 , all environmental contamination must be removed from the data and the individual tracks reconciled with each other. Key to the practical application of this approach is the ERS1 Geodetic Mission dataset, which provided a closely spaced network of tracks (with mean across-track spacing of 4 km at the equator) providing a powerful constraint on the model development. The required steps are as follows:

- (1) Filter out environmental events.
- (2) Reconcile remaining data and migrate close to zero soil moisture.
- (3) Grid to form model.

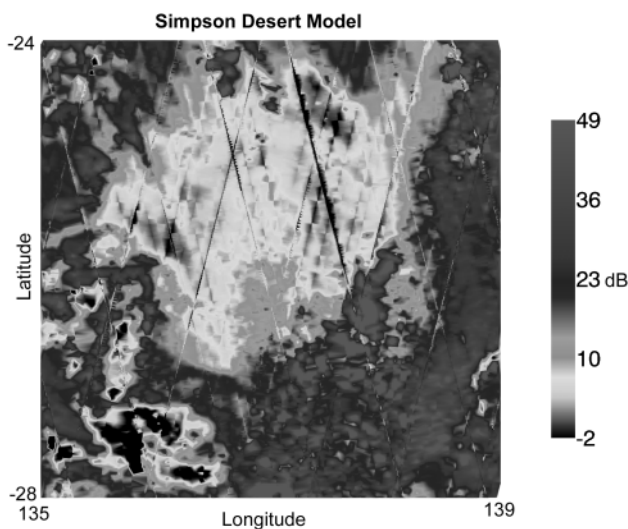


Fig. 2 σ_0 for the Simpson Desert (dB), cross-calibrated to ERS1 values.

However, this model is still not adequate to fully represent the short wavelength variation in σ_0 . In order to optimise the solution, a further step is therefore required: to use at least one year of altimeter data from the repeat mission of ERS2 to populate the model densely along the satellite ground tracks, and thus enhance the short wavelength information content prior to interpolation. In order to combine these data, cross-calibration offsets must be applied (*ibid*) to bring the σ_0 values from the two missions into a common frame of reference. Figure 2 shows the resulting model for the Simpson Desert, with gradually changing σ_0 model values over the central Simpson Desert, and more rapid variation over the large dunefields in the lower left part of the model. Several satellite tracks from one cycle of ERS2 are not yet fully reconciled in the current model; these will be aligned in the final version.

VALIDATION OF ALTIMETER SOIL MOISTURE

The arid nature of much of Australia makes it ideally suited for investigating altimeter σ_0 variation and creating “dry earth” models. In order to validate the technique, it was therefore decided to use two test areas; the Simpson desert for initial calibration and testing, and the whole of the Western desert. A model was created for the Western desert, a huge area encompassing different terrain types and varying surface roughness. Areas identified as salt pans were masked from this model, because very high salt content reduces the response of the real part of the

dielectric constant to changes in soil moisture. River systems were also excluded (Berry & Benveniste, 2010). Taking the difference between the model σ_0 and the observed value then allows a first estimate of predicted soil moisture to be calculated from the altimeter σ_0 by fitting a function of exponential form to the σ_0 differences, and this was done for the entire ERS2 mission for both areas. The resulting estimates of soil moisture then require validation.

The AussieGRASS model was used for soil moisture validation. AussieGRASS (Australian Grassland and Rangeland Assessment by Spatial Simulation) (Carter *et al.*, 2000) is a daily time step plant growth and water balance model driven by daily gridded climate data (Jeffrey *et al.*, 2001) at a spatial resolution of 0.05 degrees geographic. Model simulations of soil moisture in the top 10 cm of the profile were used to compare with altimeter derived soil moisture. For comparison with AussieGRASS, Fig. 3 shows the two test areas selected, with the EnviSat 35 day σ_0 from one cycle plotted to illustrate the altimeter coverage.

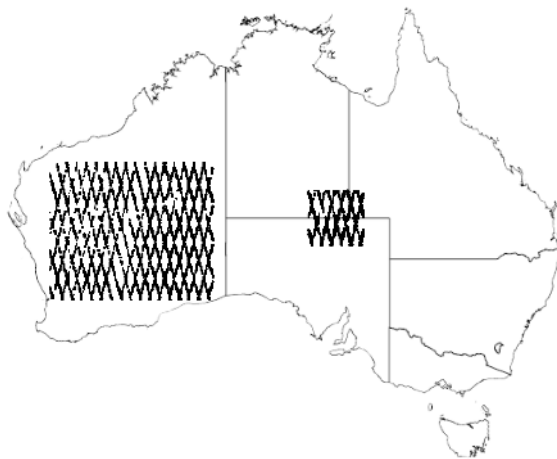


Fig. 3 Australian validation areas for AussieGRASS comparison showing 35 day track locations from ERS2.

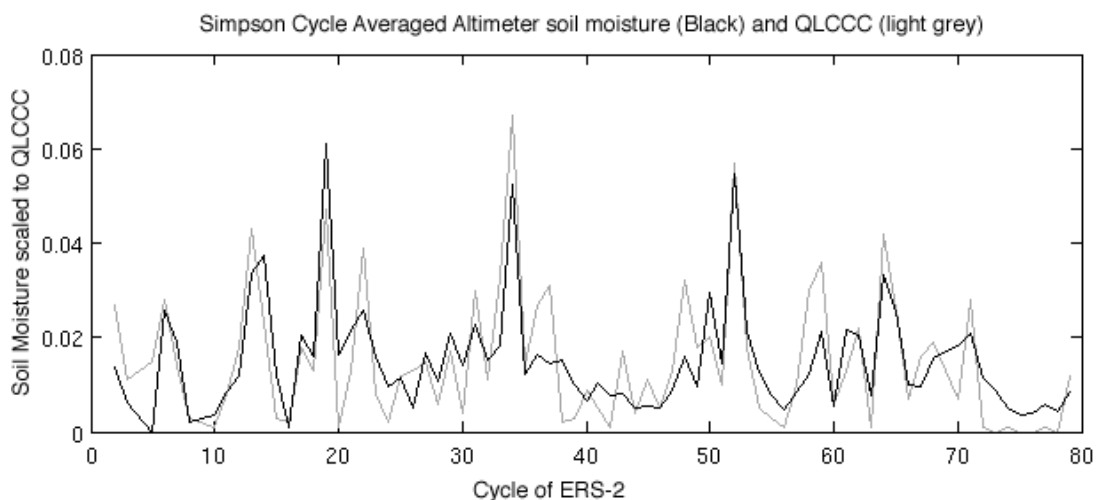


Fig. 4 Cycle based comparison over Simpson Desert of AussieGRASS model (grey) and altimeter soil moisture (black) from ERS2.

Note that the models are currently referenced to ERS1 σ_0 values. Applying the σ_0 offsets, estimated moisture values were calculated for each altimeter point, and the corresponding pixel from the AussieGRASS model was found. For first comparison, these altimeter moisture

values were then meaned for all points in each 35 day cycle to generate a single value per cycle, and the same procedure was followed for the corresponding pixels of the AussieGRASS model, to give the result over the Simpson desert (Fig. 4) and the Western desert (Fig. 5).

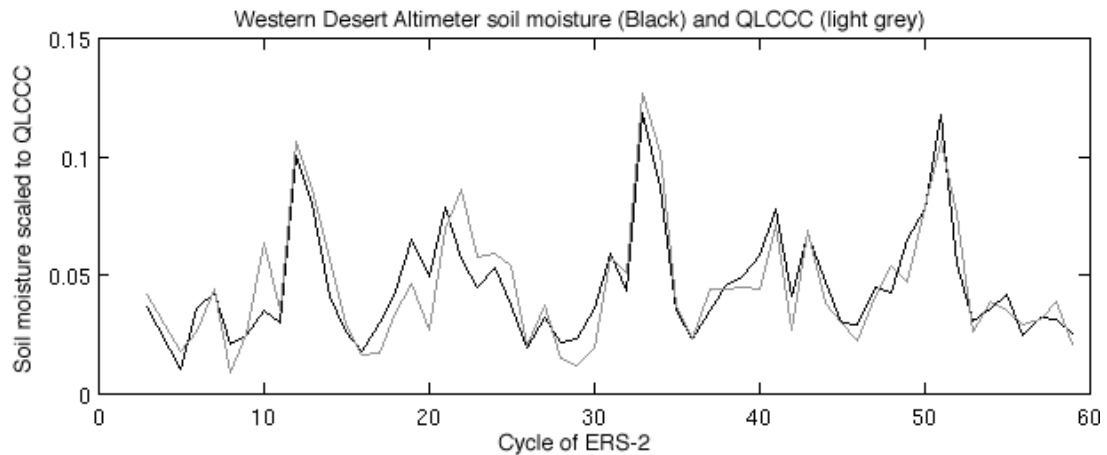


Fig. 5 Cycle based comparison over Western Desert of AussieGRASS model (light grey) with altimeter soil moisture from ERS2 (black).

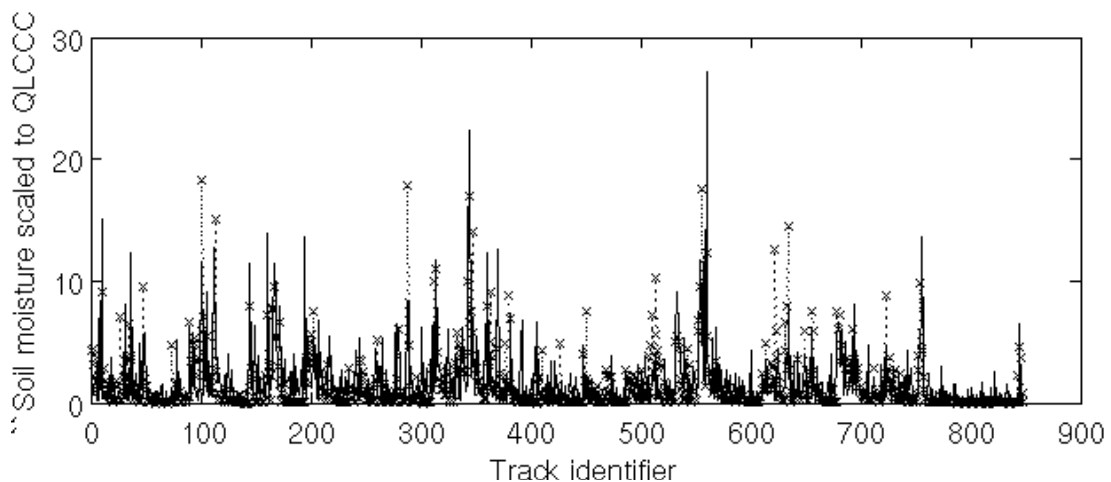


Fig. 6 Track comparison of ERS2 soil moisture (solid line) with AussieGRASS (dotted line) for the Simpson Desert.

The next step was to reduce the amount of averaging. As the first part of this, the average soil moisture was calculated for each track instead of each cycle; the first result for the Simpson Desert is shown in Fig. 6.

Here, good agreement is seen between the two datasets with deviations partially due to the very low raingauge density in these regions limiting the accuracy of the simulated water balance.

DISCUSSION

The next step in the comparison with AussieGRASS data is to reduce the spatial averaging, which is currently giving a single value for the entire track, in order to determine the minimum extent of spatial averaging required to produce meaningful results that can inform development and validation of the satellite altimeter soil moisture estimates. In parallel with this, dry earth models

for additional desert areas are being developed; to date, models have been produced for the Sahara and Arabian deserts. Further desert and semi-arid regions, including the Kalahari Desert, are now being modelled for this work. The Kalahari Desert is of particular interest, as this would allow comparison over a wider range of soil moisture conditions.

With the very successful initial results from the soil moisture comparison with ERS2 data and the AussieGRASS model, it is now intended to apply this technique for the whole ERS2 altimeter dataset and the subsequent EnviSat (Ku band) dataset to generate 15-year time series of soil moisture measurements (possible because ERS2 and EnviSat were in the same orbit repeat pattern, providing continuous measurements for this period) over a number of different desert and semi-arid regions.

Acknowledgements The authors wish to thank the European Space Agency for supply of data for this work.

REFERENCES

- Barrett, B. W., Dwyer, E. & Whelan, P. (2009) Soil moisture retrieval from active spaceborne microwave observations: an evaluation of current techniques. *Remote Sens.* **1**, 210–242.
- Bartalis, Z., Wagner, W., Naeimi, V., Hasenauer, S., Scipal, K., Bonekamp, H., Figa, J. & Anderson, C. (2007) Initial soil moisture retrievals from the METOP-A Advanced Scatterometer (ASCAT). *Geophys. Res. Lett.* **34**, L20401.
- Benveniste, J. (ed.) (2002) *ENVISAT RA-2/MWR Product Handbook, Issue 1.2*. PO-TN-ESR-RA-0050, European Space Agency.
- Berry, P., Pinnock, R. & Wilson, H. (2000) Land calibration and monitoring of EnviSat RA-2 sigma0. In: *Looking Down to Earth in the New Millennium* (ERS-EnviSat Symposium, Gothenburg, Sweden, October 2000). http://earth.esa.int/pub/ESA_DOC/gothenburg/142berry.pdf.
- Berry, P. A. M. & Benveniste, J. (2010) Measurement of inland surface water from multi-mission satellite radar altimetry: sustained global monitoring for climate change. *Int. Assoc. Geodesy Symposia* **135**, 221–230.
- Capp, P. (2001) *Altimeter Waveform Product ALT.WAP Compact User Guide, Issue 4.0*. PF-UG-NRL AL-0001, Infoterra Ltd., UK.
- Carter, J. O., Hall, W. B., Brook, K. D., McKeon, G. M., Day, K. A. & Paull, C. J. (2000) Aussie GRASS: Australian grassland and rangeland assessment by spatial simulation. In: *Applications of Seasonal Climate Forecasting in Agricultural and Natural Ecosystems – the Australian Experience* (ed. by G. Hammer, N. Nicholls & C. Mitchell), 329–250. Kluwer Academic Press, The Netherlands.
- Jeffrey, S. J., Carter, J. O., Moodie, K. B. & Beswick, A. R. (2001) Using spatial interpolation to construct a comprehensive archive of Australian climate data. *Environ. Modelling and Software* **16**(4), 309–330.
- Roca, M., Francis, R., Zelli, C., Laxon, S. & Jackson, H. (2000) RA-2 absolute range and sigma0 calibration and in-flight verification. *European Space Agency (Special Publication). ESA SP* **461**, 2310–2326.

Satellite-based estimates of vegetation density over Australia during 1988–2008

YI LIU^{1,2,4}, RICHARD DE JEU², MATTHEW McCABE¹, JASON EVANS³ & ALBERT VAN DIJK⁴

1 School of Civil and Environmental Engineering, University of New South Wales, Sydney 2052, Australia
yi.liu@student.unsw.edu.au

2 Department of Hydrology and Geo-Environmental Sciences, Faculty of Earth and Life Sciences, Vrije Universiteit Amsterdam, De Boelelaan 1085, Amsterdam, 1081 HV, The Netherlands

3 Climate Change Research Centre, University of New South Wales, Sydney 2052, Australia

4 Black Mountain Laboratory, CSIRO Land and Water, GPO Box 1666, Canberra, Australian Capital Territory 2601, Australia

Abstract Vegetation density plays an important role in the water and energy balance. Satellite based passive microwave instruments have shown an ability to monitor the total above-ground vegetation biomass at global scales. A recently developed approach to retrieving vegetation optical depth (VOD, an index of vegetation density) from microwave emissions can be used for all bands in the microwave domain, allowing data collected by different satellites (e.g. Special Sensor Microwave/Imager (SSM/I from middle 1987), Tropical Rainfall Measuring Mission (TRMM) Microwave Imager (TMI from 1998) and Advanced Microwave Scanning Radiometer – Earth Observing System (AMSR-E from middle 2002)) to yield a long-time series. However, differences in measurement specifications prevent merging the data directly. Here we develop a merged product by adjusting SSM/I and TMI products against the reference sensor (AMSR-E) using the cumulative distribution frequency matching approach. Results of Mann-Kendall trend analysis on the merged VOD product during 1988–2008 show that northwest Australia experienced considerable increases in vegetation density, whereas southeast Australia experienced considerable declines. Gridded rainfall and temperature products were used to assess climate induced changes during the study period over Australia. By performing multiple linear regression analysis over varying periods of precipitation, temperature and annual maximum monthly VOD, we identify the proportion of VOD change that is explained by precipitation and temperature, and distinguish the contribution of natural climate from human activities on the long-term change. Expanding analysis to the global scale along these lines should increase our understanding of the natural and anthropogenic impacts on terrestrial hydrology and vegetation dynamics.

Key words vegetation density; passive microwave; long term

INTRODUCTION

The Normalized Difference Vegetation Index (NDVI), derived from the Advanced Very High Resolution Radiometer (AVHRR) series of satellites (first launched in 1981), is a commonly used satellite-based long-term vegetation greenness product (Tucker *et al.*, 2005). It can provide a relatively high spatial resolution product (up to 1 km), but is affected by the atmosphere and clouds, and is limited to monitoring the canopy level. Satellite-based passive microwave instruments have shown an ability to monitor the total above-ground vegetation biomass at global scales, albeit at relatively coarse spatial resolution (>10 km) (Shi *et al.*, 2008). The advantages of microwave-based approaches are the near all-weather retrieval capacity and deeper penetration capacity into the canopy. Therefore NDVI and passive microwave vegetation products are expected to be complementary and provide more reliable vegetation information when combined.

However, there is no consistent and continuous satellite-based passive microwave program covering the period comparable with AVHRR. A recently developed approach to retrieve vegetation information from microwave emissions can be used for all bands in the microwave domain (Owe *et al.*, 2008), allowing data collected by different satellites to yield a long-term time series of vegetation optical depth (VOD, a measure of vegetation density). However, differences in measurement specifications of different satellites prevent merging the data directly.

The objective of this paper is three-fold. First, to develop a method to merge the currently available passive microwave vegetation products into one long-term data set over Australia. Second, to detect the long term change in vegetation density using the merged product, and finally to distinguish the climate or human-induced causes of long-term changes.

DATA

Vegetation Optical Depth – VOD

The VOD products used in this analysis are VU Univeristy Amsterdam – NASA (VUA-NASA) passive microwave products derived from different instruments (Owe *et al.*, 2008). Characteristics of these datasets are listed in Table 1. All vegetation products were re-sampled to 0.25° and daily interval.

Monthly average VOD from AMSR-E, TMI and SSM/I for March and September 2003 are shown in Fig. 1. All products show similar spatial and temporal patterns. High values are always observed over forests along the eastern coast. Over northern Australia, values are higher in March; over the south, values are higher in September, which are in line with rainfall seasons.

Table 1 Comparisons of major characteristics of passive microwave instruments used in this study.

	SSM/I	TMI	AMSR-E
Platform	DMSP F8, F11, F13	TRMM	AQUA
Time series used	Jan. 1988–Dec. 2007	Jan. 1998–Dec. 2008	Jul. 2002–Dec. 2008
Channel used (GHz)	19.3	10.7	6.9
Spatial resolution (km*km)	69*43	59*36	76*44
Spatial coverage	Global	38°N to 38°S	Global
Approximate equatorial crossing time	F8: ascending, 0630; F11/13: descending, 0630	Completing an orbit every 91 mins, 15.7 orbits per day	Descending, 0130

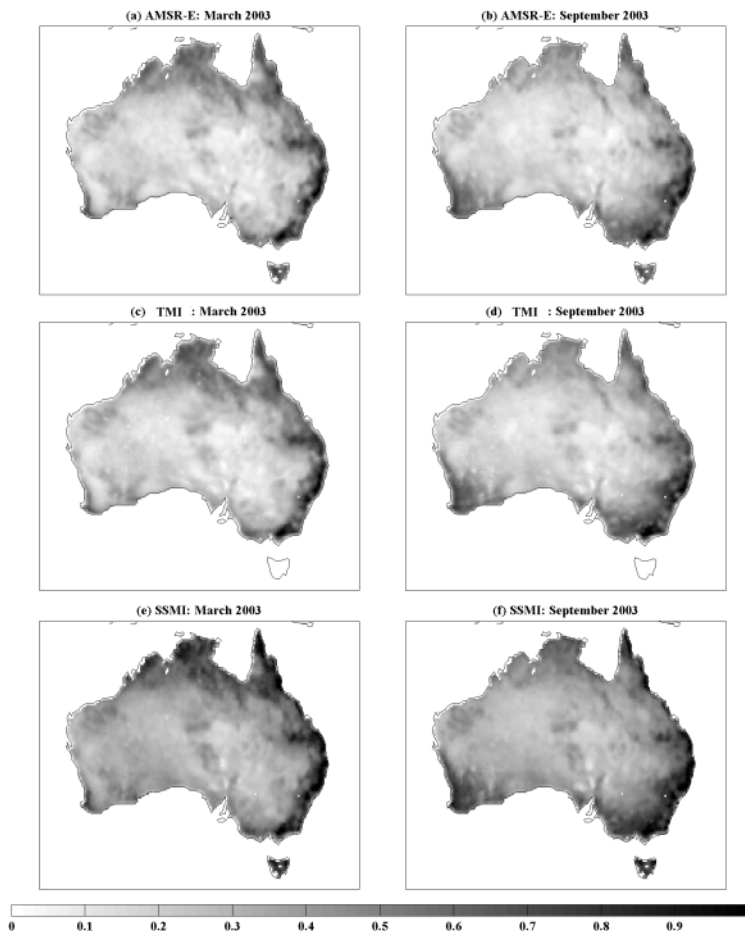


Fig. 1 Monthly average vegetation density (via optical depth) for March and September 2003 derived from (top) AMSR-E, (middle) TMI and (bottom) SSM/I.

Precipitation and temperature

To distinguish the effects of climate and human factors on long-term change in vegetation density, the gridded daily rainfall and maximum and minimum temperature data for Australia for the same period were also included in the analysis. Gridded climate data across Australia were interpolated from point observations by the Bureau of Meteorology (BoM) National Climate Centre (NCC) for the Australian Water Availability Project (Jones *et al.*, 2009). The average of daily maximum and minimum temperature was used in this analysis (referred to as mean temperature). The original 0.05° resolution gridded rainfall and mean temperature were re-sampled into 0.25° resolution to allow direct comparison.

METHODS AND RESULTS

Rescaling and merging

Although VOD values retrieved from different instruments have different absolute values (see Fig. 1), they show similar temporal patterns. Compared with SSM/I and TMI, AMSR-E has a comparatively low measuring frequency (6.9 GHz), high spatial resolution, and high temporal interval, which is expected to generate more reliable retrievals. The Pearson correlation coefficients (R) between AMSR-E and TMI and SSM/I, respectively, were calculated for their overlapping period (1 July 2002–31 December 2007) (see Fig. 2). The number of coincident values used to calculate R is more than 500 (i.e. $N > 500$), and the critical value of being significant at the level of 5% for N equal to 500 is around 0.09. Therefore, TMI and SSM/I are significantly correlated with the AMSR-E product over most of Australia, which creates the possibility to rescale SSM/I and TMI and merge them with AMSR-E to yield a long-term data set.

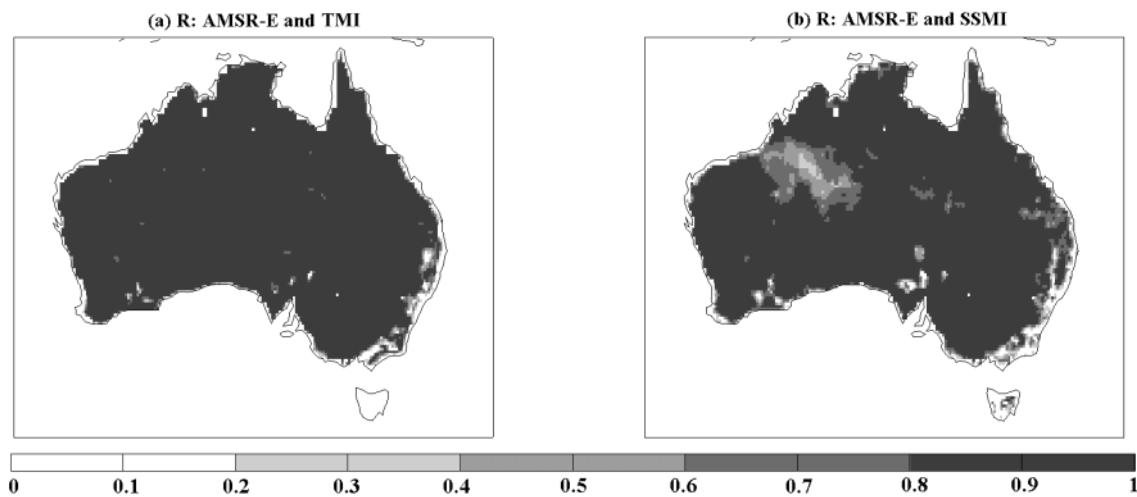


Fig. 2 Correlation coefficient (R) between (a) daily AMSR-E and TMI, (b) daily AMSR-E and SSM/I products from July 2002 until December 2007.

The cumulative distribution function (CDF) matching technique was chosen as the rescaling method. A similar approach was successfully used in previous studies (e.g. Reichle & Koster, 2004; Liu *et al.*, 2009). The piece-wise linear CDF matching analysis was conducted pixel-by-pixel according to the following steps: (1) Build CDF curves for AMSR-E, TMI and SSM/I over their overlapping period (1 July 2002–31 December 2007). (2) Use the 0, 5, 10, 20, 30, 40, 50, 60, 70, 80, 90, 95 and 100 percentiles of each CDF curve to define 12 segments. (3) For each segment, perform a linear regression to obtain a linear equation (i.e. slope and intercept) between TMI or SSM/I and AMSR-E. That is, for TMI or SSM/I values falling into every segment, there is one

linear equation to rescale them against AMSR-E values. (4) Apply the 12 segments' linear equations to TMI (1 January 1998–31 December 2008) and SSM/I (1 January 1988–31 December 2007). The TMI and SSM/I values outside of the range of CDF curves were rescaled using the linear equation of the closest value. Figure 3 displays one example how the original products were rescaled and merged into one time series.

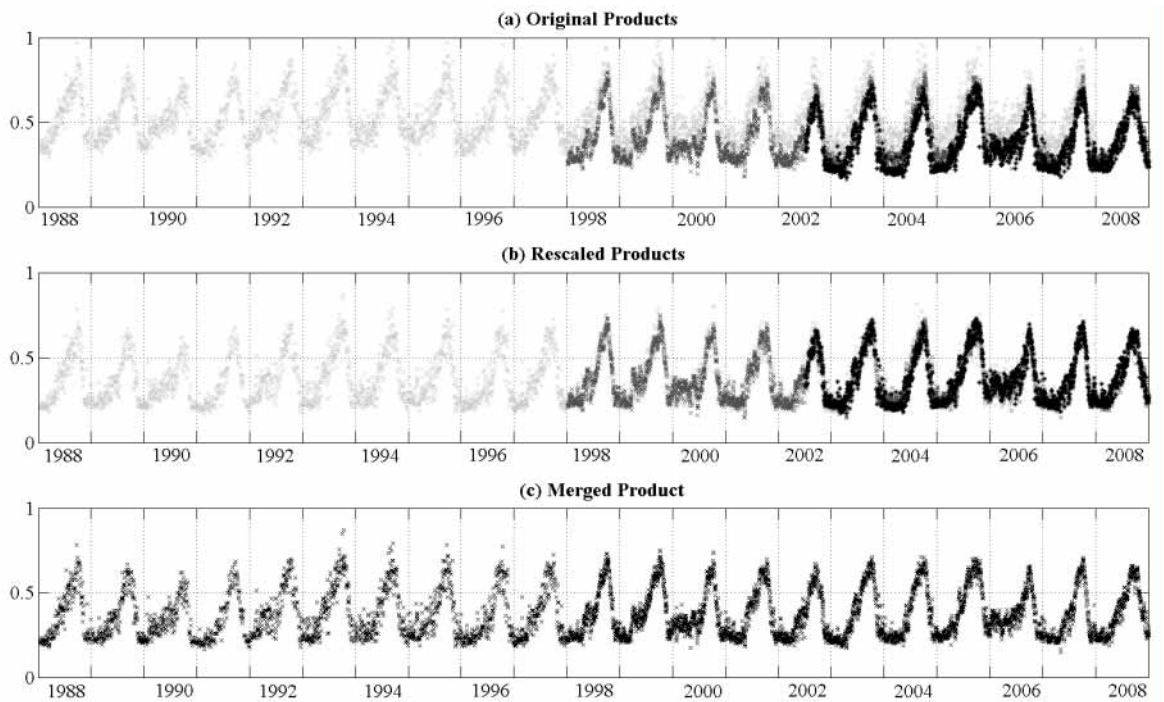


Fig. 3 Example illustrating how: (a) the original time series (SSM/I: light grey; TMI: dark grey; AMSR-E: black) were adjusted into (b) rescaled products using CDF matching technique. (c) The merged product was derived by taking the average of all rescaled products. The grid cell is centred at 32.375°S, 147.375°E.

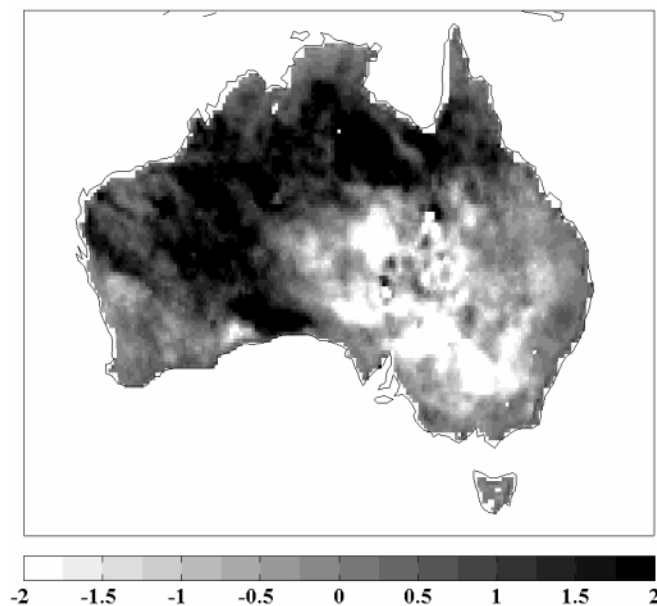


Fig. 4 Spatial distribution of changes (% / year) in vegetation density over the period from 1988 to 2008. The percentage is the annual change relative to the average over 1988 to 2008.

Trend analysis

Spatial patterns of Mann-Kendall trends in annual averages of vegetation optical depth are shown in Fig. 4. As can be seen, northwest Australia experienced increases in vegetation density, whereas southeast Australia experienced declining trends. These apparent changes may be caused by climate or human activities, or a combination of the two.

Climate or human activities

In this section we develop a method to identify and remove climate-related VOD trends over northwest and southeast Australia. Spatial patterns of Mann-Kendall trends in annual average rainfall and temperature over the same period (1988–2008) are displayed in Fig. 5. Visually, trends in VOD seem similar to those in rainfall, and to a lesser extent, temperature. To distinguish the contribution of natural climate influences on the declines observed in vegetation optical depth, we (1) selected the maximum monthly VOD value of each year to obtain a time series, referred to as VOD_{max} , (2) performed multiple linear regressions between varying periods of precipitation, temperature and VOD_{max} for each grid cell, and (3) identified the optimal “modelled VOD_{max} ” (see equation (1)) that has highest correlation coefficient with VOD_{max} (Evans & Geerken, 2004).

$$\text{Modelled } VOD_{max} = a \times P_i + b \times T_j + c \quad (1)$$

where P_i represents rainfall totals for accumulation periods of between one and eight months, and for lead times of zero to seven months prior to the timing of VOD_{max} , T_j represents temperature averages for accumulation periods of between one to eight months, and for lead times of zero to seven months prior to the timing of VOD_{max} . When the optimal modelled VOD_{max} is achieved, accumulation periods and leading times for precipitation and temperature are not necessarily the same, thus different subscripts are used for P and T . The optimal modelled VOD_{max} can be interpreted as the contribution of natural climate influences on the VOD_{max} . Mann-Kendall trends in the residuals (i.e. VOD_{max} minus “optimal modelled VOD_{max} ”) over Australia are displayed in Fig. 6. As demonstrated, the main cause for the long-term trends in VOD_{max} over Australia from 1988 to 2008, is climate.

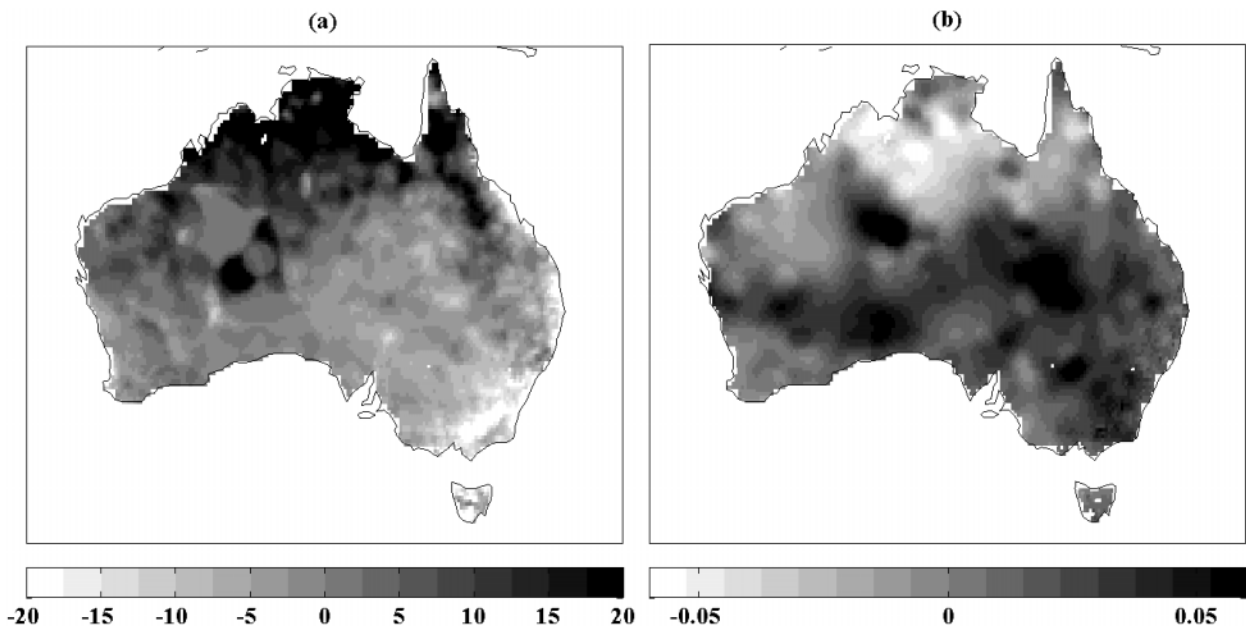


Fig. 5 Spatial distribution of changes in: (a) annual rainfall (mm/year), and (b) mean temperature (°C/year) over the period 1988–2008.

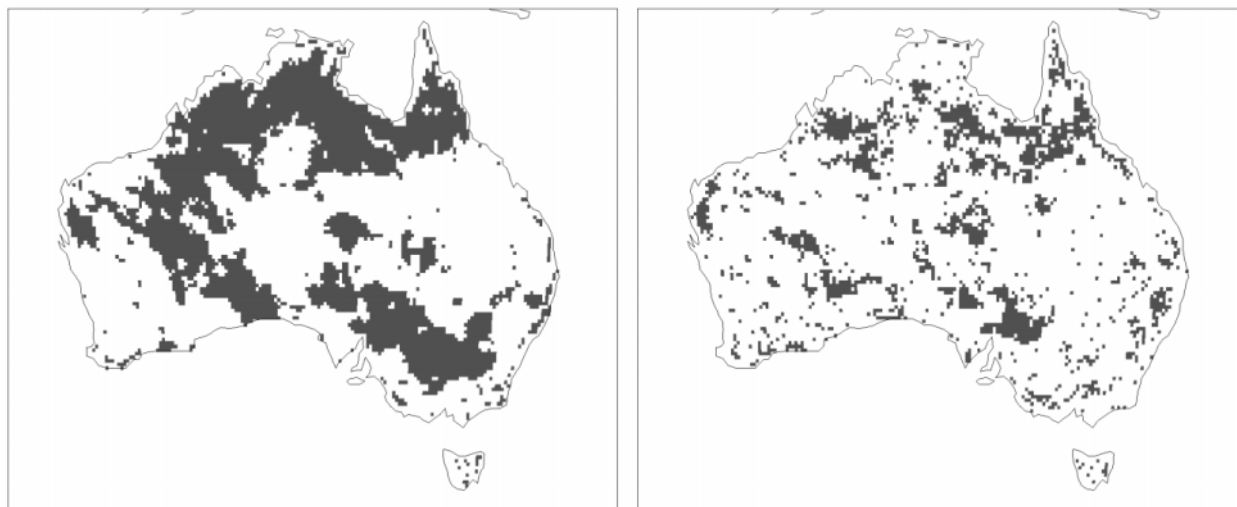


Fig. 6 Spatial patterns of changes (statistically significant at the level of 5%) in (left) VOD_{max} and (right) residuals after removing the effects of rainfall and temperature.

SUMMARY

We developed a method to merge three available passive microwave-based vegetation data sets (SSM/I, TMI and AMSR-E) into one long-term global product. Our method allows the long term product to be extended with more data being available. The potential to monitor the total above ground biomass, near all-weather retrieval capacity and high temporal interval of satellite-based passive microwave instruments, together with high spatial resolution and canopy greenness of NDVI, are expected to bring more reliable information to characterize vegetation dynamics.

Results of Mann-Kendall trend analysis on the merged product during 1988–2008 show that northwest Australia experienced considerable increases in vegetation density, whereas southeast Australia experienced considerable declines. Linear regression analysis over varying periods of precipitation, temperature and annual maximum monthly VOD revealed that the long-term change in Australia is probably mainly caused by climate factors. Further investigations along these lines should increase our understanding of the natural and anthropogenic impacts on terrestrial hydrology and vegetation dynamics.

REFERENCES

- Evans, J. & Geerken, R. (2004) Discrimination between climate and human-induced dryland degradation. *J. Arid Environ.* **57**(4), 535–554.
- Jones, D. A., Wang, W. & Fawcett, R. (2009) High-quality spatial climate data-sets for Australia. *Aust. Met. Oceanographic J.* **58**, 233–248.
- Liu, Y. Y., Van Dijk, A. I. J. M., De Jeu, R. A. M. & Holmes, T. R. H. (2009) An analysis of spatiotemporal variations of soil and vegetation moisture from a 29-year satellite-derived data set over mainland Australia. *Water Resour. Res.* **45**, W07405.
- Owe, M., De Jeu, R., & Holmes, T. (2008) Multisensor historical climatology of satellite-derived global land surface moisture. *J. Geophys. Res.* **113**(F1), F01002.
- Reichle, R. H., & Koster, R. D. (2004), Bias reduction in short records of satellite soil moisture. *Geophys. Res. Lett.* **31**(19), L19501.
- Shi, J. C., Jackson, T., Tao, J., Du, J., Bindlish, R., Lu, L. & Chen, K. S. (2008) Microwave vegetation indices for short vegetation covers from satellite passive microwave sensor AMSR-E. *Remote Sens. Environ.* **112**(12), 4285–4300.
- Tucker, C. J., Pinzon, J. E., Brown, M. E., Slayback, D. A., Pak, E. W., Mahoney, R., Vermote, E. F. & El Saleous, N. (2005) An extended AVHRR 8-km NDVI dataset compatible with MODIS and SPOT vegetation NDVI data. *Int. J. Remote Sens.* **26**(20), 4485–4498.

Global inland water monitoring from satellite radar altimetry – a glimpse into the future

PHILIPPA A. M. BERRY¹, MARK K. SALLOWAY¹, RICHARD G. SMITH¹ & JÉRÔME BENVENISTE²

¹ De Montfort University, EAPRS Lab, Faculty of Technology, Leicester LE1 9BH, UK
pamb@dmu.ac.uk

² ESA ESRIN, Via Galileo Galilei, Frascati RM I-00044, Italy

Abstract Satellite altimetry has been used to monitor the heights of the Earth's largest lakes for many years; however, river systems present far more challenging targets. Using an expert system approach, echoes from smaller lakes and river systems can be successfully retracked to yield height measurements. As the network of *in situ* gauges declines, this remote measurement technique gives a unique insight into the Earth's changing inland water resources. This paper presents a global analysis of the capability of the current generation of satellite radar altimeters to monitor inland water, including ERS2, EnviSat, TOPEX, Jason1 and Jason2. The results are analysed using an automated grading technique. A glimpse into the potential of future altimeters is gained from the EnviSat altimeter (RA-2) Individual Echoes, with 1800 Hz along-track sampling rate, demonstrating the substantial enhancement in monitoring capability afforded by the next generation of satellite altimeter missions.

Key words global; river; lake; satellite altimetry

INTRODUCTION

Measuring inland water heights from satellite radar altimetry has been used for many years to measure water levels over large lakes (Guzkowska *et al.*, 1990; Koblinsky *et al.*, 1993); today, information on the world's largest lakes can be accessed from several websites (Birkett & Reynolds, 2011; Cretaux, 2011; ESA River & Lake, 2011). However, river systems present far more challenging targets. Although they contain only a small proportion of the total inland water budget, these "river corridors" are vital for human life, transporting and distributing freshwater throughout the continents. Over these surfaces fewer echoes are returned to the altimeters, and these successfully captured echoes are frequently contaminated by responses from surrounding land, irrigation and wetlands. This requires the development of complex "retracking" techniques to identify the contribution to the returned echo shape of an underlying water body (Berry *et al.*, 2005; Berry & Benveniste, 2010). This paper presents a global analysis of echoes over inland water, processed using an expert system approach, to quantify the current capability and assess the future potential of the next generation of satellite radar altimeters.

DATASETS

In this paper, data from ERS2 (Capp, 2001), EnviSat RA2 Ku band (Benveniste, 2002), TOPEX (Benada & Digby, 1997), Jason1 and Jason2 (Zanife *et al.*, 2004) are utilized. Due to their greater spatial coverage, attention is focused on the ESA exact repeat missions ERS2 and EnviSat, which orbit the Earth on a 35-day repeat cycle. These nadir-looking altimeters acquire data with global sampling, retrieving echoes at roughly 330 m intervals along-track. The repeat cycles pass over the same ground track, within the orbit tolerance of ± 1 km.

CURRENT CAPABILITY

Global capability

To assess the current global capability of altimeter inland water measurements, multi-year datasets of echoes over inland water targets were generated globally, utilising a mask of inland water locations

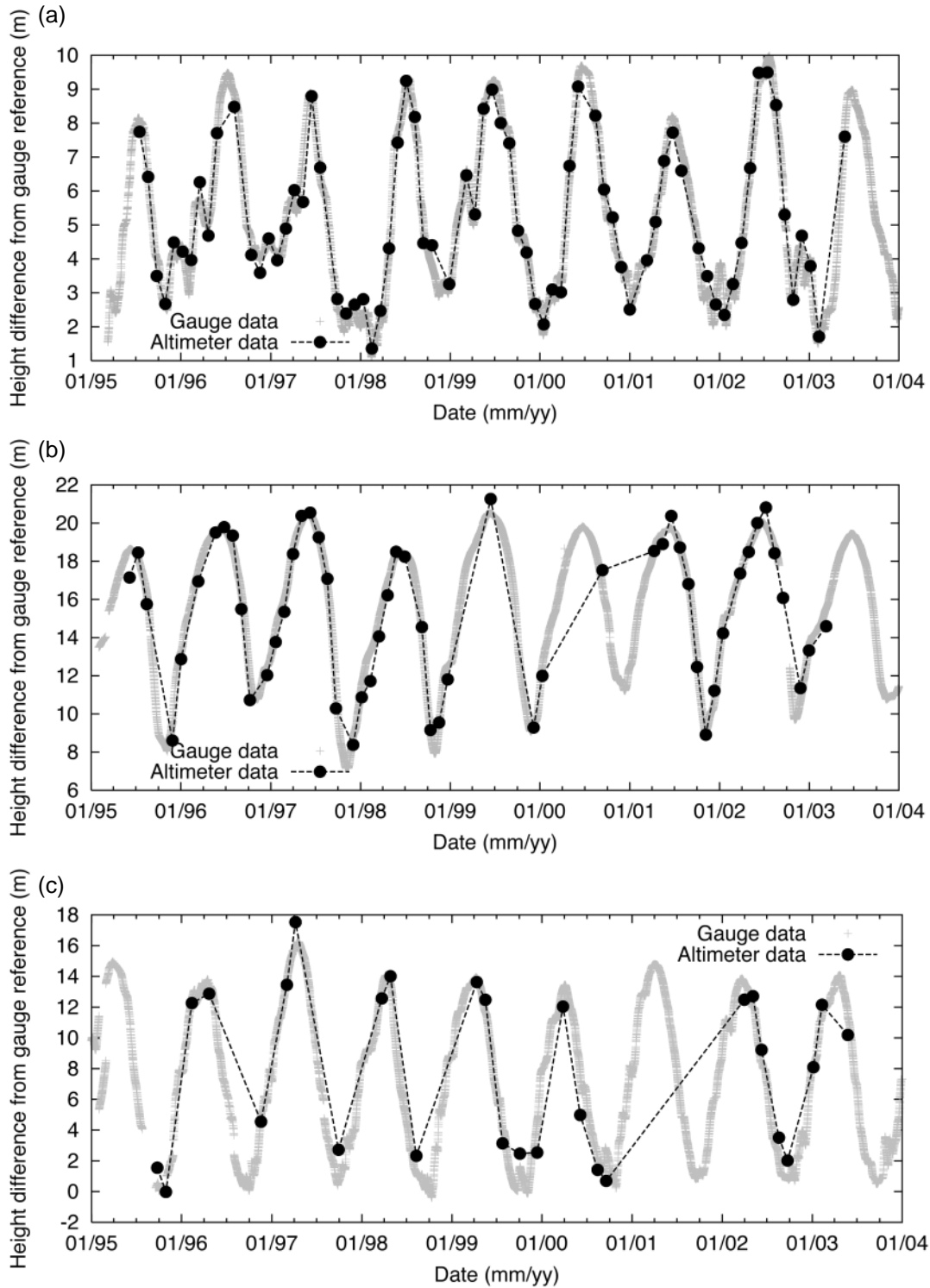


Fig. 1 Graded ERS2 timeseries (black) over Amazon basin with *in situ* gauge data (grey) (a) “Good” target: RMS 0.31 m Correlation 0.99, (b) “Fair” target: RMS 0.58 m correlation 0.99, (c) “Poor” target: RMS 1.14 m Correlation 0.98.

derived from the Global Land Characterisation Coverage (GLCC) dataset (Loveland *et al.*, 2000). The echoes were analysed and retracked (Berry & Benveniste, 2010) and a time series of water level changes were generated. These were then graded, using a combination of statistical analyses on the stability and consistency of the measurements over time, into three categories: good, fair (typically a

good time series with several outliers) and poor (not well captured). The criteria were tuned using 200 time series from ERS2 and EnviSat compared against gauge measurements over the Amazon basin, using the RMS between the gauge and altimeter height measurements and the cross-correlation coefficients. A typical example of each category is given in Fig. 1.

Here, the individual values all agree quite well with the gauge data, but for case (c) the altimeter was only able to measure the target intermittently, and the ERS2 time series was accordingly graded as “poor”. The automated grading system was then tuned to bring its grading outcomes into agreement with those from the independent gauge assessment. The criteria were then put into a full grading system, and the global database of time series was processed for both ERS2 and EnviSat; the resulting global statistics and the subset of these results for Africa are shown in Table 1.

The global total numbers of targets for TOPEX and Jason1 have also been calculated; for TOPEX 7509 targets were successfully acquired, and for Jason1, 7200; grading the results for these missions is ongoing. Despite the known difficulties with Jason1, which resulted in fewer good quality measurements being made over inland water, Jason2 where it successfully acquires a target generally allows good height estimates to be made.

Table 1 Global statistics for altimeter inland water time series recovery and Africa subsets.

Dataset	Good targets	Good with outlier	Poor	Totals
ERS2 global	841	2671	18711	22223
EnviSat global	1880	6457	17299	25636
ERS2 Africa	110	205	668	983
EnviSat Africa	202	336	531	1069

ESA near-real-time system

For the best and most stable targets, a Near-Real-Time system has been implemented (Wheeler *et al.*, 2009). Processing Jason2 and EnviSat data (until its recent orbit change), this site produces data within 3 days of the satellite overpass. The corresponding numbers of targets for the current implementation of this global pilot system are 1229 EnviSat targets, and 112 from Jason2. These altimeter measurements have now been ingested into river models (Birkinshaw *et al.*, 2010; Pereira-Cardenal *et al.*, 2011) providing an effective and powerful constraint on the models.

ENHANCED CAPABILITY

Examining the statistics for echo analysis and classification, it became apparent that many non-water echoes were being selected by the system. Many of the targets assessed as “poor” contained these echo types. Attention was therefore focused on the selections mask, and it was realized that this mask was inadequate for the retrieval of detailed river systems. An enhanced mask was therefore created for Africa, to test whether a better delineation of river courses could enhance target retrieval. The ILWIS software (52north.org, 2010) and the ACE2 GDEM (Smith *et al.*, 2010) were utilized to create this mask, and the ERS2 and EnviSat datasets were re-analysed. The success rate was extremely high, with total targets over flown and where echoes were successfully retrieved as follows: EnviSat Africa target number 8893 and for ERS2, 8275; this represents almost an order of magnitude increase in target acquisition. To illustrate the spatial distribution of these targets, Fig. 2 shows (a) the location of targets included in Table 1 over a 15×15 degree region of Africa (0–15°N, 15–30°E), and (b) the targets retrieved from the enhanced system. Of particular note, many of the complex waveform shapes retrieved occur over the smaller tributaries, where the along track sampling rate of about 330 m is a limiting factor for existing altimeters, but where Sentinel3 SRAL altimeter, with its greatly enhanced sampling rate (Le Roy *et al.*, 2007), has the potential to retrieve multiple echoes successfully.

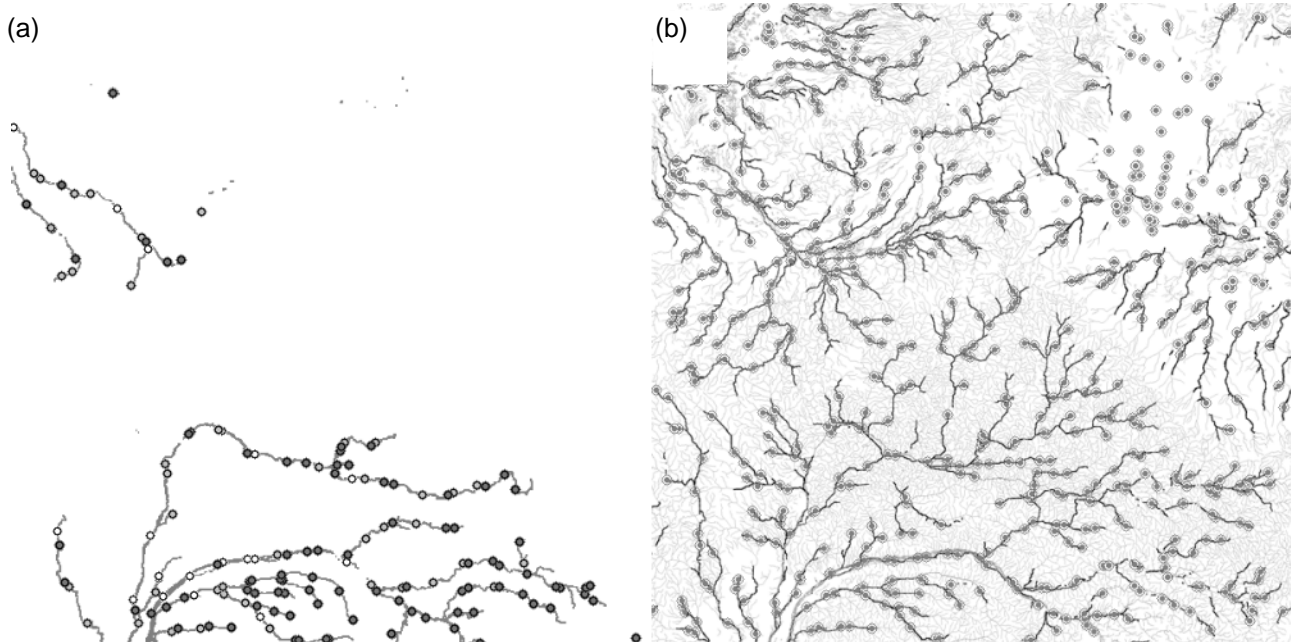


Fig. 2 Locations of river targets 0–15°N, 15–30°E using EnviSat: (a) current processing, (b) enhanced processing.

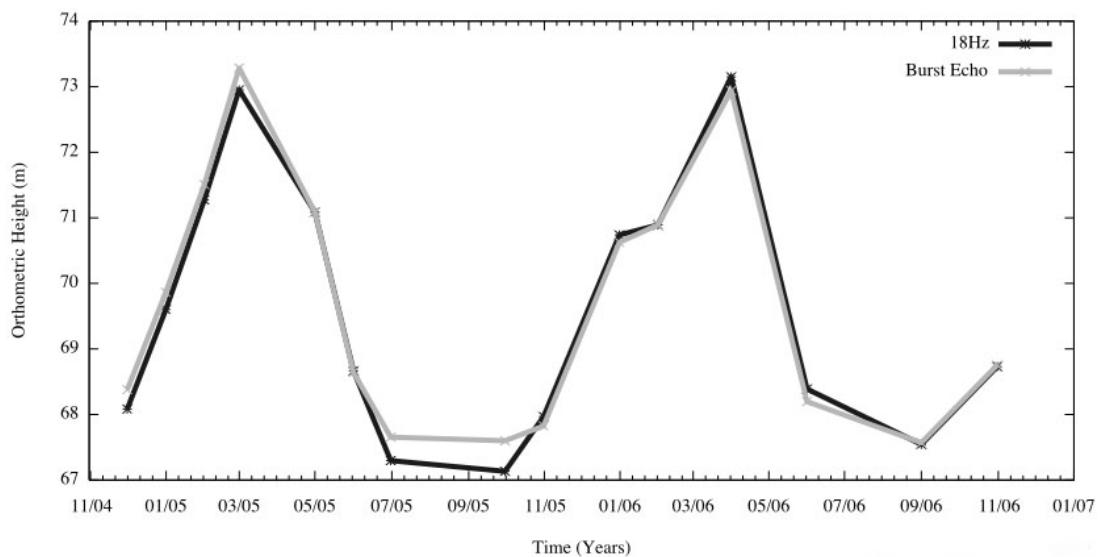


Fig. 3 Altimeter derived heights from Tapajós River at 6.472°S, 58.076°W from IEs (grey) and EnviSat SGDR (black) echoes.

To check the feasibility of spatially enhanced height measurements from an altimeter with higher Pulse Repetition Frequency (PRF), an investigation was made into the EnviSat RA-2 Individual Echoes (IEs) (Berry *et al.*, 2007). These data provide one second of echoes at full 1800 Hz sampling every three minutes over the Earth's surface. Analysis of these data over inland water (Witheridge *et al.*, 2010) demonstrates that retrieval of inland water heights is possible by “retracking” these echoes at full resolution. Over river systems, good agreement is obtained even where the number of burst echoes available is small. An example is shown in Fig. 3 for the Tapajós River (at 6.472°S, 58.076°W). Here, only part of the bursts was obtained over the river, varying between 400 and 800 echoes (1 second of data, 1800 echoes, corresponds to a distance of

about 7 km). Good agreement is seen with the “normal” EnviSat time series, confirming the stability of this method over smaller targets.

DISCUSSION

The measurement of inland water heights using satellite radar altimetry is a comparatively young and rapidly developing discipline, capable of retrieving inland water heights with an accuracy of a few centimetres. As altimeter echo analysis techniques become more sophisticated, and with a 15-year time span of multi-mission echoes already accumulated, successful target retrieval is increasingly transformed into an enhanced global monitoring capability. The ingestion of these data into river models then allows the temporal sampling constraints to be overcome. The next generation of satellite radar altimeters, exemplified by the SRAL altimeter on Sentinel3, has a greatly higher PRF, allowing measurements to be made over much smaller water bodies. The work in this paper demonstrates that this enhanced along-track sampling rate is predicted to increase the measurement capability over inland water by at least two orders of magnitude.

Acknowledgements The authors wish to thank the European Space Agency, JPL and CNES for supply of data for this work.

REFERENCES

- Benada, R. & Digby, S. (1997) TOPEX/POSEIDON Altimeter Merged Geophysical Data Record Generation B (NASA/PO.DAAC). JPL PO.DAAC 068.D002, Jet Propulsion Laboratory, Pasadena, California, USA.
- Benveniste, J. (ed.) (2002) ENVISAT RA-2/MWR Product Handbook, Issue 1.2. PO-TN-ESR-RA-0050, European Space Agency.
- Berry, P. A. M. & Benveniste, J. (2010) Measurement of inland surface water from multi-mission satellite radar altimetry: sustained global monitoring for climate change. *Int. Assoc. Geodesy Symposia* **135**, 221–230. ISBN: 978-3-642-10633-0.
- Berry, P. A. M., Benveniste, J. & Freeman, J. A. (2007) Global analysis of EnviSat RA-2 burst mode echo sequences. *IEEE Trans. Geosci. Remote Sens.* **V45**, 2869–2874.
- Berry, P. A. M., Garlick, J. D., Freeman, J. A. & Mathers, E. L. (2005) global inland water monitoring from multi-mission altimetry. *Geophys. Res. Letters* **32**(16), L16401, DOI: 10.1029/2005GL022814.
- Birkett, C. & Reynolds, C. (2011) Global reservoir and lake monitor. http://www.pecad.fas.usda.gov/cropexplorer/global_reservoir/index.cfm (accessed 1 March 2011).
- Birkinshaw, S. J., O'Donnell, G. M., Moore, P., Kilsby, C. G., Fowler, H. & Berry, P. A. M. (2010) *Satellite Altimetry Data on the Mekong. Hydrol. Processes*. doi:10.1002/byp.7811.
- Capp, P. (2001) Altimeter Waveform Product ALT.WAP Compact User Guide, Issue 4.0. PF-UG-NRL AL-0001, Infoterra Ltd., UK.
- Cretaux, J-F. (2011) Hydrology from space. <http://www.legos.obs-mip.fr/en/soa/hydrologie/hydroweb/>, (accessed 1 March 2011).
- ESA River and Lake website (2011) <http://www.earth.esa.int/riverandlake/> (accessed 1 March 2011).
- Guzkowska, M. A. J., Rapley, C. G., Ridley, J. K., Cudlip, W., Birkett, C. M. & Scott, R. F. (1990) Developments in inland water and land altimetry. ESA Contract Rep. 7839/88/F/FL, 418 pp. ESTEC, 2200 AG Noordwijk, The Netherlands.
- ILWIS software (2011) <http://52north.org/communities/ilwis/about>.
- Koblinsky, C. J., Clarke, R. T., Brenner, A. C. & Frey, H. (1993) Measurement of river level variations with satellite altimetry. *Water Resour. Res.* **29**(6), 1839–1848.
- Le Roy, Y., Deschaux-Beaume, M., Mavrocordatos, C., Aguirre, M. & Heliere, F. (2007) SRAL SAR radar altimeter for sentinel-3 mission. In: *Geoscience and Remote Sensing Symposium, IGARSS 2007* (IEEE International, 23–28 July 2007), 219–222. doi:10.1109/IGARSS.2007.4422769.
- Loveland, T. R., Reed, B. C., Brown, J. F., Ohlen, D. O., Zhu, J., Yang, L. & Merchant, J. W. (2000) Development of a global land cover characteristics database and IGBP DISCover from 1-km AVHRR Data. *Int. J. Remote Sens.* **21**(6/7), 1303–1330.
- Pereira-Cardenal, S. J., Riegels, N. D., Berry, P. A. M., Smith, R. G., Yakovlev, A., Siegfried, T. U. & Bauer-Gottwein, P. (2011) Real-time remote sensing driven river basin modeling using radar altimetry. *Hydrol. Earth Syst. Sci.* **15**, 241–254, doi:10.5194/hess-15-241-2011.
- Smith, R. G., Berry, P. A. M. & Benveniste J. (2010) ACE2: Global Digital Elevation Model, SP-686. In: *Proc. ESA Living Planet Symposium* (27 June–2 July, ESTEC, 2200 AG Noordwijk, The Netherlands), ISBN978-92-9221-250-6.
- Wheeler, J., Berry, P. A. M., Smith, R. G. & Benveniste, J. (2009) The ESA near real time river and lake system. In: *Proc. of the Earth Observation and Water Cycle Science* (18–20 November, ESA ESRIN, Frascati, Italy). ISBN 978-92-9221-238-4.

- Wetheridge, S., Berry, P. A. M. & Smith, R. G. (2010) Analysis of EnviSat RA-2 burst echoes over lake surfaces. In: *Proc. Living Planet Symposium* (27 June–2 July 2010, ESTEC, 2200 AG Noordwijk, The Netherlands). ISBN 978-92-9221-250-6.
- Zanife, O. Z., Dumont, J. P., Stum, J. & Guinle T. (2004) SSALTO Products Specifications, Volume 1: Jason-1 User Products, Issue 3.1. SMM-ST-M-EA-10879-CN, CLS/CNES, Toulouse, France.

Third Pole Environment (TPE) program: a new base for the study of atmosphere–land interaction over the heterogeneous landscape of the Tibetan Plateau and surrounding areas

YAOMING MA¹, MAOSHAN LI², XUELONG CHEN¹, SHUZHOU WANG¹,
RONGSHENG WU¹, WEIQIANG MA², LEI ZHONG¹, BINBIN WANG¹,
CHUNLING ZHU¹ & TANDONG YAO¹

¹ Key Laboratory of Tibetan Environment Changes and Land Surface Processes, Institute of Tibetan Plateau Research, Chinese Academy of Sciences, Beijing 100085, China

yyma@itpcas.ac.cn

² Cold and Arid Regions Environmental and Engineering Research Institute, Chinese Academy of Sciences, Lanzhou 730000, China

Abstract As a unique geological and geographical unit, the Third Pole area (the Tibetan Plateau and surrounding areas) dramatically impacts the world's environment and especially controls climatic and environmental changes in China, Asia and even in the Northern Hemisphere. Supported by the Chinese Academy of Sciences, various agencies in the People's Republic of China and some international organizations, the Third Pole Environment (TPE) Program is now being implemented. The TPE Program is focusing on the land-surface processes and environment over the plateau and surrounding areas, with an emphasis on atmosphere–land interaction. Firstly, the backgrounds of the TPE establishment and the establishing and monitoring plan and long-term scale of the TPE are introduced. Then the preliminary observational analysis results, such as the characteristics of land surface fluxes partitioning (diurnal variation, inter-monthly variation and inter-annual variation), the structure of the Atmospheric Boundary Layer (ABL), and the parameters of land–atmospheric interaction, are shown in this paper. The regional distribution of surface heat fluxes (net radiation, soil heat flux, sensible heat flux and latent heat flux) and surface heating field derived from satellite remote sensing data and field observations are also described.

Key words Third Pole; TPE; *in situ* and satellite data; atmosphere–land interaction; surface heat fluxes

INTRODUCTION

Like Antarctica and the Arctic, the Third Pole region (Qiu, 2008) is drawing increased attention among the international academic community. It is centred on the Tibetan Plateau, stretching from the Pamir Plateau and Hindu-Kush in the west to the Hengduan Mountains in the east, and from the Kunlun and Qilian Mountains in the north to the Himalayas in the south. Covering over 5 000 000 km² in total and with an average elevation surpassing 4000 m, the Third Pole region is home to thousands of glaciers in the tropical/sub-tropical region that exerts a direct influence on social and economic development in the surrounding regions of China, India, Nepal, Tajikistan, Pakistan, Afghanistan and Bhutan, etc. It is subject to influences from multiple climatic systems, complicated geomorphologies and various internal and external geological impacts. The result is a region with unique interactions among the atmosphere, cryosphere, hydrosphere and biosphere. In particular, the special atmospheric processes and active hydrological processes formed by glaciers, permafrost and persistent snow are especially influential, as are the ecosystem processes acting at multiple scales. These processes compose the fundamental basis for the unique geographical unit of the Third Pole region. The area demonstrates considerable feedbacks to global environmental changes, while interacting with and affecting each other in response to global climatic environmental variations.

A series of observation and monitoring programs in the Third Pole region have been widely implemented, including the Himalayas Inter-disciplinary Paleoclimatic Projects (HIPPS), GEWEX Asia Monsoon Experiment on the Tibetan Plateau (GAME/Tibet), Coordinated Enhanced Observing Period (CEOP) Asian-Australian Monsoon Project on the Tibetan Plateau (CAMP/Tibet), the Pyramid Laboratory, Monsoon Asia Integrated Regional Study (MAIRS), Tibetan Plateau-Uplifting, Environmental Changes and Ecosystem (TiP), Climate and Cryosphere Programme (CliC), and Ice Core Climate Archive Recovery Activity (ICARA), among others

(<http://www.tpe.ac.cn>). More research programs are being introduced by scientists from various nations to observe and monitor regional environment and climate in the Third Pole region, on both a long-term and short-term basis. Yet for a comprehensive understanding of the mechanisms of environmental change and their impacts on the region, current observational resources need to be integrated and perfected, and research goals and approaches need to be updated and identified (<http://www.tpe.ac.cn>). The Third Pole Environment (TPE) Program was proposed by scientists (leading scientist Prof. Yao Tandong) from the Chinese Academy of Sciences.

The general goal of the TPE program is to attract relevant research institutions and academic talents to focus on a theme of “water-ice-air-ecosystem-human” interaction in the TPE, to reveal environmental change processes and mechanisms on the Third Pole and their influences and regional responses to global changes, especially monsoon systems, and thus to serve the enhancement of human adaptation to the changing environment and the realization of human–nature harmony. The Scientific Goal of the TPE program is to reveal and quantify, from the perspectives of Earth system sciences, the interactions among the atmosphere, cryosphere, hydrosphere, biosphere and anthroposphere in the Third Pole region and their influences on the globe, in order to assess the likely future impacts of global change.

OBSERVATION AND RESEARCH PLATFORM IN TPE

With support from the Chinese Academy of Sciences and various agencies in the People’s Republic of China, a TPE Observation and Research Platform (TPEORP) is now being implemented and will focus on the land-surface processes and environment over the plateau, with an emphasis on atmosphere–land interaction. There will be 24 comprehensive observation and research stations in the TPEORP, of which 21 are in the Tibetan Plateau, China, and another three are in Tajikistan, Pakistan and Nepal (Fig. 1). TPEORP will be constructed at the end of 2012.

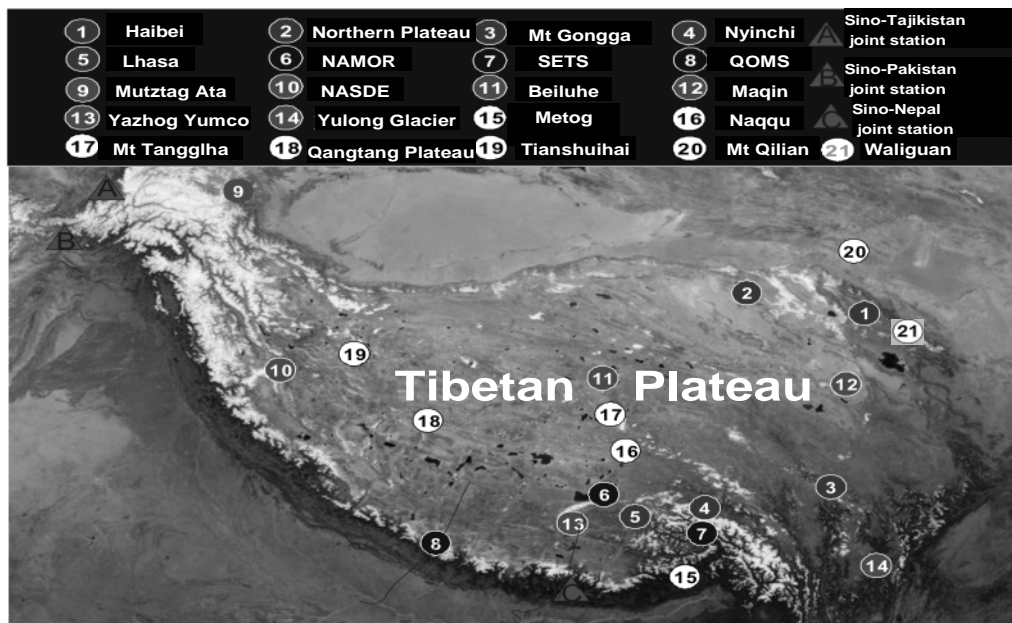


Fig. 1 TPE Observation and Research Platform (TPEORP).

Each station will include an atmospheric boundary layer (ABL) tower (or an automatic weather station (AWS)), a four-component radiation measurement system, a five-level soil moisture and soil temperature measurement system (SMTMS), and a sonic turbulent measurement system and CO₂/H₂O flux measurement system.

IN SITU DATA ANALYSIS

The characteristics of the atmospheric turbulence and the radiation energy distributions and the structure of the ABL are analysed in this section by using the data observed from a GPS radiosonde system (MW21 digiCorA III, Vaisala Company), four components radiation system (CNR-1, Kipp & Zonen Company) and a sonic turbulent measurement system (CSAT3, Campbell Company) in the TPEORP stations.

Diurnal and inter-monthly variation of local radiation fluxes and land surface heat fluxes

The field data observed at three stations (Nam Co Station-NAMOR, Mt Everest-Qomolangma Station-QOMS and Linzhi Station-SETS) of the TPEORP under a clear day in 2007 is used in this section. The distribution of radiation fluxes is shown in Fig. 2.

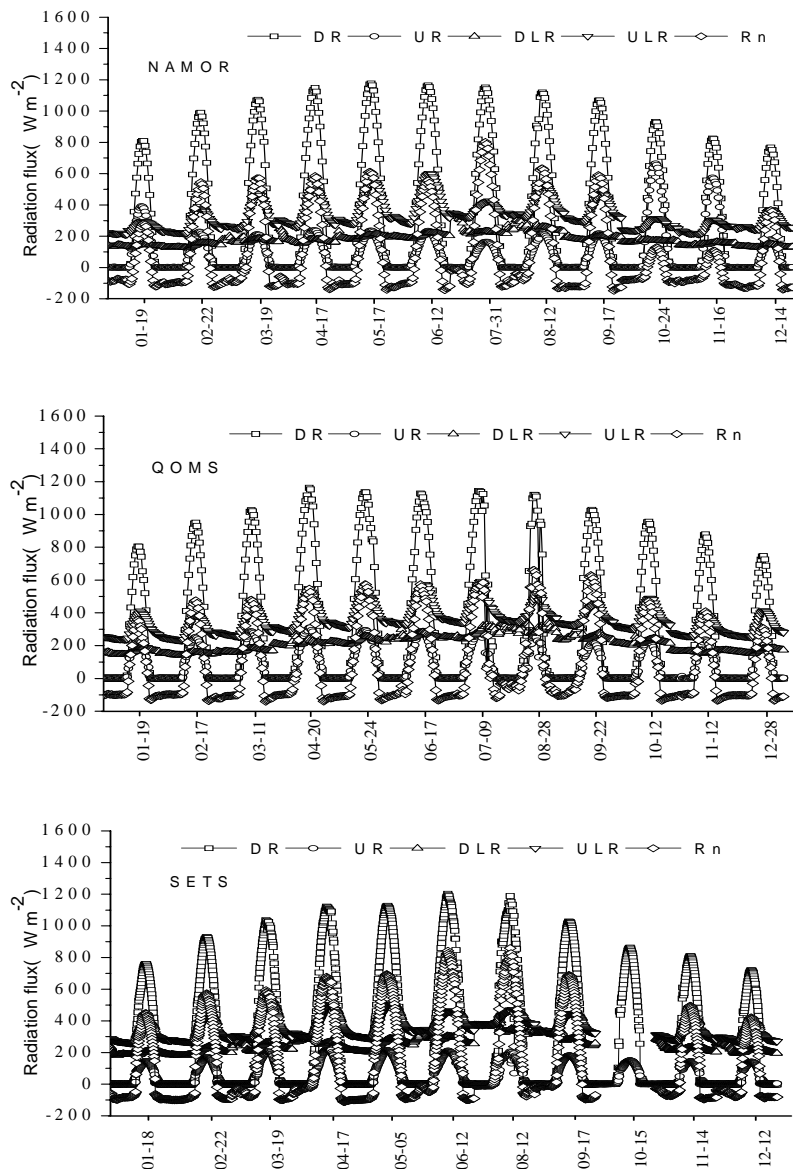


Fig. 2 The inter-monthly variation of radiation fluxes at the TPEORP stations (Nam Co Station-NAMOR, Mt Everest-Qomolangma Station-QOMS and Linzhi Station-SETS). DR: downward short-wave radiation, DLR: downward long-wave radiation, ULR: upward long-wave radiation, UR: upward short-wave radiation, and Rn: net radiation.

The results show that: (1) The inter-monthly variation of the downward short-wave radiation flux was very obvious. The summer values were much larger than those in winter, and reached the minimum value around December. Although the upward short-wave radiation had different values in different months, their inter-monthly variations were not clear (Fig. 2); (2) The downward short-wave radiation reaches about 1200 W/m^2 or more at local noon on fine days in summer. The transmission rate of incoming solar radiation from the top of the atmosphere was estimated to be about 85% in cloudless conditions. The values are about 10–15% greater than those observed at a typical sea level station. It is due to the high altitude of three TPEORP stations, thus a shallower atmospheric layer between the top of the atmosphere and the ground surface (Fig. 2); (3) The inter-monthly variation of the upward long-wave radiation flux was obvious. The summer values were larger than those in winter, and reached the minimum value around December. This means that in summer the surface temperature is higher than those in winter. Although the values of downward long-wave radiation flux in summer is a little higher than those in other months, their inter-monthly variations were not clear (Fig. 2); (4) The diurnal variations of downward short-wave radiation, upward short-wave radiation and upward long-wave radiation were very obvious, and the diurnal variation of downward long-wave radiation was not clear, especially during the pre-monsoon period (Fig. 2); (5) The diurnal variation and inter-monthly variation of the net radiation flux was very obvious. The summer values were much larger than those in winter, and reached the minimum value around December (Fig. 2); (6) Sensible heat and latent heat fluxes play different roles in the partition of net radiation flux in different months in the Tibetan Plateau. In other words, sensible heat flux plays the main role in winter and latent heat flux plays the main role in summer and autumn; (7) The land surface is a very strong heating source in the day time, but is a weak surface heating sink in the night, but the daily mean is a strong surface heating source; (8) The surface heating densities in summer are much larger than those in winter, and reach the minimum value around January. In other words, the surface of the Tibetan Plateau is a strong heating source in summer and it is a weak heating source in winter; and (9) Surface albedo over the Tibetan Plateau has different values in different seasons; it is higher in winter and spring and lower in summer and autumn.

The parameters of land–atmospheric interaction

The aerodynamic roughness length z_{0m} , thermodynamic roughness length z_{0h} and the excess resistance to heat transfer, kB^{-1} are very important parameters in the determination of the land surface heat fluxes. They were determined by using the *in situ* data observed in the three stations (Nam Co Station-NAMOR, Mt. Everest-Qomolangma Station-QOMS and Linzhi Station-SETS) of the TPEORP and the method presented by Ma & Tsukamoto (2002).

The results show that: (1) The aerodynamic roughness length z_{0m} and the thermodynamic roughness length z_{0h} are significantly different over the different land surfaces of the Tibetan Plateau. z_{0h} is one magnitude smaller than z_{0m} . This means that both the aerodynamic and thermodynamic characteristics of the land surface have effects on z_{0m} and z_{0h} ; (2) The excess resistance to heat transfer, kB^{-1} , has obvious diurnal variation over the Tibetan Plateau (Fig. 3), i.e. the kB^{-1} values derived by researchers in other areas cannot be used directly in the numerical simulation and the procedure of satellite remote sensing parameterization over the Tibetan Plateau area, as different values of kB^{-1} should be used at different times of the day.

The structure of the atmospheric boundary layer

There are constant layers of wind velocity, air humidity and potential temperature in the convective boundary layer (CBL) over the homogeneous land surfaces (Garratt, 1992). The mixed layer (ML) top was identified as the lowest level of an inversion in potential temperature, which capped a mixed layer of nearly uniform potential temperature (Stull, 1988). The constant layers of potential temperature were found over the grass land of the Tibetan Plateau, Gobi Desert and oases in Gansu Province, a northwest region of China (Ma *et al.*, 2008). The landscape of the Third Pole area is very complex. At this time, our understanding of the vertical atmospheric structure above

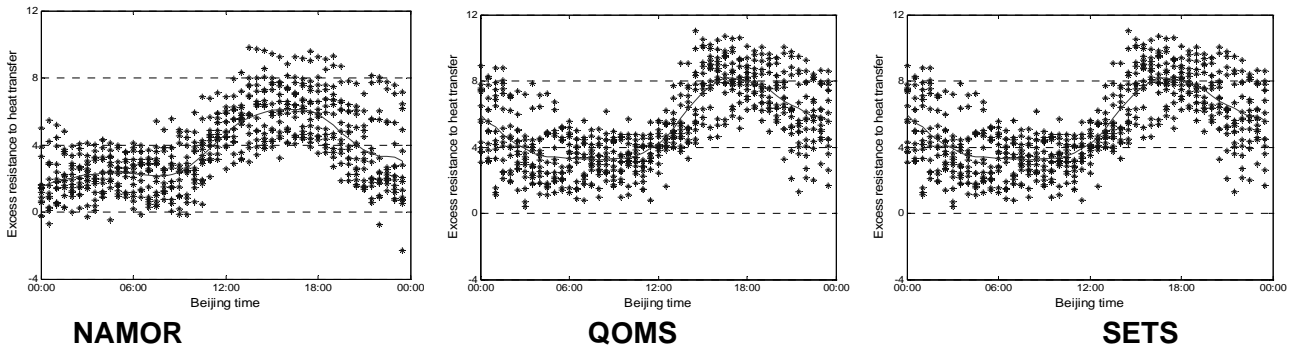


Fig. 3 The diurnal variations of kB^{-1} over the three stations (Nam Co Station-NAMOR, Mt. Everest-Qomolangma Station-QOMS and Linzhi Station-SETS) of the TPEORP.

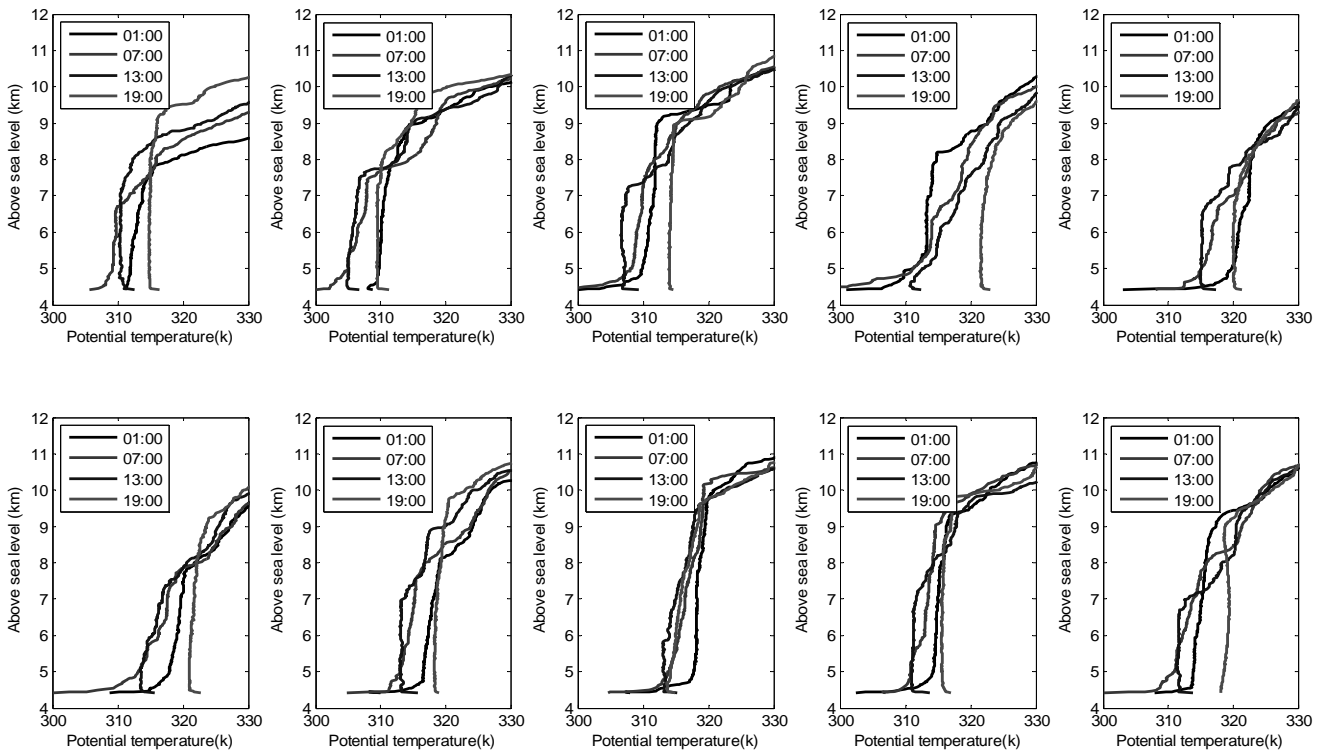


Fig. 4 Temporal variations of potential temperature from 25 February to 5 March 2008 at Gerze station in the western Tibetan Plateau. Each day there are releases at 01:00 h, 07:00 h, 13:00 h, 19:00 h local time (LT).

this area, such as the vertical profile of potential temperature and the dimensions of the boundary layer and its relation to supra-regional circulation, is limited, aggravated by local topographic and glacier wind effects.

Using the data observed from GPS radio-sonde system, it is found that there is a very clear constant layer of potential temperature existing on the northern slope of the Mt Qomolangma area at around 12:00 h (Beijing Standard Time, BST) in May 2007 and in the Gerze station (32.17°N, 84.03°E, 4415 m) in the western Tibetan Plateau from 25 February to 5 March 2008 (Fig. 4). This means that the ABL theory can be used in these two areas, even though the landscape in the region is very complex.

DISTRIBUTION OF REGIONAL LAND SURFACE HEAT FLUXES AND SURFACE HEATING FIELD

The study on the regional surface energy partitioning and its inter-monthly variation is of paramount importance over the heterogeneous landscape of the Tibetan Plateau and surrounding area (e.g. Third Pole area). Therefore, we will try to derive the regional land surface heat fluxes by using the ASTER data, Landsat-7 ETM data, MODIS data and the field observational data. Here, “Regional” land surface heat fluxes are not “aggregated” fluxes (Batchvarova *et al.*, 2001), but surface flux fields or surface heat fluxes on each pixel of ASTER images, Landsat-7 ETM images and MODIS images.

The methodology to determine regional land surface heat fluxes over the Tibetan Plateau was proposed using ASTER data, Landsat-7 ETM data, MODIS data and field observations (Ma & Tsukamoto, 2002; Ma *et al.*, 2002a,b; Zhong *et al.*, 2010). The surface reflectance for short-wave radiation (r_0) and land surface temperature (T_{sfc}), are retrieved from ASTER data, Landsat-7 ETM data and MODIS data with atmospheric correction by using the radiative transfer model MODTRAN (Berk *et al.*, 1989), four-stream radiative transfer assumption (Verhoef, 1997) and aerological observational data. The radiative transfer model also computes the downward short- and long-wave radiation at the surface. With these results the surface net radiation flux (R_n) is determined. The surface soil heat flux (G_0) is estimated from R_n , T_{sfc} , r_0 and MSAVI (Modified Soil Adjusted Vegetation Index, Qi *et al.*, 1994) which is also derived from ASTER data, Landsat-7 ETM data or MODIS data. Sensible heat flux (H) is estimated from T_{sfc} , surface and aerological data with the aid of the so-called “blending height” approach (Mason, 1988), and regional latent heat flux (λE) can be derived as the residual of the energy budget theorem for the land surface.

The regional distributions of land surface variables (surface reflectance and surface temperature), vegetation variables (MSAVI, vegetation coverage (P_v) and leaf area index (LAI) and land surface heat fluxes were derived (figures are omitted here). The land surface heat fluxes derived from satellite data were also compared with the field measurements at TPEORP stations. The field observational data, which are used for validation here, were measured at the time of satellite over pass or 10-minutes averaging value around that time. The absolute percent difference (APD) was computed as a quantitative measure of the difference between the derived results on No. i point ($H_{derived(i)}$) and the measured value on No. i point ($H_{measured(i)}$) of one scene, as;

$$APD = \frac{|H_{derived(i)} - H_{measured(i)}|}{H_{measured(i)}} \quad (1)$$

The results show that: (1) The derived surface variables (land surface reflectance and surface temperature), vegetation variables (MSAVI, P_v and LAI) and surface heat fluxes (net radiation flux (R_n), soil heat flux (G_0), sensible heat flux (H) and latent heat flux (λE)) in different months over the study area show a wide range of values due to the strong contrast of surface features. Surface reflectance, surface temperature and sensible heat flux around the lake in the distribution maps are much higher in summer (June, July and August), and at the same time, net radiation flux, soil heat flux and latent heat flux are lower in the area. The reason is that around most of the lake area is desertified grass land; (2) The derived pixel value and average value of surface temperature, net radiation flux, soil heat flux and latent heat flux in June, July and August are higher than that in December and March. This means that there is much more evaporation in summer than in winter and spring in the northern Tibetan Plateau area. It also highlights that the surface heating field ($R_n - G_0 = H + \lambda E$) in summer (1 August) is much higher than it in winter (30 January) and spring (15 April) in the Tibetan Plateau area, but the sensible heat flux is the main role in the distribution of the net radiation flux in winter and spring; (3) During the experimental periods, the derived net radiation flux was larger than that in the HEIFE area (Ma *et al.*, 2002b) due to the high altitude (the higher value of downward short-wave radiation) and land surface coverage of grassy marshland (the lower value of the upward long-wave radiation) in this area; (4) Even the resolutions of ASTER and Landsat-7 ETM are different with from MODIS, and the derived results

here are also comparable to those derived from MODIS data around the relatively homogeneous sites of the CAMP/Tibet area and the whole Tibetan Plateau area; (5) The derived surface reflectance and surface temperature in this research are close to the field measurements with APD less than 9.0%. The derived net radiation flux over the study area are very close to the field measurement with APD less than 8.0%; (6) The difference between the derived surface heating field and the field observation APD is less than 10% (Fig. 5). The mean surface heating field over the Tibetan Plateau area is increasing from January to April, October and August; the values are 315.57 W m^{-2} , 362.50 W m^{-2} , 374.05 W m^{-2} and 454.47 W m^{-2} , respectively; and (7) The derived regional sensible heat flux and latent heat flux with APD less than 9.5% at the validation site in the CAMP/Tibet area is close to the field measurements. It is pointed out that the proposed parameterization methodology for sensible heat flux and latent heat flux is reasonable, and it can be used over the northern Tibetan Plateau area.

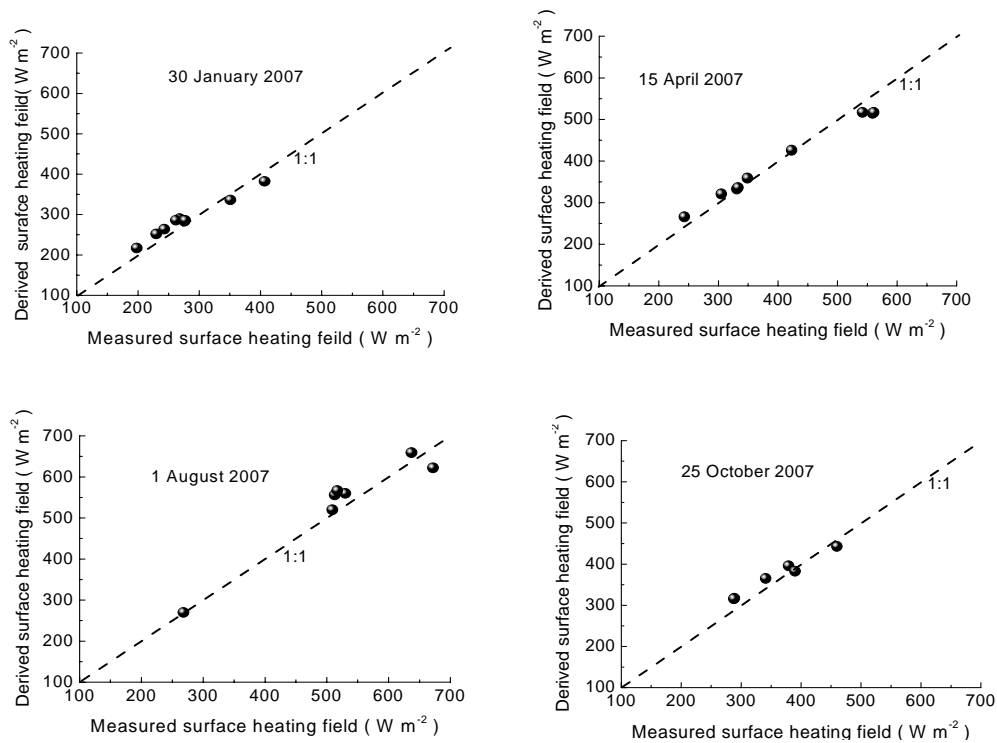


Fig. 5 Comparison of derived results with field measurements for the surface heating field over the Tibetan Plateau area, together with a 1:1 line.

CONCLUDING REMARKS

In this paper, the background of the TPE establishment and the establishing and monitoring plan of long-term scale of the TPE were introduced first. Then the preliminary observational analysis results, such as the characteristics of land surface fluxes partitioning (diurnal variation, inter-monthly variation and inter-annual variation), the structure of ABL and the parameters of land-atmospheric interaction, were shown in this paper. The regional distribution of surface heat fluxes (net radiation, soil heat flux, sensible heat flux and latent heat flux) and surface heating field derived from satellite remote sensing data were also shown by using ASTER data, Landsat-7 ETM data, MODIS data and field observations. The results are in good agreement with field observations. In other words, the regional land surface heat fluxes and surface heating field over a heterogeneous landscape can be determined by using satellite remote sensing and atmospheric boundary layer observations.

All the results in this paper are taken from the stations and meso-scale area over the Tibetan Plateau, or the whole Tibetan Plateau area. In order to up-scale the land surface heat fluxes and surface heating field to the whole heterogeneous landscape of the Third Pole region, more field observations and more satellite data should be used in the future. The proposed parameterization methodology should also be improved to determine the regional land surface heat fluxes and surface heating field over whole Third Pole region.

Acknowledgements This paper was written under the auspices of the Chinese National Key Program for Developing Basic Sciences (2010CB951701), the National Natural Science Foundation of China (40825015 and 40810059006), EU-FP7 project “CEOP-AEGIS” (212921). The authors thank all the colleagues for their very hard work in the three stations (Nam Co Station-NAMOR, Mt Everest-Qomolangma Station-QOMS and Linzhi Station-SETS, Chinese Academy of Sciences) of the Third Pole Environment (TPE) Observation and Research Platform (TPEORP).

REFERENCES

- Batchvarova, E., Gryning, S. E. & Hasager, C. B. (2001) Regional fluxes of momentum and heat over a sub-arctic landscape during late winter. *Bound.-Layer Met.* **99**, 489–507.
- Berk, A., Bernstein, L. S. & Robertson, D. C. (1989) MODTRAN, A moderate resolution model for LOTRAN 7, GL-TR-89-0122.
- Garratt, J. R. (1992) *The Atmospheric Boundary Layer*. Cambridge University Press, New York, USA.
- Ma, Y. & Tsukamoto, O. (2002) *Combining Satellite Remote Sensing with Field Observations for Land Surface Heat Fluxes over Inhomogeneous Landscape, China*. Meteorological Press, Beijing, China.
- Ma, Y., Su, Z., Li, Z.-L., Koike, T. & Menenti, M. (2002a) Determination of regional net radiation and soil heat flux densities over heterogeneous landscape of the Tibetan Plateau. *Hydrol. Processes* **16**(15), 2963–2971.
- Ma, Y., Tsukamoto, O., Ishikawa, H., Su, Z., Menenti, M., Wang, J. & Wen, J. (2002b) Determination of regional land surface heat flux densities over heterogeneous landscape of HEIFE integrating satellite remote sensing with field observations. *J. Met. Soc. Japan* **80**(3), 485–501.
- Ma, Y., Menenti, M., Feddes, R. A. & Wang, J. (2008) The analysis of the land surface heterogeneity and its impact on atmospheric variables and the aerodynamic and thermodynamic roughness lengths. *J. Geophys. Res.* **113**, D08113, doi: 10.1029/2007JD009124.
- Mason, P. (1988) The formation of areally averaged roughness lengths. *Quart. J. Roy. Met. Soc.* **114**, 399–420.
- Qi, J. G., Chehbouni, A., Huete, A. R., Kerr, Y. H. & Sorooshian, S. (1994) A modified soil adjusted vegetation index. *Remote Sens. Environ.* **48**, 119–126.
- Qiu, J. (2008) The third pole. *Nature* **454**, 393–396.
- Verhoef, W. (1997) Theory of radiative transfer models applied in optical remote sensing of vegetation canopies. PhD Thesis, Remote Sensing Department of National Aerospace Laboratory, The Netherlands.
- Zhong, L., Ma, Y., Su, Z. & Salama, M. S. (2010) Estimation of surface temperature over the Tibetan Plateau using AVHRR and MODIS data. *Adv. Atmospheric Sci.* **27**(5), 1110–1118.

Estimating root-layer soil moisture for north China from multiple data sources

XINGGUO MO¹, JIANXIU QIU¹, SUXIA LIU¹ & VAHID NAEIMI^{2,3}

¹ Key Laboratory of Water Cycle & Related Land Surface Processes, Institute of Geographic Sciences and Natural Resources Research, Chinese Academy of Sciences, Beijing 100101, China
moxg@igsnr.ac.cn

² Institute of Photogrammetry and Remote Sensing, Vienna University of Technology, 1040 Vienna, Austria

³ German Remote Sensing Data Centre, DFD, German Aerospace Centre, DLR, 82234 Wessling, Germany

Abstract Knowledge of the spatial and temporal patterns of root zone soil moisture is crucial for agronomical and water resources management. In this study, multiple data sources, including remotely sensed surface soil moisture retrieved from the European Remote Sensing Satellite-1/2 scatterometer (SCAT), soil moisture simulated by the VIP (Vegetation Interface Processes) eco-hydrological dynamical model, and *in situ* soil profile measurements were employed to assess root zone soil moisture over the Baiyang Lake Basin, north China. Correlation coefficients between the SCAT surface soil moisture dataset and VIP simulation in four seasons varied from 0.47 to 0.66 ($p < 0.01$). General agreement among remotely sensed retrieval, the eco-hydrological model prediction and *in situ* measurements shows the potential of the scatterometer for routine acquirement of surface soil moisture patterns in the study area. In addition, the overall agreement between VIP predicted root-layer soil moisture and *in situ* measurements confirms the reliability of using the VIP model for root-layer soil moisture monitoring at seasonal scales.

Key words root zone soil moisture; scatterometer; VIP model; north China

INTRODUCTION

Root zone soil moisture (RZSM) significantly affects surface energy partitioning, water cycling and crop production. Long-term RZSM time series are especially valuable for predicting trends in the soil water environment and understanding the impacts of global warming and land-use/cover change on hydrological and ecological processes, yet are harder to acquire than the surface soil moisture, as most of the remote sensors can only retrieve moisture information in the topmost soil layer.

Data from multiple sources, including remote sensing, simulation and *in situ* measurements, were used to obtain long-term surface soil moisture content in the Loess Plateau (Liu *et al.*, 2009). Remote sensing techniques, especially microwave sensors, provide powerful tools in monitoring surface soil moisture (SSM) over large heterogeneous areas under almost all weather conditions, and have been broadly used (Albergel *et al.*, 2008; Naeimi *et al.*, 2009; Brocca *et al.*, 2010; Lacava *et al.*, 2010). The global RZSM data series is under preparation by the global soil moisture team at the Technical University of Vienna, Austria.

Due to the coarse resolution of remotely sensed RZSM, getting the information of RZSM in a catchment in high resolution is still a pressing issue. In this paper, RZSM in the semi-humid Baiyang Lake Basin, north China is simulated by VIP, a physical process-based eco-hydrological dynamic model. It is then compared at both point scale and regional scale with the RZSM derived from ERS scatterometer data by the filter method proposed by Wagner (2002).

STUDY SITE

Baiyang Lake watershed is located in north China, where elevation steps down from Taihang Mountain (approximately 2627 m a.m.s.l.) in the northwest to the piedmont alluvial plain in the southeast. Soil texture mainly includes loam, sandy and clay loam. Accordingly, grassland, shrub and forest dominate the mountainous area, while cropland and urban are the principal land uses in the plain area (Fig. 1). The prevailing cropping system is the rotation of winter wheat and summer maize. Meteorological records for the last 50 years show annual mean temperatures of 6.8~12.7°, and precipitation of 548 mm, with the peak frequency of rainfall in June to August, providing 80% of the annual amount in the study basin.

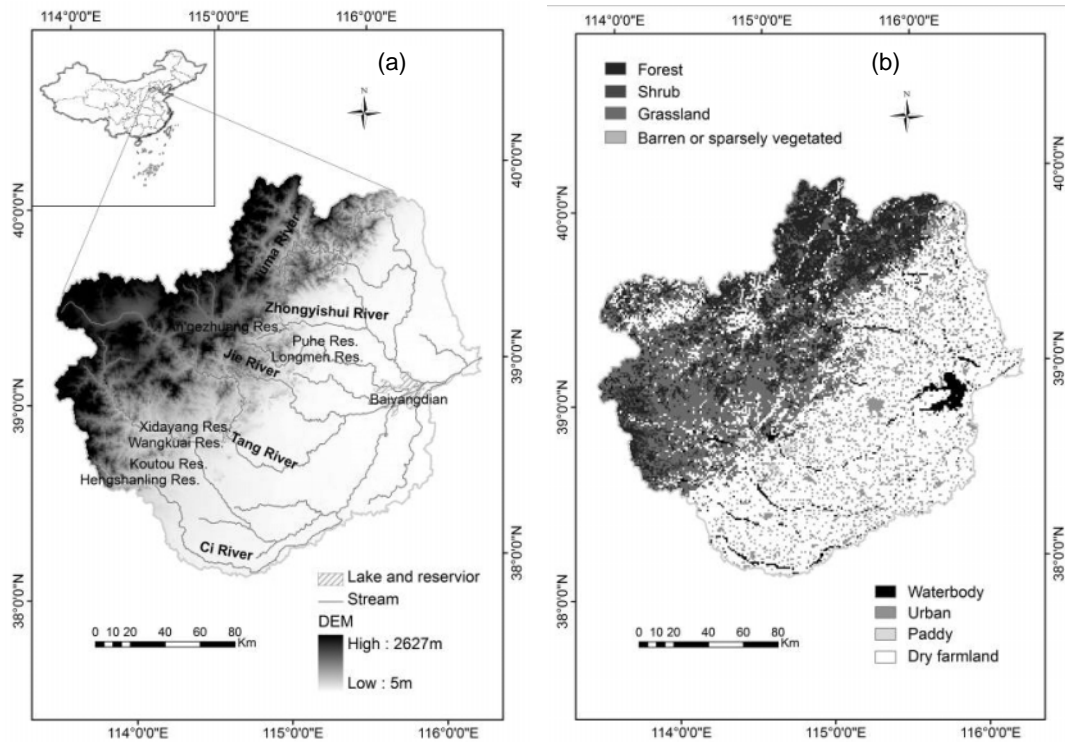


Fig. 1 DEM (a) and land-use (b) maps of the Baiyang Lake Basin.

METHODOLOGY AND DATA

Model description

The Vegetation Interface Processes (VIP) model, a process-based eco-hydrological model, is employed for soil moisture simulation here (Mo *et al.*, 2004). The ecological and hydrological processes are modelled by implementing a coupled 1-D soil–vegetation–atmosphere transfer (SVAT) scheme and remotely sensed vegetation index. In the model, soil water movement is simulated with the discrete Richards equation in three layers (2 cm, 100 cm, 60 cm) and energy fluxes are described with a two-source scheme discerning canopy and soil surface. Remotely sensed vegetation information from Terra-MODIS is used to describe the dynamics of vegetation characteristics.

ERS-1/2 SCAT derived soil moisture

The scatterometer (SCAT) on board the European Remote Sensing Satellite-1/2 (ERS-1/2) detects the radar backscattering coefficient, which is employed in the change detection method (Wagner *et al.*, 2003) to eliminate the effects of vegetation cover. The final products are a relative measure of surface soil moisture ranging from 0 (dry condition reference) to 100 (wet condition reference) obtained by scaling normalized backscatter between the historically lowest and highest values, and re-sampled to approximately 12.5 km.

A semi-empirical exponential filter expressed in equation (1) is used to convert the surface saturation degree $m_s(t_i)$ (<2 cm) retrieved from remote sensing at time t_i into a Soil Wetness Index, SWI(t) at time t , if at least four measurements have been recorded within the most recent period $[t-T, t]$, and taking all measurements within a period $[t-3T, t]$ into calculation (Wagner *et al.*, 2002; Ceballos *et al.*, 2005). In application, determination of the response time T is a crucial step, which is affected by the inter-annual climatic variability and weakly related to soil properties (clay and sand fractions, etc.) (Albergel *et al.*, 2008). Here, the time parameter T is calibrated as 20 to estimate the wetness condition at a depth of 100 cm.

$$SWI(t) = \frac{\sum_i m_s(t_i) \exp(-\frac{|t-t_i|}{T})}{\sum_i \exp(-\frac{|t-t_i|}{T})} \quad (1)$$

Meteorological and soil moisture measurements

In situ measurements, required as input to the VIP model, including daily precipitation, sunshine duration, maximum and minimum air temperature, humidity, air pressure, and wind speed, are recorded at eight national meteorological stations in and around the Baiyang Lake Basin. Relative soil moisture (a ratio of measured soil moisture to field capacity, Liu *et al.* (2008)) at depths of 10, 20 and 50 cm in the first, second and third 10-day periods from Hejian agro-meteorological station in the southeast of Baiyang Lake Basin is used for validation at the point scale.

Irrigation set-up

Irrigation amount per hectare was estimated from data collected from the Rural Statistic Annals of Hebei Province (2006), and irrigation amount was evenly assigned among seedling, recovering, heading and maturity stages of winter wheat, as well as seedling stage of summer maize, if soil water content at these critical growth stages was below 60% of field capacity.

RESULTS

Credibility of SCAT SSM

Due to temporal discontinuity of scatterometer measurements, the SCAT SSM dataset for 2006 is selected to compare with measured daily precipitation as a preliminary evaluation of the credibility of scatterometer data in the basin. Generally, the temporal pattern of soil moisture closely follows the monsoonal precipitation distribution.

Patterns of VIP prediction and SCAT SSM

Daily soil moisture in 2006 with favourable data integrity is simulated by the VIP model with 1 km resolution. Regional surface soil moisture on representative days of four seasons is illustrated in Fig. 2. The values were divided by the field capacity of each pixel according to mechanical composition (from Environmental and Ecological Science Data Centre for West China) for better display effects. It is obvious that surface soil moisture during the summertime exhibited the opposite spatial pattern to the other three seasons. In summer, much more homogeneity with higher wetness conditions of top-layer soil moisture appeared in mountainous areas, whereas in spring and autumn the moisture shows a higher gradient from the piedmont plain to mountainous areas than summer. The wetness discrepancy along the piedmont plain is clear in most cases, and this feature is altered by the monsoon controlled intensive precipitation from June to August.

By comparing Fig. 2 with the interpolated SCAT surface soil moisture map (Fig. 3), it can be inferred that VIP predictions of surface soil moisture are in strong consensus with SCAT measurements. In the three seasons other than summer, the southwest–northeast belt along Taihang Mountain is also easily identifiable, and high value centre alongside Baiyang Lake in the southeast region is depicted in winter (Fig. 3(a)). In summer, the consistency between VIP simulation and microwave data is acknowledged in detecting high values in the northeast and low values in the south (Fig. 3(c)).

The scatterometer dataset is represented as a percentage between driest and wettest conditions, while *in situ* soil moisture is recorded as a ratio of measured soil moisture to field capacity. In order to conduct the inter-comparison between the three datasets, both the modelled and *in situ*

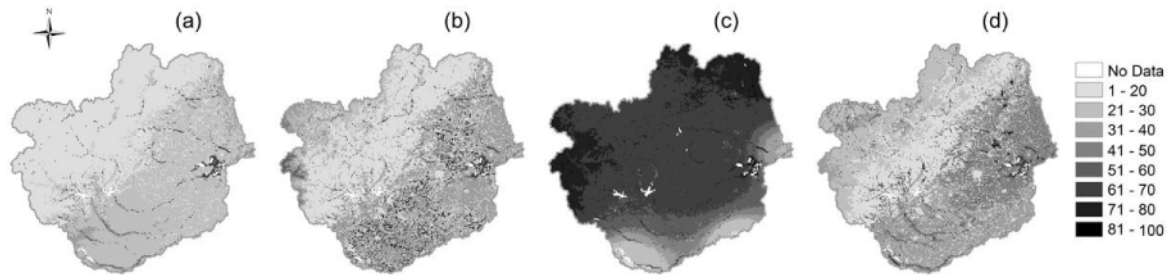


Fig. 2 VIP simulated surface soil moisture in 2006: (a) 31 January; (b) 17 April; (c) 13 August; (d) 28 October.

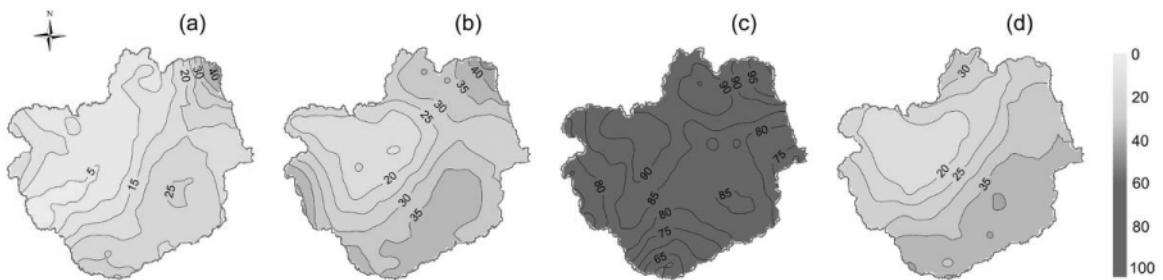


Fig. 3 Interpolated SCAT surface soil moisture with Kriging method in 2006: (a) 31 January; (b) 17 April; (c) 13 August; (d) 28 October.

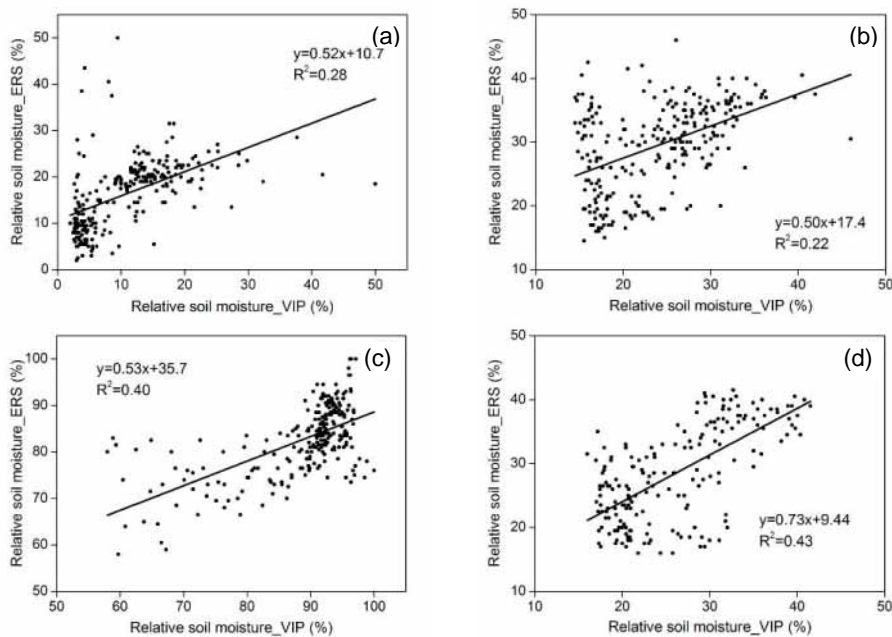


Fig. 4 Comparison of SCAT surface soil moisture with VIP simulation in all grids across the Baiyang Lake Basin in 2006: (a) 31 January; (b) 17 April; (c) 13 August; (d) 28 October.

data are scaled to the scatterometer dataset range, expressed as relative soil moisture (Liu *et al.*, 2009). Secondly, the spatial discrepancy of the model results and remotely sensed data is resolved by aggregating all simulations that fall in the corresponding SCAT grid. Then, we get a preliminary comparison, as shown in Fig. 4. It is found that throughout four seasons, the correlation coefficient (R) between VIP predicted SSM and ERS saturation degree varies from

0.47 to 0.66, whereas the correlation is relatively weak in spring and winter due to low surface wetness or snow cover, while in summer, dense vegetation may also weaken the correlation ($p < 0.01$ for all four seasons).

At point scales, the time series of surface soil moisture from SCAT retrieval, VIP simulation, and ground measurements in 2006 are demonstrated in Fig. 5. It is clear that SSM predicted by the VIP model quickly responds to rainfall and irrigation, as it increases dramatically when irrigations in March and April occur with dry antecedent conditions. Ground observation at a depth of 10 cm approximately follows the fluctuation patterns.

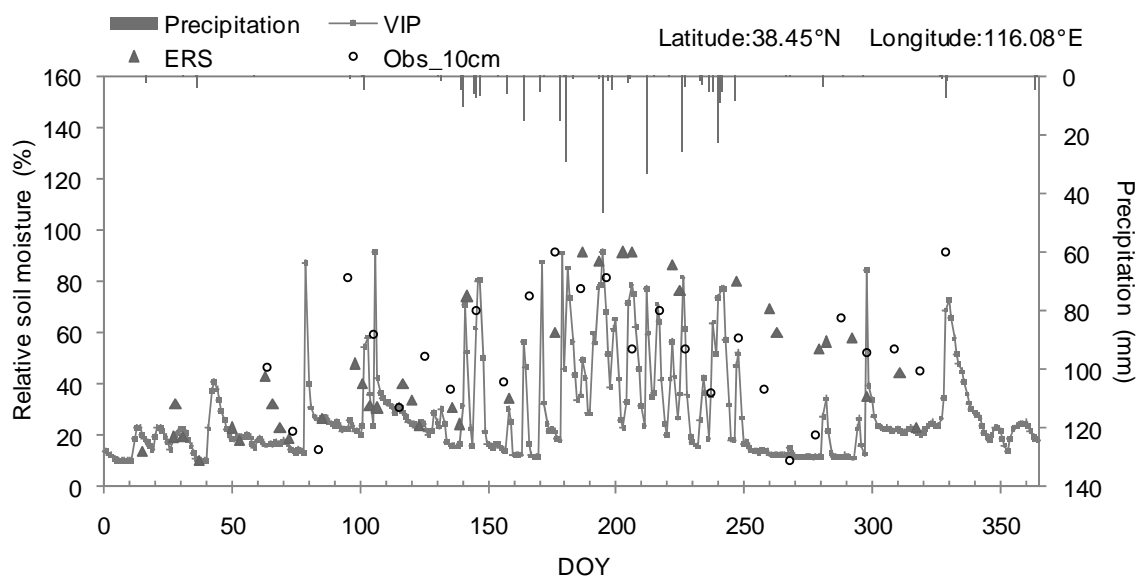


Fig. 5 Time series of surface soil moisture from SCAT retrieval, VIP simulation, *in situ* measurements and daily precipitation in 2006.

VIP simulated and SCAT derived root zone soil moisture

The maps of root zone soil moisture simulated by VIP for the four seasons (figure not shown here) are similar compared to surface soil moisture patterns. However, distinctive differences between mountainous areas and alluvial plains still feature in spring, autumn and winter; and with the supply of Baiyang Lake water, adjacent areas exhibited obvious higher root-layer water content. In summer, precipitation dominates the spatial distribution of root-layer water content, since infiltration rate determines the replenishment of the root-layer soil.

Retrieved root-layer soil moisture in spring and autumn is consistent with VIP model predictions, showing significant correlation (R^2 are 0.31 and 0.45 separately, with $p < 0.01$). However, the correlations are poor in winter and summer, with R^2 of 0.02 and 0.01, respectively. The moisture shows a narrow range of spatial variability due to low precipitation and frost in the wintertime. Also, snow cover is a crucial factor biasing remote sensing retrieval. Propagation of uncertainties due to high vegetation fraction spread from surface to root-layer moisture lead to low correlation with model prediction in summertime.

Note that different responding time parameters will result in various lag time intervals between external replenishment and root zone response, and the calibrated value 20 conforms to the general pattern of soil moisture transfer velocity under local weather processes. From Fig. 6, it can be seen that all three datasets display much smoother temporal trends than surface soil moisture. In VIP simulation, the rapid increases resulted from intense rainfall events or irrigations are still discernable. *In situ* measurements at 20 and 50 cm depths display relatively consistent distribution with the model predictions, but in a wider fluctuation amplitude.

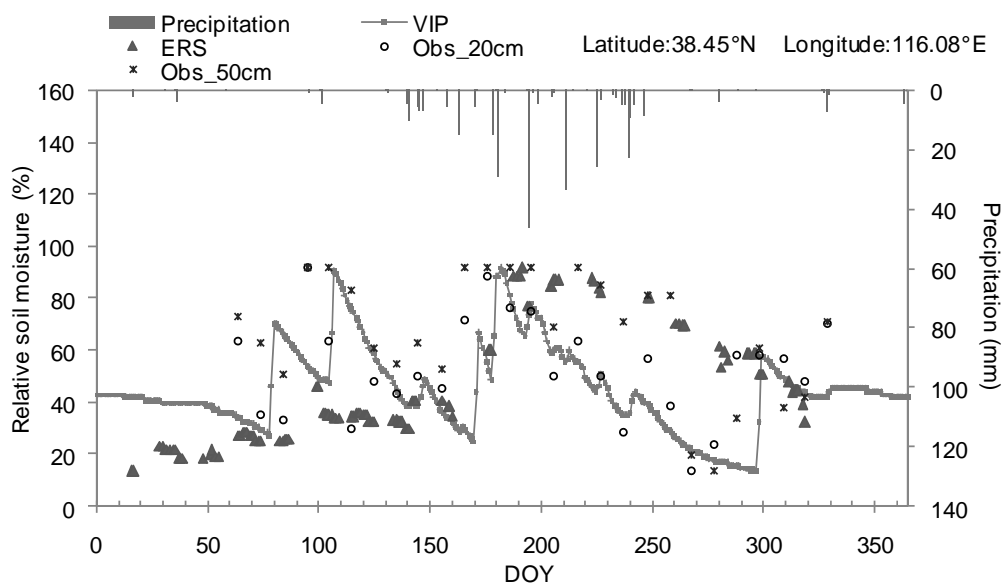


Fig. 6 Time series of root zone soil moisture from SCAT dataset, VIP simulation, ground measurements and daily precipitation in 2006.

CONCLUSIONS

In this paper, the results of the VIP model prediction are validated with ground measurements and ERS scatterometer data of surface and root-layer soil moisture time series in the Baiyang Lake Basin.

Overall, the model simulation shows a general consistency with the scatterometer dataset, having correlation coefficients from 0.47 to 0.66 throughout the four seasons; the correlation is enhanced in autumn, but decreased in summer and winter. Exponential-filter based root-layer soil moisture from SCAT data shows similar seasonal variation with the VIP simulation. However, the filtered data are less reliable on account of snow effects in winter and dense vegetation cover during summertime owing to the propagation of unreliable surface information. The close temporal consistency of model predicted root-layer soil moisture and ground truth showed the potential of the VIP model to simulate the root zone soil moisture for the Baiyang Lake Basin. Considering heterogeneity of soil moisture, for better estimation of RZSM the fusion of remotely sensed moisture with process-based models and *in situ* measurements still needs to be further explored.

Acknowledgements This study was jointly supported by the Natural Science Foundation of China grant (40830636, 41071024), the Chinese Ministry of Science and Technology for “973” project (2010CB428404, 2009CB421307), International Cooperation project (0911), Water Special Key project (2009ZX07210-006) and the Knowledge Innovation Project of Chinese Academy of Sciences (KZCX2-YW-Q06-1-3, KZCX2-YW-433) and the geoland2 project funded by the European Commission (<http://www.gmes-geoland.info/home.html>).

REFERENCES

- Albergel, C., Rüdiger, C., Pellarin, T., Calvet, J., Fritz, N., Froissard, F., Suquia, D., Petitpa, A., Pignatelli, B. & Martin, E. (2008) From near-surface to root-zone soil moisture using an exponential filter: an assessment of the method based on *in-situ* observations and model simulations. *Hydrol. Earth System Sci.* **12**, 1323–1337.
- Brocca, L., Melone, F., Moramarco, T., Wagner, W. & Hasenauer, S. (2010) ASCAT soil wetness index validation through *in situ* and modeled soil moisture data in central Italy. *Remote Sens. Environ.* **114**(11), 2745–2755.
- Ceballos, A., Scipal, K., Wagner, W. & Martinez-Fernandez, J. (2005) Validation of ERS scatterometer-derived soil moisture data in the central part of the Duero Basin, Spain. *Hydrol. Processes* **19**(8), 1549–1566.

- General Office of People's Government of Hebei Province, Statistics Bureau of Hebei Province (2007) *Rural Statistic Annals of Hebei Province*. China Statistical Publishing House, Beijing, China.
- Lacava, T., Brocca, L., Calice, G., Melone, F., Moramarco, T., Pergola, N. & Tramutoli, V. (2010) Soil moisture variations monitoring by AMSU-based soil wetness indices: A long-term inter-comparison with ground measurements. *Remote Sens. Environ.* **114**(10), 2317–2325.
- Liu, S., Mo, X., Zhao, W., Naeimi, V., Dai, D., Shu, C. & Mao, L. (2009) Temporal variation of soil moisture over the Wuding River Basin assessed with an eco-hydrological model, in-situ observations and remote sensing. *Hydrol. Earth System Sci.* **13**(7), 1375–1398.
- Liu, S., Mao, L., Mo, X., Zhao, W. & Lin, Z. (2008) Analysis of spatial variability of soil moisture and its driving force factors in the Shaanxi-Henan region along the Yellow River. *Climatic Environ. Res.* **13**(5), 645–657 (in Chinese).
- Mo, X., Liu, S., Lin, Z. & Zhao, W. (2004) Simulating temporal and spatial variation of evapotranspiration over the Lushi basin. *J. Hydrol.* **285**(1–4), 125–142.
- Naeimi, V., Bartalis, Z. & Wagner, W. (2009) ASCAT soil moisture: an assessment of the data quality and consistency with the ERS scatterometer heritage. *J. Hydrometeorol.* **10**(2), 555–563.
- Wagner, W., Lemoine, G., Borgeaud, M. & Rott, H. (2002) A study of vegetation cover effects on ERS scatterometer data. *IEEE T Geosci. Remote.* **37**(2), 938–948.
- Wagner, W., Scipal, K., Pathe, C., Gerten, D., Lucht, W. & Rudolf, B. (2003) Evaluation of the agreement between the first global remotely sensed soil moisture data with model and precipitation data. *JGR Atmos.* **108**(D19), 4611.

Modelling water re-uses of a tank cascade irrigation system based on satellite and field observations

XUELIANG CAI¹, YUANLAI CUI² & NICOLAS ROOST³

- 1 International Water Management Institute (IWMI), Southern Africa Office, Private Bag X813, Silverton 0127, Pretoria, South Africa
x.cai@cgiar.org
- 2 State Key Laboratory of Water Resources & Hydropower Engineering Science, Wuhan University, Wuhan 430072, China
- 3 IWMI, Melbourne, Australia

Abstract Many canal irrigation systems in southern China are supplemented by numerous surface storages, which are often connected to one another, leading to improved flexibility in managing water. This study aims to examine the role of storage cascades in capturing and re-using return flows through water balance modelling based on satellite and field observations. The weather data, irrigation application, and pond water level have been monitored in two selected cascades, and a water balance model is developed to account for the dynamic water balance with inputs from remote sensing and GIS analysis. The results showed that, on average, each storage structure is connected to 4.8 others, facilitating intense water re-use in the region. The return flows captured by cascades account for up to 20% of irrigation diversions. However, there are significant losses during the redistribution processes. Remote sensing and GIS-based analysis have proved powerful techniques in parameterizing complex hydrological processes.

Key words irrigation system; tank cascade; water balance; remote sensing

INTRODUCTION

The irrigation sector is the single biggest consumer of freshwater resources. While “real” water saving is still difficult to measure, water saving irrigation itself is becoming an imperative for an increasingly water-scarce world. The ever-rising pressure on water resources is pushing agricultural water users to adapt to water scarcity by producing more food with less water, which requires both technical upgrades and institutional reform.

Hydrology in irrigated areas is strongly affected by irrigation and drainage practices, which makes it extremely difficult to model the dynamic water cycling processes (Kite & Droogers, 1999). The existence of local storages such as small reservoirs/tanks and ponds adds extra complexity to the system as they often function as water collectors and distributors, which makes it possible for water losses upstream re-use downstream (Roost *et al.*, 2008b). The local storages can either be operated separately or through connection to main irrigation canals, which forms the so-called melon-on-the-vine system in China (Wang, 1984). Such systems provide added flexibility to irrigation and drainage management.

Assessing water re-use through effective water accounting helps to assess irrigation performance, and to identify irrigation potential. It is especially helpful to understand real water saving as water re-use is considered. This paper describes a water accounting approach to analyse water re-use through local storages. Evapotranspiration (ET) estimation from remote sensing is combined with field hydrometric observations to close the water budget.

STUDY SITE AND FIELD MONITORING SCHEME

The Zhanghe Irrigation System (ZIS), served by a 2 billion m³ multipurpose reservoir, is located in the Yangtze River basin, central China. The geographic extent of the system is 5540 km², which is mainly laid out in hilly areas. The area receives an average annual rainfall of 960 mm, close to 60% of which occurs between May and September. Around 29% of the command area was designed to be irrigated with supply from the reservoir. However, the actual irrigated area has shrunk significantly. The rotation of irrigated rice in summer and rainfed rapeseed in winter is the predominant cropping pattern in the region.

The system is characterized by numerous local storages, including small- to medium-sized reservoirs, in addition to the main reservoir. It was reported there were 31 150 ponds and 9 medium reservoirs in the command area of the third main canal of ZIS alone. The storage capacity of these ponds totals 106 million cubic metres (m³), which accounts for 60% of the annual average irrigation water supply from the main reservoir. These storages, scattered throughout the system, play a key role in capturing runoff and providing irrigation at dry spells (Roost *et al.*, 2008a).

Field monitoring schemes were set up for three farm ponds. The ponds were connected to one another with a drainage canal running through paddy fields, forming a pond cascade system (Fig. 1). Water depth at each pond was measured daily. Weather data including temperature (minimum, maximum, average), humidity, sun hours, precipitation, and pan evaporation was recorded at an irrigation experiment station 1 km away. Irrigation inflows were measured at canal outlets.

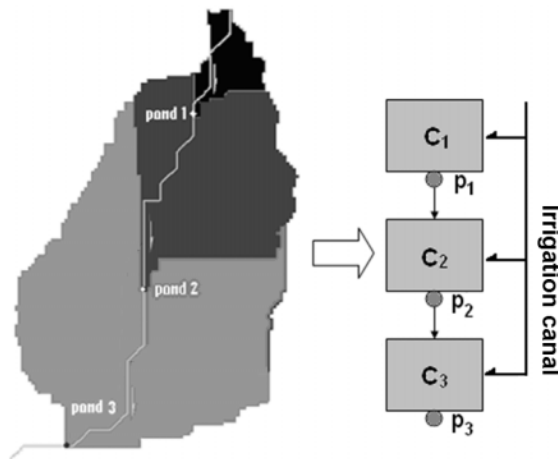


Fig. 1 Schematisation of the pond cascade. The three ponds were connected to each other and the downstream ponds collect return flows from their catchments and upstream ponds.

MODELLING WATER REUSES OF THE POND CASCADE SYSTEM

Water balance and re-uses model

Water movements in the pond cascade irrigation system involve complex processes. Figure 1 illustrates that in addition to the rainfall–runoff process, there is another process of runoff being captured and redistributed. Ponds in this case act as regulators controlling water movements and consumption. Jayatilaka *et al.* (2003) estimated pond water balance using a simplified approach to determine water availability in an irrigation tank cascade system. This study modified the model to account the daily water balance for the three monitored ponds as expressed in equation (1):

$$V_{i+1} = V_i + R \cdot A + In - E_0 \cdot A - L \cdot V_i - Irri \quad (1)$$

where V_{i+1} and V_i are pond water volumes of day $i+1$ and day i , respectively (in m³); R is direct rainfall (m) on pond surface; A is pond surface area (m²); In is the total of surface and subsurface inflow to the pond on day i ; E_0 is open water body evaporation (m); L is the coefficient of water losses due to percolation and seepage (m³) and $Irri$ is pond irrigation release on day i (m³). In equation (1) daily irrigation release is measured and water volume is calculated using a depth–volume rating curve. We used rainfall and pan evaporation measurements from the nearby station directly. Two variables, viz. daily inflow and percolation and seepage losses, then remained to be determined. The percolation and seepage losses could be estimated based on dry spell data. During dry spells there is no surface flow into the pond and subsurface inflow reaches minimum values (base flow). However, this baseflow makes no impact on pond water balance as there is always

outflow from the pond. Therefore the percolation and seepage losses excluding base flow could be estimated assuming zero inflow during a dry spell. As ponds are often small in size and the rice growing season is limited to approximately 3 months with similar weather conditions, this loss rate is assumed to be constant all through the rice growing season. This leaves In as the only variable to be solved to balance equation (1).

Water movement in the pond cascade system involves many complex processes. A significant amount of water, both from irrigation supply and rainfall, is captured and consumed through evaporation or transpiration, or lost to deep percolation. Some water, however, travels through fields and natural landscapes and joins the drainage networks, and is then captured by local storages such as ponds. The same process occurs again further downstream when the water is distributed from the pond. This continuous process is illustrated in Fig. 1 (right). The amount of returned flows captured by ponds can be estimated using equation (2) (Cai *et al.*, 2007):

$$Q_r = \sum_{m=1}^M \sum_{n=1}^{ndp_m} (A_m \cdot q \cdot \eta^{n+1} \cdot \mu^n) \quad (2)$$

where Q_r is the accumulated return flows captured by ponds given q metres of water input (including irrigation and rainfall), M is the length of pond cascade or number of ponds connected to each other, A_m is the catchment area of pond number m , ndp_m is the number of downstream ponds of the same pond; it also represents the probability of being captured again by downstream ponds, η is the coefficient of returns of an individual pond; it is calculated as pond inflow divided by catchment inflow, and μ is the pond water supply efficiency, which is calculated as pond water supply divided by total water inflow to the pond.

Remote sensing and GIS analysis for model parameterization

Pond cascades were identified through interpretations of high resolution images and GIS spatial analysis. High resolution images from IKONOS (Roost *et al.*, 2008a) were used to delineate pond surface area and land use of the catchments. The one metre resolution image acquired on 12 June, 2002 provides good details to identify boundaries of ponds and farm fields over the area of 100 km² that it covers. A Digital Elevation Model (DEM) of 25 m in resolution was used to extract the catchment boundary of each pond (Roost *et al.*, 2008a). The pond cascades were identified through topology analysis of the catchment polygons. The basic theory is that if one polygon is contained by another, then the pond corresponding to the former falls in the catchment of the pond corresponding to the latter. The analysis was performed in the ARCGIS platform until all catchment polygons are exhausted.

Actual ET was estimated by integrating weather data and Landsat ETM+ images. Daily crop potential ET was estimated using the United Nations Food and Agriculture Organization (FAO) standard approach with weather data from the nearby station. The daily potential ET values provide a good indication of temporal variation in crop water consumption under ideal conditions. However, the actual crop conditions vary significantly. There are also large non-cultivated areas which consume water at different rates. To understand the spatial distribution of ET, the Simplified Surface Energy Balance (SSEB) algorithm (Senay, 2007) was used to estimate actual ET using a Landsat ETM+ image acquired at the peak rice growing season (a detailed description is beyond the scope of this paper, but can be found in Cai & Cui (2009)). Assuming a fixed distribution of ET over the rice growing season, the seasonal ET of each grid is calculated.

RESULTS

Dense distribution of ponds is found in the study area and they are well connected. Results show 2795 storages exist within an area of 71 km², 93% of which fall in one or more pond catchments. This number is reduced to 2139 when nearby storages (within 5 m distance) were merged. About 96% of the ponds are within the catchment boundaries of other ponds. The average length of pond

cascades is 5.75 m, with the longest found to be 17 m. The spatial distribution of ponds showed no apparent pattern, but the length of pond cascades, which indicates the hydrological connectivity of ponds, shows a declining trend when slope increases (Fig. 2).

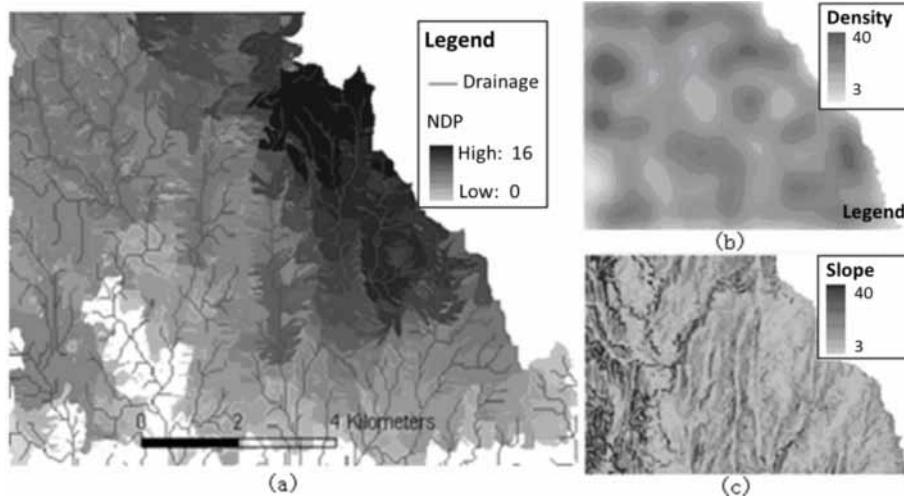


Fig. 2 The characteristics of pond cascades in the study site, (a) spatial distribution of number of downstream ponds (NDP, $NDP = \text{cascade length} - 1$), (b) pond density (number per km^2), and (c) slope (degree).

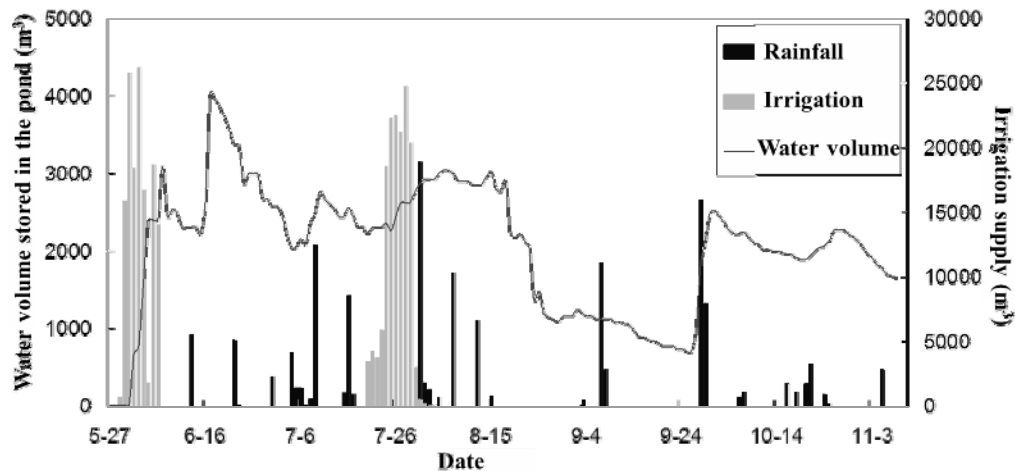


Fig. 3 Observed daily water volume, irrigation and rainfall of pond number 2.

Daily water balance components of pond number 2 are plotted in Fig. 3. The study area received two irrigation supplies: one in June and one at the end of July/beginning of August. The pond water volume curve is responsive to irrigation supply and rainfall events. A dry spell was found in September, which lasted for 3 weeks. The percolation and seepage coefficient is estimated to be 0.9%, 1.5%, and 1.3% for the three ponds, respectively.

Water balance of the three ponds for the rice growing season is summarized in Table 1. The gross inflow (rainfall plus irrigation) to the cascade catchment is 873 mm. The average return coefficients of individual pond for rainfall and irrigation are 20.9% and 16.1%, respectively. The return coefficient of irrigation is only slightly lower than that of rainfall, indicating a mismatch between irrigation supply and field crop water requirement. Excess irrigation is the major reason, while the less than optimal timing of irrigation delivery also contributes to the problem. Pond

Table 1 Summary of pond water balance and the return flows.

Pond ID	V m ³	A _m m ²	N*	E ₀ (mm)	Percolation		Rainfall			Irrigation			Irrigation release	
					L (mm)	Depth (mm)	Depth (mm)	Returns (mm)	η (%)	Depth (mm)	Returns (mm)	η (%)	Depth (mm)	% to returns
1	2372	20230	1.95	36.6	0.9	67.2	467.2	132.5	28.4	405.8	95.9	23.6	124.2	54.4
2	4100	96440	2.66	18.7	1.5	30.4	467.2	61.1	13.1	405.8	52.0	12.8	57.1	50.5
3	21603	235920	1.59	14.0	1.3	116.1	467.2	97.8	20.9	405.8	48.1	11.9	46.7	32.0
Avg.	9358	117530	2.07	23.1	1.2	71.2	467.2	97.1	20.8	405.8	65.3	16.1	76.0	45.6

Note: * is the number of refills for ponds.

number one has a much higher coefficient of returns. This is because this pond has a lower percentage of paddy fields (high water consumption) in its catchment. This pond also serves as a fish pond. Farmers were more actively engaged in the pond management.

The total water returns of the pond cascade are calculated by replacing variables with the values given in Table 1. The accumulated return flows from rainfall ($Q_{r-ra\ inf\ all}$) and irrigation ($Q_{r-irrigation}$) are 126.1 mm and 85.2 mm, respectively. The coefficients of returns for rainfall and irrigation are 27.1% and 20.7%, respectively. Both figures are higher than those of individual ponds.

Pond water capture and supplying capacity can also be estimated for the study area. The total water captured by ponds is calculated by multiplying pond storage capacity by number of refills. The total pond storage is estimated to be 11 162 255 m³ (Roost *et al.*, 2008a). The total water captured by ponds is then estimated to be 23 105 868 m³. In Table 1, the effective water supply by ponds is estimated to be 45.6% of captured water. Hence the effective irrigation supply by all ponds in the study area is 10 536 276 m³, which accounts for 21.8% of irrigation supply to the study area.

DISCUSSIONS AND CONCLUSIONS

Local storages, such as ponds, are important sources of irrigation water supply to sustain crop yields and make more efficient use of water. The highly distributed ponds supplement the main irrigation canal and form a powerful water recycling mechanism. In this study area the canal operations are less than optimal, as indicated by runoffs generated from excess irrigation supply. However, the ponds capture return flows and make the water available again to downstream users, which significantly improves water use efficiency. Conventional irrigation efficiency estimates only take into account irrigation canal to field applications, hence completely omitting water re-use.

The cascade system greatly improves the flexibility of ponds and their capacity to capture and supply water. The ponds are often naturally connected to each other through invisible drainage networks. This hydrological connection, as is often ignored in formal management plans, not only helps in water saving at field scales, but also up-scales to improve system level water management performance. Good irrigation water management comes not only from the supply side, but also from small users. Appropriate facilities, together with matching management practices, form the key to achieve better irrigation water management.

There are also a number of issues to be considered for the development of local storages. It is observed that the more ponds are interconnected, the more powerful they are in recycling water. However, more ponds also mean more open water evaporation. In this study the E₀ from the ponds accounts for 14% of the total inflow. This non-beneficial consumption has to be balanced with the positive contribution of ponds. The economic returns of pond construction also need to be assessed. The density of ponds in the study area reaches 39 per km². Further increases in the number of ponds will probably reduce inflows to the existing ponds, hence reducing their performance.

Remote sensing and GIS analysis are useful tools to parameterize hydrological models. The basic land use features supplemented by GIS spatial analysis makes it possible to identify pond cascades which are often limited to the spatial extent of less than 1 km². Remote sensing based ET estimates also enables evapotranspiration to be more precisely calculated – a key component of the water balance.

REFERENCES

- Cai, X. L., Cui, Y. L., Dai, J. F. & Luo, Y. F. (2007). Small storage based return flows estimation and evaluation in melon-on-the-vine irrigation system. *J. Wuhan University (Engng edn)* **40**(2), 46–50.
- Cai, X. L. & Cui, Y. L. (2009) A simplified ET mapping algorithm and the application in Zhanghe Irrigation District. *J. Irrig. Drain.* **28**(2), 51–54.
- Jayatilaka, C. J., Sakthivadivel, R., Shinogi, Y., Makin, I. W. & Witharana, P. (2003) A simple water balance modelling approach for determining water availability in an irrigation tank cascade system. *J. Hydrol.* **273**, 81–102.
- Kite, G. & Droogers, P. (1999) Irrigation modelling in the context of basin water resources. *Int. J. Water Resour. Dev.* **15**(1), 43–54.
- Roost, N., Cai, X. L., Molden, D. & Cui, Y. L. (2008a) An assessment of distributed, small-scale storage in the Zhanghe Irrigation System, China. Part I: Storage capacities and basic hydrological properties. *Agric. Water Manage.* **95**, 698–706.
- Roost, N., Cai, X. L., Turrall, H., Molden, D. & Cui, Y. L. (2008b) An assessment of distributed, small-scale storage in the Zhanghe Irrigation System, China. Part II: Impacts on the system water balance and productivity. *Agric. Water Manage.* **95**, 685–697.
- Senay, G. B., Budde, M., Verdin, J. P. & Melesse, A. M. (2007) A coupled remote sensing and simplified surface energy balance approach to estimate actual evapo-transpiration from irrigated fields. *Sensors (special issue: Remote Sensing of Natural Resources and the Environment)* **7**, 979–1000.
- Wang, T. (1984) *Water accounting of Melon-on-the-Vine Irrigation System*. Water Resources and Hydropower Publishers, Beijing, China.

3 Hydrological Application

A remote sensing based ET algorithm for Australian agro-ecosystems: SAM-ET

MOHSIN HAFEEZ, YANN CHEMIN & UMAIR RABBANI

International Centre of Water for Food Security, Charles Sturt University, Wagga Wagga 2678, NSW, Australia
mhafeez@csu.edu.au

Abstract On the Australian continent, approximately 90% of the precipitation that falls on the land is returned back to the atmosphere through actual evapotranspiration (ET_a). However, it is almost impossible to measure it directly at a meaningful scale in space and time through traditional methods. Since the late 1990s, numerous algorithms have been developed to estimate ET using remote sensing (RS) data. However, Australian environmental conditions are unique and so full adaptation of the overseas-developed RS-based ET algorithms is needed before their use in Australia. A Spatial Algorithm for Mapping ET (SAM-ET) is a two source energy balance algorithm which has been continually developed and evaluated on water-related projects within Australian irrigation systems initially, over several years. This article provides an overview of ground truth data collected using a leaf area index meter, crop reflectance data from CROPSCAN, two Eddy Covariance Systems and two Large Aperture Scintillometers in the heterogeneous landscapes since 2007 to measure ET_a fluxes. The ground truth data were collected to develop new empirical and semi-empirical relationships for improving a SAM-ET algorithm dedicated to Australian agro-ecosystems. Initial results of the SAM-ET model are encouraging and this research work is a stepping stone in the development of an operational ET monitoring system which will be linked with on-going testing and development of a modelling framework for estimation of water productivity across different spatial scales in the Murray-Darling basin.

Key words remote sensing; actual ET; SAM-ET; Australia; irrigation

INTRODUCTION

In Australia, an increased demand for the scarce water has shifted irrigation water management strategies from increasing water supplies to innovatively managing the existing water resources at sustainable levels. An accurate spatial and temporal knowledge of the complex hydrological processes at different spatial scales is essential for water sharing, resources planning and regulation in any irrigation system. The current ground-based monitoring and measuring techniques have limited ability to capture the spatial and temporal variation of different hydrological variables (rainfall, actual evapotranspiration (ET_a), recharge and soil moisture) when determining spatial water balances at regional and catchment scales (Schmugge *et al.*, 2002). Remote sensing (RS) data can resolve some of the difficulties associated with determining spatial water balances due to scientific developments in the estimation of spatially distributed ET_a with the use of modern satellite imagery. On the Australian continent, approximately 90% of the precipitation that falls on the land is returned back to the atmosphere through ET_a . ET_a is the most important but uncertain component in a closing water balance of any irrigation system.

Different RS methods for estimating ET_a are broadly categorised, i.e. analytical *versus* (semi) empirical approaches. Analytical approaches include detailed biophysical processes and require various parameters, mainly the surface biophysical attributes, which can be retrieved either through satellite-based remote sensing or through field campaigns (Jackson *et al.*, 1981, 1988). The foundation of the analytical approaches was laid by Menenti (1984) by proposing a two layer combination equation for a drying soil to be able to reduce to the Penman-Monteith combination equation. Menenti & Choudhury (1993) extended the Crop Water Stress Index (CWSI) concept to the Surface Energy Balance Index (SEBI) approach, which was based on the use of Planetary Boundary Layer (PBL) scaling. However, SEBI results for the Aral Sea region revealed that the parameterization was not universally applicable (Menenti *et al.*, 2001). Another two-source model (Norman *et al.*, 1995) calculates the surface fluxes separately for the soil and vegetation components from RS and ground-based observations and then sums to satisfy the total energy balance at each pixel. RS inputs are radiometric temperature and NDVI. However, this model can overestimate the ET_a over certain land surface conditions, i.e. dry and bare soil (Savage *et al.*, 2005).

Cleugh *et al.*, (2004) used convective boundary layer (CBL) budget methods for estimating regionally-averaged sensible and latent heat fluxes in OASIS experimentation in Australia. However, this method requires detailed information about atmospheric boundary layer (ABL) profiles, meteorological and physiological parameters, vegetation descriptions and antecedent data (rainfall, soil moisture), which is difficult to obtain at a catchment level. Compared to all previous RS algorithms for heat flux estimation, the Surface Energy Balance System (SEBS) developed by Su (2002) has an important advantage through its inclusion of a physical model for the estimation of the roughness height for heat transfer, which is the most critical parameter in the parameterization of the heat fluxes of a land surface, and SEBS validations have been completed successfully in different geographical locations at different scales (Su & Jacobs 2001; Su *et al.*, 2003; Su, 2005).

On the empirical side, the work of Nieuwenhuis *et al.* (1985) was among the earliest attempts but was valid only for a single crop. Later, the Surface Energy Balance Algorithm for Land (SEBAL), an intermediate approach using both empirical relationships and physical parameterizations, was developed in Spain (Bastiaanssen *et al.*, 1998a,b). SEBAL is a thermodynamically-based model, which partitions the sensible heat flux and latent heat of vaporization flux. Many field validations of the SEBAL model have been undertaken in different areas, especially in arid and semi-arid areas. However, due to the difficulties associated with defining exactly the right pixels of dry and wet condition, its application is limited to a certain degree (Su, 2005). To resolve some of the limitations of the SEBAL model, some corrections have been made by Su (2002) to improve its applicability. Su & Pelgrum (1999) remedied a theoretical problem with SEBAL and added a scheme to apply NWP fields with an up-scaling and down-scaling approach. In another effort, Roerink & Su (2000) developed a new method to derive the surface energy fluxes from RS measurements, called the Simplified Surface Energy Balance Index (S-SEBI), which fits dry and wet cases present in the spatial radiometric data and showed reasonable success for application of the approach to semi-arid areas (Roerink & Su, 2000). Recently, Allen *et al.*, (2007) modified SEBAL to overcome uncertainties and developed METRIC (Mapping Evapotranspiration with high Resolution and Internalized Calibration), an energy-balance-based ET mapping approach which is tied down and partly calibrated using ground-based reference ET (from weather data) to work well in advective conditions of the western USA.

The major reason causing uncertainties in the various RS-based algorithms for estimation of ET_a over agro-ecosystems in Australia is that almost all the algorithms were developed for different climatic conditions, i.e. not in Australia. Therefore, there is a need to develop an indigenous robust and dynamic spatial algorithm for mapping of ET_a using RS for Australian agro-ecosystems. In 2007, the Australian National Water Commission (NWC) launched a major initiative on standardising and adapting complex RS-based algorithms developed overseas to Australian agro-ecosystem conditions. One of the innovative ET project is "Spatial Algorithm for Mapping ET (SAM-ET) for Water Productivity and Vegetation Health in the Australian Agro-Ecosystem", for the development of an RS-based algorithm to estimate ET_a in Australia and to validate these fluxes with *in situ* measurements collected using eddy covariance flux towers and large aperture scintillometers (LAS).

This research expands on the continuous collection of ground truth data to feed into various semi-empirical relationships enabling the calibration of a simple two-source energy balance in order to provide instantaneous RS-based ET under Australian conditions. Standard satellite RS products of the Terra/MODIS satellite, such as NDVI, LST, LAI and albedo correlations to ground truth through scales differences are explored. The present paper explains the relationship developed between MODIS satellite and ground-based instrument data under Australian conditions and presents initial results of the SAM-ET model for estimation of daily ET_a in the Murray Darling Basin (MDB).

STUDY AREA AND DATA COLLECTION

The project is being implemented in four agro-ecosystems of the MDB, i.e. Murrumbidgee, Coleambally, Limestone Coast and the McIntyre Brook Queensland (Fig. 1(a)) to collect various

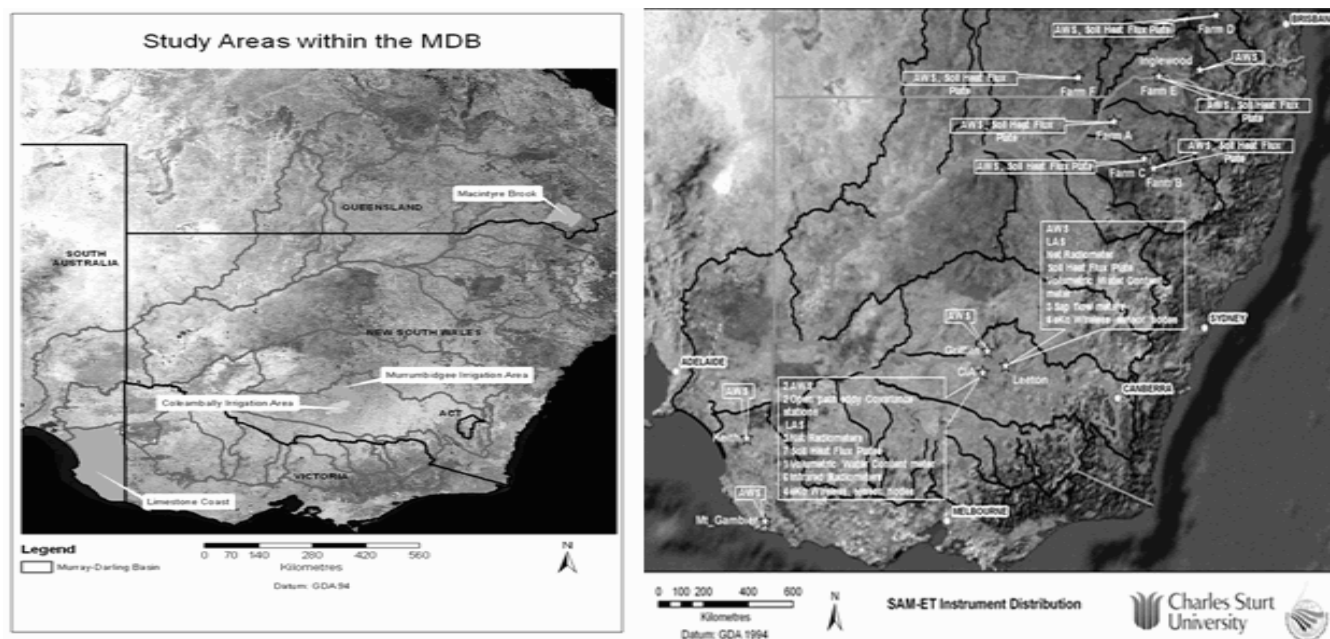


Fig. 1 (a) Study areas within the MDB; and (b) SAM-ET instrument distribution within MDB.

critical vegetation-related data, meteorological data and flux data. The project team has access to continuous time series data from two automatic weather stations (AWS), two eddy covariance systems and two LAS installed in the irrigated areas (Fig. 1(b)), which are used for the validation of ET_a results. More details can be found in Hafeez *et al.* (2010). The extensive field campaigns have been carried out in the Murrumbidgee (MIA; 230 000 ha) and the Coleambally irrigation areas (CIA; 79 000 ha) since the beginning of 2008 to develop the empirical relationship for validating the SAM-ET framework for mapping ET_a across the regions. There is a variety of land cover types in MIA and CIA ranging from horticulture (grapes and citrus), rice, cereals, vegetables to pasture and others. Field campaigns have also been carried out in Macintyre Brook catchment and Limestone Coast on a need basis during the different growing seasons since 2008.

The project also used the CROPSCAN Multispectral Radiometer (MSR) and LAI meter (Li-COR 2000 Plant Canopy Analyser) on row crops including corn (maize), sorghum, cotton, canola and winter grains such as barley and wheat in the study areas. Two to three scans per point are taken so that both the crop and inter-row soil is measured. Scans are taken on homogenous (pure pixels) as either crop or ground to represent satellite image pixels (mix of canopy and ground soil). Averaged MSR scans were considered as mixed pixels (mix of canopy and soil) to avoid bias in canopy or soil.

METHODOLOGY

The proposed formulation follows a two-source energy balance approach, inspired especially by TSEB (Kustas & Norman, 1999) and SEBS (Su, 2002). SAM-ET is a two-source energy balance algorithm based on thermodynamic flux and radiation equilibrium within the Earth skin surface (Hafeez *et al.*, 2009; Hafeez & Chemin, 2010; Chemin & Hafeez, 2010). The model is being continually developed and has been evaluated on water-related projects in Australia for several years. This algorithm is an image-processing technique comprised of 32 computational steps that calculate ET_a and other energy exchanges at the Earth's surface using optical/thermal satellite imagery. The imagery source is standardized by using a common and identical pre-processing procedure. The pre-processing parameters required for the SAM-ET model include the NDVI, surface emissivity, broadband surface albedo and surface temperature (LST) and LAI. These

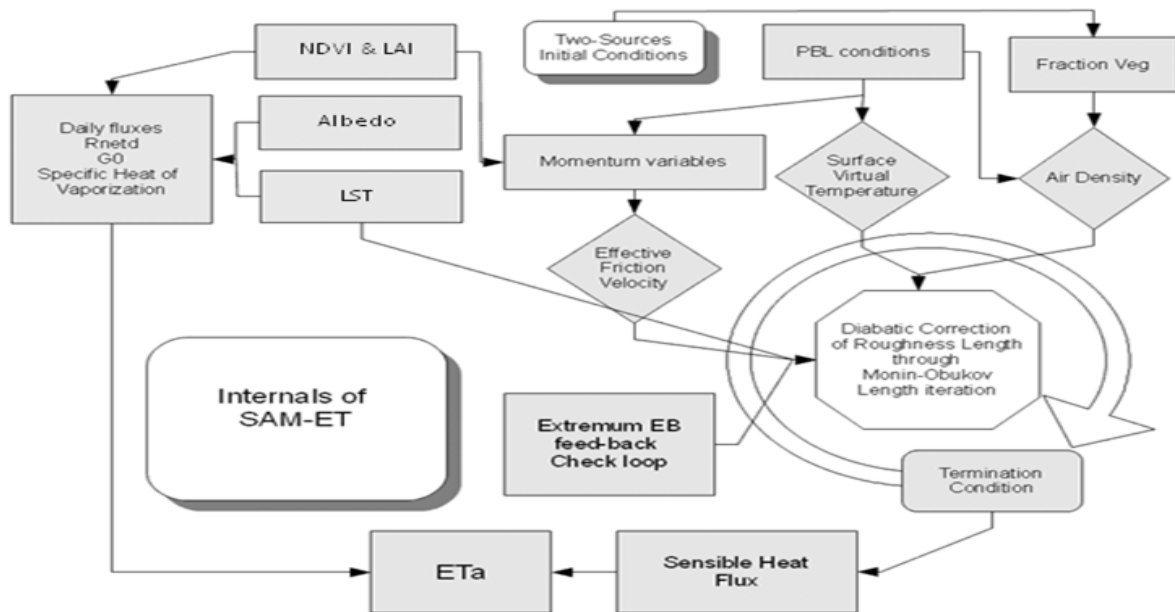


Fig. 2 Method Used for SAM-ET.

parameters are fully standardized for operational optical-thermal satellites such as Landsat 5 TM/7 ETM+, Terra/MODIS and Terra/ASTER. A conceptual diagram of the SAM-ET model is shown in Fig. 2.

Initialization of the sensible heat flux was found through an analytical solution of the diabatically uncorrected energy balance. This permits initialization of the energy balance and structures the two-source separation conditions at a pixel level to enable diabatic correction. This also removes the need to externally assess the initial fraction of vegetation cover, being an unknown of high importance in the two-source energy balance. Planetary conditions are set from various available sources and constrain the momentum variables and friction velocity. They feed into the standard iteration of diabatic fluxes through the Monin-Obukhov length. While this two-source formulation separates soil and vegetation, the redefinition of extreme energy balance conditions at each iteration permits additional confidence in the convergence process. A minimization-based convergence is pre-defined to condition the self-termination of the iteration process.

SAM-ET was enhanced by Fourier versions of 2-m high T_{\min} and T_{\max} in given areas, while relative humidity was found to be between 0.15 and 0.3 at midday, when the satellite imagery is taken, and this depends on the latitude within MDB, but not the month. These empirical equations derived from the ground information were embedded into the algorithm and in addition provided a way to reduce the number of cumbersome input data sets. Diurnal net radiation and soil heat fluxes follow the relationships observed at the AWS at different locations. These ground-to-RS relationships are critical to balance out the diurnal energy available to partition between sensible and latent heat fluxes. Indeed, the net radiation and the soil heat flux combine to provide the radiation-conduction energy, which is equal to the convection-vaporization energy term. SAM-ET looks into some empirical relationships of those grouped terms for various crops and development stages in Australian agro-ecosystem environment. More detail about the theoretical formulation of the SAM-ET model and methodology can be found in Hafeez *et al.*, 2010 and Chemin & Hafeez (2010).

RESULTS AND DISCUSSION

MODIS satellite product (MOD15A2), comprising LAI of every 8 days at 1-km resolution, was downloaded for the study area from November 2008 to October 2010. The ground data using Li-COR 2000 were also collected for various land-use and land-cover classes in the study area.

Figure 3(a) presents the statistical relationships between the LAI modelled (satellite product) with observed LAI (ground data) over the study area and shows a very strong linear relationship with R^2 of 0.941. In order to develop a relationship between thermal infrared observations and satellite-derived land surface temperature, the project deployed four thermal infrared radiometer (TIR) stations to measure temperature from the major land covers including pasture, irrigated cropping and bare soil in CIA from 2009–2011. The results of the relationship developed between MODIS LST and on-ground TIR derived LST from 880 data sets are quite reasonable (Fig. 3(b)) with R^2 of 0.705.

$$LST_{Ground} = 95.44 + (0.67 \times LST_{Modis}) \tag{1}$$

For NDVI on-ground measurement, the project team used the CROPSCAN Multi-Spectral Radiometer (MSR) to monitor reflectance in wavelengths from 450 to 1720 nm from various types of land use including perennial vegetation, irrigated crops, horticulture and bare soil within the study areas. The CROPSCAN MSR bands coincide with the Landsat 5 TM and MODIS satellites, therefore, the relationship obtained between satellite and CROPSCAN MSR collected for on-ground data showed two distinct clusters of pixels (Fig. 3(c), i.e. for the top group it appears that there is no relationship between satellite NDVI and ground NDVI, whereas there may be a weak positive relationship for the lower group. This relationship needs additional data, which is being collected in the CIA. Ground surface albedo was taken from net short wave radiation sensors installed at two eddy covariance flux towers (FT), which were placed in the middle of the irrigated fields in CIA. Similarly, albedo product MCD43B3, being a mixed Terra/Aqua platforms for MODIS data, was used to increase the reliability of Bidirectional Reflectance Distribution Function (BRDF) corrections of albedo from November 2008 to December 2010. The statistical linear relationship between albedo from MODIS and on-ground data shows a high

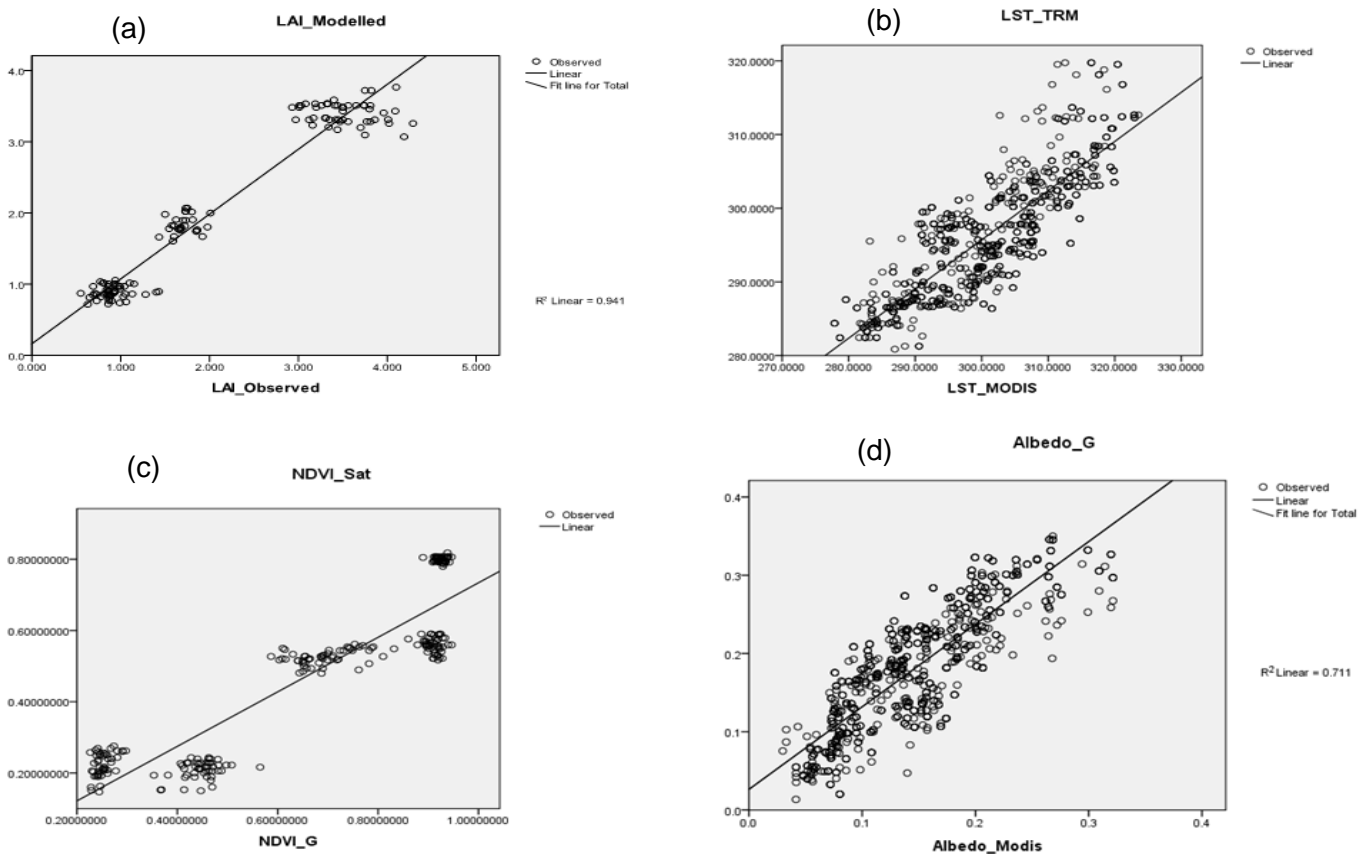


Fig. 3 Empirical relationship between MODIS satellite derived products and on-ground data collected in irrigated areas of Australia.

R^2 value of 0.711 with a standard deviation of 0.032 (Fig. 3(d)). The relationship relating albedo from MODIS 1 km to the flux tower data is given below:

$$Albedo_{Ground} = 0.674 \times Albedo_{Modis} + 0.0245 \quad (2)$$

The ground to RS relationships obtained were used to balance out the diurnal energy available to partition the sensible and latent heat fluxes. The net radiation and the soil heat flux join together provide the radiation-conduction energy which is equal to the convection-vaporization energy term. The SAM-ET model provides daily ET_a as an output by solving energy balance fluxes at two sources (canopy and soil). Initial results of SAM-ET model for estimation of daily spatial variation of ET_a fluxes in the MDB area using Terra MODIS satellite for summer days (4 December 2009, 4 January 2010, and 25 March 2010) and a winter day (8 July 2009) are shown in Fig. 4. For the MDB area, the ET_a ranges from 0.5–3.2 mm/day on 8 July, to 0.8–9.8 mm/day on 4 December, 0.9–10 mm/day on 4 January and 1.1–7.2 mm/day on 25 March. Initial results of the SAM-ET model showed that daily ET_a flux values are realistic after validation with flux tower and LAS data and represent the actual condition of summer and winter days in MDB. Overall results show that the developed semi-empirical relationships fit very well within this two-source formulation for Australian agro-ecosystems.

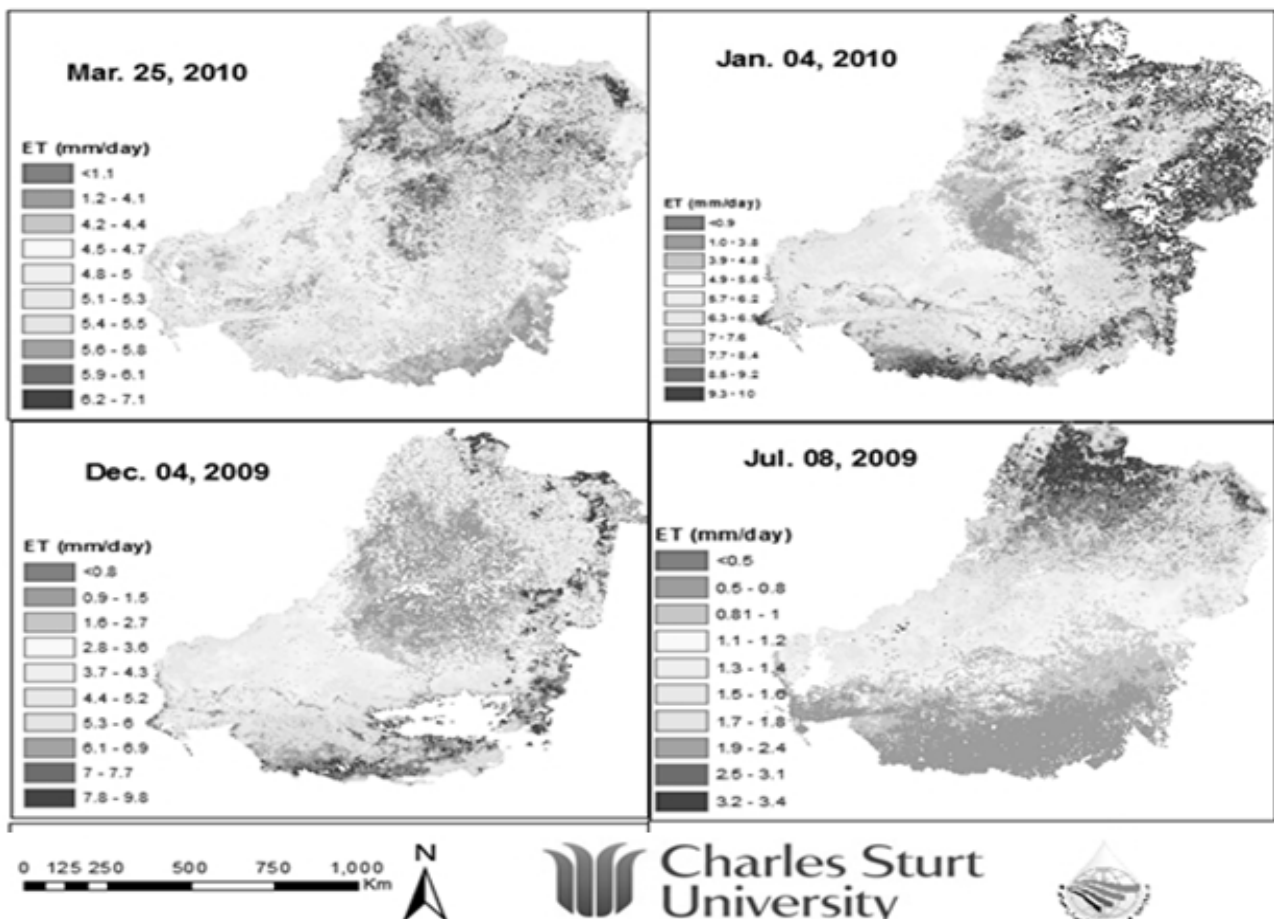


Fig. 4 Spatial variation of daily actual ET in Murray Darling Basin during 2009–2010.

CONCLUSIONS AND WAY FORWARD

The semi-empirical correlations developed with ground-truth knowledge acquired using many different hand-held sensors and MODIS satellite-derived variables are working very well for

solving energy balance fluxes in various parts of the MDB ecosystem. Initial results of the SAM-ET model application for MODIS satellites are quite encouraging and show a great potential for estimation of daily ET_a using the newly developed two-source energy balance model for Australian agro-ecosystems. This research work is a stepping stone in the development of an operational ET monitoring system which will be linked with the on-going testing and development of a modelling framework for estimation of water productivity across different spatial scales (farm to irrigation) over four irrigation systems. Further development of the model will continue for using high spatial resolution optical-thermal satellites data like Terra/ASTER and Landsat 5 TM and also for very-high resolution optical-thermal data from drones for all major irrigated crops of Australia.

REFERENCES

- Allen, R. G., Tasumi, M. & Trezza, R. (2007) Satellite-based energy balance for Mapping Evapotranspiration with Internalized Calibration (METRIC) model. *J. Irrig. Drain. Engng* **133**(4), 380–394.
- Bastiaanssen, W. G. M., Menenti, M., Feddes, R. A. & Holtslag, A. A. M. (1998a) A remote sensing Surface Energy Balance Algorithm for Land (SEBAL): 1. Formulation. *J. Hydrol.* **212–213**, 198–212.
- Bastiaanssen, W. G. M., Pelgrum, H., Wang, J., Ma, Y., Moreno, J. F., Roerink, G. J. & van der Wal, T. (1998b) Surface energy Balance Algorithm for Land (SEBAL): 2. Validation. *J. Hydrol.* **212–213**, 213–229.
- Chemin, Y. & Hafeez, M. (2010) Methodological development of an energy balance algorithm in irrigated area of Australia. *Int. J. Remote Sensing* (submitted).
- Cleugh, H. A., Raupach, M. R., Briggs, P. R. & Coppin, P. A. (2004) Regional-scale heat and water vapour fluxes in an agricultural landscape: an evaluation of CBL budget methods at OASIS. *Boundary-Layer Met.* **110**(1), 99–137.
- Hafeez, M. M. & Chemin, Y. (2010) An Australian algorithm for ET: SAM-ET. Proceeding of 15th Australasian Remote Sensing & Photogrammetry Conference (ARSPC), Alice Springs, Northern Territory, Australia.
- Hafeez, M. M., Chemin, Y. & Rabbani, U. (2009) Spatial observation and models for crop water use in Australia (2009) American Geophysical Union Fall Meeting, 14–18 December 2009, San Francisco, USA.
- Hafeez, M. M., Chemin, Y., Rabbani, U., Louis, J., Sixsmith, J. & Faux, R. (2010) Spatial Algorithm for Mapping ET (SAM-ET) for water productivity and vegetation health in the Australian Agro-ecosystems. Technical Report submitted to National Water Commission, Australia.
- Jackson, R. D., Idso, S. B., Reginato, R. J. & Pinter P. J. Jr (1981) Canopy temperature as a crop water stress indicator. *Water Resour. Res.* **17**(4), 1133–1138.
- Jackson, R. D., Kustas, W. P. & Choudhury, B. J. (1988) A re-examination of the crop water stress index. *Irrigation Science* **9**, 309–317.
- Kustas, W. P. & Norman, J. M. (1999) Evaluation of soil and vegetation heat flux predictions using a simple two-source model with radiometric temperatures for partial canopy cover. *Agric. For. Met.* **94**, 13–29.
- Menenti, M. (1984) Physical aspects of and determination of evaporation in deserts applying remote sensing techniques. Institute for Land and Water Management Research (ICW) 10. Australia.
- Menenti, M. & Choudhury, B. J. (1993) Parameterization of land surface evapotranspiration using a location-dependent potential evapotranspiration and surface temperature range. In: *Exchange Processes at the Land Surface for a Range of Space and Time Scales* (ed. by H. J. Bolle, R. A. Feddes & J. D. Kalma), 561–568. IAHS Publ. 212. IAHS Press, Wallingford, UK.
- Menenti, M., Choudhury, B. J. & Di Girolamo, N. (2001) Monitoring of actual evaporation in the Aral Basin using AVHRR observations and 4DDA results. In: *Advanced Earth Observation – Land Surface Climate* (ed. by Z. Su & C. Jacobs), 79–83. National Remote Sensing Board (BCRS), USP-2(01–02).
- Nieuwenhuis, G. J. A., Schmidt, E. A. & Tunnissen, H. A. M. (1985) Estimation of regional evapotranspiration of arable crops from thermal infrared images. *Int. J. Remote Sensing Environ.* **6**, 1319–1334.
- Norman, J. M., Kustas, W. P. & Humes, K. S. (1995) A two-source approach for estimating soil and vegetation energy fluxes from observations of directional radiometric surface temperature. *Agric. For. Met.* **77**, 263–293.
- Roerink, G. J. & Su, Z. (2000) S-SEBI: A simple remote sensing algorithm to estimate the surface energy balance. *Physics and Chemistry of the Earth* **25**, 147–157.
- Savign, C., Western, A. W., Walker, J. P., Kalma, J. D., French, A. N. & Abuzar, M. (2005) Obtaining surface energy fluxes from remotely sensed data. In: Proceedings 16th Congress of the Modelling and Simulation Society of Australia and New Zealand, 12–15 December 2005, Melbourne, 2946–2952.
- Schmugge, T., Kustas, W. P., Ritchie, J. C., Jackson, T. J. & Rango, A. (2002) Remote sensing in hydrology. *Int. J. Adv. Water Resour.* **25**, 1367–1385.
- Su, Z. (2002) The Surface Energy Balance System (SEBS) for estimation of turbulent heat fluxes. *Hydrol. Earth System Sci.* **6**(1), 85–99.
- Su, Z. (2005) Estimation of the surface energy balance. In: *Encyclopaedia of Hydrological Sciences* (5 vols) (ed. by M. G. Anderson & J. J. McDonnell), vol.2, 731–752. Wiley & Sons, Chichester, UK. ISBN: 0-471-49103-93.
- Su, Z. & Pelgrum, H. (1999) Aggregation effects of surface heterogeneity in land surface processes. *Hydrol. Earth System Sci.* **3**(4), 549–563.
- Su, Z. & Jacobs, C. (2001) Advanced Earth observation – land surface climate. National Remote Sensing Board (BCRS), USP-2(01–02).
- Su, Z., Li, X., Zhou, Y., Wan, L., Wen, J. & Sintonen, K. (2003) Estimating areal evaporation from remote sensing. In: *Proceedings of the International Geoscience and Remote Sensing Symposium*, 21–25 July 2003, Toulouse, France.

Estimating soil heat flux using Distributed Temperature Sensing

J. H. A. M. JANSEN¹, P. M. STIVE¹, N. C. VAN DE GIESEN¹, SCOTT W. TYLER², S. C. STEELE-DUNNE¹ & L. WILLIAMSON²

¹ Water Resources Management, Civil Engineering & Geosciences, Delft University of Technology, The Netherlands
n.c.vandegiesen@tudelft.nl

² Department of Geological Sciences and Engineering, University of Nevada, Reno, Nevada, USA

Abstract Often the smallest component of the surface energy balance, surface heat flux, is assumed to have low spatial variability. The standard measurement technique, which makes use of a heat flux plate, is thus considered to be appropriate. In this paper a method is presented to measure the spatial variability of surface heat flux. A custom-designed plough system deployed three fibre-optic cables at three different depths close to the soil surface. Distributed Temperature Sensing was then used to gather temperatures with a spatial and temporal resolution of 1 m and 30 seconds, respectively. These measurements clearly indicated large spatial variability in surface heat flux along a 70 m stretch. Variations of up to 100% between points 15 m apart could be observed. These results demonstrate the need for distributed soil heat flux measurements.

Key words soil heat flux; surface energy balance; spatial variability; Distributed Temperature Sensing, DTS

INTRODUCTION

Surface heat flux is an important component of the surface energy balance:

$$R_n = G + \lambda E + H \quad (1)$$

where R_n (W/m^2) is net radiation, G (W/m^2) is surface heat flux, and λE (W/m^2) and H (W/m^2) are the latent and sensible heat fluxes. Most of the energy that enters the soil during the day leaves the soil during the night through terrestrial long-wave radiation. Therefore, G is often the smallest component in the daily surface energy balance. Sometimes G is even neglected, which can lead to large errors in the energy balance, especially in instantaneous or hourly estimates (Sauer *et al.*, 2005). It is therefore important to be able to measure G accurately.

Furthermore, spatial variability in G is rarely considered. The standard method to measure G is with a soil heat flux plate. While using this method, one implicitly assumes that G does not vary greatly over space. Yet several studies have shown that spatial variation of G under field conditions can be significant (McCaughey, 1982; Ham & Kluitenberg, 1993; Tuzet *et al.*, 1997; Kustas *et al.*, 2000). Variation in G (measured at 0.08 m depth) between adjacent locations with similar cover in a dune with an uneven surface and partial shrub cover has been found to be greater than 200 Wm^{-2} (Sauer *et al.*, 2005). In order to analyse this spatial variability, simultaneous measurements of surface heat flux at multiple locations are necessary. In this paper we present a method to determine G in time and space over a large area with the use of Distributed Temperature Sensing (DTS) (Selker *et al.*, 2006; Tyler *et al.*, 2009; Sayde *et al.*, 2010; Steele-Dunne *et al.*, 2010). Since soil heat flux is a function of the change in temperature over depth, high resolution temperature measurements of the soil are a useful tool to determine soil heat flux.

METHODS AND MATERIALS

The study area for this research was an agricultural field on the Main Station Field Laboratory of the University of Nevada, Reno, USA (39°30'44"N, 119°42'56"W). The soil has a silt-loam texture and is covered with grass. Along a stretch of 100 m, three armoured two-fibre multi-mode 50/125 μ optic cables from Kaiphone Technology were installed under the soil surface. A custom designed cable plough was used to install the cables. The plough guides the cables through a blade that cuts through the soil under a 45 degree angle and leaves the cables at 1 cm, 6 cm and 11 cm

depth. The blade cuts through the soil like a knife and soil disturbance is minimal. A Sensonet Sentinel DTS unit with a 4-channel Multiplexer Expansion Unit (Sensonet LTD, UK) was used. This DTS unit is suitable for use with cables up to 8 km long, can detect temperature variations of 0.01K at an integration time of 15 minutes, and has a maximal spatial resolution of 1 m. Air temperature, humidity, wind speed, and net radiation were measured at the site.

Thermal conductivity is dependent on moisture content, θ (-). In this case, moisture content is unknown and thermal conductivity has to be obtained from the relationship between diffusivity, $D(\theta)$ (m^2/s), conductivity, $K(\theta)$ ($\text{J}/\text{m}\cdot\text{K}\cdot\text{s}$), and heat capacity, $C(\theta)$ ($\text{J}/\text{K}\cdot\text{m}^3$): $D(\theta)=K(\theta)/C(\theta)$.

Diffusivity can be calculated with the diffusion equation:

$$\frac{\partial T}{\partial t} = D(\theta) \frac{\partial^2 T}{\partial z^2} \quad (2)$$

with T as temperature (K), t as time (s), and z as depth (m). Heat capacity is a linear function of soil moisture:

$$C = n(1 - S_r) \rho_a c_a + S_r n \rho_w c_w + (1 - n) \rho_s c_s \quad (3)$$

where the subscripts a , w and s denote the air, water and soil solids, respectively, ρ (kg/m^3) is the density, c ($\text{J}/\text{kg}\cdot\text{K}$) is the specific heat capacity, S_r (-) is the relative saturation and n (-) is the porosity and $\theta = n \cdot S_r$. Numerous models exist for the relationship between thermal conductivity and soil moisture. Here, the McCumber & Pielke (1981) model was used, with the Van Genuchten (1980) moisture/tension relationship, parameterized with the silt loam soil data provided by Al Nakshabandi & Kohnke (1965). Caution is needed regarding different relations between thermal conductivity and moisture content and moisture content and soil moisture tension because these relations are generally derived from rather small data sets. To obtain the thermal conductivity, first equation (2) is solved to obtain a diffusivity value for each location and each time step. The second step is to calculate the thermal conductivity and, finally, the moisture content can be determined with the use of the McCumber-Pielke model.

From the three temperature measurements along the cable, two layer-average heat fluxes can be calculated, one at 4.1 cm and one at 9.0 cm depth. Soil heat flux is proportional to the temperature change over the depth, according to $G_z = -K(\theta) \cdot dT/dz$. The fluxes at depths z are not equal to the surface heat flux (G_s). An additional term is needed to reflect the change in heat storage in the layer(s) between the surface and the depth of the calculated soil heat flux (G_z) (Mayocchi & Bristow, 1994). The surface heat flux equals the flux at depth plus the change in heat stored over time in the soil layer with thickness Δz : $G_s = G_z + S$ (Oke, 1987) with $S = C \cdot \Delta z \cdot dT/dt$. The method used here directly enables one to calculate this change in heat storage due to the presence of fibre-optic cables in the specific layers. This is an advantage over the conventional heat flux plate method, where additional thermometers are needed. The surface heat flux derived from the upper and lower soil heat fluxes should be similar in amplitude, but should have a small phase difference.

RESULTS

In Fig. 1, calibrated temperatures from the DTS measurements are presented for the middle cable ($z = 0.06$ m). The diurnal signal in temperature changes is clearly visible. Not shown here are temperatures at the other depths, but the data show a clear decrease in temperature amplitude with increasing cable depth. Temperatures in the upper cable range from -13.8°C to 18.6°C , while in the middle and lower cable the temperatures range from -13.6°C to 7.4°C and -12.5°C to 5.6°C , respectively. A distinct spatial variation along the cable is also visible. This variation can be due to differences in soil moisture, soil structure, or variation in cable depth.

The surface heat flux, calculated for the soil layer between the upper and middle cables, is plotted in Fig. 2. Values of the surface heat flux range from -147 W/m^2 up to 309 W/m^2 . Two important different effects can be seen. First, as expected, there is an upward heat flux during the

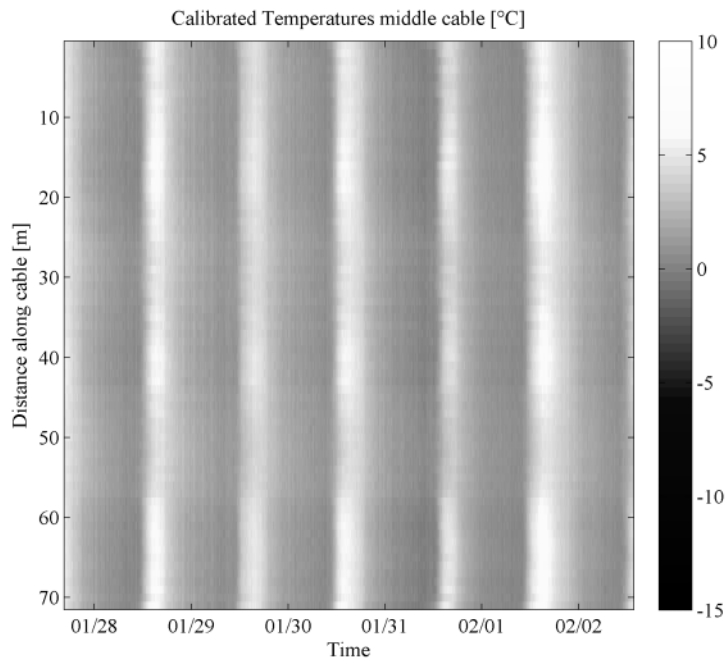


Fig. 1 Calibrated temperatures from the middle cable; the legend give temperatures in °C.

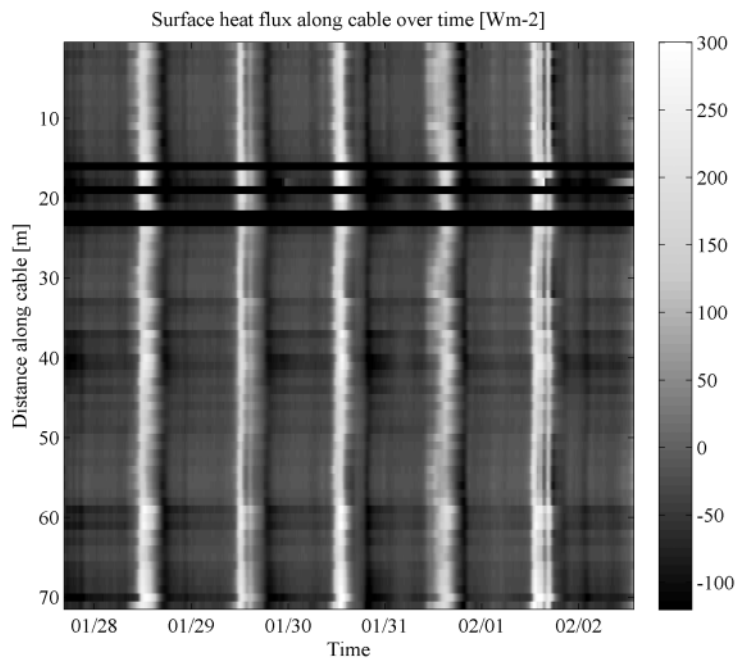


Fig. 2 Surface heat flux along the cable, the legend gives fluxes in W/m^2 .

night changing to a downward heat flux during the day. Second, spatial differences in soil heat flux of up to 100% are found along the cable. The values for the surface heat flux during the day are relatively large compared to those found in the literature (Sauer *et al.*, 2005), as they are up to 30% of net radiation during the late morning. Differences of up to 100% can be found between points only 15 m apart, which is an indication of large spatial variability. The gaps in Fig. 2 (black horizontal lines at 17, 19, 22 and 23 m along the cable) are due to estimated diffusivity values that were outside the physical boundaries of the used model. On some points, no diffusivity could be fitted, which resulted in gaps in heat flux calculations.

The soil heat flux calculated from the temperatures of the upper and middle cable does not directly reflect the surface heat flux. The change in heat storage over time in the layer above the cables needs to be added to the heat flux at depth to obtain the surface heat flux. When the change in heat storage is not taken into account, errors of up to 100 Wm^{-2} can occur. The difference between the surface heat flux calculated from the lower soil heat flux estimate (Surface HF 2) and the upper soil heat flux estimate (Surface HF 1) can be seen in Fig. 3. The robustness of the overall method is demonstrated by the fact that the difference between the two is less than 10%.

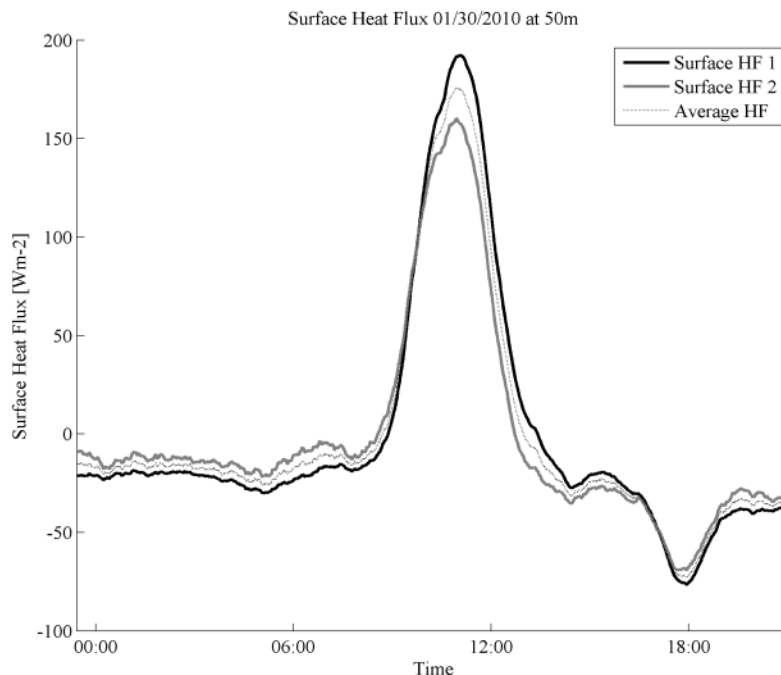


Fig 3 Surface heat flux as determined by the heat flux calculated by the top and middle cables (HF 1) and by the middle and bottom cables (HF 2).

DISCUSSION

The starting hypotheses of this paper were that spatial variability in surface heat flux may be significant and that DTS could be a useful tool to estimate this surface heat flux. The results show that, with the use of high resolution temperature measurements from DTS, a good estimate of surface heat flux can be made. Also, spatial variability was clearly visible in the results (Fig. 2). The cause of this spatial variation in surface heat flux remains to be investigated. As stated before, variations can be caused by differences in soil moisture, soil structure or cable depth. However, we do not know the extent to which each of these contributes to the variability.

Taking cable depth measurements into account (measurements not shown here), one can see that the pattern of cable depth variation is not similar to the pattern of spatial surface heat flux variation. A reasonable assumption is to expect a larger temperature amplitude and heat flux amplitude on locations where the cable is closer to the surface. Such heat flux characteristics were found at 20, 40 and 60 m. However, at 40 and 60 m the cable was roughly at its average depth and not very close to the surface. At 20 m some problems with unsteady cable depths occurred. These problems resulted in diffusivity values outside the physical boundaries of the McCumber Pielke model, which in turn resulted in blank spots in the surface heat flux calculations. In all, there is a strong indication that soil moisture is a dominant factor in spatially varying surface heat fluxes. Still, our method is strongly dependent on accurate cable depths. The way forward would be to work with longer time series with which the constant cable depths can be determined.

Surface heat flux was shown to be a significant part of the instantaneous energy balance, especially at the end of the morning. This paper shows spatial variability in surface heat flux of up to 100% within a 15 m span. The standard field technique to measure surface heat flux using heat flux plates can cause large errors due to significant spatial variability shown in this paper. Neglecting spatial variability can lead to significant errors when one tries to close the energy balance.

The spatial variability found in this paper occurred with a silt loam soil in a flat field. Similar studies will need to be performed on different soil types and topographies to see if such strong patterns occur elsewhere as well. To further reduce the influence of the cable on the soil characteristics it is advisable to conduct the same study after the cable has been in the ground for about a year, so the soil has time to “recover”. For example, any cracks caused by the ploughing will then have disappeared and will no longer influence the measurements.

Acknowledgements The authors would like to thank Mark Hausner and Chris Sladek from the University of Nevada, Reno for their efforts during the experiments in January 2010.

REFERENCES

- Al Nakshabandi, G. & Kohnke, H. (1965) Thermal conductivity and diffusivity of soils as related to moisture tension and other physical properties. *Agric. Meteorol.* **2**, 271–279.
- Ham, J. M. & Kluitenberg, G. J. (1993) Positional variation in the soil energy balance beneath a rowcrop canopy. *Agric. For. Met.* **63**, 73–92.
- Kustas, W. P., Prueger, J. H., Hatfield, I. L., Ramalingam, K. & Hipps, I. E. (2000) Variability in soil heat flux from a mesquite dune site. *Agric. For. Met.* **103**, 249–264.
- Mayocchi, C. L. & Bristow, K. L. (1995) Soil surface heat flux: some general questions and comments on measurements. *Agric. For. Met.* **75**, 43–50.
- McCaughey, J. H. (1982) Spatial variability of net radiation and soil heat flux density on two logged sites in Montmorency, Quebec. *J. Appl. Met.* **21**, 777–787.
- McCumber, M. C. & Pielke, R. A. (1981) Simulation of the effects of surface fluxes of heat and moisture in a mesoscale numerical model. *J. Geophys. Res.* **86**(C10), 9929–9938.
- Sauer, T. J. & Horton, R. (2005) *Micrometeorology in Agricultural Systems*. American Society of Agronomy: Crop Science Society of America: Soil Science Society of America, Madison, Wisconsin, USA.
- Sayde, C., Gregory, C., Rodriguez, M., Tuffiaro, N., Tyler, S., Van de Giesen, N., English, M., Richard Cuenca, R., & Selker, J.S. (2010) Feasibility of soil moisture monitoring with heated fiber optics. *Water Resour. Res.* **46**, W06201, doi:10.1029/2009WR007846.
- Selker, J. S., Thévenaz, L., Huwald, H., Mallet, A., Luxemburg, W., Van de Giesen, N., Stejskal, M., Zeman, J., Westhoff, M., & Parlange, M. B. (2006) Distributed fiber optic temperature sensing for hydrologic systems. *Water Resour. Res.* **42**(12), W12202, doi:10.1029/2006WR005326.
- Steele-Dunne, S. C., Ruttan, M. M., Krzeminska, D. M., Hausner, M., Tyler, S. W., Selker, J., Bogaard, T. A. & Van de Giesen, N. C. (2010) Feasibility of soil moisture estimation using passive distributed temperature sensing, *Water Resour. Res.* **46**, W03534, doi:10.1029/2009WR008272.
- Tuzet, A., Castell, I-F., Perrier, A. & Zurfluh, O. (1997) Flux heterogeneity and evapotranspiration partitioning in a sparse crop: The fallow savanna. *J. Hydrol.* **188-189**, 482–493.
- Tyler, S. W., Selker, J. S., Hausner, M. B., Hatch, C. E., Torgersen, T., Thodal, C. E. & Schladow, S. G. (2009) Environmental temperature sensing using Raman spectra DTS fiberoptic methods, *Water Resour. Res.* **45**, W00D23, doi:10.1029/2008WR007052.
- Van Genuchten, M. Th. (1980) A closed-form equation for predicting the hydraulic conductivity of unsaturated soil. *Soil Sci. Soc. Am. J.* **44**, 892–898.

A study on actual evapotranspiration estimation based on the Todorovic method

GUOSHUI LIU^{1,2}, MOHSIN HAFEEZ², YU LIU¹ & DI XU¹

¹ Department of Irrigation & Drainage, China Institute of Water Resources and Hydropower Research, Beijing 100048, China

liuyu@iwhr.com

² International Centre of Water for Food Security, Charles Sturt University, Wagga Wagga, New South Wales 2678, Australia

Abstract A method to simulate surface resistance proposed by Todorovic was investigated for a winter wheat surface by comparing actual evapotranspiration (ET) estimates from the Penman-Monteith model, where surface resistance was derived on the basis of the Todorovic method with ET measurement from a weighing lysimeter located at the Daxing experimental station of the China Institute of Water Resources and Hydropower Research (IWHR). The field work was conducted from March to June 2007. The study proves that, on a daily basis, estimated daily ET showed strong agreement with measured daily ET. The average daily value of measured ET and estimated ET was 3.73 mm/d and 3.96 mm/d, respectively, and the MAE and RMSE for estimated ET was 0.663 mm/d and 0.793 mm/d, respectively. On an hourly basis, the model could only perform well when the field was fully covered. The combination of the Todorovic method and the Penman-Monteith model could be used to estimate daily winter wheat ET when the field was fully covered.

Key words evapotranspiration; lysimeter; surface resistance; Penman-Monteith model; Todorovic method

INTRODUCTION

Evapotranspiration (ET), as a component of the water cycle and energy balance, plays an essential role in understanding various aspects of agronomy (Ritchie & Basso, 2008), forestry (Shi *et al.*, 2008) and hydrology (Anderson *et al.*, 2007). Many instruments are designed and applied to measure actual ET data directly or indirectly, such as lysimeters (Bhantana & Lazarovitch, 2010; Luo & Sophocleous, 2010), eddy covariance flux towers (Sun *et al.*, 2008; Novick *et al.*, 2010), Bowen ratio towers (Savage *et al.*, 2009; Zhang *et al.*, 2010), and large aperture scintillometers (Asanuma & Lemoto, 2007; Marx *et al.*, 2008). The measured ET data exhibit high temporal resolution and high accuracy. However, these methods are time consuming and expensive when daily and regional ET data are required (Barcza *et al.*, 2009; Timmermans *et al.*, 2009), which results in low utilization of these instruments. Models to derive ET data from meteorological data offer an easy and reliable alternative, which are consequently widely used (Shoemaker *et al.*, 2006; Zhao *et al.*, 2010). Of those models, the Penman-Monteith model is the most popular.

Surface resistance is the key parameter influencing the Penman-Monteith model. So far, there are many methods proposed to determine surface resistance for a specific crop surface or restricted condition (Allen *et al.*, 2006; Whitley *et al.*, 2008; Rana *et al.*, 2009). However, surface resistance is still difficult to express properly, which may be the main limit of the Penman-Monteith model. A mechanistic method was recommended by Todorovic (1999), which did not require local calibration and was reported to have good performance under specific crop surfaces (Lecina *et al.*, 2003; Steduto *et al.*, 2003; Perez *et al.*, 2006). The objective of this study is to investigate the performance of the Todorovic method under a winter wheat surface by comparing actual ET estimates derived from the Penman-Monteith model where the surface resistance was calculated based on the Todorovic method, against ET measurement by a weighing lysimeter. The lysimeter was located at the Daxing experimental station of the China Institute of Water Resources and Hydropower Research (IWHR) from March to June 2007.

MATERIALS AND METHODS

Study area and data

The study was conducted at the Daxing experimental station of the IWHR (116°25'E, 39°37'N, 30 m above sea level with an area of 15 ha) from March to June 2007, when the crop surface was

winter wheat. This area is characterized by a semi-arid continental monsoon climate, which is typically cold, with a small amount of snow in the winter, dry and windy in the spring, and hot and rainy in the summer. The mean annual temperature is 12.1°C. The mean annual rainfall is 540 mm, with more than 80% of that falling during the rainy season (June–September). The mean annual frost-free period is 185 days. There are 2600 annual hours of sunshine and the annual evaporation of surface water is over 1800 mm.

A standard weather station was located at the Daxing experimental station to measure routine meteorological data, namely rainfall, wind speed, wind direction, air temperature, soil temperature, relative humidity, water surface evaporation, incoming solar radiation, net radiation and duration of sunshine. The data was recorded every 30 minutes.

Winter wheat ET was measured by a weighting lysimeter (2 × 2 m wide, 2.3 m deep), which was located at the centre of the experimental field. The weighting lysimeter value was recorded every hour with an accuracy of 0.02 mm. In order to control the data quality, any collected data that met one of the following conditions was deleted: data that were an apparently abnormal record, data collected when the sensor was under examination, and data collected during irrigation or precipitation conditions. Finally, 45 days were selected from the winter wheat season as the validation data for model performance.

METHOD

Assuming that the field was fully covered by a “big leaf” (Alves *et al.*, 1998), the well known Penman-Monteith model can be expressed as (Winter & Eltahir, 2010):

$$\lambda ET = \frac{\Delta(R_n - G) + \rho_a c_p \frac{(e_s - e_a)}{r_a}}{\Delta + \gamma \left(1 + \frac{r_s}{r_a}\right)} \quad (1)$$

where Δ is the slope of the saturation vapour pressure temperature relationship at about 2 m above ground level (kPa/°C), R_n is the net radiation (J/(m² s)), G is the soil heat flux (J/(m² s)), ρ_a is the mean air density at constant pressure (kg/m³), c_p is the specific heat of the air (J/(kg °C)), $(e_s - e_a)$ is the vapour pressure deficit of the air (kPa), r_a is the aerodynamic resistance (s/m), γ is the psychrometric constant (kPa/°C), and r_s is the surface resistance (s/m).

Following similar assumptions to the Penman-Monteith model, Todorovic (1999) proposed to determine surface resistance in the form of the quadratic equation;

$$a\left(\frac{r_s}{r_i}\right)^2 + b\left(\frac{r_s}{r_i}\right) + c = 0 \quad (2)$$

with

$$r_i = \frac{\rho_a c_p (e_s - e_a)}{\gamma(R_n - G)} \quad (3)$$

$$a = \frac{\Delta + \gamma(r_i / r_a)}{\Delta + \gamma} (r_i / r_a)(e_s - e_a) \quad (4)$$

$$b = -\gamma \left(\frac{r_i}{r_a}\right) \frac{\gamma}{\Delta} \frac{(e_s - e_a)}{\Delta + \gamma} \quad (5)$$

$$c = -(\Delta + \gamma) \frac{\gamma}{\Delta} \frac{(e_s - e_a)}{\Delta + \gamma} \quad (6)$$

Equation (2) has only one positive solution. After solving equations (3), (4), (5), (6) and calculating the surface resistance from equation (2), estimated ET can be derived by substituting surface resistance in equation (1).

Assessments

The mean absolute error (MAE) and root mean square error (RMSE) were selected to assess the model's performance (Harmel *et al.*, 2007).

$$\text{MAE} = N^{-1} \sum_{i=1}^n |P_i - O_i| \quad (7)$$

$$\text{RMSE} = \sqrt{N^{-1} \sum_{i=1}^n (P_i - O_i)^2} \quad (8)$$

where O_i is the measured ET value, P_i is the estimated ET value, and N is the number of days.

RESULTS AND DISCUSSION

Daily basis

Comparison of estimated and measured daily ET over 45 days is presented in Fig. 1, which indicates good model performance. The determination coefficient (r^2) was 0.83. The mean daily value of estimated and measured ET was 3.96 mm/d and 3.73 mm/d, respectively. The two-tailed Student t test at 5% level of significance showed the difference between daily estimated ET and measured ET was not statistically significant. The standard deviation of estimated and measured ET was 1.67 mm/d and 1.85 mm/d, respectively. The MAE for estimated ET (0.66 mm/d) was less than 50% of measured standard deviation, indicating strong model agreement (Colaizzi *et al.*, 2006). The RMSE for estimated ET (0.79 mm/d) was not greater than 50% of MAE, indicating that there were no outliers (Colaizzi *et al.*, 2006).

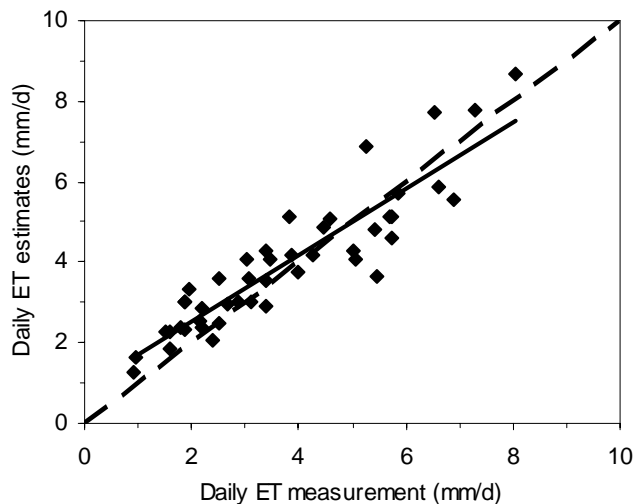


Fig. 1 Comparison of daily ET estimates and ET measurement over 45 days.

Figure 2 shows the relative error for ET estimates, where relative error was defined as $[(O_i - P_i)/O_i] \times 100\%$. From this, it can be seen that the model apparently overestimates at lower ET values, and underestimates at high ET values. The daily ET estimates were less than 10% higher than ET measurements, indicating that ET estimates were close to ET measurements.

Hourly basis

Two clear days from two typical winter wheat periods were chosen to compare the hourly ET estimates against the hourly ET measurement.

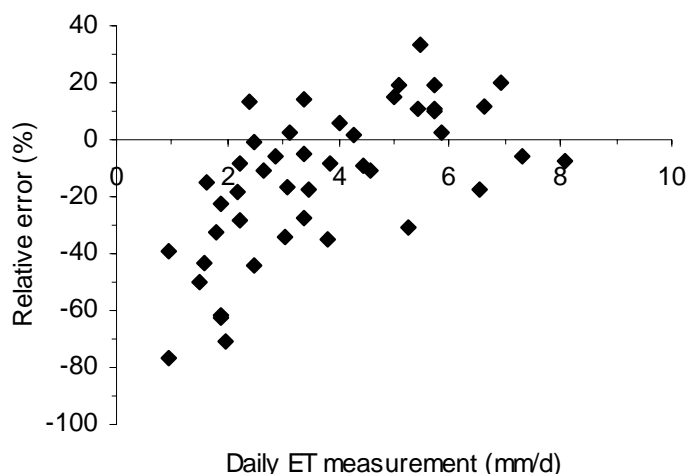


Fig. 2 Relative error for daily ET estimates.

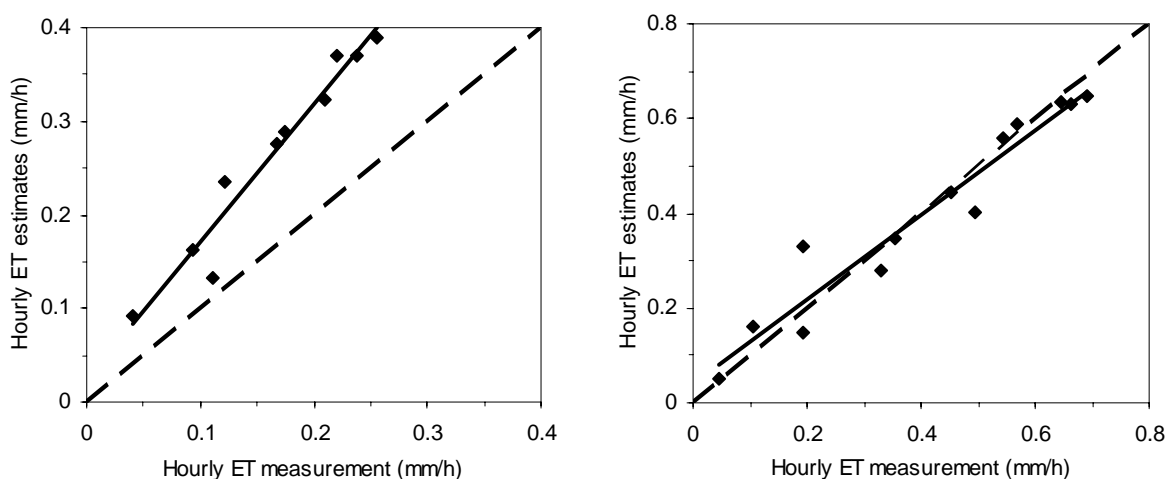


Fig. 3 Comparison of hourly ET estimates and ET measurement on two golden days (a) 27 March 2007; (b) 10 May 2007.

The regression between estimated and measured ET on 27 March 2007 (turning green period), when the field was not fully covered by winter wheat is shown in Fig. 3(a). The determination coefficient (r^2) was 0.95. The mean hourly value of estimated and measured ET was 0.26 mm/h and 0.16 mm/h, respectively. The two-tailed Student t test at the 5% level of significance indicated that the hourly value of estimated ET in 27 March 2007 was significantly different from the hourly ET measurement. The standard deviation of estimated and measured ET was 0.11 mm/h and 0.07 mm/h, respectively. The MAE of estimated ET (0.1 mm/h) was more than 50% of measured standard deviation, which implies poor model performance.

Figure 3(b) shows the relationship between estimated and measured ET on 10 May 2007 (filling period), when the field was fully covered by winter wheat. The determination coefficient (r^2) had a value of 0.94. The mean hourly value of estimated and measured ET was 0.4 mm/h and 0.41 mm/h, respectively. The two-tailed Student t test at 5% level of significance indicated that the difference between hourly estimated ET and measured ET on 10 May 2007 was not statistically significant. The standard deviation of estimated and measured ET was 0.2 mm/h and 0.22 mm/h, respectively. The MAE and RMSE of estimated ET were 0.04 mm/h and 0.05 mm/h, respectively. The MAE for estimated ET was less than 50% of measured standard deviation, which indicates strong model agreement. The RMSE for estimated ET was not greater than 50% of MAE, illustrating that the results were almost free of outliers.

Based on the experimental results described so far, it can be stated that the model can only perform well when the field coverage was close to the assumption of the Penman-Monteith model.

CONCLUSIONS

In this paper, the methods to calculate surface resistance proposed by Todorovic was investigated for a winter wheat surface by comparing actual ET estimates from the Penman-Monteith model where surface resistance was estimated on the basis of the Todorovic method, with actual ET measurement by a weighing lysimeter from March to June 2007. On a daily basis, the model showed good performance. The average daily estimated ET (3.73 mm/d) was close to average daily measured ET (3.96 mm/d). The RMSE (0.793 mm/d) was not greater than 50% of the MAE (0.663 mm/d). On an hourly basis, the model showed poor agreement when the field was not fully covered by winter wheat, but showed strong agreement when the field was fully covered by winter wheat. Based on the evidence presented in this paper, the combination of the Penman-Monteith model and the Todorovic method can be confidently used to derive daily ET data when the field is fully covered by winter wheat.

Acknowledgements The work was supported by the National Major Fundamental Research Program of China (no. 2006CB403405) and the China Institute of Water Resources and Hydropower Research (IWHR) Excellent PhD Thesis Innovative Research Fund.

REFERENCES

- Allen, R. G., Pruitt, W. O., Wright, J. L., Howell, T. A., Ventura, F., Snyder, R., Itenfisu, D., Steduto, P., Berengena, J., Yrisarry, J. B., Smith, M., Pereira, L. S., Raes, D., Perrier, A., Alves, L., Walter, I. & Elliott, R. (2006) A recommendation on standardized surface resistance for hourly calculation of reference ET₀ by the FAO56 Penman-Monteith method. *Agric. Water Manage.* **81**(1–2), 1–22.
- Alves, L., Perrier, A. & Pereira, L. S. (1998) Aerodynamic and surface resistances of complete cover crops: how good is the “big leaf”? *Trans. ASAE* **41**(2), 345–351.
- Anderson, M. C., Norman, J. M., Mecikalski, J. R., Otkin, J. A. & Kustas, W. P. (2007) A climatological study of evapotranspiration and moisture stress across the continental United States based on thermal remote sensing: 1. Model formulation. *J. Geophys. Res.* **112**(D10117), doi:10.1029/2006JD007506.
- Asanuma, J. & Lemoto, K. (2007) Measurements of regional sensible heat flux over Mongolian grassland using large aperture scintillometer. *J. Hydrol.* **333**(1), 58–67.
- Barcza, Z., Kern, A., Haszpra, L. & Kljun, N. (2009) Spatial representativeness of tall tower eddy covariance measurements using remote sensing and footprint analysis. *Agric. For. Met.* **149**(5), 795–807.
- Bhantana, P. & Lazarovitch, N. (2010) Evapotranspiration, crop coefficient and growth of two young pomegranate (*Punica granatum* L.) varieties under salt stress. *Agric. Water Manage.* **97**(5), 715–722.
- Colaizzi, P. D., Evett, S. R., Howell, T. A. & Tolck, J. A. (2006) Comparison of five models to scale daily evapotranspiration from one-time-of-day measurements. *Trans. ASABE* **49**(5), 1409–1417.
- Harmel, R. D. & Smith, P. K. (2007) Consideration of measurement uncertainty in the evaluation of goodness-of-fit in hydrologic and water quality modeling. *J. Hydrol.* **337**(3–4), 326–336.
- Lecina, S., Cob, A. M., Perez, P. J., Villalobos, F. J. & Baselga, J. J. (2003) Fixed versus variable bulk canopy resistance for reference evapotranspiration estimation using the Penman–Monteith equation under semiarid conditions. *Agric. Water Manage.* **60**(3), 181–198.
- Luo, Y. & Sophocleous, M. (2010) Seasonal groundwater contribution to crop–water use assessed with lysimeter observations and model simulations. *J. Hydrol.* **389**(3–4), 325–335.
- Marx, A., Kunstmann, H., Schuttemeyer, D. & Moene, A. F. (2008) Uncertainty analysis for satellite derived sensible heat fluxes and scintillometer measurements over Savannah environment and comparison to mesoscale meteorological simulation results. *Agric. For. Met.* **148**(4), 656–667.
- Novick, K. A., Oren, R., Stoy, P. C., Siqueira, M. B. S. & Katul, G. G. (2010) Nocturnal evapotranspiration in eddy-covariance records from three co-located ecosystems in the southeastern US: implications for annual fluxes. *Agric. For. Met.* **149**(9), 1491–1504.
- Perez, P. J., Lecina, S., Castellvi, F., Cob, A. M. & Villalobos, F. J. (2006) A simple parameterization of bulk canopy resistance from climatic variables for estimating hourly evapotranspiration. *Hydrol. Processes* **20**(3), 515–532.
- Rana, G. & Katerji, N. (2009) Operational model for direct determination of evapotranspiration for well watered crops in Mediterranean region. *Theor. Appl. Climatol.* **97**(3–4), 243–253.
- Ritchie, J. T. & Basso, B. (2008) Water use efficiency is not constant when crop water supply is adequate or fixed: The role of agronomic management. *Europ. J. Agronomy* **28**(3), 273–281.
- Savage, M. J., Everson, C. S. & Metelerkamp, B. R. (2009) Bowen ratio evaporation measurement in a remote montane grassland: Data integrity and fluxes. *J. Hydrol.* **376**(1–2), 249–260.

- Shi, T., Guan, D., Wang, A., Wu, J., Jin, C. & Han, S. (2008) Comparison of three models to estimate evapotranspiration for a temperate mixed forest. *Hydrol. Processes* **22**(17), 3431–3443.
- Shoemaker, W. B. & Summer, D. M. (2006) Alternate corrections for estimating actual wetland evapotranspiration from potential evapotranspiration. *Wetland* **26**(2), 528–543.
- Steduto, P., Todorovic, M., Calciandro, A. & Rubino, P. (2003) Daily reference evapotranspiration estimates by the Penman-Monteith equation in Southern Italy. Constant vs variable canopy resistance. *Theor. Appl. Climatol.* **74**(3–4), 217–225.
- Sun, G., Noormets, A., Chen, J. & McNulty, S. G. (2008) Evapotranspiration estimates from eddy covariance towers and hydrologic modeling in managed forests in Northern Wisconsin, USA. *Agric. For. Met.* **148**(2), 257–267.
- Timmermans, W. J., Su, Z. & Olioso, A. (2009) Footprint issues in scintillometry over heterogeneous landscapes. *Hydrol. Earth Syst. Sci.* **13**(11), 2179–2190.
- Todorovic, M. (1999) Single-layer evapotranspiration model with variable canopy resistance. *J. Irrig. Drainage Engng* **125**(5), 235–245.
- Whitley, R., Zeppel, M., Armstrong, N., Ng, C. M., Yunusa, I. & Eamus, D. (2008) A modified Jarvis-Stewart model for predicting stand-scale transpiration of an Australian native forest. *Plant Soil* **305**(1–2), 35–47.
- Winter, J. M. & Eltahir, E. A. B. (2010) The sensitivity of latent heat flux to changes in the radiative forcing: A framework for comparing models and observations. *J. Climate* **23**(9), 2345–2356.
- Zhang, B., Kang, S., Li, F. & Zhang, L. (2010) Comparison of three evapotranspiration models to Bowen ratio-energy balance method for a vineyard in an arid desert region of northwest China. *Agric. For. Met.* **148**(10), 1629–1640.
- Zhao, W. Z., Ji, X. B., Kang, E. S., Zhang, Z. H. & Jin, B. W. (2010) Evaluation of Penman-Monteith model applied to a maize field in the arid area of Northwest China. *Hydrol. Earth Syst. Sci.* **7**(1), 461–491.

Surface-layer sensible heat flux using large-aperture scintillometer over irrigated horticulture in Murrumbidgee irrigation area

U. RABBANI¹, M. HAFEEZ¹, R. FAUX¹ & J. LOUIS²

¹ International Centre of Water for Food Security, Charles Sturt University, Wagga Wagga, Australia
urabbani@csu.edu.au

² School of Computing and Mathematics, Charles Sturt University, Wagga Wagga, Australia

Abstract Accurate estimation of regional evapotranspiration (ET) is essential for water sharing, water resources planning and water regulation in any irrigation system/catchment. ET is estimated by solving the energy balance at different spatial scales, ranging from farm to catchment. The most complex component of the energy balance is sensible heat flux (H), which needs to be better estimated to improve the accuracy of ET measurements. A scintillometer is an instrument that consists of a transmitter and a receiver, which measures intensity fluctuations in the radiation emitted by the transmitter caused by refractive scattering of turbulent eddies in the scintillometer path. Several investigations have demonstrated the potential of using scintillometers to measure sensible heat fluxes over path lengths similar to satellite pixel scales. However, scintillometer techniques have not been applied to understand irrigated area flux patterns under Australian climatic conditions. A comprehensive experiment is being conducted to investigate the potential and the limitations of using a large aperture scintillometer (LAS) to infer path-average sensible heat flux from irrigated horticulture in the Murrumbidgee Irrigation Area of the Murray Darling Basin, Australia. Scintillometer based estimates of sensible heat provide a better understanding of energy balance, which will assist with local validation of remote sensing based energy balance models under Australian climatic conditions.

Key words scintillometer; Murrumbidgee; LAS; evapotranspiration; sensible heat flux; latent heat flux; refractive index; energy balance

INTRODUCTION AND BACKGROUND

Many climatic, hydrological, meteorological and environmental studies require representative large-area estimates of turbulent fluxes of momentum, sensible heat and latent heat. Specifically in hydrological sciences, quantification of fluxes (net radiation, sensible heat, soil heat and latent heat) is essential for accurate estimation of ET by solving the energy balance. The most uncertain component of the energy balance cycle is the sensible heat flux (H). Direct methods like lysimeters and eddy covariance, hydrological models like SWAP (Droogars, 2000) or SLURP (Kite, 2000), or more recently, applied remote sensing methods like SEBAL (Basstiaanssen, 2000) and SEBS (Su, 2002) are all examples of methods used to estimate important energy balance terms i.e. H and latent heat flux (λE) (Meijninger & De Bruin, 2000).

The objective of this paper is to test the applicability of large aperture scintillometer (LAS) techniques to estimate the surface-layer sensible heat flux from large irrigated fields equivalent to satellite pixel scales in an irrigated horticulture environment in the Murrumbidgee Irrigation Area (MIA). Since the scintillometer path length is comparable to the pixel size of satellite imagery, the LAS enables verification of remote sensing models used to estimate ET of crops. A disadvantage of this method over the eddy covariance technique is that it is based on semi-empirical Monin-Obukhov Similarity Theory (MOST) (Rabbani, 2008). Several authors, as listed by Meijninger & De Bruin (2000), applied and tested MOST, demonstrating that the scintillation method is a good alternative for estimating areally-averaged sensible heat flux. They conclude that under unstable conditions and for Bowen ratios larger than approximately 0.75, the method appears to be reliable over homogeneous fields. However, large-scale irrigated agriculture often results in very high values of evaporation from fields surrounded by dry desert. It is important to assess the accuracy of the structure parameter method (Beyrich *et al.*, 2002) under these conditions.

The idea behind the use of the scintillometer is based upon the consideration that the structure parameter of the refractive index of air measured directly by the scintillometer (C_N^2) can be related to the structure function parameter of temperature (C_T^2) used to derive H. With the assumption

that, in the visible and infra-red spectrum, temperature and humidity fluctuations are perfectly correlated, the above relation is mathematically described as:

$$C_T^2 = C_N^2 \left(\frac{T^2}{-0.789 \times 10^{-6} p} \right)^2 \left(1 + \frac{0.03}{Bo} \right)^{-2}$$

where, T is the air temperature, p is the atmospheric pressure and Bo is the Bowen ratio. De Wekker (1996) has shown that Bo can be neglected if $Bo > 0.6$, which is generally the case in arid and semi-arid areas. For daytime non-stable stratification, the turbulent sensible heat flux density (H) was determined from scintillometer measurements using the following equation (Beyrich *et al.*, 2002):

$$H = \rho c_p \langle w' \Theta' \rangle_0 = \rho c_p \frac{\sqrt{C_T^2} (z-d)^{\frac{1}{3}} u_*}{\sqrt{a_1}} \left(1 - a_2 \frac{z-d}{L} \right)^{\frac{1}{3}}$$

where ρ is the air density, c_p the specific heat of air at constant pressure, z is the height, d the displacement height u^* the friction velocity, and L the Monin-Obukhov length. Different values for constants a_1 and a_2 have been given in the literature. However, for the present analysis the widely used values of a_1 and a_2 by DeBruin *et al.* (1993) were used.

EXPERIMENTAL DESIGN

A comprehensive experiment has been setup in the MIA to investigate the potentials and the limitations of using a LAS to infer path-average sensible heat flux. The study site is a horticulture farm with a consistent and uniform citrus crop located near the town of Leeton, NSW, Australia. The LAS transmitter and receiver were installed at a height of 4.3 m above the ground, with a path length of 1400 m. A cluster of five eKo Pro wireless sensors were also installed within the line of sight of the receiver and the LAS transmitter. Each eKo Pro node is equipped to read and transmit wind speed, wind direction, air temperature, humidity, soil temperature, soil moisture and rainfall information. Figure 1 shows the configuration of the full experimental design including the LAS transmitter and receiver, eko Pro wireless cluster and automatic weather station (AWS) at the LAS receiver end. Figure 2 shows the LAS receiver (a) and transmitter (c) configured at the roof-top of two structures 1400 m apart, and an eKo Pro wireless node (b) at the study site.

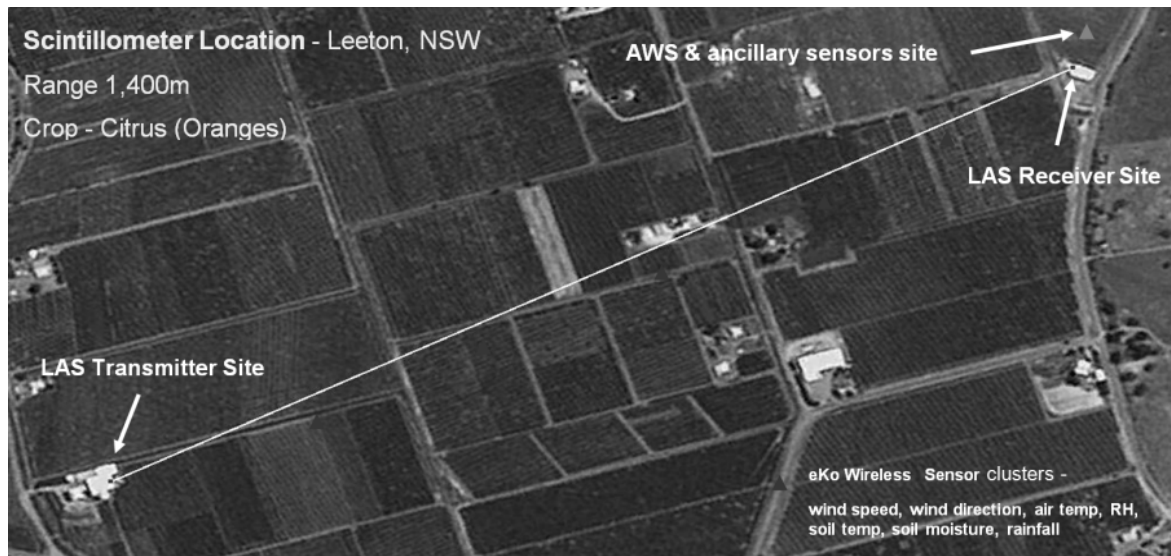


Fig. 1 Illustration of LAS, eKo cluster sensors and AWS.

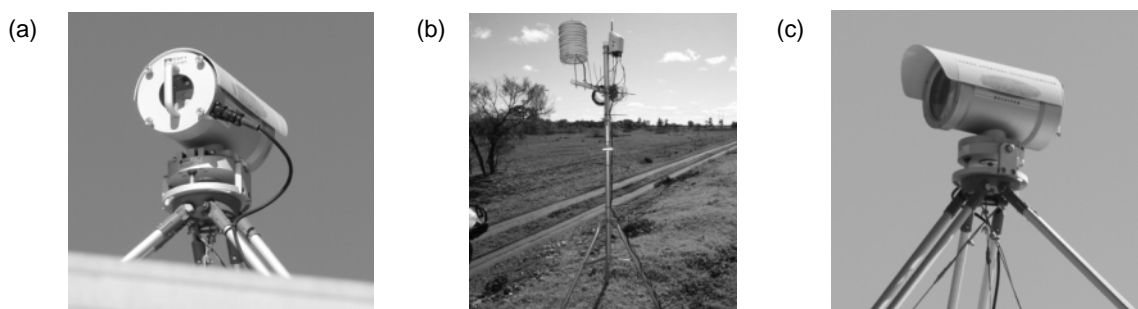


Fig. 2 LAS receiver (a), an eKo Pro wireless node (b) and LAS transmitter (c) at the study site.

At the LAS receiver site, a Campbell scientific micro-data logger CR-3000 was set up which logs the LAS data every second. A set of ancillary sensors, i.e. a net radiometer (NR-Lite), two soil heat flux plates (HFP015) and volumetric water content sensor, are also configured with the data logger to generate ancillary information. Beyrich *et al.* (2002) stated that since the scintillometer measures in the inertial-convective sub-range of frequencies, it provides statistically stable data within a minimum range of 10 minutes. Therefore, the logger was programmed to sample half-hourly, i.e. to generate half-hour average tables containing information from the LAS receiver, the net radiometer, soil heat flux plates and volumetric water content. A 3G modem was setup with a CR3000 data logger that enabled real-time data acquisition from the field to the data server at the research centre in Wagga Wagga, NSW, which is located 145 km southeast of Leeton. The LAS has been operating since October 2009 and there is minimum maintenance required in order to ensure stable operation. This includes a control of the alignment and of the status of the windows of the transmitter and receiver.

DATA ANALYSIS AND RESULTS

The CR3000 loggers generate the data in Campbell Scientific's proprietary binary data format, which needs to be converted to ASCII using either Campbell's LoggerNet software or preferably by using the open-source Camp2ascii utility (<http://mathias.bavay.free.fr/software/camp2ascii/>). Beyrich *et al.* (2002) reported a signal reduction if the visibility of the air became less than 5 km. However, this has not been a problem since the path length of our LAS set-up was only 1.4 km. For this paper, LAS data was processed using Kipp & Zonen's WinLAS software application to estimate sensible heat flux for the duration of October 2009 to June 2010, showing the flux patterns in winter and summer seasons.

In order to calculate sensible heat fluxes, the LAS measurements of the refractive index structure parameter C_n^2 can either be calculated from the combination of UC_n^2 and Demod, or from the combination of PUC_n^2 and Demod (Kipp & Zonen, 2007). In this study, we estimated H from both the above-mentioned methods for the whole duration. Figure 3 shows minimal variance between the estimates of H from both these methods.

The sensible heat flux was calculated from LAS at a half hour time step. For solving the energy balance, we used the values of soil heat flux measured from a Huskeflux plate and net radiation from the net radiometer at the same time step as the LAS. The latent heat flux was then estimated by solving an energy balance from the fluxes measured from these instruments, and H calculated from LAS. Figures 4 and 5 show a typical sinusoidal trend of the variation of energy balance components during a summer (1 February 2009) and winter day (6 June 2010), respectively. The grey areas of the plot indicate time before sunrise and after sunset, where the derived fluxes become meaningless.

The day time H on 1 February 2010 ranges from 6 to 298 W/m^2 , having a mean value of 135 W/m^2 and standard deviation of 89 W/m^2 . R_n ranges from 162 to 781 W/m^2 , with a mean value of 498 W/m^2 and standard deviation of 176 W/m^2 . The latent heat flux varies from 153 to 483 W/m^2

with a mean value of 338 W/m², suggesting high latent flux on a summer day when the temperature was 37°C. Similarly, the day time H on 6 June 2010 varies from 16 to 144 W/m² with a mean

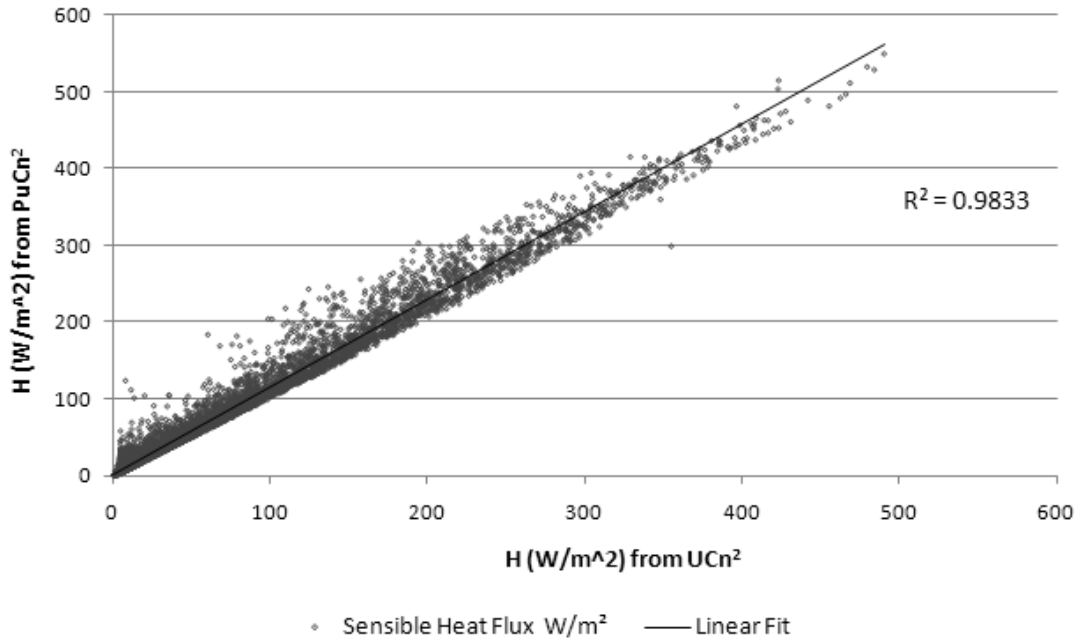


Fig. 3 Relationship between UC_n² derived H and PUC_n² derived H.

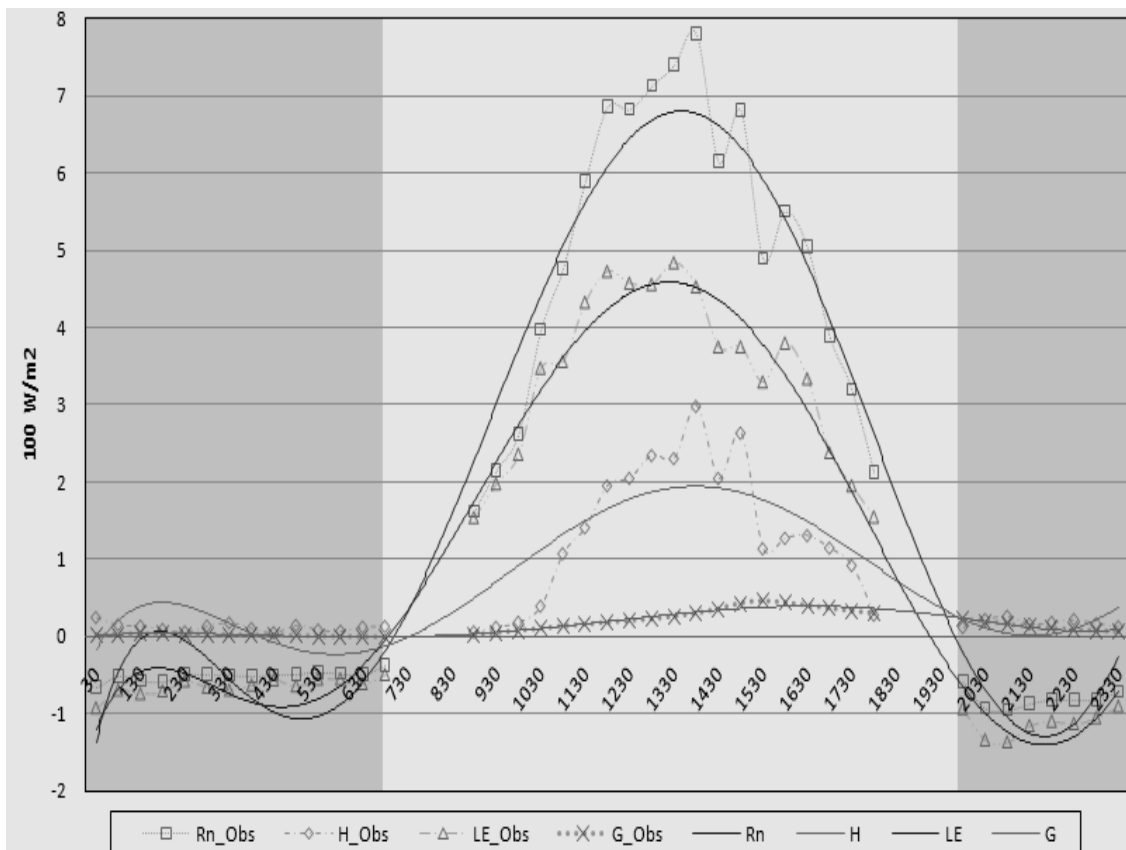


Fig. 4 LAS derived H in the energy balance cycle for 1 February 2010.

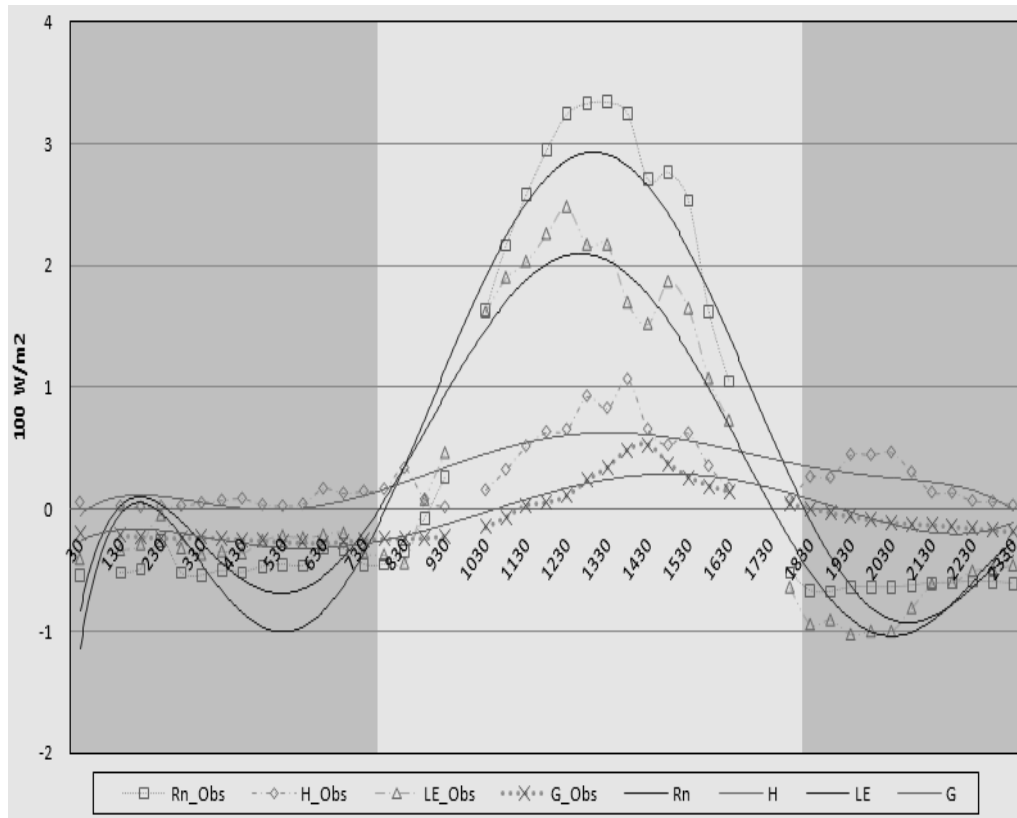


Fig. 5 LAS derived H in the energy balance cycle for 6 June 2010.

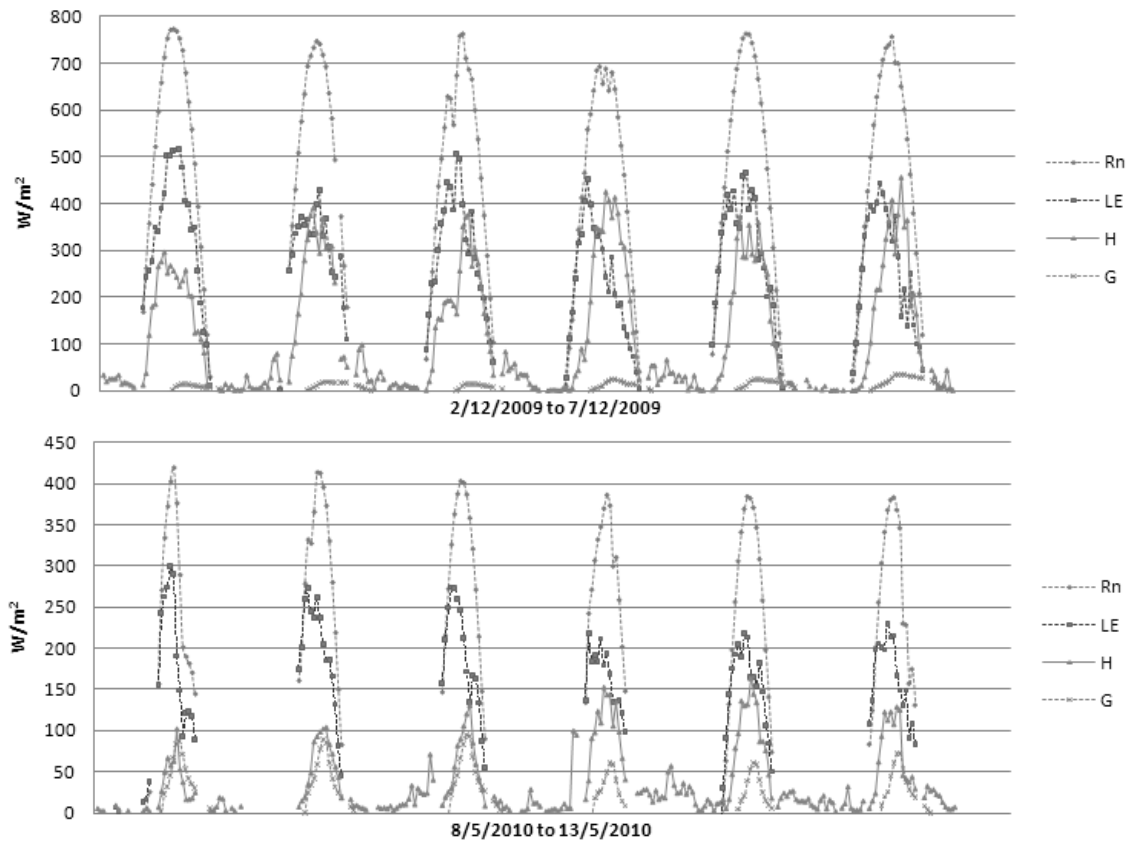


Fig. 6 Shows the graph of Rn, G, H, and LE for a period of two separate weeks in December 2009 and in May 2010.

value of 77 W/m^2 , and R_n ranges from 89 to 322 W/m^2 . This results in latent heat flux from 64 to 203 W/m^2 with a mean value of 155 W/m^2 , suggesting a realistic flux value on a winter day (temperature of 15°C). The change in the intensity of fluxes between summer and winter seasons is also evident from the above figures. This valid energy balance closure suggests that for the current configuration, the LAS is performing well for the purpose of heat flux estimation, provided the data is filtered for bad or missing values generated by various meteorological conditions (i.e. cloud cover, rainfall, etc.) or sensor errors.

Figure 6 shows the graph of R_n , G , H , and LE for a period of two separate weeks, in a summer week of December 2009 and a winter week of May 2010. During the summer week, average maximum net radiation is 780 W/m^2 , while average maximum net radiation is 400 W/m^2 during the winter week. Both the graphs show consistent partitioning with H being around 40% in summer and 35% in winter. We observed a noticeable difference between G in summer (around 4–5%) and in winter (18%) due to factors such as excessive irrigation and high density of canopy in the summer. Similarly, the average maximum latent heat flux is observed to be about 56% during the week in summer and 47% during the week in winter.

CONCLUSION

The initial results from the large aperture scintillometer are very encouraging and show great potential to estimate sensible heat flux during summer and winter seasons over large irrigated areas in Australia. The experimental set-up of the scintillometer is providing robust data sets with minimum maintenance required, and it provides the opportunity to use the set-up as a continuous flux monitoring site for the Murrumbidgee catchment. Also, the flux determined from the LAS is providing a calibration and validation platform for satellite derived energy balance fluxes for the region.

Acknowledgements This research is a part of National Water Commission (NWC) funded SAM-ET project. The authors are also thankful to NWC for providing funds to conduct this research and the local MIA farmers for their continuous support.

REFERENCES

- Bastiaanssen, W. (2000) SEBAL-based sensible and latent heat fluxes in the irrigated Gediz Basin, Turkey. *J. Hydrol.* **229**(1–2), 87–100.
- Beyrich, F. H., De Bruin, A. R., Meijninger, W. M. L., Schipper, J. W. & Lohse, H. (2002) Results from one-year continuous operation of a large aperture scintillometer over a heterogeneous land surface. *Boundary-Layer Meteorology* **105**(1), 85–97.
- De Bruin, H. A. R., Kohsiek, W. & van den Hurk, B. J. J. M. (1993) A verification of some methods to determine the fluxes of momentum, sensible heat, and water vapour using standard deviation and structure parameter of scalar meteorological quantities. *Boundary Layer Meteorology* **63**, 231–257.
- DeWekker, S. F. J. (1996) The estimation of areally-averaged sensible heat fluxes over complex terrain with a Large-Aperture Scintillometer. MS Thesis, Dept. of Meteorology, Wageningen Agricultural University, The Netherlands.
- Droogers, P. (2000) Estimating actual evapotranspiration using a detailed agro-hydrological model. *J. Hydrol.* **229**(1–2), 50–58.
- Hill, R. J. (1992) Review of optical scintillation methods for measuring the refractive index spectrum, inner scale and surface fluxes. *Waves in Random Media*, 2, p194
- Kite, G. & Droogers, P. (2000) Comparing evapotranspiration estimates from satellites, hydrological models and field data. *J. Hydrol.* **229**(1–2), 3–18.
- Kipp & Zonen (2007) LAS & X-LAS Instruction Manual (<http://www.kippzonen.com>). p74
- Meijninger, W. & De Bruin, H. (2000) The sensible heat fluxes over irrigated areas in western Turkey determined with a large aperture scintillometer. *J. Hydrol.* **229**(1–2), 42–49.
- Meijninger, W., Beyrich, F., Lüdi, A., Kohsiek, W. & De Bruin, H. A. R. (2006) Scintillometer-based turbulent fluxes of sensible and latent heat over a heterogeneous land surface – a contribution to Litfass-2003. *Boundary Layer Meteorology* **121**(1), 89–110.
- Rabbani, U. (2008) Spatial estimation of crop stresses using remote sensing, MPhil Dissertation, International Centre of Water for Food Security, Charles Sturt University, Australia, 104 p.
- Su, Z. (2002) The Surface Energy Balance System (SEBS) for estimation of turbulent heat fluxes. *Hydrol. Earth System Sci.* **6**(1), 85–99.

Irrigation demand forecasting using remote sensing and meteorological data in semi-arid regions

KALEEM ULLAH & MOHSIN HAFEEZ

International Centre of Water for Food Security (IC Water), Charles Sturt University, Locked Bag 588, Wagga Wagga, New South Wales 2678, Australia
mullah@csu.edu.au

Abstract Irrigated agriculture is a major consumer of freshwater, but a large part of the water used for irrigation is wasted due to poor management. Improving water management in irrigated areas requires the estimation of real time water demand, which is important for planning sustainable use of irrigation water. Real time irrigation demand forecasting entails a complete understanding of the spatio-temporal variability of meteorological parameters and evapotranspiration (ET). For improved irrigation system management and operation, a holistic approach of integrating remote sensing derived ET from the SEBAL method with forecasted meteorological data and water-use efficiency was used to forecast net irrigation demand in the Coleambally Irrigation Area (CIA), located in the southern Murray Darling Basin. In order to capture the spatial variability, the CIA has been divided into 22 nodes based on direction of flow and connectivity. All hydrological data of inflow and outflow were estimated at all nodes of the CIA for the estimation of water-use efficiencies. Ten Landsat 5 TM satellite images were used for mapping irrigated crops and estimation of actual ET for the summer cropping season of 2008–2009. This estimated actual ET and forecasted meteorological data was used for demand forecasting for seven days. The results were compared with the data obtained for irrigation supplies. Initial results for forecasted demand are quite promising and provide a practical way for water saving at the node scale by matching demand and supply.

Key words irrigated agriculture; water management; remote sensing; evapotranspiration

INTRODUCTION

Water scarcity is rapidly becoming a vital issue for many countries in the developed and developing world, and could lead to a severe global water crisis (IWMI, 2009). It has been observed that in many parts of the world, water demand already exceeds supply, and a continuously rising population will result in water scarcity in many more areas of the world (Teixeira, 2008). Pressure to meet the growing water demands have resulted in greater competition among traditional water consumers, namely agriculture, industry and cities, for available water resources. Among all users, irrigated agriculture is the largest consumer, accounting for 70% of global water withdrawals; from this water, nearly 40% of the world's food is produced. Maintaining enough freshwater for agricultural production will become increasingly difficult in the near future due to climate change, growing water competition among various sectors and rapid population growth. Water scarcity will force irrigated agriculture to produce more with less water in the future, which requires effective management of water.

Improving water management in irrigated areas and the assessment of irrigation performance are critical activities which require a complete understanding of all terms of the water balance at various spatial scales i.e. farm to basin levels (Khan & Hafeez, 2007). In such circumstances, water management in irrigation districts can be improved by analysing the irrigation water demand information (Pulido-Calvo *et al.*, 2007). Water demand information in irrigated areas is basic information for the development and implementation of successful tools for water resources management (Pulido-Calvo & Gutierrez-Estrad, 2009). For water demand estimation, it is important to understand how the irrigation system behaved in the past, what the current trends are, and what is expected in the future through accurate knowledge of various hydrological processes (ET, rainfall, runoff, seepage, etc.) and different factors (land use changes) affecting these hydrological processes in space and time.

An appropriate and reliable irrigation demand forecasting tool based on a complete understanding of hydrological behaviours and novel remote sensing technologies can improve water management in an irrigation area. This study aimed to develop and a methodology for irrigation demand forecasting based on spatial land-use and land-cover analysis, remote sensing

derived actual ET (ET_a), crop coefficients and meteorological data at the node as well as the irrigation system level.

STUDY AREA

The Coleambally Irrigation Area (CIA) is located in the lower part of the Murrumbidgee River catchment in the southern part of the Murray Darling Basin (Fig. 1(a)). The CIA contains approximately 79 000 ha of intensive irrigation, 42 000 ha of irrigation/dryland farms and 297 000 ha of the Outfall District area, supplying water to 478 farms owned by 362 business units (CICL, 2007). Principal summer (November–April) crops include rice, soybeans, maize (corn), grapes, prunes, sunflowers and lucerne, while principal winter (May–October) crops include wheat, canola, sunflowers and lucerne. Pasture for grazing is grown in both seasons. Average rainfall is 396 mm per year and the average annual evaporation is 1723 mm. The recent drought, a significant reduction in water allocations and concerns about climate change have all highlighted the need to manage water demand and supply water more sustainably, especially in the CIA.

MATERIALS AND METHODS

The CIA is a large irrigation area using a gravity flow system; water released from the dams takes seven days to reach the system, which makes the development of a robust methodology for water demand forecasting for the period of highest evaporative demand a necessity. High evaporative demand occurs in the months of December–February, when 75% of the area is planted to rice. The irrigation system comprises of one main canal and a number of secondary and tertiary canals. As an initial step in water demand forecasting, spatial and temporal boundaries of the domain were specified and further divided into 22 nodes based on direction of flow and connectivity (Fig. 1(b)). Due consideration was given to spatial distribution of rainfall, potential ET, soil texture and rooting depth of land cover.

The methodology for irrigation demand forecasting is based on spatial land use and land cover analysis, remote sensing derived actual ET (ET_a) and efficiencies, crop coefficients and meteorological data at the node and system level. To get information about the irrigated crops grown within the CIA and various nodes, land-use and land-cover classification was carried out using a simplified hybrid classification approach. This approach is based on a supervised classification algorithm in combination with false colour composite images, GIS-based farm boundary data and water order data of each farmer from the SCADA system.

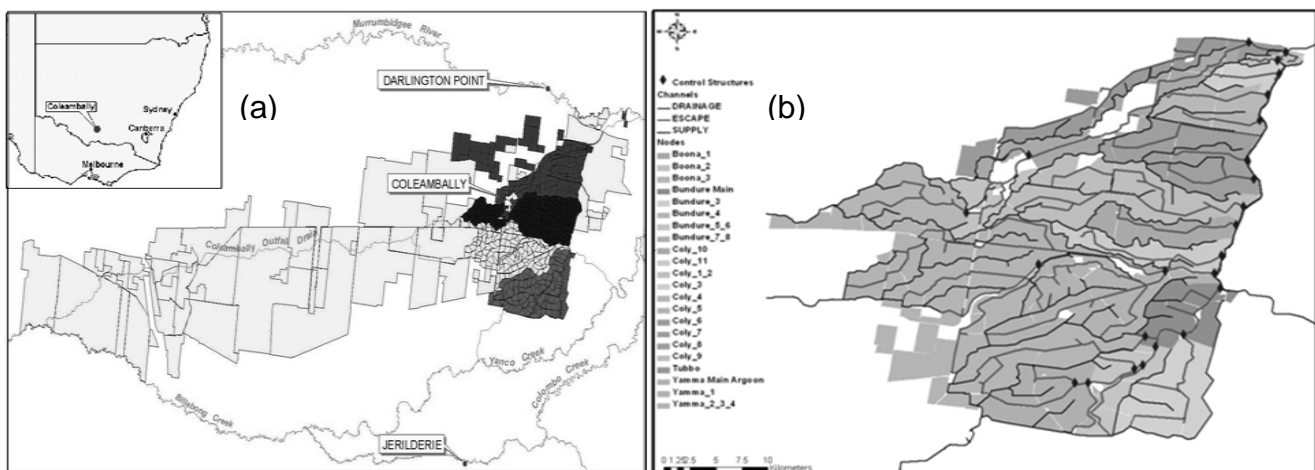


Fig. 1 (a) CICL operational area including CIA and outfall district (CICL, 2009); and (b) spatial distribution of nodes with supply and drainage channels and selected control points

In order to get information about actual crop water consumption, the SEBAL model, based on the surface energy balance equation and developed by Bastiaanssen *et al.* (1998a,b), was applied to 10 Landsat 5 TM satellite images covering the period of October 2008–March 2009. The pre-processing parameters required for the SEBAL model includes the normalized difference vegetation index (NDVI), surface emissivity, broadband surface albedo and surface temperature. The model was calibrated using the meteorological parameters measured from automatic weather stations at the selected farms. The daily ET_a was calculated from the instantaneous evaporative fraction, Λ , and the daily averaged net radiation, R_{n24} . The study provided ET_a maps on a monthly and seasonal basis for the entire study area.

For demand forecasting, irrigated crops in the CIA were clustered into rice and non-rice crops (others) in order to derive different hydrological and crop parameters. This developed methodology is not only based on analytical and empirical approaches, but also takes into account the physical processes as well as the spatial variability of different physical parameters influencing crop water requirement. A new and simplified methodology has been developed using remote sensing technology and field based estimates for forecasting irrigation demands for the CIA (Ullah, 2011). This methodology was applied in two steps; in the first step, efficiencies at the field scale as well as the system level were determined using remote sensing derived ET_a for different irrigated crops, and in the second step irrigation demand was forecast based on remote sensing derived crop coefficients and forecasted meteorological data. More details can be found in Ullah (2011). The water-use efficiencies adopted in this methodology are different from traditional efficiency terms used in irrigation systems. The water-use efficiencies defined here for both system and field or node levels were mainly used for the purpose of forecasting the demand for improvement of irrigation water management. These water-use efficiencies were determined from local historical data of water-use efficiencies, satellite based data of ET and actual applied water to the fields.

RESULTS AND DISCUSSION

The irrigated area was mapped using the Landsat TM satellite image (spatial resolution of 30 m) of 3 November 2008 (Fig. 2(b)). Irrigated crops were classified into rice and other summer crops.

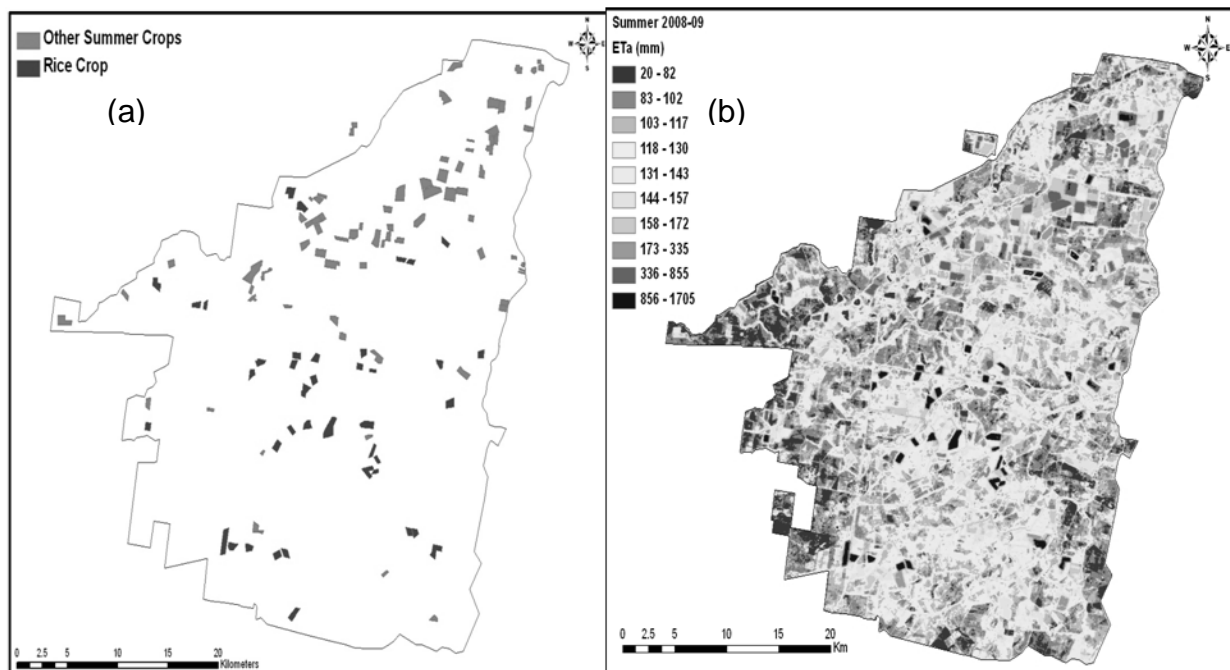


Fig. 2 (a) Maps of irrigated crops within CIA; and (b) seasonal actual ET of 2008–2009.

Only 3.8% of the area was under all crops during summer 2008–2009, and rice was grown on an area of just 1025 ha.

The seasonal actual evapotranspiration (ET_s) was estimated using 10 Landsat 5 TM images for 2008–2009, while the missing ET_a values were obtained by daily calculation of reference evapotranspiration (ET_o) as proposed by Tasumi *et al.* (2000). The output of SEBAL is a pixel-based spatially distributed seasonal estimate of ET_a for the CIA, as shown in Fig. 2(b). The seasonal actual ET values range from 20 mm to 1705 mm, with a mean value of 159 mm and standard deviation of 216 mm. To validate the remote sensing results, a comparison of ET_a produced by the SEBAL algorithm with ET data from the AWS and two eddy covariance systems installed in local rice and maize fields, shows good agreement within the expected range (Ullah, 2011).

In this study, daily irrigation demand for the next seven days was forecast using remote sensing based water-use efficiencies and K_c values, and was applied at the individual node as well as the system level. The water-use efficiencies are a combination of field level water-use efficiency (FWUE) and conveyance system loss. The FWUE was calculated for both rice crops and other crops. For rice fields, FWUE varies from 63% in Yamma Main_Argoon to 81% in Tubbo and the average FWUE was 71%. Similarly for other crops, the highest and lowest water-use efficiency was 81% for Coly 5 and 97% for Bundure 4 and the average efficiency was 89%. Overall, the average FWUE for rice fields was 71% and 89% for other crops at the system level.

The conveyance system loss, based on the area under each node, can provide reasonable estimation for water demand forecasting in systems that have fixed conveyance system loss regardless of the quantity of water that flows through the system. For proportional distribution of conveyance system loss over the entire nodes, the average conveyance system loss of high evaporative demand months (i.e. December, January and February) was estimated using the average monthly value of these months. The conveyance system loss per day varies from 0.79 ML for Coly 1_2 to 17.30 ML for Yamma 2_3_4. This variation in daily conveyance system losses depends entirely on the total area of the node; the larger the area, the greater the daily conveyance system loss.

Similarly, the calibrated images of ET_a were used for the estimation K_{c_act} at the pixel level over each node for rice crop and other crops separately. The K_{c_act} values for rice vary from a minimum of 0.86 in Coly 9 for the image of 3 November 2008 to a maximum of 1.06 for Yamma Main_Argoon for the image from the 22 January 2009. The average value derived for rice by Meyer *et al.* (1999) in this area ranges from 0.9 at initial stage to 1.1 at crop development and mid-season stage. The K_{c_act} values for other crops exhibited very high variability across the nodes and even within the nodes because of different crop combinations. It varies from 0.08 in Bundure 7_8 for the 22 January 2009 image to 1.20 in Bundure 3 for the 31 January 2009 image. The lowest value is related to pasture, which was completely finished by January in Bundure 7_8, while the highest value was found for lucerne in Bundure 3.

Results of irrigation demand forecasting indicate that the net irrigation demand forecast for fields at the node level (NIDFFN) shows a relatively high difference across the nodes. However, net irrigation demand forecast for fields at the system level (NIDFFS) shows no significant difference and has good agreement with actual water being delivered to fields. For 2008–2009, NIDFF at the system level (NIDFFS) was 4364 ML, 9387 ML and 9073 ML with demand supply ratio (DSR) of 0.69, 1.06 and 1.20 for December 2008, January 2009 and February 2009 respectively. In terms of net irrigation demand forecast at system level, NIDFS, making an allowance for conveyance system loss, results indicate that monthly forecasted irrigation water demand was higher for the selected months of 2008–2009 compared to actual water diverted into the system (Fig. 3). It was found that the forecast demand was higher by 57%, 25% and 22% in December, January and February, respectively.

The main reason for the higher values of net irrigation demand at the system level is due to the use of a fixed value of conveyance system loss to maintain system operation. The fixed value of conveyance system loss is proportionally significant as compared to total water diverted due to extremely limited irrigation supplies in this season. In addition to conveyance system loss, the lower forecast demand is attributed to lower values of NIDFFN and NIDFFS, which was

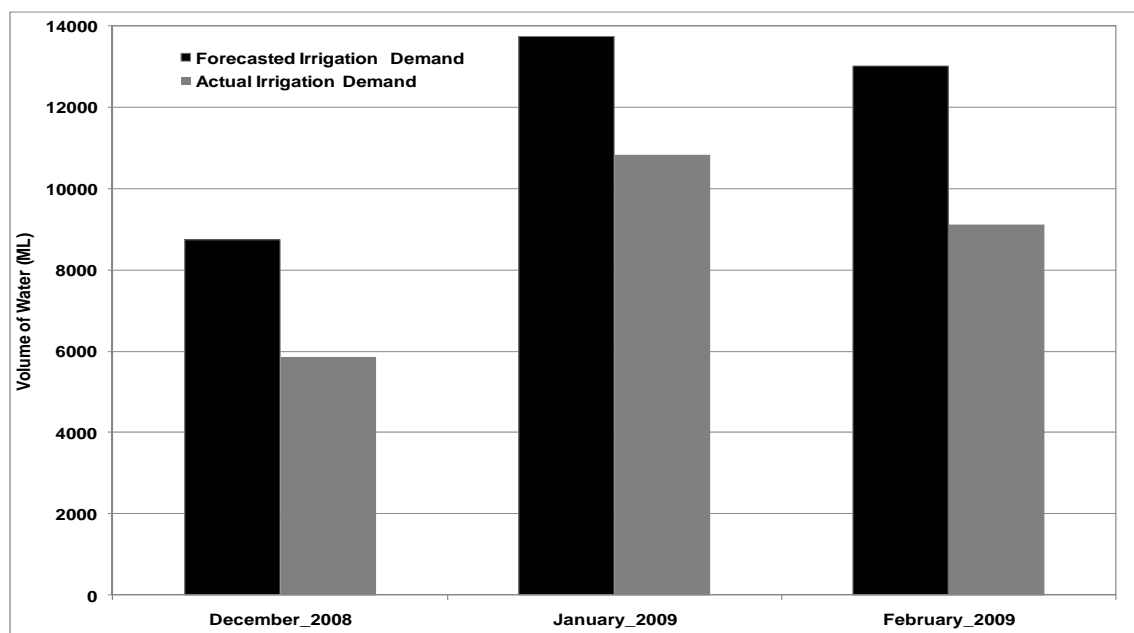


Fig. 3 Comparison of forecasted irrigation demand and actual diverted water in the high evaporative months of 2008–2009.

influenced by a lag time in updating K_{c_act} , inaccurate assessment of groundwater, change in water-use efficiencies and remote sensing image analysis for ET_a estimation. However, overall the demand forecasts have reasonable agreement with actual water diverted to the system, and can help in improving irrigation water management.

CONCLUSION

The applied methodology is very simple and cost effective for a demand driven irrigation system that has a good database, and daily demand can be forecast and updated by using remote sensing image analysis with minimum time input. This demand forecasting tool is based on a sound understanding of hydrological behaviour, novel remote sensing technology and forecasted meteorological data, and is useful for improved irrigation water management ranging from node to system levels. It may reduce the risks associated with over and under irrigation application by more accurately matching demand and supply. This methodology for demand forecasting will be tested for another cropping season in the near future.

Acknowledgements The authors would like to thank the Australian Centre for International Agriculture Research (ACIAR) project (LWR/2005/144) and Coleambally Irrigation Company Limited (CICL) Water Smart Australia project for providing the financial support to carry out this study.

REFERENCES

- Bastiaanssen, W. G. M., Menenti, M., Feddes, R. A. & Holtslag, A. A. M. (1998a) A remote sensing Surface Energy Balance Algorithm for Land (SEBAL): Part 1. Formulation. *J. Hydrol.* **212–213**, 198–212.
- Bastiaanssen, W. G. M., Menenti, M., Feddes, R. A. & Holtslag, A. A. M. (1998b) The Surface Energy Balance Algorithm for Land (SEBAL): Part 2 Validation. *J. Hydrol.* **212–213**, 213–229.
- CICL (2007) Annual report, Coleambally Irrigation Cooperative Limited (CICL), Australia.
- CICL (2009) Annual compliance report, Coleambally Irrigation Cooperative Limited (CICL), Australia.
- IWMI (2009) Water for a food secure world. International Water Management Institute (IWMI) Strategic Plan 2009–2013.

- Khan, S. & Hafeez, M. M. (2007) Spatial mapping of water productivity in irrigation system using geo-information techniques. In: *Int. Congress on Modelling and Simulation* (10–13 December 2007, University of Canterbury, Christchurch, New Zealand).
- Meyer, W. S., Smith, D. J & Shell, G (1999) Estimating reference evaporation and crop evapotranspiration from weather data and crop coefficients: An addendum to research project 84/162 quantifying components of water balance under irrigated crop. CSIRO Land and Water, Technical Report 34/98.
- Pulido Calvo, I. P., Montesinosb, P., Roldanb, J. & Navarro, F. R. (2007) Linear regressions and neural approaches to water demand forecasting in irrigation districts with telemetry systems. *Biosystem Engng* **97**, 283–293.
- Pulido-Calvo, I. & Gutierrez-Estrada, J. C. (2009) Improved irrigation water demand forecasting using soft computing hybrid model. *Biosystems Engng* **102**(2), 202–218.
- Tasumi, M., Bastiaanssen, W. G. M. & Allen, R. G. (2000) Application of the SEBAL methodology for estimating consumptive use of water and stream flow depletion in the Bear River Basin of Idaho through Remote Sensing. Appendix C: A step-by-step guide to running SEBAL. EOSDIS Project Final Report, The Raytheon Systems Company and the University of Idaho, USA.
- Teixeira, A. H. de C. (2008) Measurements and modelling of evapotranspiration to assess agricultural water productivity in basins with changing land use patterns, A case study in the Sao Francisco River Basin, Brazil. PhD thesis, University of Delft, Netherlands.
- Ullah, M. K. (2011) A geoinformatics approach for spatial water accounting and irrigation demand forecasting for a gravity irrigation system. Charles Sturt University, PhD Thesis.

Ground-based laserscanning – a new method for measuring fluvial erosion on steep slopes?

F. HAAS, T. HECKMANN, M. BECHT & B. CYFFKA

*Physical Geography, Cath. University of Eichstaett-Ingolstadt, Ostenstr.18, 85072 Eichstaett, Germany
florian.haas@ku-eichstaett.de*

Abstract In the presented study, a high resolution Terrestrial Laserscanner (Riegl LMSZ 420i) is used for scanning steep and barely vegetated slopes over a period up to 20 months between 2009 and 2010. The produced multitemporal ground-based laserscanning data on these slopes in combination with a 3-D-Software (Riscan Pro) and a GIS (LIS Desktop) are used to quantify fluvial erosion by cut and fill analyses. To consider different climatic, surface and soil conditions these measurements are carried out in two areas, which are situated in the Alps (south Tyrol/Italy) and in the Mediterranean region (Island of Elba-Tuscany/Italy). Since the investigations focus on the methodological approach, the data acquisition and the data processing are described in detail in the first part of the paper. The second part shows first results of using the method for cut and fill analyses for two test plots within the scanned slopes of both investigation areas. The results show that the amount of erosion and accumulation can be well detected by ground-based laserscanning. Due to the very high spatial resolution of the derived surface changes, the paper also shows the high capability of the method for detailed process analysis, which could lead to a better process understanding for erosion on steep and barely vegetated slopes.

Key words fluvial erosion; steep slopes; ground-based LIDAR; terrestrial laserscanning; GIS; Italy; Alps

INTRODUCTION

Fluvial erosion is not only a widely noticed problem for agricultural landscapes (Diodato & Bellocchi, 2008; Auerswald *et al.*, 2009), but due to the process intensity it also plays a major role for the geomorphic system (Bryan, 2000), especially on steep and barely vegetated slopes, such as badland gullies. Up to now, erosion on such steep slopes was measured e.g. by using erosion pins or sediment traps (cf. Becht, 1995; Sirvent *et al.*, 1997; Clarke & Rendell, 2006; Evans & Warburton, 2005; Haas & Heckmann, 2007; Haas, 2008; Della Seta *et al.*, 2009). If used alone, these methods are both error-prone by influencing the slopes and are hard to use, particularly on very steep slopes with limited accessibility (Haas, 2008). Besides this, erosion is normally measured only with a small number of pins or traps (low resolution, small sample) and thus with restrictions for the interpretation and the transferability of the results.

The use of ground-based laserscanning can help to solve the described problems and limitations. First tests on steep slopes in the Alps showed that using this method, fluvial erosion can be measured very accurately, with a very high spatial resolution, by not entering and therefore not influencing the slopes (Haas & Heckmann, 2007; Haas, 2008). This relatively new method is already used for measuring other hydromorphological processes that are shaping the Earth's surface (cp. Rowlands *et al.*, 2003; Heritage & Hetherington, 2007; Milan *et al.*, 2007; Baldo *et al.*, 2009; Hodge *et al.*, 2009; Lim *et al.*, 2009).

This paper shows the experiences of using laserscanning for measuring fluvial erosion on steep slopes in Italy during a 20-month survey between 2009 and 2010, with the main focus of the paper on the data acquisition and on data processing in a GIS.

STUDY AREA

To consider different climatic, surface and soil conditions, fluvial erosion was measured on slopes in two different areas (Fig. 1), which are located in the Southern Alps (south Tyrol/Italy) and in the Mediterranean region (Island of Elba-Tuscany/Italy).

The Alpine investigation area is situated at 2000 m a.s.l. in the upper Val di Funes valley (northern Dolomites), which is a tributary to the Eisack valley. The measured slope is barely vegetated, has an extent of 1050 m², with a maximum flow length of 30 m and consists of fine to

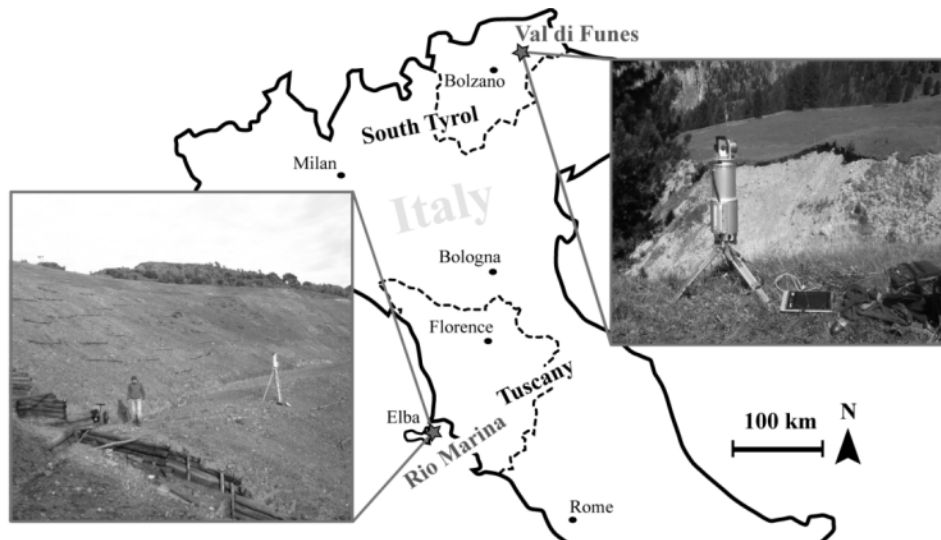


Fig. 1 Location of the study areas in Tuscany and south Tyrol. The photographs show the monitored slopes.

coarse ground moraine deposits (composite of permian and triassic sedimentary rocks). The slope angles are between 8° and 54° , with a mean of 32° . The climatic conditions are characterised by a mean annual rainfall of around 640 mm (weather station Brixen at 560m a.s.l.), a mean annual temperature of 11.2°C and a temporal snow cover during winter. The main snow melting period is from April until the end of May.

The Mediterranean investigation area is situated at a recultivated former iron ore mine (haematite and pyrite) at Rio Marina at an altitude of around 50 m a.s.l. on the east coast of the Island of Elba, which is located close to the western coast of Italy. The investigated slopes are also barely vegetated, but have barriers for erosion control (see Fig. 1), have an extent of 500 and 650 m^2 and consist of mainly coarse (>sand) mine filling material and slag. The slope angles lie between 14° and 69° , with a mean of 39° .

The climatic conditions are characterised by a mean annual rainfall of around 750 mm, with the main precipitation during the winter period (83% of rainfall between September and April) and normally without any snow cover. The mean annual temperature is around 15.3°C .

MATERIALS AND METHODS

Scanner system

For the presented measurements, the terrestrial laser scanner system Riegl LMS Z420i was used. This long-range 3-D laser scanner has a maximum measurement range up to 1000 m (under natural conditions ~ 700 m for bare soils) with distance accuracy of 0.01 m (by single shot) and a scanning rate of 8000 points per second. The laser wavelength used is near infrared with a beam divergence of 0.25 mrad. This corresponds to an increase in the laser footprint by 0.0025 m per 100 m (manufacturer information). Besides laser scanning, a digital SLR camera (Canon EOS 350D) is mounted on the scanner for taking referenced high-resolution pictures of the scanned objects. Due to the SLR camera, every single point can not only be defined by space coordinates, but can also be characterized by a RGB value. These RGB values are applicable for colorizing the point clouds (better visualization) or for filtering of vegetation. Both the scanner and the SLR camera are operated by an external PC and the scanner software Riscan Pro.

Data acquisition and processing

Up to now the slopes were scanned at three time steps from a distance of around 50 m and by a scanning resolution of 0.05° (stepwidth of the scanning signal). This corresponds to a point density

of around 400 points per square metre. According to manufacturer information, the distance error of the measurement can be reduced (0.01 m to 0.005 m) by scanning the slopes at least four times and by averaging these four single scans. This can be done by a scan-sequence mode. Using this mode, slopes can be measured repeatedly with the same alignment. Averaging is done afterwards in Riscan Pro. During these investigations, every slope was scanned using this procedure of measuring four consecutive scans.

For accurate referencing of the scans of the single time steps, a specific number of tie points on or near the slopes are required (Fig. 2). During this investigation a minimum of five tie points were used (reflector buttons with a diameter of 0.05 m). They were fixed by using screws or nails on unmoveable objects like big roots and trees, or on wooden debris flow barriers for the Mediterranean slopes. For every time step and prior to the scanning of the slopes, every single tie point was scanned very accurately by using a fine scan mode (around 2000 single shots).



Fig. 2 Scanned slopes in the Val di Funes valley (A) and on the slopes at Rio Marina/Elba (B) and the locations of the fixed tie points.

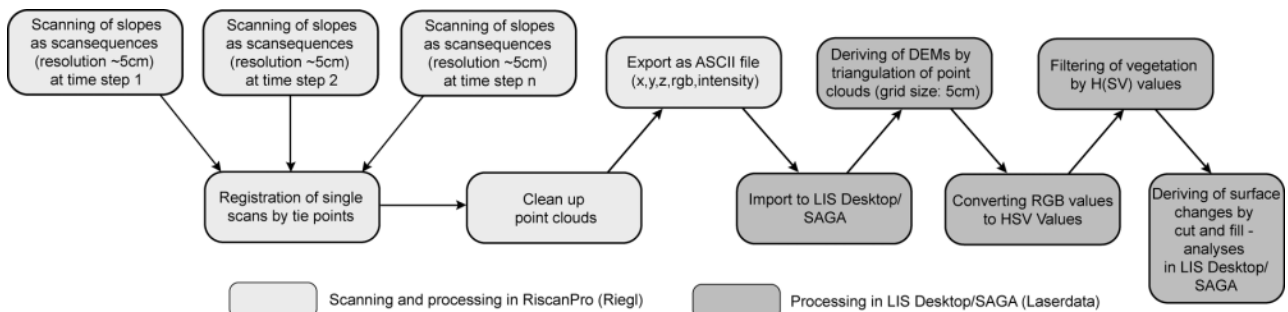


Fig. 3 Workflow of data processing and the analysing process.

After the data acquisition in the field, the software Riscan Pro (3-D scanner software) was used for post-processing of the raw data (Fig. 3). At first the single scans (point clouds) were matched (registered) by using the scanned tie points. After this step, point clouds were manually corrected in order to delete items such as artefacts, birds or bigger vegetation.

After this, point clouds (x,y,z-coordinates and the RGB values) were imported into the database of LIS Desktop/SAGA GIS, to carry out the following processing and analysing steps. Primarily, DEMs of the slopes with a grid size of 0.05 m were derived by triangulating the point clouds. In order to filter vegetation, the RGB values were used to produce colourized datasets (grid with RGB values). Since RGB values are not appropriate for automated filtering processes, they were afterwards transformed into the HSV colour model. Thus vegetation could be eliminated from the DEMs by using the H value (e.g. by green or brown colours). Following this, the amount of surface changes were derived by subtraction of the filtered DEMs of the single time steps (cut and fill analyses).

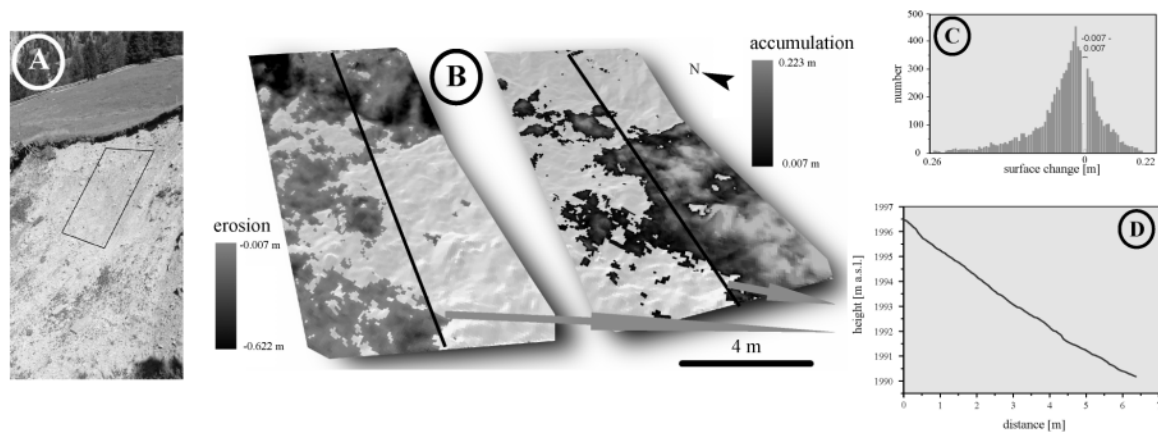


Fig. 4 Test plot of the slope in the Val di Funes valley (A), 3-D view of the erosion map for this test plot (B), histogram of erosion and accumulation (C) and slope profile of the test plot (D).

Accuracy of the measurements

To define the accuracy of the cut and fill analyses, a part of the slopes was scanned four times with the same alignments at one time step. Using the four derived DEMs, the measurement error could be clearly defined. For this test set-up, a mean standard deviation between the four DEMs of 0.0068 m ($n = 4531$) for the alpine slope and 0.0074 m ($n = 4221$) for the Mediterranean slope was derived. Based on these results, erosion or accumulation under 0.007 m was defined as not detectable by the experiment design used. Therefore, all calculated surface changes below this error were set to “no data” in the surface change maps and were not used for the statistical analyses. Additionally, the error is displayed behind every measurement result (e.g. 0.05 m \pm 0.007 m).

RESULTS AND DISCUSSION

Val di Funes

At the Val di Funes valley, the measurement results are shown for a randomly chosen single test plot (Fig. 4(A)) of the measured slope. The extension of the test plot is around 23 m² by a flow length of nearly 6.5 m. The mean slope angle of the plot is 40.7° by a maximum of 62.7° and a minimum of 27.1°. The measured point density of this scan is around 350 points m⁻² and the derived DEMs have a grid size of 0.05 m.

The results of the measurements show that erosion exceeds accumulation (Fig. 4(C)) on this test plot. Over a 12 month period (September 2009–September 2010), the surface change amounts to a mean value of $-0.063 \text{ m year}^{-1} \pm 0.007 \text{ m}$, by a maximum of $-0.62 \text{ m year}^{-1} \pm 0.007 \text{ m}$. This corresponds to a sediment yield of $1575 \times 10^{-7} \text{ m}^3 \text{ m}^{-2} \text{ year}^{-1} \pm 105 \times 10^{-7} \text{ m}^3 \text{ m}^{-2} \text{ year}^{-1}$. Figure 4(B) shows the spatial distribution of the erosion and accumulation on the plot. It is obvious that

erosion is very high on the upper third of the slope. In contrast, accumulation is very high in the lower part of the test plot due to a slight flattening (Fig. 4(D)). In total the mean amount of surface changes is slightly higher in contrast to the measured results on steep alpine slopes in moraine deposits by other studies using erosion pins or sediment traps (cf. Becht, 1995; Haas 2008). However, the maximum values of erosion are considerably higher in this study, and are comparable to the first laserscanning tests in the study of Haas & Heckmann (2007) and Haas (2008). This is because pins can lead to a stabilization or destabilization of bigger blocks in moraine deposits and thus the erosion of such blocks is not measurable by pins, but very well measured by laserscanning.

Rio Marina

At Rio Marina, the results of the measurements are shown also for a randomly chosen single test plot (Fig. 5(A)) of the measured slope (slope Nr.2 in Fig. 2). The extension of the test plot is around 23 m^2 by a flow length of nearly 6.5 m and thus comparable to the test plot in the Alps. The mean slope angle of the plot is 32.3° with a maximum of 52.1° and a minimum of 12.8° and is slightly lower than on the alpine slope. Due to a shorter scanning distance, the point density of this scan is slightly higher ($400 \text{ points m}^{-2}$), but the grid size of the derived DEM was also set to 0.05 m .

The measurements show that in contrast to the Val di Funes, there is only very slight deposition within the test plot and thus erosion clearly exceeds accumulation (Fig. 5(C)). The surface change amounts to a mean value of $-0.031 \text{ m} \pm 0.007 \text{ m}$ ($0.019 \text{ m year}^{-1} \pm 0.007 \text{ m}$), by a maximum of $-0.17 \text{ m} \pm 0.007 \text{ m}$, for a 20 month period (April 2009–November 2010). This corresponds to a sediment yield of $456 \times 10^{-7} \text{ m}^3 \text{ m}^{-2} \text{ year}^{-1} \pm 105 \times 10^{-7} \text{ m}^3 \text{ m}^{-2} \text{ year}^{-1}$. Figure 5(B) shows the spatial distribution of the erosion on the test plot. Because accumulation is very low on this slope, accumulation values are not displayed in the figure due to visual causes. It is obvious that on this test plot erosion is very high on the steep lower part of the slope (Fig. 5(D)) and in the rills (up to the maximum of $0.17 \text{ m} \pm 0.007 \text{ m}$) and there is only slight erosion at the inter-rill zone (around $0.01 \text{ m} \pm 0.007 \text{ m}$).

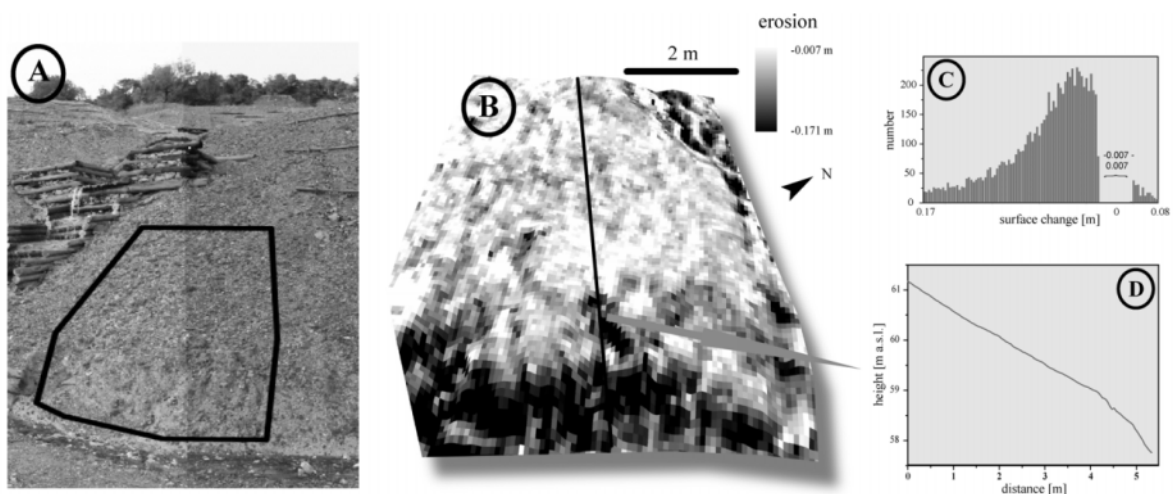


Fig. 5 Test plot of the slope near Rio Marina (A), 3-D view of the erosion map for this test plot (B), histogram of erosion and accumulation (C) and slope profile of the test plot (D).

Compared to the results of the alpine slopes, the mean surface changes are considerably lower on the Mediterranean slopes (only half). The higher mean values, and also the higher maxima of surface changes, are certainly the cause of the specific conditions on the alpine slopes such as the presence of snow, freezing and thawing processes, and especially of the specific conditions of the moraine deposits (with particle sizes from fine to very coarse debris).

CONCLUSION

The results presented show that ground-based laserscanning is an appropriate method for generating high resolution multitemporal DEMs, which can be used for quantification of the surface changes (erosion and accumulation) on steep slopes. Furthermore the investigation indicates that particular attention has to be paid to the accurate fitting of the scans of the single time steps, since fitting errors have a significant effect on accuracy of the measuring result. The experiment design used, coupled with the low scanning distance (beyond 50 m), the use of the scansequence mode with averaging the single scans and the registration process by fine scanning of more than five tie points for every single slope, lead to a sufficient accuracy of the measurements, with a very high spatial resolution, and no touching or influencing the measured slopes.

Thus the first results show the high potential of ground-based laserscanning, not only for very accurate quantification of erosion on steep slopes and a better measuring result in inhomogeneous moraine deposits, but especially for detailed spatial and statistical analyses. These analyses could lead to a better process understanding (e.g. interaction of different processes, the influence of the slope angle or flow length, etc.) in terms of modelling erosion on such slopes, especially if the measurements were carried out at a better temporal resolution.

Acknowledgements This work was supported with an initial founding from the PROFOR program (program for research promotion) of the Cath. University of Eichstaett-Ingolstadt. Many thanks also to Christian Breitung, Peter Fischer, Paula Haas and the students for their support in the field. The authors also want to thank the reviewers for their helpful comments.

REFERENCES

- Auerswald, K., Fiener, P. & Dikau, R. (2009) Rates of sheet and rill erosion in Germany – a meta-analysis. *Geomorphology* **111**, 182–193.
- Baldo, M., Bicocche, C., Chiochino, U., Giordan, D. & G. Lollino (2009) LIDAR monitoring of mass wasting processes: the Radicofani landslide, Province of Siena, Central Italy. *Geomorphology* **105**, 193–201.
- Becht, M. (1995) Untersuchungen zur aktuellen Reliefentwicklung in alpinen Einzugsgebieten (Investigations of the current landform development in alpine drainage basins). Münchener geogr. Abh., Bd. A47. Munich, Germany (in German).
- Clarke, M. L. & Rendell, H. M. (2006) Process-form relationships in Southern Italian badlands: erosion rates and implications for landform evolution. *Earth Surf. Processes Landf.* **31**, 15–29.
- Della Seta, M., Del Monte, M., Fredi, P. & Lupia Calmieri, E. (2009) Space-time variability of denudation rates at the catchment and hillslope scales on the Tyrrhenian side of Central Italy. *Geomorphology* **107**, 161–177.
- Diodato, N. & Bellocchi, G. (2008) Assessing and modelling changes in rainfall erosivity at different climate scales. *Earth Surf. Processes Landf.* **34**, 969–980.
- Evans, M. & Warburton, J. (2005) Sediment budget for an eroding peat-moorland catchment in northern England. *Earth Surf. Processes Landf.* **30**, 557–577.
- Haas, F. & Heckmann, T. (2007) Slope wash. In: *SEDIFLUX Manual: Analysis of Source-to-Sink-Fluxes and Sediment Budgets in Changing High-Latitude and High-Altitude Cold Environments* (ed. by A. Beylich, & J. Warburton). Geological Survey of Norway publication 2007.053 (ISSN 0800-3416), 72–75.
- Haas, F. (2008) Fluviale Hangprozesse in Alpinen Einzugsgebieten der Nördlichen Kalkalpen – Quantifizierung und Modellierungsansätze (Fluvial processes on alpine slopes of the northern Alps – Quantification and basic modelling approaches). Eichstätter Geographische Arbeiten Bd. 17, Munich, Vienna, Germany (in German).
- Heritage, G. & Hetherington, D. (2007) Towards a protocol for laser scanning in fluvial geomorphology. *Earth Surf. Processes Landf.* **32**(1), 66–74.
- Hodge, R., Brasington, J. & Richards, K. (2009) *In situ* characterization of grain-scale fluvial morphology using Terrestrial Laser Scanning. *Earth Surf. Processes Landf.* **34**(7), 954–968.
- Lim, M., Rosser, N. J., Allison, R. J. & Petley, D. N. (2010) Erosional processes in the hard rock coastal cliffs at Staithes, North Yorkshire. *Geomorphology* **114**(1–2), 12–21.
- Milan, D. J., Heritage, G. & Hetherington, D. (2007) Application of a 3D laser scanner in the assessment of erosion and deposition volumes and channel change in a proglacial river. *Earth Surf. Processes Landf.* **32**(11), 1657–1674.
- Rowlands, K. A., Jones, L. D. & Whithworth, M. (2003) Landslide Laser Scanning: a new look at an old problem. *Quarterly J. Engng Geol. Hydrogeol.* **36**, 155–157.
- Sirvent, J., Desir, G., Gutierrez, M., Sancho, C. & Benito, G. (1997) Erosion rates in badland areas recorded by collectors, erosion pins and profilometer techniques (Ebro Basin, NE-Spain). *Geomorphology* **18**, 61–75.

A preliminary analysis of the total column water vapour retrieved from COSMIC data

WEIJIA WANG¹ & XINJIA ZHOU²

¹ Weather Modification Office of Sichuan Province, Chengdu, China
wjwang999@sohu.com

² University Corporation for Atmospheric Research, Boulder, USA

Abstract Using the total column water vapour from the Constellation Observing System for Meteorology, Ionosphere and Climate (COSMIC) wet profile data, this paper analyses the distribution of the COSMIC soundings in southwest China and its adjacent area (the study area), and the water vapour distribution of the study area, in order to study the methods of analysing regional water vapour with COSMIC data. The analysis shows that according to the high-resolution of COSMIC soundings, COSMIC data will complement the lack of operational meteorological stations in the study area and provide more water vapour information. The analysis of the water vapour graph from COSMIC data shows that in southwest China and its adjacent area, the total column water vapour is influenced significantly by the topography and the altitude. The Tibetan Plateau is a large dry region, and its water vapour structure is obviously different from its surroundings. Further analysis shows that the water vapour accumulation over the Tibetan Plateau is through the following accesses: the Great Yalu Zangbu Canyon all the year round, southwest of the Himalayas from June to August, the northern areas in July, and some small local areas by heat convection from May to September. The water vapour over the north of the Bay of Bengal is relatively short in January, increases obviously in April, and reaches a maximum in July.

Key words GPS RO; COSMIC; total column water vapour; water vapour; Tibetan Plateau

INTRODUCTION

As a follow-on project of Global Positioning System/Meteorology (GPS/MET), in which atmospheric limb soundings were obtained from a low-Earth-orbit satellite with high vertical resolution (Ware *et al.*, 1996), the Constellation Observing System for Meteorology, Ionosphere and Climate (COSMIC) project will improve understanding of the global water cycle and climatology of water vapour (Anthes *et al.*, 2000). The study area encompasses the Tibetan Plateau, Sichuan Basin and Yunnan-Guizhou Plateau in southwest China and its adjacent area (the study area: 78.408°E–110.191°E, 21.148°N–36.486°N). As one of the world's most data sparse areas, the study area has a lack of favourable water vapour measurements. Meanwhile, the water vapour distribution of the study area plays a crucial role in Asia, and even in global weather and climate due to the special topography and geographical position. Recently COSMIC has begun using Global Positioning System/Radio Occultation (GPS RO) (Kursinski *et al.*, 1997) measurements to gain globally distributed water vapour profiles. Here, total column water vapour (TCWV) calculated from COSMIC wet profile data will be used to analyse the water vapour distribution of the study area.

DATA AND METHODS

COSMIC is currently providing between 1500 and 2500 profiles per day globally, with high vertical resolution. Here TCWV in the study area (78.408°E–110.191°E, 21.148°N–36.486°N) is calculated from COSMIC water vapour profiles during 2008.

RESULTS

There were 5096 COSMIC RO soundings uniformly distributed around the study area during 2008, as shown in Fig. 1. As the traditional technique for water vapour measurements, there are 41 operational meteorological radiosonde sites located in southwest China. Figure 1 only includes operational meteorological radiosonde sites in southwest China. These radiosonde sites are

administered by the China Meteorological Administration, which operationally launches radiosondes twice a day. A new technique that has been applied there is the ground-based GPS network (Wang *et al.*, 2010), which has a total of 25 stations. The ground-based GPS network with the sites shown in Fig. 1 was established in September 2007 by a China-Japan cooperation project (Japan International Cooperation Agency), which continuously retrieves precipitable water vapour. Accordingly, COSMIC data will complement the lack of operational meteorological stations and provide additional water vapour information in the study area.

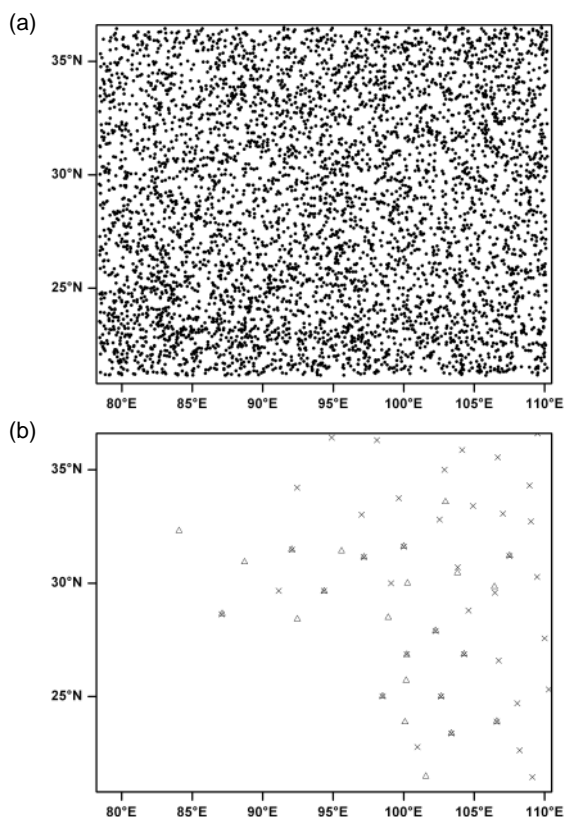


Fig. 1 COSMIC RO soundings during 2008 are shown as dots (a), location of ground-based GPS sites as triangles (b), and location of radiosonde sites as crosses (b).

Figure 2 shows the distribution of the 5096 COSMIC RO soundings varying with date (Fig. 2 (a)), longitude (Fig. 2 (b)), and latitude (Fig. 2(c)) in the study area during 2008. The average of daily occurrence of COSMIC RO soundings is 14, the maximum is 29, and the minimum is 1 (Fig. 2(a)). By 1° longitude band, the average occurrence of COSMIC RO soundings is 154, the maximum is 189, and the minimum is 36 (Fig. 2(b)). By 1° latitude band, the average occurrence of COSMIC RO soundings is 318, the maximum is 425, and the minimum is 165 (Fig. 2(c)). Obviously, COSMIC RO soundings show favourable spatial and temporal resolution in all weather.

Figure 3 shows a map of COSMIC TCWV in the study area with continuous data during 2008. The map includes data from 5096 COSMIC RO soundings. As is shown by this map, TCWV in the study area does not progressively decrease from low-latitude regions to high-latitude regions. The Tibetan Plateau is a remarkably large, dry region. Moreover, its water vapour structure, which is probably impacted by its unique thermodynamic structures (Wu *et al.*, 2005), is obviously different from its surroundings. Meanwhile, the Himalayas on the south of the Tibetan Plateau block off water vapour from the Bay of Bengal and the Indian Ocean. The one and only apparent wet region in the Tibetan Plateau is the Great Yalu Zangbu Canyon. On the east of the Tibetan Plateau, the Sichuan Basin is a moist region, where some moister places coincide with the

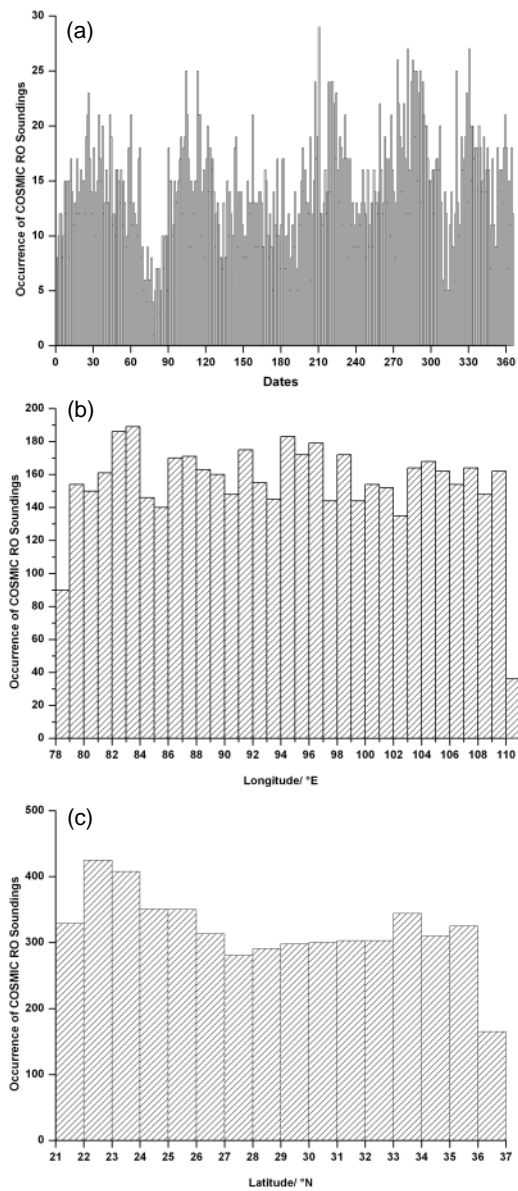


Fig. 2 Distribution of COSMIC RO sounding events during 2008: (a) distribution with date, (b) distribution with longitude, (c) distribution with latitude.

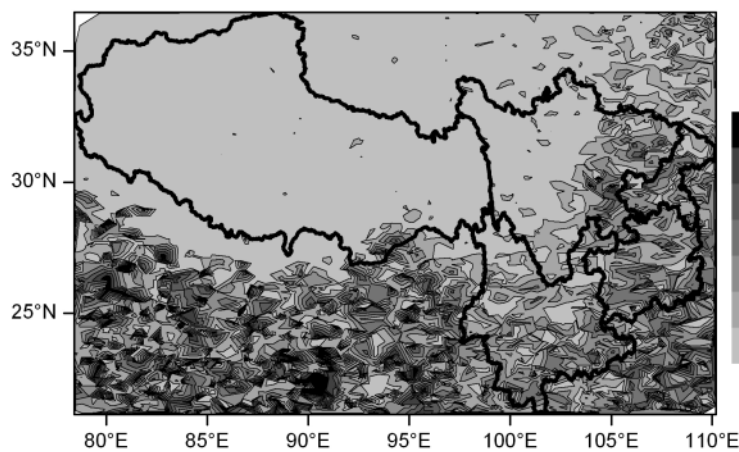


Fig. 3 Total column water vapour with continuous data during 2008.

places where rivers confluence. The Yunnan-Guizhou Plateau is relatively moister owing to its lower altitude and latitude compared with the Tibetan Plateau. In addition, the moistest region in

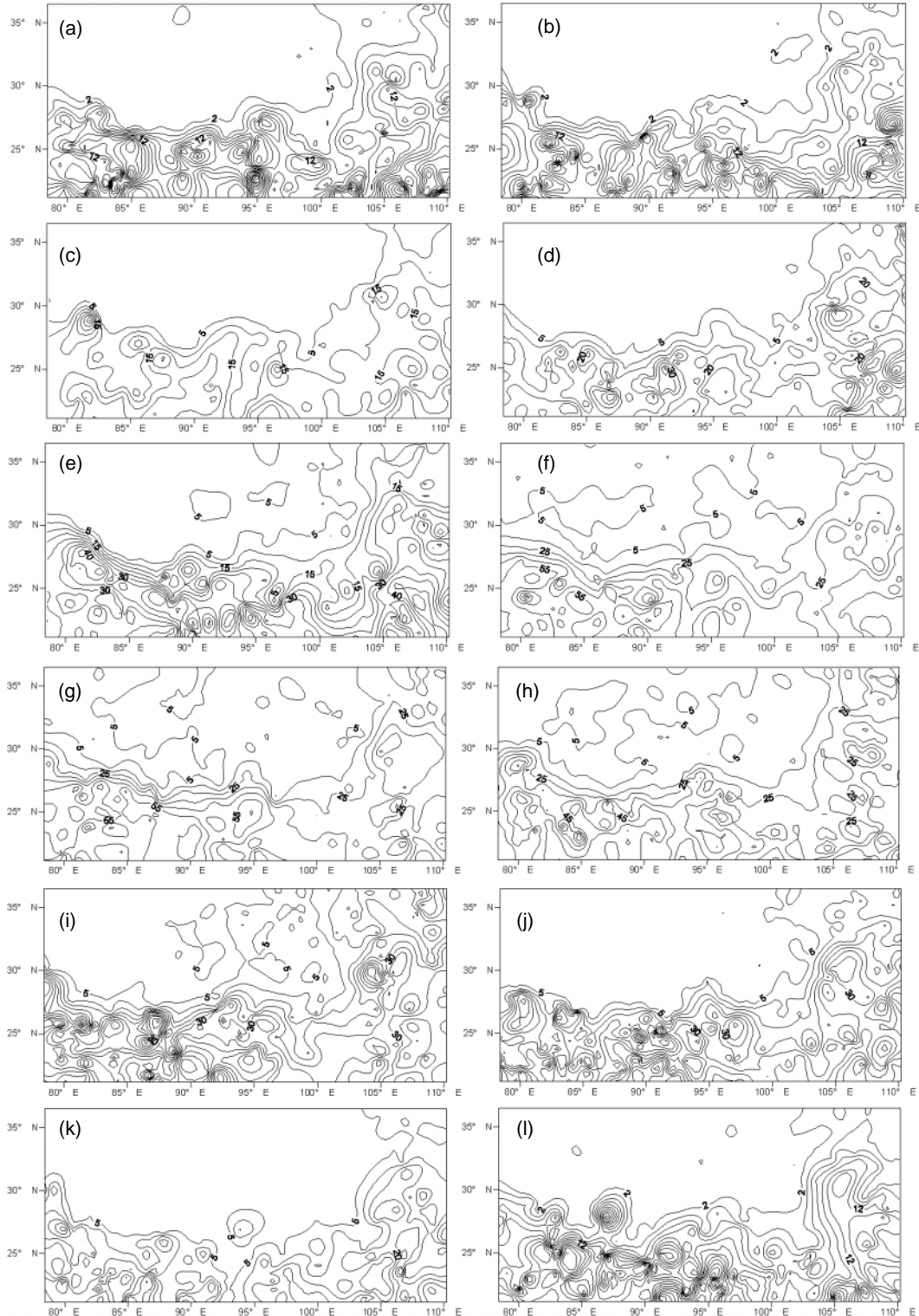


Fig. 4 Total column water vapour from January to December (Unit: mm). (a) Jan., (b) Feb., (c) Mar., (d) Apr., (e) May, (f) Jun., (g) Jul., (h) Aug., (i) Sept., (j) Oct., (k) Nov., (l) Dec. (The intervals of the contour lines of (a), (b), (l) are 2 mm; the intervals of the contour lines of (c), (d), (e), (i), (j), (k) are 5 mm; the intervals of the contour lines of (f), (g), (h) are 10 mm.)

the study area is the north of the Bay of Bengal. TCWV over the north of the Bay of Bengal is much higher than TCWV over the Beibu Bay, at the same latitude in the study area. To the south of the Tibetan Plateau, higher TCWV often appears along great rivers. Besides, TCWV over the Ganges in the Indian subcontinent is a bit higher than TCWV over the river valleys in the west of the Indo-China Peninsula. Furthermore, TCWV over the river valleys in the west of the Indo-China Peninsula is higher than TCWV over the Red River in the east of the Indo-China Peninsula. TCWV over the Red River is also higher than TCWV over the Mekong. Consequently, TCWV over the study area is influenced significantly by the topography and the altitude.

Figure 4 shows TCWV from January to December in the study area. It is observed that from January to December water vapour passes through the Great Yalu Zangbu Canyon to the southeast of Tibet. January is the driest month in the study area; the Tibetan Plateau is a large continuous dry region with TCWV mostly <2 mm. Water vapour develops most strongly over the Irrawaddy River in the Indo-China Peninsula; at that time TCWV over the north of the Bay of Bengal is lower than TCWV over the Beibu Bay. In February, the continuous dry region in the Tibetan Plateau with TCWV lower than 2 mm becomes a bit narrower. In March, TCWV over the continuous dry region in the Tibetan Plateau mostly becomes <5 mm. In April, water vapour over the north of the Bay of Bengal and water vapour over the west of the Indo-China Peninsula strengthen obviously. In May, the continuous dry region in the Tibetan Plateau shrinks northwards and westwards; in the continuous dry region are several small moist areas, which are probably caused by local ascending motion and shear lines (Xu *et al.*, 1996). In June, moisture penetrates over the southwest of the Himalayas into the Tibetan Plateau; the dry region in the Tibetan Plateau with TCWV lower than 5 mm shrinks sharply, and relatively moist areas also appear in the Tibetan Plateau. At the same time, in the Tibetan Plateau there are some small water vapour accumulation areas, which are probably caused by local heat convection. July is the wettest month in the study area; water vapour over the north of the Bay of Bengal reaches its peak and moisture spreads eastwards along the southwest of the Himalayas, deeply into the Tibetan Plateau, as well as a narrow band of moisture that spreads into the Tibetan Plateau from the north. In the meantime, there are some small water vapour accumulation areas in the east of the Tibetan Plateau. August is the second wettest month. In September, the dry region in the Tibetan Plateau becomes continuous again, and still there are some small water vapour accumulation areas in the east of the Tibetan Plateau. In October, the dry region in the Tibetan Plateau widens dramatically; TCWV over the Tibetan Plateau is mainly below 5 mm. In November, the dry region with TCWV lower than 5 mm widens eastwards. In December, the TCWV of the dry region in the Tibetan Plateau becomes mainly below 2 mm.

CONCLUSION

From what has been analysed above, it can be concluded that:

- (1) With high resolution in southwest China and its adjacent area (the study area), COSMIC TCWV will complement the lack of high resolution data of water vapour measurements in the study area and provide more water vapour information.
- (2) TCWV in the study area is significantly influenced by topography and altitude, and it does not progressively decrease from low-latitude regions to high-latitude regions.
- (3) The Tibetan Plateau is a continuous large, dry region, and its water vapour structure is obviously different from its surroundings. Throughout the year water vapour passes through the Great Yalu Zangbu Canyon to the Tibetan Plateau. In June, July and August, water vapour climbs up through the southwest of the Himalayas to the Tibetan Plateau. A small quantity of water vapour drifts from the north to the Tibetan Plateau in July. Water vapour also accumulates over some small local areas by heat convection from May to September.
- (4) Water vapour over the north of the Bay of Bengal is relatively low in January, increases obviously in April, and reaches a maximum in July.

Acknowledgements Thanks to the University Corporation for Atmospheric Research for providing COSMIC data. Thanks to Emeritus Prof. J. Mao and S. Zhang for thoughtful comments.

REFERENCES

- Anthes, R. A., Rocken, C. & Kuo, Y.-H. (2000) Applications of COSMIC to meteorology and climate. *TAO* **11**(1), 115–156.
- Kursinski, E. R., Hajj, G. A., Schofield, J. T., Linfield R. P. & Hardy, K. R. (1997) Observing the Earth's atmosphere with radio occultation measurements using the Global Positioning System. *J. Geophys. Res.* **102**(D19), 23429–23465.
- Wang, W. & Zhao, X. (2010) Characteristics of Precipitable Water from Ground-Based GPS Measurements in Western Sichuan Plateau. *J. Arid Met.* **28**(3), 279–284 (in Chinese).
- Ware, R., Exner, M., Feng, D., Gorbunov, M., Hardy, K., Herman, B., Kuo, Y.-H., Meehan, T., Melbourne, W., Rocken, C., Schreiner, W., Sokolovskiy, S., Solheim, F., Zou, X., Anthes, R., Businger, S. & Trenberth, K. (1996) GPS sounding of the atmosphere from low Earth orbit: Preliminary results. *Bull. Am. Met. Soc.* **77**, 19–40.
- Wu, G., Liu, Y., Liu, X., Duan, A. & Liang, X. (2005) How the heating over the Tibetan Plateau affects the Asian climate in summer. *Chinese J. Atmospheric Sci.* **29**(1), 47–56 (in Chinese).
- Xu, J., Zheng, X., Xu, H. & Fang, X. (1996) Upper tropospheric moisture distribution over the Tibetan plateau as revealed from GMS-5 water vapour images. *J. Appl. Met. Sci.* **7**(2), 246–251 (in Chinese).

The impact of temporal and spatial resolution on developing risk maps: case study of the Tubma basin, Thailand

S. VISESSRI, N. McINTYRE & C. MAKSIMOVIC

Department of Civil and Environmental Engineering, Imperial College London, London SW7 2AZ, UK
sv1008@ic.ac.uk

Abstract Flood and drought prevention and correction measures should be prioritised towards areas that most suffer, with the aid of a risk assessment. Flood and drought risk assessments in Thailand are often conducted based on runoff estimation from models with coarse temporal and spatial resolutions. This has the benefit of being easy to apply with modest data requirements. To improve the accuracy and resolution of runoff estimation, however, a model with higher temporal and spatial resolutions is suggested. This paper investigates whether, given readily available data, the ArcSWAT framework results in risk maps different from those produced using the rational formula at a relatively coarse spatial-temporal scale. Using the Tubma basin as a case study, the two methods produced significant differences in the sub-basin scale drought risk map, but not the flood risk map. Both the ArcSWAT model and rational formula yielded identical priority-area maps developed from the overlay of the flood and drought risk maps. This indicated that a model with coarse temporal and spatial resolutions, i.e. the rational formula, is comparable to a more complex model, i.e. ArcSWAT, when used for developing sub-basin scale priority maps given readily available data in Thailand. However, the potential for ArcSWAT or other distributed models to deliver higher resolution results with sufficient reliability needs to be further investigated.

Key words risk map; risk assessment; water balance; spatial resolution; temporal resolution; Thailand; Tubma basin; water availability

INTRODUCTION

Thailand has been an agricultural country, but increasing industrialisation in recent decades and associated urbanisation, is increasing demand for water. Communities in many regions of Thailand, including the industrial regions, have frequently suffered not only from water shortages, but also floods caused by variations in climate, unsuitable attention to detail in risk assessment, and unsuccessful management practices.

Instead of developing a full risk assessment, this paper aims to investigate a method that can be applied efficiently at a national scale, using readily available data, to identify priority areas where there is the highest potential risk. Conventionally, such a risk assessment in Thailand is performed at a monthly scale and for entire sub-basins (Chitradon *et al.*, 2009) with areas ranging from 160 km² to 12 800 km² (Hydro and Agro Informatics Institute, 2007). As a result, the conventional risk assessment may not represent well the timing and location of floods and droughts, since the relevant time-scales (especially for flood risk) may be smaller than a month, and the risks may occur in local areas smaller than the entire sub-basin. With the aim of improving the temporal and spatial resolutions of the risk assessment, estimation of runoff via a continuous distributed rainfall-runoff model is an attractive option. With increasing computer power and nationally-available spatial data sets to support hydrological modelling, this type of approach is becoming feasible. However, the value of using such a complex model depends on how much extra value it adds to the risk analysis, considering the underlying data and model limitations, over and above the simpler broader-scale analysis. The value of using higher temporal and spatial resolution models for developing prioritisation risk maps will be addressed in this paper using a case study of the Tubma basin in the east of Thailand.

DESCRIPTION OF THE STUDY CATCHMENT

The Tubma basin (197 km²) (Fig. 1) has suffered from water shortage due to the loss of wetlands and a rapid increase in water demand. The terrain is plain, alternating with hilly slopes. Based on

the information of the Department of Mineral Resources, the geology of the Tubma basin consists of discontinuous layers of rocks ranging in age from the oldest Precambrian to Quaternary. The prevalent soil type in the basin is a deep layer of sandy loam with high porosity, and thus good drainage ability, but poor capacity to absorb water. Potato, oil palm, fruit tree, and rubber tree are examples of common crops. The Tubma basin is susceptible to high erosion owing to its undulating hills and ploughing of the soil for agriculture. About 55% of the basin is agricultural, 35% is residential, official and industrial areas, 8.6% wetland, and 1.1% open water.

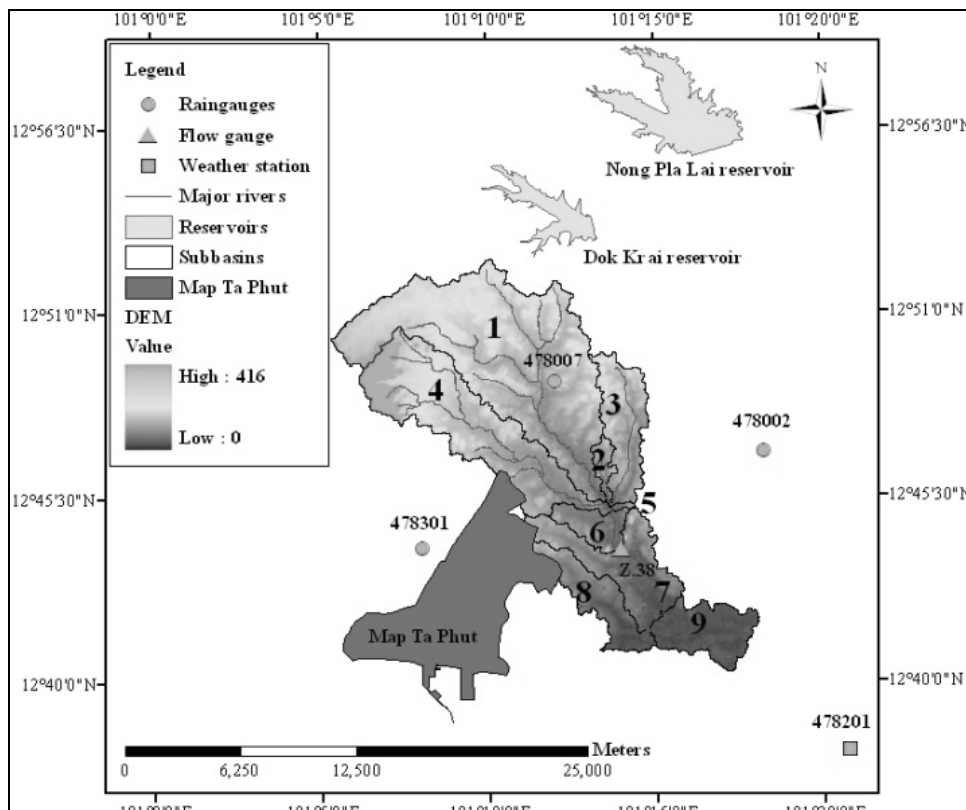


Fig. 1 Location of the Tubma basin with main rivers, sub-basins, gauging stations and the associated industrial region.

The Tubma basin has a tropical climate with three seasons – rainy, winter, and summer – which are mainly characterised by the southwest and northeast monsoons (Thai Meteorological Department, 2007). The southwest monsoon is formed in a high pressure zone in the Indian Ocean causing the rainy season between mid-May and mid-October, while the northeast monsoon originates from a high pressure zone near Mongolia and China, bringing dry and cold air to the Tubma basin between mid-October and mid-February. Summer, the transition period between the southwest and northeast monsoons, starting from mid-February to mid-May, is usually dry and hot, but thunderstorm, and strong breezes occasionally occur due to the convergence of hot air covering Thailand and cold air spreading from China. The Tubma basin receives relatively high rainfall compared to other regions of Thailand because it is situated on the windward side of the country during the southwest monsoon. The mean annual rainfall, calculated based on the rainfall data between 1973 and 2006, is 2092 mm, while the rainfall in other regions, except for the west coast basin of Thailand, ranges from 964 to 1972 mm (Royal Irrigation Department, 2010). The Tubma basin is subjected to tropical cyclones, usually arriving in October. Most flooding has been caused by heavy rainfall generated by tropical depressions rather than the more severe rainfall that comes with typhoons. This is because of the higher occurrence of the former type of event. Shortages of water usually take place in January–April and July–August (Hydro and Agro Informatics Institute, 2010).

METHODOLOGY

Flood and drought risk maps were developed using the difference between water supply and demand as a risk index. Thus, the aim is screening for areas likely to be most at risk, rather than absolute measures of risk. The total supply to each sub-basin (see Fig. 1) was an aggregate of three components, including: the runoff obtained from the ArcSWAT model or rational formula, flow from upstream sub-basin(s), and additional water from the Dok Krai and Nong Pla Lai reservoirs (as shown in Fig. 1) supplied for industrial use. Water demand consists of demand from household, agriculture, and industry. Household demand was estimated based on the population of each sub-basin and rate of water usage (6 m³/head/month) (Koonthanakulvong, 2006). The industrial water consumption depends primarily on the type of industry and it was estimated from the typical water consumption rate per unit of power (m³/hp/month). Agricultural demand was calculated based on crop type, crop area, crop water usage, and amount of effective rainfall.

Once the water supply and demand were determined, the water balance for each sub-basin was obtained by deducting the total demand and environmental flow from the total supply. The environmental flow for each sub-basin was approximated to be 10% of the total runoff in that sub-basin. A positive water balance is a surplus and indicates flood risk, while a negative water balance indicates drought risk. The values of maximum/minimum monthly water balance of each sub-basin were drawn from the entire period of simulation (from 1 January 1993 to 31 December 2005) and compared across all nine sub-basins. The level of flood/drought risk was classified into three classes — high, medium, and low. The three sub-basins with the maximum surplus or deficit were labelled as areas with relatively high potential risk. The next three sub-basins having lower/higher values of water balance were classified as medium risk-prone areas, and the last three sub-basins, having the least surplus or deficit, were labelled as areas with low potential risk. The priority maps were the end result of superimposing the flood and drought risk maps according to criteria set by the Hydro and Agro Informatics Institute: for example, sub-basins with high flood and high drought risks were classified to have high priority; sub-basins with medium flood risk and low drought risk were classified to have medium priority.

SURFACE WATER ESTIMATION USING THE ArcSWAT MODEL

To estimate runoff using the ArcSWAT model (Neitsch *et al.*, 2005), daily rainfall, daily maximum and minimum temperature, and geographical data including the digital elevation model (DEM), land use, and soil type were input into the model. The watershed delineation tool in the ArcSWAT model was employed to delineate the nine sub-basins shown in Fig. 1. The location of streamflow gauge Z.38 (Fig. 1) was manually added into the model for the purpose of calibration. The nine sub-basins were divided into 146 hydrologic response units (HRUs) based on judging hydrological uniformity in terrain, land use, and soil type. The crop parameters were estimated from the database embedded in the ArcSWAT tool. The soil parameters were calculated from the Usersoil database created by the Hydro and Agro Informatics Institute based on the data from the Land Development Department. Potential evapotranspiration was estimated based on the Penman-Monteith equation. The rainfall distribution in each sub-basin was generated based on the records of three raingauges, as shown in Fig. 1. A mixed exponential distribution was adopted for temporal infilling of rainfall (using ArcSWAT's weather generator program, WXGEN) (Neitsch *et al.*, 2005). The modelled streamflow was calibrated against observed monthly flow between 1 January 1995 and 31 December 2000. The validation period was from 1 January 2001 to 31 December 2005. The best calibration yielded $r^2 = 0.75$ and Nash-Sutcliffe Efficiency (NSE) = 0.63. The r^2 and NSE values for the validation period were 0.65 and 0.38, respectively. This validation performance might be improved by the identification of a more suitable model structure, but for the purpose of this study it was considered acceptable. In comparison, the NSE obtained in a previous application of ArcSWAT to the Klong Yai catchment, with an area of about 322 km², was 0.34 (Nuim, 2006). The estimated surface runoff was used as net runoff for developing risk maps.

RUNOFF ESTIMATION USING THE RATIONAL FORMULA

The monthly runoff coefficients used in this paper were estimated using the monthly average flow from 1993 to 2005 at the catchment outlet divided by the monthly average rainfall over the catchment. The monthly runoff coefficients for all sub-basins were assumed to be equal, regardless of spatial differences in terrain, soil type, and land cover. The areal rainfall for each of the sub-basins was estimated by the Thiessen polygon method. The potential evapotranspiration was calculated based on the Penman-Monteith equation and records at the weather station 478201, as shown in Fig. 1. The actual evapotranspiration, obtained by the multiplication of a crop coefficient and the potential evapotranspiration, was deducted from the total runoff. The remaining runoff was used as the water supply of the sub-basin. In summary, the primary differences between this method and the ArcSWAT model are: the finer space and time scale used for runoff calculation in ArcSWAT; the nonlinear runoff generation processes in ArcSWAT; and the use of default ArcSWAT parameters, subject to some calibration, rather than the empirical monthly runoff coefficients used in the rational method.

RESULTS AND DISCUSSION

The interpretation of results can be separated into two perspectives. The first perspective concerns local risk assessment (for a particular sub-basin) and another perspective is the prioritisation of sub-basins (comparing degree of risk at a particular sub-basin with the other eight sub-basins). Based on the maximum risk out of all months, both the ArcSWAT model and rational formula yielded identical flood risk maps but slight variations in drought risk maps as shown in Fig. 2(a),(b), and Fig. 3(a),(b). The priority maps obtained based on the ArcSWAT model and rational formulas were identical. However, this may be influenced by the criteria for priority risk mapping set by Thailand's Hydro and Agro Informatics Institute: a change in thresholds used to classify level of risk may lead to different results.

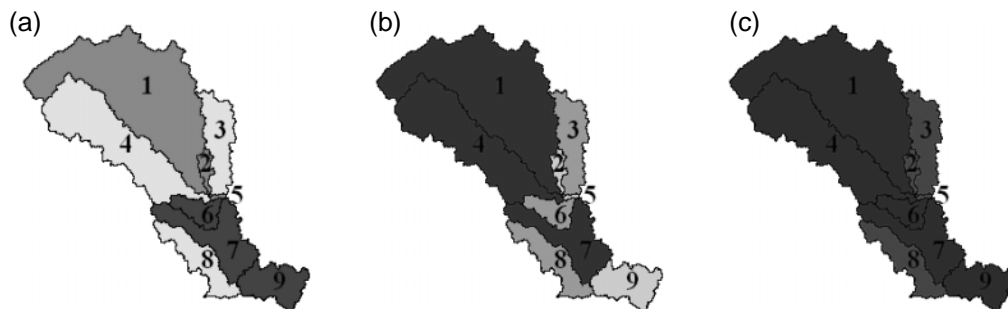


Fig. 2 Risk maps based on the ArcSWAT model: (a) flood risk map, (b) drought risk map, (c) priority risk map. Darker shades represent the higher risks.

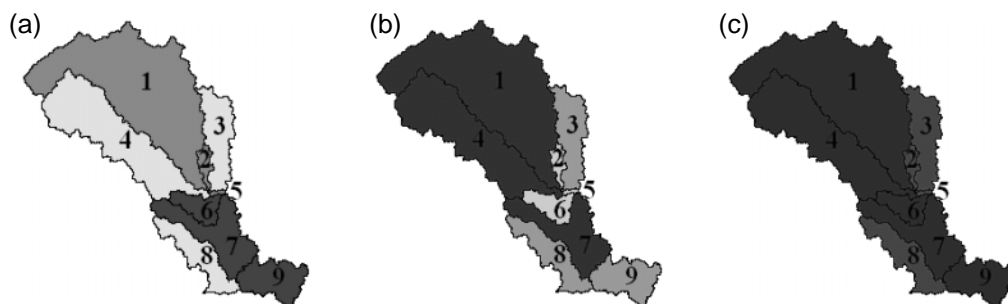


Fig. 3 Risk maps based on the rational formula: (a) flood risk map, (b) drought risk map, (c) priority risk map. Darker shades represent the higher risks.

Considering a particular sub-basin and month, the ArcSWAT model and rational formula showed some conflicting results for water balance (not shown in this paper). While the ArcSWAT model indicated negative water balance, the rational formula may indicate positive water balance, or *vice versa*. The ArcSWAT model may provide a more accurate simulation at this scale because the temporal and spatial variations within a sub-basin have an effect on the water balance at a sub-basin scale. Additionally, the ArcSWAT model potentially allows priority areas to be defined at as small a scale as HRUs. Also, unlike the rational formula or other simple models, the ArcSWAT model is able to estimate hydrological components other than flow, i.e. actual evapotranspiration, lateral flow, and groundwater yield. And, in the case of a particular flood event, an analysis can be performed by selecting a sub-daily simulation in ArcSWAT. Given the new availability of high resolution spatial data sets covering Thailand, there is therefore a potential opportunity to improve the accuracy and resolution of national-scale flood and drought risk assessment.

However, this relies on the ability to adequately reduce the uncertainties inherent to using models such as ArcSWAT. Uncertainties related to ArcSWAT in this study were believed to be caused largely by the estimates of soil parameters. These were estimated from the Usersoil database instead of the embedded database in ArcSWAT. The advantage of using the tailor-made Usersoil database is its greater relevance to the soil type in the Tubma basin. However, the development of the Usersoil database was partly subjective, and it was not easy to match the soil types provided by the Land Development Department to the soil table that supports the ArcSWAT model. The Usersoil database contained a smaller number of soil properties compared to ArcSWAT's embedded database, hence judgement was required to specify suitable values of the corresponding parameters, and these were assumed to be uniform over the sub-basin. Thus, the results from the ArcSWAT model may be more reliable if more extensive information regarding soil and groundwater properties can be acquired. Uncertainty also arises from rainfall, climate, and streamflow data. Having more flow gauges, ideally for each individual sub-basin, would make calibration possible for each sub-basin.

Hence there is some doubt about whether ArcSWAT can provide the required reliability with the available data, particularly regarding soils and rainfall-flow data for calibration. It may be that an intermediate-level model, which is more dynamic than the applied rational method, and may be applied in a distributed manner, but is less data demanding than ArcSWAT, may be useful. For example, the IHACRES model (i.e. Scocimarro, 1999; Schreider *et al.*, 2002; Jakeman & Letcher, 2003), and the NAM model (i.e. Shamsudin & Hashim, 2002; Mapiam & Sriwongsitanon, 2009) have shown some promise in these previous applications to Thai catchments.

CONCLUSION

This paper begins to investigate the suitable level of complexity of a rainfall-runoff model to support screening of flood and drought risk over Thailand. Simple indices of flood and drought risk were used at a monthly and sub-basin scale. On one hand, using a model with higher temporal and spatial resolutions (ArcSWAT) had a significant effect on the water balance calculations at a sub-basin scale. On the other hand, it did not contribute to any change in the priority sub-basins over the entire basin. It is therefore concluded that, given the available data and given that the purpose is to screen for priority areas, the simpler model is suitable. However, the growing availability of spatial data, although perhaps not yet adequate to support ArcSWAT, promises to make higher resolution screening possible in the near future. Thus, continued efforts at developing national hydrological databases are recommended. In terms of modelling, more effective use of existing data may be achieved by regionalisation (for predicting flows in ungauged sub-basins) and testing of alternative medium-complexity hydrological models.

Acknowledgements The first author is grateful to the Thai government for financial support and to the Royal Irrigation Department, Department of Water Resources, Thai Meteorological

Department, Land Development Department, and Hydro and Agro Informatics Institute for providing the data used in this research.

REFERENCES

- Chitradon, R., Boonya-Aronnet, S. & Thanapakpawin, P. (2009) Risk management of water resources in Thailand in the face of climate change. *Sasin J. Manage.* 64–73.
- Department of Mineral Resources (2010) *Geology of Thailand*. Bangkok, Thailand: DMR. http://www.dmr.go.th/ewtadmin/ewt/dmr_web/main.php?filename=GeoThai_En (accessed 29 December 2010).
- Hydro and Agro Informatics Institute (2007) Thai subbasins. Bangkok, Thailand.
- Hydro and Agro Informatics Institute (2010) The study of Monkey cheeks water detention in the Tubma basin, Rayong. Bangkok, Thailand: Hydro and Agro Informatics Institute. http://job.haii.or.th/tabma/index.php?option=com_content&task=section&id=10&Itemid=81 (accessed 9 July 2010).
- Jakeman, A. J. & Letcher, R. A. (2003) Integrated assessment and modelling: features, principles and examples for catchment management. *Environmental Modelling & Software* **18**, 491–501.
- Koonthanakulvong, S. (2006) Water Usage and Water Balance Assessment in Khlong Yai Basin. CU-WRSRU.
- Mapiam, P. P. & Sriwongsitanon, N. (2009) Estimation of the URBS model parameters for flood estimation of ungauged catchments in the upper Ping River basin, Thailand. *ScienceAsia* **35**, 8.
- Neitsch, S. L., Arnold, J. G., Kiniry, J. R. & Williams, J. R. (2005) SWAT (Soil and Water Assessment Tool) Texas, USA.
- Nuim, B. (2006) The impact of climate change, land use and environmental protected areas on the quality of the surface runoff of the upper watersheds of the three reservoirs: Dokgray, Nongpla-Lai and Klon-Yai. PhD Dissertation, Burapha University.
- Royal Irrigation Department (2010) Average rainfall in 25 national basins. Bangkok, Thailand: Royal Irrigation Department. http://water.rid.go.th/hyd/hyd_isohyetal/hyd_isohyetal.html (accessed 1 March 2011).
- Schreider, S. Y., Jakeman, A. J., Gallant, J. & Merritt, W. S. (2002) Prediction of monthly discharge in ungauged catchments under agricultural land use in the Upper Ping basin, northern Thailand. *Mathematics and Computers in Simulation* **59**, 19–33.
- Scoccimarro, M. (1999) A framework for integrated catchment assessment in northern Thailand. *Environmental Modelling & Software* **14**, 567.
- Shamsudin, S. & Hashim, N. (2002) Rainfall runoff simulation using MIKE1. *J. Civil Engng* **15**, 13.
- Thai Meteorological Department (2007) Climate of Thailand. General Climatic Conditions (Department of Mineral Resources,

A new automatic calibration approach based on rating curves: first results with ENVISAT altimetric data

AUGUSTO C. V. GETIRANA

LEGOS, UPS-Toulouse 3, IRD, Toulouse, France
augusto.getirana@legos.obs-mip.fr

Abstract This study presents preliminary results obtained with a new procedure for the automatic calibration of hydrological models based exclusively on spatial altimetry data. The technique is based on the minimization of biases between discharges computed by the hydrological model and by stage *versus* discharge relationships ($h \times Q$ model) derived from the combination of spatial altimetry data and modelled discharges at virtual stations. The study area is the Branco River basin, located in the northern Amazon basin. Spatial altimetry data provided by the ENVISAT satellite at four virtual stations are used in the optimization process for the 2002–2006 periods. For altimetry-based cases, the Nash-Sutcliffe (NS) coefficient varied from 0.66 to 0.94, the NS for the logarithms of streamflows from 0.61 to 0.95 and the relative error (RE) from 0.18 to 0.73. The best values for discharge-based cases were 0.94, 0.96 and 0.16, respectively. The results show that the new altimetry-based optimization approach can provide improved solutions and reliably reproduce discharges time series. It also gives results similar to those provided by discharge-based optimization approaches, with competitive computational costs.

Key words automatic calibration; spatial altimetry; hydrological modelling; rating curve

INTRODUCTION

A recent study has demonstrated the feasibility of integrating spatial altimetry data into the automatic calibration of hydrological models by using a previously defined stage–discharge relationship (also known as a rating curve equation) distributed to convert simulated discharges into water depths at the catchment scale (Getirana, 2010). Objective functions adapted to the difference between water depths and altimetric data conducted the automatic calibration process toward optimal parameter sets. The ongoing research on this issue has revealed a new hydrological model optimization procedure which does not require observed discharge data at gauge stations nor previously defined stage *versus* discharge relationships. The new approach allows one to automatically calibrate distributed hydrological models by considering only water levels derived from, for example, radar altimetry satellites. The technique is based on the coupling of an $h \times Q$ model with the optimization scheme composed of stage *versus* discharge relationships. These relationships are derived from the combination of spatial altimetry data and modelled discharges at virtual stations. The automatic calibration proceeds with the minimization of biases between discharges computed by the hydrological model and by the $h \times Q$ model coupled with the optimization scheme. The $h \times Q$ model is supplied with spatial altimetry data and modelled discharges at virtual stations and generates best fitted rating curves represented by their coefficients such as the zero-flow water height (z). The optimization process calibrates parameters of both the hydrological model and the $h \times Q$ model. The main objective of this paper is to introduce this new automatic calibration procedure and to evaluate its potential of providing accurate water discharges. An analysis is also performed in order to evaluate the sensitivity of the method to different objective functions (OFs) and rating curve equations used in the optimization scheme, and to identify which of these OFs and rating curves are the best suited for the study case.

The study area is the Branco River basin, located in the northern Amazon basin, which has a drainage area of about 190 000 km² (Fig. 1 left). The Branco River basin has mean precipitation and runoff rates of 5.6 mm/day and 2.4 mm/day, respectively. Its hydrological cycle is composed of well defined wet and dry seasons, with floods occurring between May and August, reaching peaks in June and July (Getirana *et al.*, 2010).

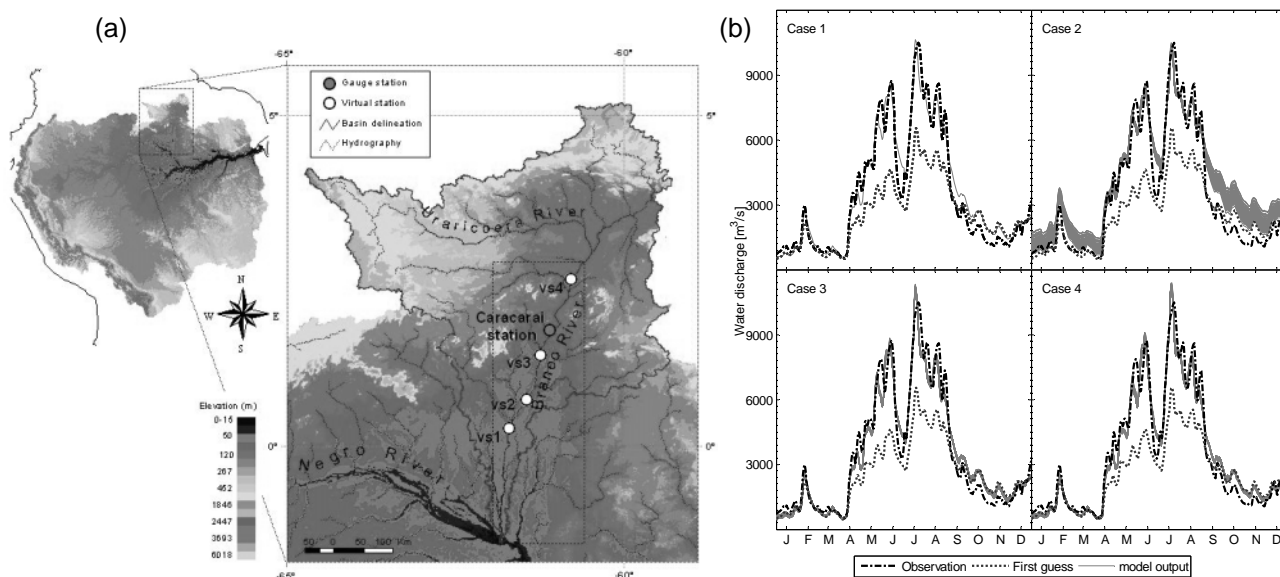


Fig. 1 (a) Location of the study area, the Branco River basin. Four virtual stations (vs1, vs2, vs3 and vs4) and one gauge station (Caracará station) are used to calibrate the hydrological model. (b) Hydrographs at the Caracará station in 2005 resulted from the four cases analysed.

DATASETS

The topography was derived from the SRTM DEM (<http://srtm.csi.cgiar.org/>). The land cover map was obtained from a classification of multi-temporal JERS-1 images, as described by Martinez & Le Toan (2007). The soil map was acquired from the Food and Agriculture Organization (FAO) database. The Branco River basin is equipped with 41 raingauge stations operated by the Brazilian Water Agency (Agência Nacional de Águas – ANA). Additional stations located within the Negro and Orinoco river basins have also been considered for creating the precipitation field of the study area. Meteorological data (air temperature and humidity, solar radiation, surface pressure and wind speed) were derived from the NCEP/DOE AMIP-II reanalysis (Roads *et al.*, 2002). Discharge data at the Caracará station are considered in this study (Fig. 1(a)). This station is located 400 km upstream of the confluence of the Branco and Negro rivers, draining an area of 126 000 km².

Data provided by the altimeter onboard the ENVISAT satellite is used in this study. Errors in altimetric time series along rivers within the Amazon basin are from 0.07 m to 0.40 m, with an average of 0.22 m (Frappart *et al.*, 2006). A comprehensive description of ENVISAT data processing and acquisition over the Negro River basin (including the Branco River basin) can be found in Roux *et al.* (2010) and Getirana *et al.* (2009b, 2010). Altimetric data at four virtual stations (vs1, vs2, vs3 and vs4) along the Branco River, from October 2002 to November 2006, are considered in this study (Fig. 1(a)). The VS provides time series with 34 to 38 altimetric observations for the study period, depending upon the track.

METHODOLOGY

Briefly, eight model parameters of the MGB-IPH hydrological model (Collischonn *et al.*, 2007) were automatically calibrated for the 2002–2006 period with the MOCOM-UA multi-criteria global optimization algorithm (Yapo *et al.*, 1998). A number, n_s , of parameter sets, including the set of initial guess parameters, were randomly distributed into a hyper-domain limited by the minimum and maximum parameters values. The parameter sets are represented by a matrix θ_0 of dimensions $[n_{vs}, n_s]$, where n_{vs} stands for the number of virtual stations. The parameter sets, together with the precipitation field, meteorological forcings, soil and land cover distribution and other topography-derived hydrological information, are used to run the MGB-IPH model

(Collischonn *et al.*, 2007; Getirana *et al.*, 2010), resulting in the vector $Q_{sim_{i,j}} = [q_{sim_{i,j,1}}, \dots, q_{sim_{i,j,k}}]$ (or simply Q_{sim}) of discharges simulated by the hydrological model, where i and j are indexes for the ns parameter sets and the nvs virtual stations, respectively, and k is the number of time steps of the altimetric time series. Altimetric data at virtual stations $H_{alt_j} = [h_{alt_{j,1}}, \dots, h_{alt_{j,k}}]$ (or simply H_{alt}) and Q_{sim} are combined in the $h \times Q$ model, resulting in best fitted rating curve equations. The combination is performed for each parameter set i , resulting in ns rating curves for each virtual station j . The H vectors are merged with rating curves of the respective virtual stations, deriving new discharges $Q'_{sim_{i,j}} = [q'_{sim_{i,j,1}}, \dots, q'_{sim_{i,j,k}}]$ (or simply Q'_{sim}). The MOCOM-UA multi-objective optimization scheme evolves the ns parameter sets by minimizing the multi-objective vector $F_{ij} = [f_{i,j,1}, \dots, f_{i,j,m}]$ (or simply F), where m is the number of objective functions. F is minimized as a function of Q_{sim} and Q'_{sim} , where the latter one stands as the target.

The application of the proposed methodology is constrained by two main conditions:

- (1) Adequate representation of the hydrological seasonality:
 - (a) by the altimetric data – the errors attributed to altimetric data must be sufficiently low and the data availability sufficiently high. The instant when data are acquired also contributes to an adequate representation of river seasonality;
 - (b) by the rainfall data – spatial and temporal distribution of rainfall over the watershed must be consistent with the “true” precipitation.
- (2) Backwater effects at virtual stations must be insignificant. This means that the stage \times discharge relationship at a given station can be represented by a single rating curve.

The $h \times Q$ model

The stage \times discharge relationship is a hydraulic property of a given river section and is unknown *a priori*. This relation must be approximated to a curve (the rating curve), normally achieved from *in situ* measures and supported by the analysis of streamflow parameters (Jacon & Cudo, 1989). In general, the stage \times discharge relationship at a river section can be expressed by mathematical expressions as a continuous curve or as successive linear reaches. The most frequently used form is the exponential one:

$$Q = a \cdot h^{b'} = a \cdot (H - z)^{b'} \quad (1)$$

where Q stands for the estimated discharge, h , H and z are the river depth, the river water height and the zero-flow water height, respectively, which can be approximated to the river bed height. a and b' are coefficients defined for a given period and location. If river depth equals zero-flow water height, the discharge provided by a rating curve is zero. The linear form of equation (1) is given as $\ln(Q) = \ln(a) + b' \cdot \ln(H - z)$.

Sets of coefficients a and b' and the zero flow height z are obtained by a single search algorithm. A range of z values are used in a linear regression and the set of coefficients that results in the best regression are considered to represent the rating curve.

Model set-up

The Branco River basin was discretized into 447 cells of sizes up to 625 km. The precipitation and meteorological forcings (temperature, air humidity, pressure and solar radiation) were spatially distributed throughout the basin using the inverse squares of distances approach. River length and slope were derived from the SRTM DEM processing. Table 1 lists the eight parameters considered in the optimization procedure. A more detailed description of these parameters can be found in Collischonn *et al.* (2007) and Getirana *et al.* (2010).

Table 1 Model parameters subjected to the automatic calibration.

Parameter	First guess	min and max values	Hydrological process
b [-]	1	[0.01–2]	Variable infiltration curve
Kint [mm.d ⁻¹]	25	[0.25–50]	Sub-surface flow
Kbas [mm.d ⁻¹]	10	[0.1–20]	Groundwater flow
CS [-]	35	[0.35–70]	Surface flow
CI [-]	100	[1–200]	Sub-surface flow
Wc [mm]	0.55 × Wm	[0.1–0.825×Wm]	Groundwater vertical flux
Wm ₁ [mm]	1500	[150–3000]	Water storage on the soil (GRU ₁)
Wm ₂ [mm]	1500	[150–3000]	Water storage on the soil (GRU ₂)

Cases

The cases have been created by combining, two by two, three performance coefficients: the Nash-Sutcliffe performance coefficient (NS), the logarithmic Nash-Sutcliffe (LNS) and the relative error (RE) of predicted discharges. They are given as:

$$NS = 1 - \frac{\sum_{t=1}^{nt} (O_t - S_t)^2}{\sum_{t=1}^{nt} (O_t - \bar{O})^2} \quad (3)$$

$$LNS = 1 - \frac{\sum_{t=1}^{nt} [\ln(O_t) - \ln(S_t)]^2}{\sum_{t=1}^{nt} [\ln(O_t) - \ln(\bar{O})]^2} \quad (4)$$

$$RE = \frac{1}{nt} \times \sum_{t=1}^{nt} \left| \frac{O_t - S_t}{O_t} \right| \quad (5)$$

where t is the time step, nt the total number of days disposing of observed data, O and S are, respectively, the target (observed) and simulated signals at time step t , and \bar{O} the mean value of the target signal for the entire period. NS and LNS range from $-\infty$ to 1, where 1 is the best optimum. RE varies from zero to $+\infty$, where zero is the optimum.

Two cases are optimized using the proposed approach with ENVISAT altimetric data at four virtual stations (Fig. 1(a)). They are composed of two pairs of objective functions. The $h \times Q$ model follows equation (1). The sets of objective functions are: $NS_H \times LNS_H$ and $NS_H \times RE_H$ (the subscript H means that performance coefficients were calculated with altimetric data). At each virtual station, a pair of performance coefficients are calculated. The objective functions used in the optimization scheme are the weighted sum of these values. For practical reasons, performance coefficients at all VS's have been weighted homogeneously.

In order to evaluate how close the proposed approach can get from standard optimization approaches (i.e. using *in situ* data), two additional cases using observed discharges at the Caracará station have been considered. They are composed of two pairs of objective functions $NS_Q \times LNS_Q$ and $NS_Q \times RE_Q$ (the subscript Q means discharge data); ns was fixed to 100.

RESULTS

Optimal solutions provided by altimetry-based cases had mean Nash-Sutcliffe values for streamflows NS_Q varying from 0.90 (case 2) to 0.94 (case 1). These values represent a significant improvement when compared to the first guess ($NS_Q = 0.65$) and are close to those obtained with discharge-based

cases 3 and 4 (0.94, as shown in Table 2). Best mean LNS_Q and RE_Q values were found in case 1 with 0.95 and 0.19, respectively. These scores are also similar to those provided by discharge-based cases ($LNS_Q = 0.95$ and $RE_Q = 0.18$) and better than the first guess ($LNS_Q = 0.84$ and $RE_Q = 0.28$). However, not all altimetry-based cases resulted in improved LNS_Q and RE_Q . For example, case 2 had mean LNS_Q and RE_Q values of 0.82 and 0.43, respectively, which are inferior to those obtained with the first guess parameter set. Figure 1(b) shows daily discharges in 2005 of the four cases. Note that case 2 (using RE_H) had more inaccurate discharges, especially in low water seasons. This resulted in LNS_Q and RE_Q with wider ranges overlapping the first guess (not shown).

Table 2 Results of the automatic calibration processes: generations and evolutions of each case, and scores NS, LNS and RE for streamflows. Scores correspond to the mean values of the ns-point population.

Case	Objective function	Generations	Evolutions	Optimal of values			Scores for streamflows		
				NS_H	LNS_H	RE_H	NS_Q	LNS_Q	RE_Q
First guess	–	–	–				0.65	0.84	0.28
1	$NS_H \times LNS_H$	3318	502	0.82	0.88	–	0.94	0.95	0.19
2	$NS_H \times RE_H$	2833	472	0.82	–	0.26	0.90	0.82	0.43
3	$NS_Q \times LNS_Q$	2925	366	–	–	–	0.94	0.95	0.18
4	$NS_Q \times RE_Q$	2911	377	–	–	–	0.94	0.95	0.18

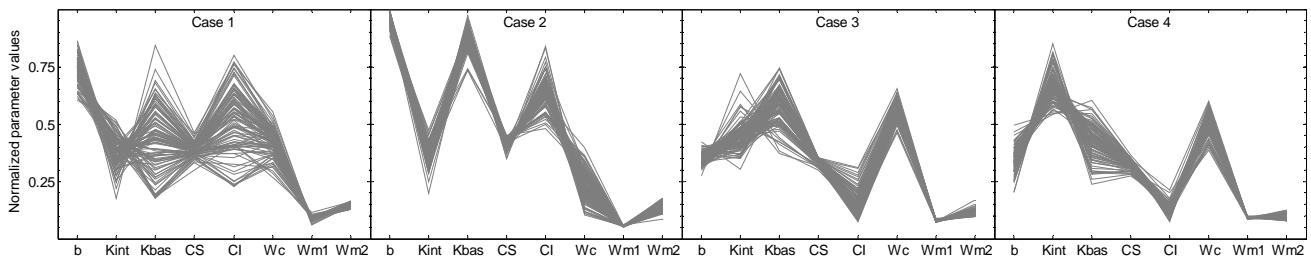


Fig. 2 Parameter sets resulted from the optimization processes.

The high heterogeneity of parameter sets is evidence that optimal results can be found with different parameterizations (Fig. 2). This can be explained by the fact that objective functions have different impacts on parameter sets, that some cases can improve discharges but not exactly refining parameters, or that there exists a compensation of parameters representing similar physical processes in the model. On the other hand, Wm_1 converged to similar values in all cases. This reveals high model sensitivity to this parameter, which is influenced significantly by the predominance of GRU_1 over the basin, covering about 77% of the draining area. The main differences between optimal parameters in discharge-based cases are observed in Kint and Kbas.

CONCLUSIONS

This study presented a new methodology to integrate radar altimetry data into the automatic calibration of distributed hydrological models by means of the coupling of an $h \times Q$ model (stage \times discharge relationships) and a multi-criteria global optimization approach. As the technique is entirely free from *in situ* discharge data, the targets of the optimization process are discharge time series derived from the rating curves fitted among radar altimetry data and discharge simulated by the model using random parameter sets.

The results show that the new methodology provides improved solutions when compared to the first guess parameter set, and can reliably reproduce observed discharges at the selected gauge station (Caracaráí station) with Nash-Sutcliffe coefficients (NS and LNS) and relative error (RE)

for discharges varying from NS = 0.90, LNS = 0.82 and RE = 0.43, to NS = 0.94, LNS = 0.95 and RE = 0.19. Also, it demonstrated its capability of providing competitive costs when compared with standard optimization approaches.

The application and adjustment of this methodology are recommended for other locations in the Amazon basin and other tropical basins. By subjecting this novel technique to different hydrological conditions and monitoring, the positive and negative aspects of the introduction of spatial altimetry data into the automatic calibration of computational models can be studied and refined.

Acknowledgements This work benefited from hydrological data made available by Agência Nacional de Águas (ANA). ENVISAT data were provided by ESA under the form of Geophysical Data Records (GDRs).

REFERENCES

- Collischonn, W., Allasia, D., Silva, B. C., Tucci, C. E. M. (2007) The MGB-IPH model for large-scale rainfall-runoff modelling. *Hydrol. Sci. J.* **52**(5), 878–895.
- Frappart, F., Calmant, S., Cauhope, M., Seyler, F. & Cazenave, A. (2006) Preliminary results of ENVISAT RA-2-derived water levels validation over the Amazon basin. *Remote Sens. Environ.* **100**(2), 252–264.
- Getirana, A. C. V., Bonnet, M. P., Rotunno Filho, O. C., Collischonn, W., Guyot, J.-L., Seyler, F. & Mansur, W. J. (2010) Hydrological modelling and water balance of the Negro River basin: evaluation based on *in situ* and spatial altimetry data. *Hydrol. Processes* **24**(22), 3219–3236. doi: 10.1002/hyp.7747.
- Getirana, A. C. V., Bonnet, M. P., Rotunno Filho, O. C. & Mansur, W. J. (2009a) Improving hydrological information acquisition from DEM processing in floodplains. *Hydrol. Processes* **23**, 502–514. doi:10.1002/hyp.7167.
- Getirana, A. C. V. (2010) Integrating spatial altimetry data into the automatic calibration of hydrological models. *J. Hydrol.* **387**, 244–255. doi:10.1016/j.jhydrol.2010.04.013.
- Jacon, G. & Cudo, K. J. (1989) *Curva-chave: análise e tratado*. DNAEE.
- Martinez, J.-M. & Le Toan, T. (2007) Mapping of flood dynamics and spatial distribution of vegetation in the Amazon floodplain using multitemporal SAR data. *Remote Sens. Environ.* **108**(3), 209–223. doi:10.1016/j.rse.2006.11.012.
- Pareto, V. (1971) *Manual of Political Economy*. A.M. Kelley, New York, USA.
- Roux, E., Silva, J. S., Getirana, A. C. V., Bonnet, M.-P., Calmant, S. & Seyler, F. (2010) Producing time-series of river water height by means of satellite radar altimetry – comparison of methods. *Hydrol. Sci. J.* **55**(1), 104–120. doi:10.1080/02626660903529023.
- Yapo, P. O., Gupta, H. V. & Sorooshian, S. (1998) Multi-objective global optimization for hydrologic models. *J. Hydrol.* **204**, 83–97.

Informing hydrological models with ground-based time-lapse relative gravimetry: potential and limitations

PETER BAUER-GOTTWEIN¹, LARS CHRISTIANSEN² & DAN ROSBJERG¹

¹ DTU Environment, Kgs. Lyngby, Denmark

pbau@env.dtu.dk

² COWI A/S, Kgs. Lyngby, Denmark

Abstract Coupled hydrogeophysical inversion emerges as an attractive option to improve the calibration and predictive capability of hydrological models. Recently, ground-based time-lapse relative gravity (TLRG) measurements have attracted increasing interest because there is a direct relationship between the signal and the change in water mass stored in the subsurface. Thus, no petrophysical relationship is required for coupled hydrogeophysical inversion. Two hydrological events were monitored with TLRG. One was a natural flooding event in the periphery of the Okavango Delta, Botswana, and one was a forced infiltration experiment in Denmark. The natural flooding event caused a spatio-temporally distributed increase in bank storage in an alluvial aquifer. The storage change was measured using both TLRG and traditional piezometers. A groundwater model was conditioned on both the TLRG and piezometer data. Model parameter uncertainty decreased significantly when TLRG data was included in the inversion. The forced infiltration experiment caused changes in unsaturated zone storage, which were monitored using TLRG and ground-penetrating radar. A numerical unsaturated zone model was subsequently conditioned on both data types. Inclusion of TLRG data again led to a significant decrease in parameter uncertainty. Both experiments indicate that TLRG data are useful for hydrological model calibration. However, application of TLRG in hydrology remains challenging, because of limited instrument sensitivity, time changes in gravity due to unmonitored non-hydrological effects, and the requirement of a gravitationally stable reference station. Application of TLRG in hydrology should be combined with other geophysical and/or traditional monitoring methods.

Key words hydrological model calibration; time-lapse gravity; groundwater; vadose zone

INTRODUCTION

Over the past 20 years, research in the field of hydrogeophysics has focused on the use of geophysical observations for improved monitoring, characterization and simulation of hydrological processes. Hinnell *et al.* (2010) have recently completed an overview of the different approaches used to extract hydrological information from geophysical signals. They differentiate between uncoupled and coupled hydrogeophysical inversion (HGI). In uncoupled HGI, a traditional geophysical inversion is completed first, which provides the subsurface distribution of a geophysical parameter, e.g. electric conductivity. The geophysical parameter is subsequently transformed into a hydrological state using a petrophysical relationship such as Archie's law. Finally, geophysical observations and traditional observations of the hydrologic state are used in hydrological model calibration. In contrast, in coupled HGI, a hydrological model run is performed with an initial set of hydrological model parameters. Subsequently, a geophysical forward model run transforms the simulated hydrological states into simulated geophysical observations. The fits and sensitivities of both the simulated hydrological observations and the simulated geophysical observations are then used to update the hydrological parameters iteratively. Among the applications of coupled HGI are solute transport modelling (e.g. Kemna *et al.*, 2002), and vadose zone flow (e.g. Kowalsky *et al.*, 2004).

We present a coupled HGI approach to hydrogravity and demonstrate its utility with two field applications. Due to the success of GRACE and due to a new generation of absolute and relative gravimeters, interest in ground-based hydrogravity applications has been increasing over the past few years. Recent contributions to the field include both synthetic studies (Damiata & Lee, 2006; Blainey *et al.*, 2007) and field applications. Creutzfeld *et al.* (2008, 2010) assessed hydrological gravity signals around the Wettzell superconducting gravimeter, both from a geodetic and hydrological perspective. From a geodesist's point of view, hydrological gravity signals are part of the noise, and the aim is to efficiently remove hydrological noise from the signal. From a hydrologist's point of view, the hydrological contributions are the most valuable part of the total

gravity signal. Krause *et al.* (2009) and Naujoks *et al.* (2010) performed similar work for the Moxa superconducting gravimeter site. Jacob *et al.* (2008, 2009, 2010) used both absolute and relative gravimetry to investigate karst hydrology. Their work included both time-lapse and gradient observations of the gravity field. Pfeffer *et al.* (2010) jointly used absolute gravimetry and magnetic resonance sounding to quantify the annual water storage variation in western Africa.

All the cited studies confirm that ground-based relative and absolute gravimetry are sufficiently sensitive to detect hydrological storage variations. The detection limit depends on the measurement technique and the time scale of the hydrological process of interest. Time-lapse gravity observations can thus be used along with traditional hydrological observations in a coupled HGI framework. For two main reasons, time-lapse gravity is particularly attractive for this type of application: (i) gravimetry directly senses mass, i.e. no petrophysical relationship is required to convert the geophysical parameter to the hydrological state, and (ii) there is no other non-invasive technology that can monitor water storage changes in the subsurface. Coupled HGI using time-lapse gravity data thus has the potential to significantly reduce hydrological model parameter uncertainty and increase the predictive capabilities of operational hydrological models.

MATERIALS AND METHODS

Ground-based time-lapse relative gravimetry (TLRG)

We used ground-based TLRG to monitor local hydrological storage changes that occur over a relatively short time period (typically a few weeks). Repeated measurement of a gravity network is an efficient approach in this case. The gravity network included a reference station, which was located sufficiently far from the local hydrological storage change, along with several measurement stations. The gravity reading at the reference station was thus not affected by the hydrological storage change of interest and only reflected large-scale effects such as the tides, ocean loading, atmospheric pressure variations and continental hydrology. As all relative gravimeters exhibit instrument drift, each repeated measurement of the gravity network included several re-occupations of the reference station and the measurement stations. A detailed description of the TLRG measurement method for hydrological targets is provided in Christiansen *et al.* (2011c). The processed dataset consisted of a time series of gravity differences for each measurement station:

$$\Delta g_i(t) = g_i(t) - g_r(t) \quad (1)$$

In this formula, $g_i(t)$ indicates the gravity value recorded at time t and station i and $g_r(t)$ is the gravity value recorded at time t at the reference station. Typically, the differences can be determined with an accuracy of about 4 μGal ($= 4 \times 10^{-8} \text{ ms}^{-2}$) using the Scintrex CG-5 relative gravimeter.

Modelling TLRG signals caused by hydrological storage changes

Hydrological time-lapse gravity signals are caused by changes in subsurface density, which are due to water content changes. In principle, a ground-based gravity measurement integrates over all density changes occurring at any distance from the instrument. However, contributions are weighted with an inverse square distance weight. Using Newton's law, the gravity change observed at site i and caused by a spatially distributed density change ($\Delta\rho$) can be expressed as:

$$\Delta g = \int_{-\infty}^{+\infty} \int_{-\infty}^{+\infty} \int_{-\infty}^{+\infty} \gamma \cdot \Delta\rho(x, y, z) \cdot \frac{-(z - z_i)}{\left((x - x_i)^2 + (y - y_i)^2 + (z - z_i)^2\right)^{3/2}} dz dy dx \quad (2)$$

where γ is the universal gravitational constant ($6.67 \times 10^{-11} \text{ Nm}^2 \text{ kg}^{-2}$). In practical applications, the integration can be truncated at finite distances from the gravimeter (Leiriao *et al.*, 2009). For shallow groundwater systems, where total water storage change is dominated by groundwater storage change, the region of density change will be the region between the groundwater tables at

the beginning and at the end of the time-lapse interval. In vadose zone systems, water content will change throughout the soil profile, but may change by variable amounts at different depths. Leiriao *et al.* (2009) presented an efficient algorithm to transform water storage variations computed by finite-difference hydrological models into time-lapse gravity signals using equation (2). We use this algorithm in combination with a groundwater model for the Okavango Delta case study, and in combination with a 1-D vadose zone model in the forced infiltration case study.

Coupled hydrogeophysical inversion using TLRG data

Figure 1 presents a flow chart for the coupled HGI scheme used in this study. The workflow started with the development of a conceptual hydrological model, the preparation of the hydrological forcings and the development of *a priori* parameter estimates. Subsequently, a numerical hydrological model was implemented. The model run produced simulated hydrological observations. Simulated hydrological states were converted into simulated TLRG observations using the algorithm of Leiriao *et al.* (2009). An overall objective function is computed from the fit of both the hydrological and TLRG observations. Subsequently, the parameter estimates are iteratively adjusted using a Levenberg-Marquardt gradient search method.

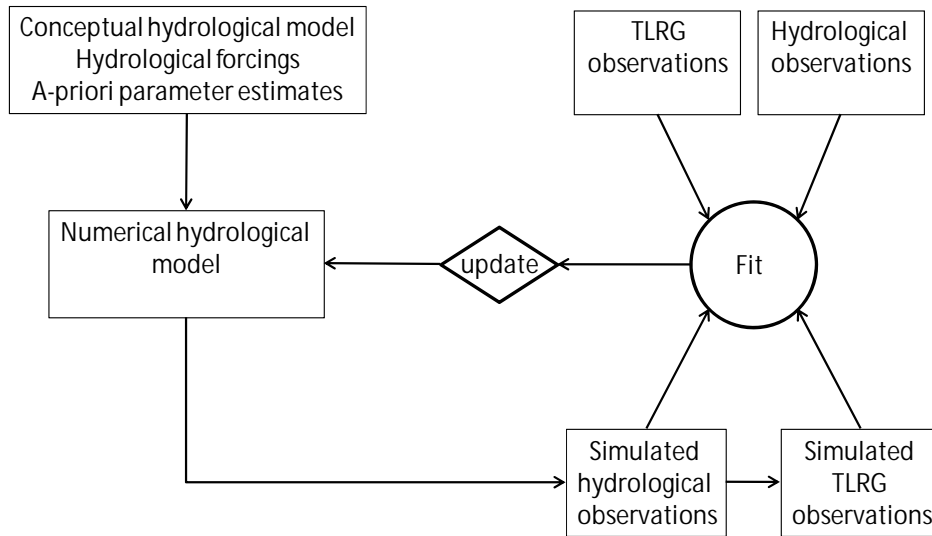


Fig. 1 Flowchart of the coupled hydrogeophysical inversion scheme using TLRG data.

For the evaluation of the fit, the following objective function was used:

$$\begin{aligned}\Phi_{total} &= (1 - w) \cdot \Phi_h + w \cdot \Phi_{\Delta g} \\ \Phi_h &= (n_h \cdot \sigma_h^2)^{-1} \sum_{i=1}^{n_h} (h_{obs,i} - h_{sim,i})^2 \\ \Phi_{\Delta g} &= (n_{\Delta g} \cdot \sigma_{\Delta g}^2)^{-1} \sum_{i=1}^{n_{\Delta g}} (\Delta g_{obs,i} - \Delta g_{sim,i})^2\end{aligned}\quad (3)$$

In this formula, w denotes a subjective weight placed on the gravity observations, n is the number of observations, σ are the standard errors of the observations, h stands for hydrological observations and Δg for TLRG observations. The parameter covariance matrix is computed from the residuals and the Jacobian matrix at the calibrated solution. Parameter confidence intervals are subsequently computed from the parameter covariance matrix.

RESULTS

Natural river bank storage in the Okavango Delta

In this case study, TLRG data were used in a coupled HGI approach to inform a groundwater flow model of an alluvial aquifer. Details of the study are presented in Christiansen *et al.* (2011a). The case study location is the periphery of the Okavango Delta in Botswana, Southern Africa. The Okavango Delta is characterized by significant seasonal flooding dynamics (Milzow *et al.*, 2009). Due to the sandy geology of the area, rivers are usually in good hydraulic contact with the surrounding alluvial aquifers. The alluvial aquifers are recharged by the annual flood event and are subsequently depleted by phreatic evapotranspiration. This leads to seasonal groundwater level fluctuations between 2 and 3 m. Many of the aquifers are used for rural water supply and their sustainable yield is of concern in groundwater resources management. Due to its ability to directly sense water mass, TLRG offers a unique opportunity to determine the specific yield of the aquifers.

Figure 2 shows the dataset of hydrological and TLRG observations. The observations are aligned along a transect perpendicular to the river. The figure also shows the simulated observations produced by the calibrated groundwater model. The groundwater model is set up as a single-layer vertical cross-section model, with a time-variable Cauchy boundary condition representing the river and a diffuse sink term due to phreatic evapotranspiration. The four calibration parameters are the hydraulic conductivity of the aquifer, the specific yield, the riverbed hydraulic conductance and the evapotranspiration rate.

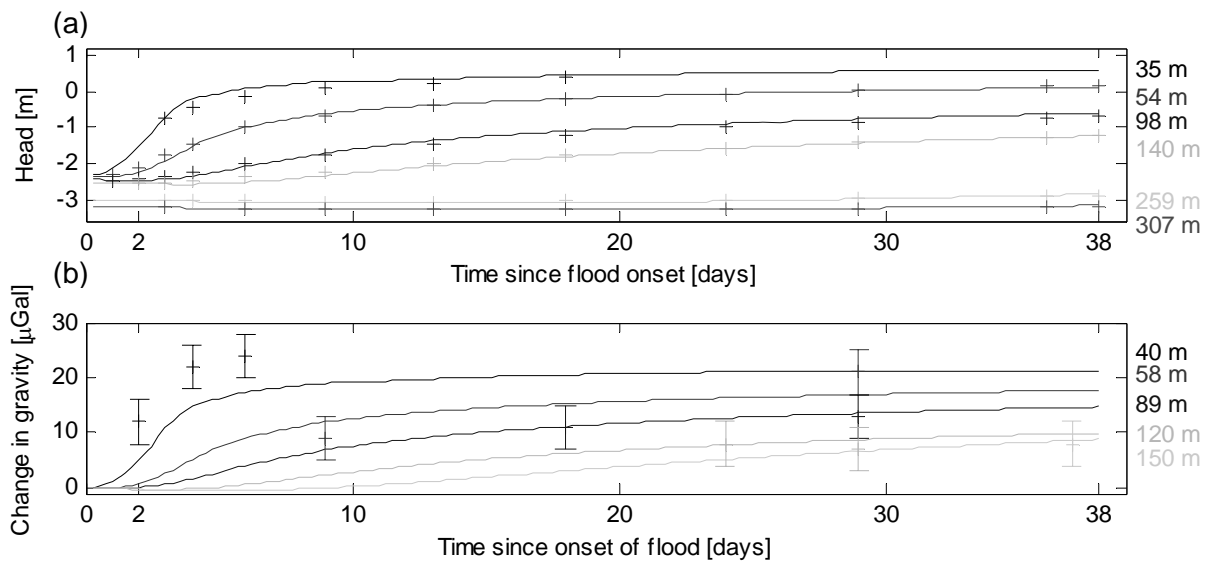


Fig. 2 Monitoring natural river bank storage in the Okavango Delta using (a) piezometers and (b) TLRG. Distances are given in metres from the centre of the river. Solid lines are model results, markers are field data. Markers in the TLRG chart indicate one standard deviation.

If only hydraulic heads are used as calibration observations ($w = 0$ in equation (3)), parameter confidence intervals become very wide and parameter correlation coefficients are all close to one. The head dataset clearly contains insufficient information to constrain the four parameters of this model. However, if TLRG data are injected into the HGI using a weight of $w = 0.5$, all parameters become identifiable and the parameter correlation coefficients are reduced significantly. A weight of $w = 0.5$ implies that all observations are weighted with their standard error, irrespective of the type of observation. Table 1 shows the fitted parameter values and corresponding 90% confidence intervals for $w = 0.5$. For $w = 1$ (gravity observations only) no unique solution can be found for the calibration problem, because the fitted parameters are highly correlated.

Table 1 Fitted parameter values and 90% parameter confidence intervals (CI) for $w = 0.5$. K, hydraulic conductivity; SY, specific yield; C_{riv} , riverbed conductance; ET, evapotranspiration rate.

K (m/day)	CI of K	SY (-)	CI of SY	C_{riv} (m ² /day)	CI of C_{riv}	ET (m/day)	CI of ET
9.58	7.96–11.54	0.21	0.18–0.24	4464	3118–6390	1.9×10^{-3}	1.4×10^{-3} – 2.7×10^{-3}

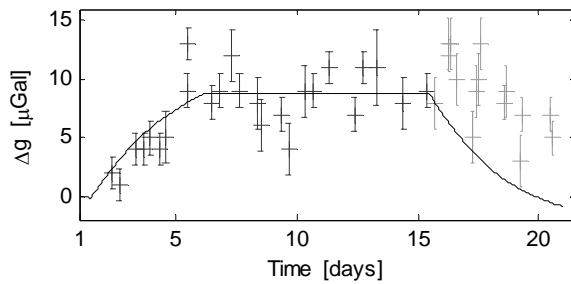


Fig. 3 Forced infiltration in Denmark monitored with TLRG. The solid line is the calibration curve produced by the first HGI trial (fitting θ_s only). Markers indicate field data with one standard deviation. Grey field data were not included in the HGI.

Forced infiltration in Denmark

In this case study, TLRG data were used in a coupled HGI approach to inform a 1-D vadose zone model. Details of the study are presented in Christiansen *et al.* (2011b). The rationale behind the field experiment was to find to what extent TLRG can be used to non-invasively determine the van Genuchten parameters of a soil under forced infiltration. Forced infiltration was performed over a square area of 107 m². A reference gravity station was established about 50 m from the infiltration plot and TLRG data were collected at intervals over the irrigation period of 14 days and the following drainage period.

Figure 3 shows the dataset, which in this case consists of TLRG observations only. All observations are taken at the centre of the infiltration plot. The figure also shows the simulated observations produced by the calibrated 1-D vadose zone model, which solves the Richards equation with the van Genuchten parameterization of the retention curve and the unsaturated hydraulic conductivity.

Different calibration trials were performed. It was found that the HGI had a stable and unique solution if only the saturated water content (θ_s) of the soil was adjusted and all other parameters were fixed at their *a priori* values. Likewise, the saturated hydraulic conductivity (K_s) could be determined, if all other parameters were held fixed. The only combinations of two free parameters that resulted in well posed hydrogeophysical inverse problems were θ_s and K_s and θ_s and van Genuchten’s n , respectively. Table 2 shows the fitted parameter values and the corresponding 90% confidence intervals for the four HGI runs.

In both field applications (Okavango and Denmark), the drift of the relative gravimeter was removed from the TLRG observations using least squares network adjustment (Hwang *et al.*, 2002). The gravity differences used in the calibration could be determined with an accuracy of about 3 μ Gal, depending on site conditions.

Table 2 Fitted parameter values and 90% parameter confidence intervals for the different HGI trials.

HGI trial	θ_s (-)	CI of θ_s	K_s (m/s)	CI of K_s	n (-)	CI of n
θ_s	0.32	0.30–0.34				
K_s			6.99×10^{-5}	4.98×10^{-5} – 9.80×10^{-5}		
θ_s, K_s	0.48	0.42–0.54	12.72×10^{-5}	6.27×10^{-5} – 2.58×10^{-4}		
θ_s, n	0.21	8.9×10^{-2} –0.50			1.48	0.55–3.99

DISCUSSION AND CONCLUSIONS

The two presented case studies demonstrate that TLRG can deliver valuable data for HGI for both groundwater and vadose zone models. TLRG is a powerful tool if the hydrological storage change of interest is spatially confined to a relatively small area. This allows for the establishment of a stable reference station outside the radius of influence of the storage change. Large-scale storage changes must be investigated using absolute gravimetry. Both studies show that signal-to-noise ratios of TLRG are still quite low for typical hydrological storage changes. This is not so much an issue of instrument sensitivity as of our ability to accurately predict and remove non-hydrological time-lapse gravity effects. Such effects can be on the order of several micro-Gals and are thus of the same magnitude as many hydrological signals. One way to overcome this limitation in the future may be gravity gradiometry, where two gravimeters are used to measure simultaneously at a given horizontal or vertical separation. The advantage of gradiometry is that large-scale non-hydrological time-lapse effects will cancel out. A particularly attractive option appears to be vertical gradiometry in boreholes. If the two instruments can be placed such that one is above and one below the hydrological storage change of interest, signal-to-noise ratios can be doubled.

TLRG data lends itself ideally for inclusion into HGI. No petrophysical relationship is required to convert the hydrological model states to the geophysical signals. Moreover, time-lapse gravity is the only non-invasive technique that provides data on water storage change in the subsurface. When used in HGI, TLRG data should and typically will be combined with other data types. The issue of weighting the different data types remains an interesting research topic and will become more important as more and more geophysical data types are injected into HGI. In the context of hydrogravimetry, HGI has significant advantages over traditional inversion of gravity data. Due to the equivalence problem in gravity surveying, traditional inversion of gravity data is difficult, particularly if only a few stations are available such as in the TLRG studies presented above. Inverting for a spatially distributed subsurface density distribution based on a regular grid using the few TLRG measurements would most likely not result in a unique solution. The hydrological models thus inject essential constraining information into the inverse problem.

REFERENCES

- Blainey, J. B., Ferre, T. P. A. & Cordova, J. T. (2007) Assessing the likely value of gravity and drawdown measurements to constrain estimates of hydraulic conductivity and specific yield during unconfined aquifer testing. *Water Resour. Res.* **43**(12).
- Christiansen, L., Binning, P., Rosbjerg, D., Andersen, O. B. & Bauer-Gottwein, P. (2011a) Using time-lapse gravity for groundwater model calibration: An application to alluvial aquifer storage. *Water Resour. Res.* doi:10.1029/2010WR009859.
- Christiansen, L., Haarder, E. B., Hansen, A. B., Looms, M. C., Binning, P., Rosbjerg, D., Andersen, O. B. & Bauer-Gottwein, P. (2011b) Calibrating unsaturated zone models with time-lapse gravity data. *Vadose Zone Journal* (in press).
- Christiansen, L., Lund, S., Andersen, O. B., Binning, P., Rosbjerg, D. & Bauer-Gottwein, P. (2011c) Measuring gravity change caused by water storage variations: performance assesment under controlled conditions. *J. Hydrol.* doi:10.1016/j.jhydrol.2011.03.004.
- Creutzfeldt, B., Guntner, A., Klugel, T. & Wziontek, H. (2008) Simulating the influence of water storage changes on the superconducting gravimeter of the Geodetic Observatory Wettzell, Germany. *Geophysics* **73**(6): WA95–WA104.
- Creutzfeldt, B., Guntner, A., Vorogushyn, S. & Merz, B. (2010) The benefits of gravimeter observations for modelling water storage changes at the field scale. *Hydrol. Earth System Sci.* **14**(9), 1715–1730.
- Damiata, B. N. & Lee, T. C. (2006) Simulated gravitational response to hydraulic testing of unconfined aquifers. *J. Hydrol.* **318**(1–4), 348–359.
- Hinnell, A. C., Ferre, T. P. A., Vrugt, J. A., Huisman, J. A., Moysey, S., Rings, J. & Kowalsky, M. B. (2010) Improved extraction of hydrologic information from geophysical data through coupled hydrogeophysical inversion. *Water Resour. Res.* **46**, W00D40.
- Hwang, C. W., Wang, C. G. & Lee, L. H. (2002) Adjustment of relative gravity measurements using weighted and datum-free constraints. *Computers & Geosciences* **28**(9), 1005–1015.
- Jacob, T., Bayer, R., Chery, J., Jourde, H., Le Moigne, N., Boy, J. P., Hinderer, J., Luck, B. & Brunet, P. (2008) Absolute gravity monitoring of water storage variation in a karst aquifer on the larzac plateau (Southern France). *J. Hydrol.* **359**(1–2), 105–117.
- Jacob, T., Bayer, R., Chery, J. & Le Moigne, N. (2010) Time-lapse microgravity surveys reveal water storage heterogeneity of a karst aquifer. *J. Geophys. Res. – Solid Earth* **115**.
- Jacob, T., Chery, J., Bayer, R., Le Moigne, N., Boy, J. P., Vernant, P. & Boudin, F. (2009) Time-lapse surface to depth gravity measurements on a karst system reveal the dominant role of the epikarst as a water storage entity. *Geophys. J. Int.* **177**(2), 347–360.

- Kemna, A., Vanderborght, J., Kulesa, B. & Vereecken, H. (2002) Imaging and characterisation of subsurface solute transport using electrical resistivity tomography (ERT) and equivalent transport models. *J. Hydrol.* **267**(3–4), 125–146.
- Kowalsky, M. B., Finsterle, S. & Rubin, Y. (2004) Estimating flow parameter distributions using ground-penetrating radar and hydrological measurements during transient flow in the vadose zone. *Adv. Water Resour.* **27**(6), 583–599.
- Krause, P., Naujoks, M., Fink, M. & Kroner, C. (2009) The impact of soil moisture changes on gravity residuals obtained with a superconducting gravimeter. *J. Hydrol.* **373**(1–2), 151–163.
- Leiriao, S., He, X., Christiansen, L., Andersen, O. B. & Bauer-Gottwein, P. (2009) Calculation of the temporal gravity variation from spatially variable water storage change in soils and aquifers. *J. Hydrol.* **365**(3–4), 302–309.
- Milzow, C., Kgotlhang, L., Bauer-Gottwein, P., Meier, P. & Kinzelbach, W. (2009) Regional review: the hydrology of the Okavango Delta, Botswana—processes, data and modelling. *Hydrogeol. J.* **17**(6), 1297–1328.
- Naujoks, M., Kroner, C., Weise, A., Jahr, T., Krause, P. & Eisner, S. (2010) Evaluating local hydrological modelling by temporal gravity observations and a gravimetric three-dimensional model. *Geophys. J. Int.* **182**(1), 233–249.
- Pfeffer, J., Boucher, M., Hinderer, J., Favreau, G., Boy, J. P., de Linage, C., Cappelaere, B., Luck, B., Oi, M. & Le Moigne, N. (2010) Local and global hydrological contributions to time-variable gravity in Southwest Niger. *Geophys. J. Int.* (in press).

Key word index

- actual ET, 133
- Alps, 163
- Amazon basin, 72
- AMSR-E, 9
- arid regions, 92
- ASTER, 53
- at-a-station hydraulic geometry, 59
- atmosphere–land interaction, 110
- Australia, 41, 53, 133
- Australia
 - Western Australia, 3
- automatic calibration, 181

- China, north, 118
- climate change, 34
- COSMIC, 169
- cracks, 28

- Distributed Temperature Sensing, DTS,
 - 140

- EGM 2008, 16
- energy balance, 151
- evaporative fraction, 47
- evapotranspiration, 145, 157

- fissures, 28
- flood monitoring, 78
- fluvial erosion, 163

- geoid, 16
- geoidal slope, 16
- GIS, 163
- global, 104
- GPS RO, 169
- GRACE satellites, 16
- GRACE, 9, 28
- gravity monitoring, 34
- gravity, 16
- gridded Xinanpang model, 85
- ground-based IIRAR, 163

- groundwater, 22, 66, 187
- groundwater
 - assessment, 4

- hydrodynamic modelling, 22
- hydrogeology, 3

- hydrological model calibration, 187
- hydrological modelling, 22, 72, 181

- in situ* and satellite data, 110
- Indo-Gangetic plains, 28
- Indus Plain, 16
- Inner Niger Delta, 78
- irrigated agriculture, 157
- irrigation, 133
- irrigation
 - areas, 53
 - system, 125
- Italy, 163

- lake, 104
- Land Surface Diversions, 41
- land surface
 - heat fluxes, 53
 - temperature, 47
- LAS, evapotranspiration, 151
- latent heat flux, 151
- long term, 98
- lysimeter, 145

- Mali, 78
- mass change, 34
- Mishui Basin, 85
- MODIS, 41
- Murrumbidgee, 151

- passive microwave, 98
- Peninsular shield, 28
- Penman-Monteith model, 145
- principal component analysis, 9

- Radarsat-2, 78
- rainfall, 28
- rainfall–runoff model, 59
- rating curve, 181
- refractive index, 151
- remote sensing, 9, 22, 28, 125, 133, 157
- risk assessment, 175
- risk map, 175
- river, 66, 104
- river cross-sectional water surface
 - width, 59
- river
 - discharge, 59

- root zone soil moisture, 118
- RS, 41
- SAM-ET, 41, 133
- satellite
 - altimetry, 92, 104
 - GRACE, 3
 - gravimetry, 9
 - precipitation product, 85
- scatterometer, 118
- scintillometer, 151
- SEBS, 53
- sensible heat flux, 151
- soil
 - heat flux, 140
 - moisture, 9, 28, 92
- spatial
 - altimetry, 181
 - resolution, 175
 - variability, 140
- SPOT, 78
- steep slopes, 163
- storage change, 34
- streamflow simulation, 85
- surface
 - energy balance, 140
 - heat fluxes, 110
 - resistance, 145
 - waters, 22
- synthetic aperture radar, 59
- tank cascade, 125
- temporal resolution, 175
- terrestrial laserscanning, 163
- Thailand, 175
- Third Pole, 110
- Tibetan Plateau, 169
- time-lapse gravity, 187
- TOA radiance, 47
- Todorovic method, 145
- total column water vapour, 169
- TPE, 110
- TRMM, 72
- Tubma basin, 175
- unaccounted water, 41
- vadose zone, 187
- vegetation density, 98
- VIP model, 118
- water, 66
- water
 - availability, 175
 - balance, 125, 175
 - management, 157
 - vapour, 169
- Western Australia, 3
- WGHM, 9